THÈSE

En vue de l'obtention de

L'HABILITATION À DIRIGER LES RECHERCHES DE L'UNIVERSITÉ DE TOULOUSE

Délivré par : *l'Université Toulouse 3 Paul Sabatier (UT3 Paul Sabatier)*

Présentée et soutenue le *04/12/2014* **par :**

Guillaume PUIGT

CFD dedicated techniques applied to industrial problems

JURY

Christophe AIRIAU	Professeur d'Université	Membre du Jury
Frédéric ALAUZET	Directeur de Recherches	Président du Jury
Bertrand AUPOIX	Directeur de Recherches	Membre du Jury
Paola CINNELLA	Professeur d'Université	Membre du Jury
Robert KERR	Professeur d'Université	Membre du Jury
Pierre-Henri MAIRE	Professeur d'Université	Membre du Jury

École doctorale et spécialité :
MEGEP : Dynamique des fluides
Unité de Recherche :
Centre Européen de Recherche et de Formation Avancée en Calcul Scientifique
Parrain de l'Habilitation à Diriger les Recherches :
Bertrand AUPOIX
Rapporteurs :
Paola CINNELLA, *Robert KERR* et *Pierre-Henri MAIRE*

Contents

Disons qu'en mathématiques, il y a deux sources inépuisables de phénomènes à l'état brut qui sont, d'un côté l'arithmétique, et, d'un autre, la physique. Alain Connes.

Scientific advice: "In CFD as in computer science, never forget PEBKAC[1]*!"*

---

[1] Problem Exists Between Keyboard And Chair

Acknowledgements

C'est un très grand plaisir pour moi d'écrire ces lignes. D'abord parce que ce sont les seules lignes en Français de ce document. Surtout, parce que ce sont les mots de la fin qu'on place au début... Drôle de retournement de situation? Encore un truc typique des papiers scientifiques pour lesquels on commence toujours par le document et on finit par l'introduction... Est-ce que j'arriverai à rédiger un jour un papier dans un ordre non chronologique ? Sans doute pas? "But! Yes! This is the end!" La rédaction du manuscrit et la soutenance sont aujourd'hui derrière moi.

Je commencerai par remercier les trois rapporteurs pour tout le travail qu'ils ont fait, en commençant par lire ce document. Sans eux, point de salut... et surtout point de soutenance... Merci beaucoup Paola Cinnella, Pierre-Henri Maire et Robert Kerr pour le temps que vous m'avez accordé ! Paola et Pierre-Henri, je suis ravi qu'on ait réussi à contourner toutes les difficultés informatiques de la soutenance en webex et je n'oublierai pas que je vous dois une (vraie !) coupe de champagne. Mes remerciements vont également à Frédéric Alauzet et Christophe Airiau qui ont accepté d'être président et examinateur de ce travail. Frédéric, tu as un statut à part parce que cela fait plus de 10 ans qu'on se connaît mais on n'a jamais travaillé ensemble ! Je retiens ta proposition de collaboration sur les maillages courbes. Christophe, c'est notre ami commun Hugues Deniau qui nous a introduit pour Aerotranet-2. Je tiens à te remercier pour plusieurs choses : d'abord, pour avoir accepté de participer au jury de cette HDR dès que je te l'ai proposé, ensuite parce que j'apprécie beaucoup travailler avec toi, enfin, parce que j'ai trouvé en toi un fan de la planète Dagobah ! On est plusieurs au CERFACS à partager cette culture... Y'a même une machine Dagobah, c'est tout dire !

Bertrand Aupoix mérite à lui seul un remerciement spécifique. D'abord, parce que Bertrand a été l'homme providentiel : j'ai commencé par prendre contact avec Grégoire Casalis pour la procédure d'HDR et il m'a immédiatement conseillé de te voir. Choix plus que judicieux car j'ai vu en toi un parrain exceptionnel. D'abord, parce que tu as participé à l'amélioration du manuscrit. Grâce à tes papiers sur les modèles de turbulence, j'ai pu continuer à apprendre sur le sujet. C'est une thématique que je n'adressais plus depuis longtemps. Ensuite, tu m'as époustouflé en me sortant tes papiers qui contiennent une analyse mathématique des modèles de turbulence. Enfin, tu m'as parfaitement aiguillé pour la soutenance. Tu as vu que j'avais l'habitude des séminaires industriels, mais grâce à toi, j'ai corrigé le tir et j'espère t'avoir convaincu que je pouvais aussi faire des séminaires académiques. Aux lecteurs motivés par une HDR, allez voir Bertrand !

Vous six, membres du jury de mon HDR, je vous remercie encore une fois pour votre implication dans ce projet !

Une HDR est aussi une tranche de vie. Cette thèse n'aurait pas pu être menée à son terme sans la participation active de ma famille. D'abord Jessica et mes enfants Lily et Rafael qui m'ont soutenu au quotidien et qui ont fait preuve de beaucoup de patience durant ces 9 derniers mois. Maintenant, je vais avoir à nouveau du temps pour vous ! Ensuite, mes parents qui eux aussi m'ont poussé dans cette voie de l'HDR et en plus, ils se sont occupés du pot ! Enfin, mes frères, beaux frères et belles sœurs qui m'ont fait le plaisir d'être là physiquement ou par la pensée.

Je remercie également mes collègues en commençant par celui qui partage mon bureau Marc Montagnac. Je te promets que je vais moins pester sur mon anglais médiocre et que je vais pouvoir maintenant "retravailler normalement". En tout cas, j'espère arriver à te motiver assez pour que tu suives la même route que moi ! Mon chef Jean-François Boussuge a permis que cette thèse soit rédigée en libérant mon emploi du temps plus que chargé : 100 000 mercis car rien n'aurait avancé sans cela. Enfin, Jean-Christophe Jouhaud a été un "détonateur" : je te libère maintenant de l' "encadrement" des doctorants en méthodes numériques pour la CFD.

En guise de conclusion, je souhaite remercier ici toutes les personnes qui se sont associées, de près ou de loin, aux différents résultats de ce manuscrit et à l'organisation de cette HDR (Merci Marie !). Je ne citerai personne pour être sûr de n'oublier personne dans cette liste! Mais j'ai une pensée spéciale pour les personnes associées aux perspectives introduites brièvement dans ce document : presque toutes les questions du jury ont porté sur nos travaux communs. Ce document est donc aussi la reconnaissance du travail des chercheurs post-doctorants Nadège Villedieu et Guillaume Daviller, des doctorants Pierre Cayot, Carlos Pérez Arroyo, Sophie Le Bras, Christophe Coreixas, Julien Vanharen, des stagiaires Marie Lemesle, Isabelle Marter, Aurélien Genot et David De Oliveira Amorin et de l'ingénieur HPC Adrien Cassagne.

Merci à tous !

Symbols and mathematical notations

Basic physical quantities

The physical domain of interest is assumed to be the open space Ω of $\mathbb{R}^n$ ($n = 2$ or $n = 3$) and it is analysed during a time interval $[0,T']$. The following symbols will represent physical quantities:

- $x \in \Omega$: a point inside Ω,
- $t \in [0, T']$: a time instant,
- $(x, t) \in \Omega \times [0, T']$ is the couple to define any quantity depending on both space position and time instant,
- $\rho(x, t) \in \mathbb{R}_+^*$: density in $kg.m^{-3}$,
- $\vec{u}(x, t) \in \mathbb{R}^k$: velocity vector in $m.s^{-1}$,
- $p(x, t) \in \mathbb{R}_+^*$: pressure in Pa,
- $e(x, t) \in \mathbb{R}_+^*$: specific internal energy in $m^2.s^{-2}.kg^{-1}$,
- $T(x, t) \in \mathbb{R}_+^*$: temperature associated with internal energy in K,

Mathematical functions / operators

This thesis is devoted to the analysis of partial differential equations which are composed of different mathematical operators. In this section, f represents a function, $\vec{g}$ and $\vec{l}$ are vectors (which components are g_i and l_i respectively) and A and B are two matrices. All quantities are assumed to depend on both space and time. Let:

- $\partial_t f = \dfrac{\partial f}{\partial t}$ represent the derivative of f with respect to the time t,
- $\partial_j f = \dfrac{\partial f}{\partial x_j}$ represent the derivative of f with respect to the $j - th$ space direction,
- ∇f be the gradient of f, a vector which components are the derivatives of f with respect to all space directions,
- $\nabla \vec{g}$ be a second order tensor such that $(\nabla \vec{g})_{ij} = \partial_i g_j$

- $\nabla \cdot \vec{g}$ be the divergence of $\vec{g}$: $\nabla \cdot \vec{g} = \sum\limits_i \partial_i g_i$,

- $\nabla \cdot A$ be a vector which *j-th* component is: $\sum\limits_i \partial_i A_{ji}$,

- $\vec{g} \cdot \vec{l}$ be the scalar product: $\vec{g} \cdot \vec{l} = \sum\limits_i g_i l_i$,

- $\vec{g} \cdot \nabla f = \sum\limits_i g_i \partial_i f$,

- $A : B = \sum\limits_{ij} A_{ij} B_{ji}$,

- $\vec{g} \otimes \vec{l}$ be the second order tensor: $(\vec{g} \otimes \vec{l})_{ij} = g_i \, l_j$,

- Δf be the Laplacian (scalar) of f defined by: $\Delta f = \nabla \cdot (\nabla f)$,

- $\|\vec{g}\|$ represents the length of $\vec{g}$ (L^2 norm of $\vec{g}$): $\|\vec{g}\|^2 = \sum\limits_i g_i^2$.

- In the following, *a.e.* means almost everywhere. This notation has a strong meaning for the (mathematical) measure theory. It means that the space on which a property does not hold is a set of measure 0. In the following, a.e. will be used with the Lebesgue measure associated with the classical integration rules.

Remark: *The Einstein summation convention is applied to the whole document: summation over a set of indexed terms in a formula is implicit.*

Symbol Definitions

Subscript and upper script symbols

x_w	x at the wall
$\overline{x}$	ensemble average of x (Reynolds average)
$\widetilde{x}$	mass-weighted average of x
x'	Fluctuations of x with respect to Reynolds average
x''	Fluctuations of x with respect to mass-weighted average
x_e	x evaluated at the nearest node outside the boundary layer
x_{ref}	Reference value for x

Greek symbols

α_t	Turbulent thermal conductivity for thermal turbulence
ξ	Second Lamé coefficient
λ	Laminar thermal conductivity
λ_t	Turbulent thermal conductivity
δ	Parameter for wall functions
δ^+	Dimensionless parameter for wall functions
ε	Rate of dissipation of turbulent kinetic energy
κ	von Kármán constant
μ	Laminar dynamic viscosity
μ_t	Turbulent dynamic viscosity
ν	Laminar kinematic viscosity
ν_t	Turbulent kinematic viscosity
τ	Reynolds stress tensor
τ_h	Time scale for thermal turbulence
τ_d	Time scale for dynamic turbulence
τ_s	Reynolds stress tensor contribution due to mesh velocity
τ_r	Reynolds stress tensor contribution due to relative velocity
γ	Polytropic coefficient
Γ_c	Boundary of the computational domain with wall-laws
Γ_w	Wall boundary
$\theta - \phi$	Alternative turbulence model
θ, θ_s	Alternative turbulence model near the wall

Roman symbols

C_{hr}	Heat transfer coefficient on rough wall
C_{h0}	Heat transfer coefficient on smooth wall
C_p	Specific heat at constant pressure
C_V	Specific heat at constant volume
E	Total energy
f_r	Reichardt function
h	Enthalpy
k	Turbulent kinetic energy
L	Length
L_0	Reference length
L_μ	Turbulent length scale for μ_t
L_ε	Turbulent length scale for ε
Ma	Mach number
Ma_∞	Inflow Mach number
$\vec{n}$	Unit vector normal to the wall
P	Production term in turbulence models
Pr	Laminar Prandtl number

Pr_t	Turbulent Prandtl number
P_t	PANT coefficient
q	Energy flux density transported by thermal conduction
$\mathcal{R}$	Perfect gas constant ($8.3144\, J.K^{-1}.mol^{-1}$)
R	Air constant
Re_∞	Reynolds number
R_t	Local turbulent Reynolds number
S	Symmetric tensor based on velocity gradients
$\vec{t}$	Unit vector tangential to the wall
U	Tangential component of the velocity ($U = \vec{u} \cdot \vec{t}$)
u_τ	Friction velocity
y	Distance to the wall
y^+	Dimensionless distance to the wall
Y_L	Maximum limit where low-Reynolds turbulence model is applied
F	Convective operator

Acronysm

AEL	AeroELastic computation
ALE	Arbitrary Lagrangian Eulerian
ACARE	Advisory Council for Aviation Research and Innovation in Europe
AGARD	Advisory Group for Aerospace Research and Development
APFE	AProximated Finite Element diffusion scheme
APFT	Almost-Periodic Fourier Transform
BIMN	Block Interface with Mismatched Nodes
BPF	Blade Passing Frequency
BGK	Bhatnagar-Gross-Krook
CAD	Computer-Aided Design
CFD	Computational Fluid Dynamics
CPU	Central Processing Unit
DFT	Discrete Fourier Transform
DNS	Direct Numerical Simulation
EB	Edge-Based diffusion scheme
elsA	ensemble logiciel de simulation en Aérodynamique
EXFE	EXact Finite Element diffusion scheme
LES	Large Eddy Simulation
LUR	Linearized Unsteady Reynolds-averaged Navier-Stokes equations
LS	Least-Square diffusion scheme
HBM	Harmonic Balance Method
HTP	Horizontal Tail Plane
IDFT	Inverse Discrete Fourier Transform
LU-SSOR	Lower-Upper Symmetric Successive Over-Relaxation
PANT	PAssive Nosetip Technology
RANS	Reynolds Averaged Navier-Stokes
VTP	Vertical Tail Plane

Chapter 1

Introduction and context

The numerical computation of a flow in a domain limited by boundary conditions is generally done by solving the Euler or Navier-Stokes equations. In all this document, attention is paid on the compressible version of the equations since compressibility effects cannot be neglected for transonic flows around aircrafts or inside turbomachinery, nor for reentry flows at supersonic or hypersonic conditions.

This introductory chapter is organised as follows. First, the Computational Fluid Dynamics Science is introduced and a link is done with CFD for industry. Attention is then focused on the description of flow physics of interest for understanding some choices regarding the flow features to capture. Then, the Euler and Navier-Stokes equations are presented and their closure briefly explained. Finally, the outline of this document is introduced and justified.

1.1 What is CFD?

Computational Fluid Dynamics -CFD- is a quite recent science which is a branch of Fluid Dynamics. It aims to give numerical methods and algorithms able to compute flows and analyse the solution(s). The goal is therefore to solve the equations in a computational domain limited by prescribed boundary conditions. Solving the Euler or Navier-Stokes equations is a complex task because of their mixed hyperbolic / elliptic / parabolic nature and of their intrinsic non-linear feature.

Nowadays, CFD needs computers from the simplest ones (laptop) to the most powerful ones -see top 500 supercomputers on www.top500.org-. Indeed, CFD can be addressed following several directions and among them, one can consider Mathematics, High Performance Computing / Algorithms, Physics, Computer Science (and also other sciences such as chemistry). Therefore, CFD can be seen as a melting pot of several expertise and CFD researchers can have different scientific profiles.

1.1.1 Towards a new work on CFD simulations

As defined in section 1.1, CFD numerically solves non-linear equations on computers. A lot of work has been done to solve the Euler or Navier-Stokes equations during the last fifty years. The first CFD codes were written at university and a famous contributor is Prof. Antony Jameson from Stanford University with his FloXX CFD code suite (first version called Flo57 in 1981). The first challenge for industry was to introduce CFD in the design process and to recruit a new generation of engineers able to perform CFD computations, to increase solution accuracy and to define best practices. Nowadays, this transfer from academic codes to industry ones is still on-going: there remains the need for best practices and the main difficulty lies in the definition of best techniques to keep robustness. We recall that robustness is a quantity that cannot be measured directly: it represents the ability of the CFD code to perform a converging computation. Robustness is of great importance for the modern high-order accurate techniques used for aeroacoustic computations.

In the following sections, the current status of CFD computations in industries (the ones the author worked in close cooperation with) are summarised.

1.1.2 CFD computations at Airbus

Let's take the example of Airbus industry [83]. Airbus first introduced numerical computations in the design process with the use of potential flow techniques (instead of solving the Euler and Navier-Stokes equations). This technique includes an inherent limitation. Finally, the "true" CFD process (solving the non-linear Euler and Navier-Stokes equations) began in the middle of the nineties. At that time, the need for computations was limited and one computation with 150 000 control volumes was performed each 5 months. By the 2000's, increase in computational power, accuracy and in robustness enabled one to perform about 4 CFD computations each month with 30 Million control volumes, with Airbus engineers now performing thousands of CFD computations on more than 100 Million cell meshes per month. As a consequence, there was an exponential increase in CFD demands and since lots of comparison between experiments and numerical simulations were performed, scientists also increased their confidence in numerical solutions. However, do not forget that these computations form a small part of the total amount of fluid computations and millions of potential flow simulations are still performed each month during the preliminary design steps. But the total numerical cost of such computations is much lower than the ones to solve the Navier-Stokes equations around a full aircraft.

Presently, RANS and Unsteady RANS computations are accurate enough to successfully couple Fluid Dynamics with other dynamics. For example, one goal is to increase the portion of composite materials in order to decrease the global mass. Composite materials are known to be more flexible and the flexibility must be accounted for inside a fluid-structure framework. Airbus has developed a strong knowledge in fluid-structure interactions, based upon the analysis of the response of the flow to periodic structure deformation according to its modes, following the P-K approach [69].

Another scientific topic concerns a more accurate prediction of turbulence effects with the use of Large Eddy Simulation. In this case, large turbulence scales are computed explicitly and small ones are modelled with an algebraic subgrid scale model or with a filter. This approach has been used for aeroacoustic computations with complex boundary conditions and very high order numerics to accurately capture pressure fluctuations not larger than $100Pa$ in a flow at a mean pressure of $101\,000Pa$. This kind of work is motivated by the ACARE recommendations. Concerning noise, remember that the ACARE (Advisory Council for Aviation Research and Innovation in Europe) target for 2050 is a perceived-noise reduction by 65% relative to year 2000 [45].

1.1.3 CFD computations at Safran

On a practical point of view, there are not many differences between a turbomachinery computation and one for an aircraft: the kernel of the CFD code can be shared. Differences mainly occur in the boundary condition choice and in the treatment of fixed / mobile parts of the mesh. For an aircraft, the external conditions come from the far-field and the adiabatic wall. For an engine, outflow with fixed pressure and injection are also required. For turbomachine, an injection condition and an outflow generally defined by a mass flow rate are needed. For URANS computation, many numerical treatments follow the Tyler and Sofrin theory [136] that defines the different unsteady modes present in a turbomachinery following the number of blades per row.

1.1.4 CFD computations at CEA/CESTA for reentry flows

After many years of experimental tests, President Jacques Chirac decided in 1995 to stop experimental campaigns for nuclear weapons and gave numerical methods the role of guaranteeing nuclear weapons stockpile. For the design of these military weapons, this decision had many consequences: confidence in physics and in dimensioning process must be established and errors need to be quantified. The need for simulation is a key point to design the core of the weapon, but it has also consequences on the thermal protection system. During reentry, different physics are encountered and for the sake of clarity, they are summarised in the following paragraph.

For flows at high altitude (altitude larger than 60km), the media cannot be assumed continuous and the density is very low. This is a transitional regime between a free molecular regime and the continuous regime. For altitudes lower than 60km, the continuum assumption of fluid mechanics is valid and several flow regimes can be encountered along the flight path:

- The flow is laminar but air is hot near the body and the perfect gas assumption (mixture of N_2 and O_2 with fixed proportions, no reactions between the components) is not valid. In high speed flow, the adjustment of chemical composition requires certain time and chemical equilibrium or chemical non-equilibrium can be considered. If the characteristic time for chemical reactions to reach local equilibrium is of the same order of magnitude as the characteristic time of the fluid flow, the flow is said at chemical non-equilibrium. The most complex chemistry modelling appears at chemical non-equilibrium when the characteristic time for translation and various internal energy modes to reach local equilibrium is of the same order as the characteristic time of the fluid flow: this is the thermal non-equilibrium. In addition with the chemical reactions inside the flow, the thermal protection of the reentry object encounters very high heat flux and heterogeneous chemical reactions on the thermal protection decrease the protection thickness.

- At the lowest altitudes, the flow becomes turbulent. Transition first occurs on the body and then, it moves upstream to the nose. Due to ablation, transition never occurs on a clean smooth boundary. The thermal protection is generally based on carbon resin material and heterogeneous reactions do not perform equally on carbon and resin. As a consequence, the wall is said to be rough. Roughness influences transition location and the local heat flux. In particular, it was shown in [38] that roughness can increase wall heat flux by a factor up to 3! This is the reason why wall heat flux is one of the most important parameter for reentry object design.

1.1.5 Link between CFD and this thesis

This introduction shows that the importance of CFD becomes greater and greater in industry. In this thesis, some techniques to solve industrial problems involving CFD are presented. Some CFD aspects will be discussed, using Mathematics and Physic considerations. Transition will not be addressed.

All this work was performed with the motivation to:

1. Increase solution accuracy
2. Decrease the CPU cost to obtain the solution
3. Increase code robustness
4. Build reduced models by the integration of physical properties in simplified forms of initial equations

1.2 Organisation of this thesis

This thesis is divided into three parts.

1.2.1 Physical aspects of RANS turbulence modelling

The first part is dedicated to turbulence modelling and the analysis is done entirely in the continuous regime. The computational part of the work is necessary for validation only. This work was performed during my PhD, during my position at CEA/CESTA and during the first years of my current position at Cerfacs. After an introduction of dynamic turbulence models, coupled thermal / dynamic turbulence models are introduced and discussed. Then, a new two-layer thermal turbulence model in presented. The last topic is wall functions. Wall functions enable coarser meshes and use *a priori* quantity behaviours in the boundary layer.

In this part, the presentation of our results follows the procedure to build wall functions:

1. Turbulence models valid up to the wall are introduced and their behaviour fully analysed. The stiffness of the turbulence model comes from the new terms added to cope with the presence of the wall. These new terms are generally built as damping functions to correctly reproduce the behaviour of quantities in the points located close to the wall. This is for sure the part of the boundary layer that is CPU consuming and it will be avoided by the use of wall functions.

2. Two-layer turbulence model are then discussed. The idea is to define a simpler model near the wall using some physical properties and to avoid the necessity to use damping terms in the transport equation(s). To do so, the version without damping terms of the turbulence model is considered far from the wall. One equation is kept unchanged and it is applied up-to the wall. The other transport equation is replaced by algebraic expressions using physical knowledge. Damping terms are nearly always found in the algebraic expressions. For example, let us consider a standard two-equation turbulence model. Far from the wall, equations remain more or less unchanged (some damping terms can be neglected). However, only one partial differential equation is kept near the wall and the second variable is defined algebraically. Two-layer models are known to be

more robust and more CPU efficient but their validity domain is more limited than the original two-equation models from which they were built.

3. A simple mathematical analysis of the integral form of Navier-Stokes equations shows that the key point is to link conservative variables and their gradients to evaluate surface integrals issued from diffusion terms. Computing accurately these gradients needs very refined meshes in areas of strong variable variations, especially near the wall. The principle of wall functions is to replace numerical schemes by new relations linking variables and their derivatives in order to compute surface integrals. Since the new relations use knowledge of the boundary layer, the mesh constraints are less severe and a coarser mesh can be considered. For the mean flow, wall laws link conservative quantities to wall gradients through shear stress and heat flux. Another key point concerns the turbulent equation closure. At this level, a simple expression (generally for the turbulent kinetic energy k) is introduced and the Dirichlet condition for the second turbulence variable comes directly from the two-layer model.

1.2.2 Mathematical analysis of RANS turbulence models

The second part of the thesis draws a strong link between physical models and mathematics. It is well-known that many turbulence models need user-defined corrections / expertise in order to guarantee some physical properties such as positivity and boundedness. In this context, this part can be seen as a bridge between physicists and mathematicians. First, some results regarding the high-Reynolds version of the $\theta-\phi$ turbulence model derived from the $k-\varepsilon$ model (without damping terms to account for wall boundaries) are recalled. Then, theoretical results obtained on a low-Reynolds extension of two-layer $\theta-\phi$ model (in which only equation on θ is kept) are proved. This theoretical work is performed using incompressibility assumption and simplified equations. However, for compressible flows encountered in this thesis, the initial version of the $\theta-\phi$ turbulence model does not respect the physics of the boundary layer and in particular, it cannot recover a positive value for the turbulent Prandtl-Schmidt constant of θ equation. A new way to treat the problem is finally introduced and an alternative $\theta-\phi$ turbulence model defined with constants having the “good” sign is presented. This work was performed during my PhD, extended by a student under my supervision at CEA/CESTA and then stopped because new activities were treated at Cerfacs.

1.2.3 Discretisation of the Euler and Navier-Stokes equations

The third part is devoted to the discretisation of physical models. In this part, different topics addressed recently are summarised. The first chapter deals with the time integration for periodic or almost-periodic flows. For periodic flows, it is clear that the best numerical efficiency is attained if the time integration procedure does not follow a simple hyperbolic framework: the future is a simple copy of the past at a different time instant. Our contributions for the industrial use of the Harmonic Balance Method in the industrial solver *elsA* are fully described.

Diffusion schemes for multi element shape unstructured grids are discussed in the second chapter. In a cell vertex framework, the finite element approach gives a natural definition of gradients on triangles / tetrahedra using shape functions. But for other element shapes (prism, pyramid and hexahedron), the situation is not so clear and we proposed a new scheme with desirable properties for use in an industrial solver. For cell-centred solvers, the situation is even less clear. Many diffusion schemes were published but none of them is accurate enough and simple enough to be implemented in a code with the High Performance Computing constraints needed by Large Eddy Simulations. The last chapter is issued from the training period of J. Vanharen and is a short resume of the paper submitted to *Journal of Computational Physics* in August 2014. The goal is to give a new analysis of Block Interface with Mismatched Nodes (BIMN). BIMN interfaces are encountered in many industrial applications but their behaviour for unsteady flows was never studied in the past. Our theoretical and numerical results confirm the capability of BIMN to handle unsteady flows with similar cell sizes on both sides of the interface. In regions of strong coarsening, spurious modes can be produced by the BIMN and a way to correct this undesirable behaviour is proposed and validated.

1.2.4 Conclusion and perspectives

Finally, the last two chapters give a conclusion of the work presented and introduce some directions of research for the near 5 years.

Before entering into details, it is necessary to fix notations and to introduce Euler and Navier-Stokes equations.

Chapter 2

The Euler and Navier-Stokes equations

One can derive the Euler or Navier-Stokes equations from different considerations. The first approach is based on a molecular analysis of collisions between particles. For the second approach, a macroscopic analysis is performed.

2.1 Microscopic analysis - collisions between particles

The Boltzmann equation represents the molecular interactions. Therefore, it involves a term to represent particle collisions. A famous collision term expression is the one from Bhatnagar-Gross-Krook (BGK model [12]). The Euler and Navier-Stokes equations can be derived from the BGK equations by approximations on the collision term. Standard CFD quantities (density ρ, momentum $\rho\vec{u}$ and total energy ρE) can be estimated by taking moments of the repartition function of the BGK model.

2.2 Macroscopic analysis - quantity balance inside a given domain

Another way to proceed consists in deriving the equations simply by analysing the evolutions of density, momentum and energy inside a domain. Physical considerations enable to write the final system. For more details, one can read the booklet [116]. This booklet can also be downloaded on Cerfacs web pages (see `http://elearning.cerfacs.fr/numerical/schemes/mesh/index.php`).

2.3 The Navier-Stokes equations

If one performs a balance of quantities entering and leaving the domain of interest, the integral form of the Navier-Stokes equations can be developed easily. Since this integral form is true on any domain of interest, it is generally transformed in the following point-wise formulation:

$$\begin{cases} \partial_t \rho + \nabla \cdot (\rho\vec{u}) = 0 \\ \partial_t (\rho\vec{u}) + \nabla \cdot (\rho\vec{u} \otimes \vec{u} + p\mathbf{I}) = \nabla \cdot \tau \\ \partial_t (\rho E) + \nabla \cdot (\vec{u}(\rho E + p)) = \nabla \cdot (\vec{u}\tau) - \nabla \cdot q \,, \end{cases} \tag{2.1}$$

where τ is called the constraint tensor and q represents the energy flux transported by thermal conduction. Eq. 2.1 is an open system of equations with more unknowns than equations.

New relations need to be introduced to close the system. The first kind of closure is called behaviour law and links q and τ with the main variables, while the last closure equation is based on chemistry and links pressure, temperature and density.

2.3.1 Closure for τ

The shear stress tensor τ depends by nature on the fluid viscosity. The viscosity measures the resistance of a flow and induces constraints inside the flow. Air is assumed to be a Newtonian fluid, which means that in the planar Couette flow, the fluid velocity depends linearly on the height h between both plates. The constant coefficient between the velocity and the height depends on the viscosity and on the test case definition (force applied on the moving plate...). Following Landau and Lifchitz [81], a general definition for τ is:

$$\tau = \mu(\nabla\vec{u} + \nabla\vec{u}^\top) + \xi\nabla\cdot\vec{u}\mathbf{I} \text{ with } \mu \geq 0\,, \tag{2.2}$$

where μ and ξ represent two scalar values with a definition close to Lamé's coefficients for linear elasticity. The first real scalar is called dynamic viscosity and the second one is the second viscosity coefficient. The dynamic viscosity is a positive coefficient. Eq. 2.2 is also known as *Newton's law for the viscosity* and the fluid which respects Eq. 2.2 is said *Newtonian*.

Remark 2.3.1 *The kinetic theory [139] gives a validity limit for Eq. 2.2:* $\tau_m\|\nabla\vec{u}\| << c$*, with* τ_m *the mean free path and* c *a characteristic molecular velocity such as the speed of sound.*

Eq. 2.2 can be written in a different way, introducing spherical and deviator contributions [22]:

$$\tau = \mu\left(\nabla\vec{u} + \nabla\vec{u}^\top - \frac{2}{3}\nabla\cdot\vec{u}\mathbf{I}\right) + \left(\xi + \frac{2}{3}\mu\right)\nabla\cdot\vec{u}\,\mathbf{I} \text{ with } \mu \geq 0 \text{ and } \xi + \frac{2}{3}\mu \geq 0,$$

which shows that $\eta = \xi + 2\mu/3$ plays the role of a volume viscosity, in the sense that it is associated with volume variations.

The Stokes hypothesis introduces a new level in the modelling for τ. It comes from thermodynamic assumptions at equilibrium: the mechanic pressure $p_m = p + \eta\nabla\cdot\vec{u}$ is strictly equal to the dynamic pressure p. Surface force is therefore coupled to the pressure coming from the internal energy: $\eta = 0$ and $3\xi + 2\mu = 0$. Stokes' hypothesis means that the relaxation time needed for dynamic and mechanic pressures to equilibrate is infinitely small. With Stokes' relation, Eq. 2.2 becomes the *Newton-Stokes law*:

$$\tau = \mu\left(\nabla\vec{u} + \nabla\vec{u}^\top - \frac{2}{3}\nabla\cdot\vec{u}\,\mathbf{I}\right)\,. \tag{2.3}$$

At this level of modelling, one can compute the shear stress if a law is given for the viscosity.

2.3.2 Closure for q

Remember that q is the energy flux density transported by thermal conduction. If the temperature gradient is low, q can be expressed as a power of the temperature gradient. The first order term [81] is written:

$$q = -\lambda\nabla T\,. \tag{2.4}$$

where λ is called thermal conductivity. This relation is known as *Fourier's law.* The thermal conduction coefficient λ is always positive since the conductive energy flux goes from high temperature regions to low temperature regions. Therefore, q and ∇T must have opposite signs. In practice, λ is related to μ: $\lambda = C_p \, \mu / Pr$ where C_p is the heat capacity at constant pressure (it depends on the state equation of the gas) and Pr is a non-dimensional number, called the Prandtl number. Pr represents the ratio of the thermal diffusion time over the dynamic diffusion time for a fixed reference length.

Remark 2.3.2 *The kinetic theory [139] gives a validity limit for Eq. 2.4:* $\tau_m \|\nabla T\| << T$*, where* τ_m *is the mean free path.*

2.3.3 Defining a viscosity law

For air at non extreme conditions of temperature and pressure, μ follows Sutherland's law:

$$\mu(T) = \mu_{ref} \left(\frac{T}{T_{ref}} \right)^{1.5} \left(\frac{T_{ref} + 110.4}{T + 110.4} \right) , \tag{2.5}$$

where $T_{ref} = 273.15$ K and $\mu_{ref} = 1.711 \ 10^{-5} \ Kg.m^{-1}.s^{-1}$. For temperature lower than $1500K$, Eq. 2.5 is a good approximation of μ. For aircrafts or turbomachinery flows, it is the preferred relation to define μ.

2.3.4 Perfect gas assumption

Remark 2.3.3 *The final version of the equations will be presented. Readers are referred to classic books of thermodynamics to know the hypothesis needed to obtain the perfect gas equation.*

Maxwell wrote the main parts of the kinetic theory for perfect gas in 1859. It is based on the molecular representation of gas suggested by Avogadro in 1811 and on some statistical considerations. At the macroscopic scale, the large number of molecules (remember the meaning of Avogrado's number $\mathcal{N}_A = 6.02253 \times 10^{23}$) gives the law for a perfect monatomic gas:

$$p = nkT \, , \tag{2.6}$$

where k is the Boltzmann's constant ($k = 1.3806581 \times 10^{-23} J.K^{-1}$) and n is the number of molecules per volume unit.

Then if $\mathcal{M}$ is the molar mass, density is $\rho = n\mathcal{M}/\mathcal{N}_A$ and by Eq. 2.6, $p = \rho T k \mathcal{N}_A / \mathcal{M}$. The product $\mathcal{R} = k\mathcal{N}_A$ represents the perfect gas constant $\mathcal{R} = 8.3144 \, J.K^{-1}.mol^{-1}$ and $R = \mathcal{R}/\mathcal{M}$ is the perfect gas constant for the considered gas. To conclude, a perfect gas is characterised by:

$$p = \rho R T \, , \tag{2.7}$$

with $R \simeq 287 J.K.kg^{-1}$ for air.

Introducing the specific enthalpy $h = e + p/\rho$ with e internal energy, the heat capacities at constant pressure or constant volume (in $J/(K.kg)$) are respectively:

$$C_p = \left(\frac{\partial h}{\partial T} \right)_p \text{ and } C_V = \left(\frac{\partial e}{\partial T} \right)_V .$$

Under perfect gas assumption, one can also prove that **internal energy e and enthalpy $h = e + p/\rho$ are functions of the temperature** only, leading to $de = C_V(T)dT$ and $dh = C_p(T)dT$, with $C_p(T) - C_V(T) = R$. For a monatomic gas, C_p and C_V are constant numbers if the electronic temperature is negligible compared to the classical temperature, while they vary for polyatomic gases.

For transonic flows around civil aircraft and for turbomachinery, we assume in this thesis that air is a perfect gas. This means that air is *perfect following the thermodynamic theory* and also that it is *a perfect polytropic gas characterised by constant C_p and C_V coefficients.* For this gas, the polytropic coefficient γ is $\gamma = C_p/C_V$. Following perfect gas relations, it comes easily that $e = C_V T$ and $h = C_p T$ and finally, denoting E to total energy per mass unit, one has: $E = C_V T + 0.5 \|\vec{u}\|^2$ with $\|\vec{u}\|$ Euclidean norm of the velocity vector.

2.4 Mach and Reynolds numbers

It is of great importance to introduce two dimensionless numbers:

- The Mach number $Ma = \|\vec{u}\|/c$ is the ratio of the fluid velocity over the speed of sound c. Any flow with $Ma > 0.2$ is generally assumed compressible and is of interest for this work.
- The Reynolds number Re is defined as $Re = \dfrac{\rho\|\vec{u}\|L}{\mu}$, where L is a characteristic length of the object in movement. The Reynolds number measures the importance of viscosity in the flow relative to momentum forces. For high Reynolds number flows, the viscous force is lower than the kinetic force on the object in movement. Low Reynolds number flows are generally organised, easily reproducible (laminar flow). For high Reynolds flows, the importance of the viscosity is lower and its regularisation effects on the flow are much lower. In this case, variables are varying in time and space and this kind of flow is said to be turbulent.

  There is no criterion to decide if the flow is laminar or turbulent *a priori*, except for some very simple (academic) cases. Moreover, the mechanisms for a flow to turn from the laminar regime to the turbulent one, which is called transition, are partially understood but cannot be estimated nor located *a priori* with standard industrial techniques used in CFD.

2.5 Closed version of the Navier-Stokes and Euler equations

The Navier-Stokes system of equations is thus closed with the introduction of modelling and with the perfect gas assumption. Its (conservative) form is:

$$\begin{cases} \partial_t \rho + \nabla \cdot (\rho \vec{u}) = 0 \\ \partial_t (\rho \vec{u}) + \nabla \cdot (\rho \vec{u} \otimes \vec{u}) + \nabla p - \nabla \cdot \tau = 0 \\ \partial_t (\rho E) + \nabla \cdot \Big(\vec{u}(\rho E + p) \Big) = \nabla \cdot (\vec{u}\tau + \lambda \nabla T) \end{cases} \tag{2.8}$$

where $\tau = \mu(\nabla\vec{u} + \nabla\vec{u}^\top) - \dfrac{2\mu}{3}\nabla \cdot \vec{u}\,\mathbf{I}$, $\lambda = \dfrac{C_p\mu}{Pr}$ and $p = \rho RT$.

The Euler equations are simply obtained assuming that the fluid is not viscous. Mathematically, the Euler equations are derived from the Navier-Stokes ones simply by taking $\mu = \lambda = 0$.

In contrary with many linear physical phenomena, the Euler and Navier-Stokes equations are non-linear and solving these equations is still an active research area called the Computational Fluid Dynamics science. The non-linear aspect of equations seems to be responsible of the transition to turbulence at high-Reynolds number and obtaining a proof is one of the Millennium Prize Problems. Turbulence for industry is the first topic addressed in this thesis.

Part I

Analysis of physical models in continuous regime

In this part, attention is paid on turbulence modelling in RANS simulations. Two key points will be carried out. First, following a process established for pure dynamic turbulence model, the different steps to build a two-layer coupled thermal / dynamic turbulence model are defined. This development was done during the PhD thesis of S. Galera at CEA/CESTA. The second topic addressed is related to wall functions or wall-laws. The first kind of wall functions is dedicated to dynamic turbulence only. Wall laws were first defined for simulations over smooth walls and were then extended to account for rough walls. The second kind of wall laws was introduced during the PhD of S. Galera and it is dedicated to thermal treatment. The last extension of wall-laws concerns moving and / or deformable mesh encountered in pitching airfoil simulations.

Associated papers:
− Wall Functions in Computational Fluid Dynamics, B. Mohammadi and G. Puigt. *Computers and Fluids*, 35(10), pp.1108-1115, 2006.
−Turbulence modelling for Hypersonic Flows Over Isothermal Walls, S. Galera, B. Mohammadi and G. Puigt. *International Journal of Computational Fluid Dynamics*, 20(8), pp. 549-561, september 2006.
− Generalized Wall functions for Rough Walls Based on Data Assimilation, B. Mohammadi and G. Puigt. *International Journal of Computational Fluid Dynamics*, 17(6), pp. 453-465, 2003.
− Generalized Wall Functions for High Speed Flows over Adiabatic and Isothermal Walls, B. Mohammadi and G. Puigt. *International Journal of Computational Fluid Dynamics*, 14(3), pp. 183-200, 2001.

Conference papers:
− Wall-Laws for Heat Transfer Predictions in Thermal Turbulent Flows, S. Galera, L. Hallo, B. Mohammadi, G. Puigt. 38*th* AIAA Thermophysics Conference, Toronto, Ontario, June 6-9, 2005. AIAA Paper AIAA-2005-5200.
− Wall-Laws Including Thermal Modelling for Hypersonic Turbulent Flows, S. Galera, G. Puigt, L. Hallo and B. Mohammadi. 4*th* International Symposium on Atmospheric Reentry Vehicles and Systems, organized by AAAF and EADS Space, 21-23 Mars 2005, Arcachon (France).
− Les lois de paroi en mécanique des Fluides supersoniques, G. Puigt and B. Mohammadi, Conference organized by Société de Mathématiques Appliquées et Industrielles (SMAI), 28 mai - 1 juin 2001, Pompadour, France (in French).
− Generalized Wall Functions for Adiabatic and Isothermal Walls, G. Puigt and B. Mohammadi, European Congress on COmputational Methods for Applied Sciences - ECCOMAS 2000, 11 - 14 september 2000, Barcelone (Spain).
− Generalized Wall Functions for High-Speed Flows over Adiabatic and Isothermal Walls, G. Puigt and B. Mohammadi, Fluids With Interactions Conference, organized by CNRS (GDR 1135) and INRIA, 11 - 14 october, 1999, Sophia Antipolis (France).

People I worked directly with:
- Prof. Bijan Mohammadi
- Dr. Ludovic Hallo (CEA/CESTA)
- Dr. Stéphane Galera (CEA/CESTA and University of Montpellier II)
- Vincent Arrecgros (training period at CEA/CESTA)
- Olivier Frayssinet (training period at CEA/CESTA)
- Delphine Lizarazu (training period at Cerfacs)
- Emmanuel Germaine (training period at Cerfacs)

Chapter 3

Turbulence modelling for industry

3.1 Introduction

The non-linearity of the Navier-Stokes equations can lead to “strange” effects in a flow. If the Reynolds number is high (for industrial application, the Reynolds number per meter is about 10^6), the resulting turbulent flow is composed of vortices covering a range of scales and energies. Capturing the whole turbulence spectrum means computing vortices from the largest scales (the scale of the object) to the lowest scales (defined as scales at which diffusion effect are large enough to dissipate vortices in heat sources). This requires very refined meshes since the mesh size must be chosen to compute the lowest wavelengths. Roughly theoretical analysis shows that the number of degrees of freedom in the mesh varies as $Re^{9/4}$.

The turbulent nature of the flow occurs in more than 99.99% of aeronautical applications and the corresponding Reynolds number is generally larger than 10^7. As a consequence, computing all turbulence scales may need a mesh with more than $10^{63/4} = 10^{15.75} \simeq 562.34 \times 10^{13}$ degrees of freedom. Computing all turbulence scales is not feasible on real industrial configurations: the limit in mesh degrees of freedom is fixed by computer architecture and code efficiency. In 2011, one of the largest computation of all turbulent scales (Direct Numerical Simulation DNS) was performed by Jacqueline H. Chen [24] on Department Of Energy supercomputer (USA) and the mesh contained seven billion mesh nodes. The biggest DNS was performed in 2013 by Lee, Malaya and Moser. The mesh was composed of 242 billion degrees of freedom and the computation ran on 768 000 cores [85]. Of course, such an approach mainly interests researchers because the high fidelity computation gives the opportunity to have access to all quantities at all discrete space and time locations, which is not feasible in physical tests.

Currently, most of industrial turbulent computations are done under the assumption of separation of mean and fluctuating parts of all variables. The goal is to compute the mean effect of turbulence on the flow and to forget the computation of turbulent fluctuations. Formally, this is possible for the conservative form of the Navier-Stokes equations and it leads to the Reynolds Averaged Navier-Stokes (RANS) equations. In this chapter, RANS equations are firstly introduced with an emphasis on obtaining equations and turbulence modelling approximations for closure, followed by a focus on the weakness of the approach, namely the turbulence closure. Finally, thermal turbulence for compressible flows is discussed.

3.2 Averaging turbulence effects

The Reynolds average assumes that density ρ, internal energy e or enthalpy h and all components of the velocity vector $\vec{u} = (u_1, u_2, u_3)$ can be written as a mean part (with upper script $\overline{}$) and a fluctuating part (with prime $'$) following an ensemble average:

$$\left\{\begin{array}{l} \rho = \overline{\rho} + \rho' \text{ with } \overline{\rho'} = 0 \\ u_i = \overline{u_i} + u_i' \text{ with } \overline{u_i'} = 0 \\ e = \overline{e} + e' \text{ with } \overline{e'} = 0 \text{ or } h = \overline{h} + h' \text{ with } \overline{h'} = 0, \end{array}\right. \tag{3.1}$$

but this form is not adequate for the compressible version of the Navier-Stokes equations. This is due to the non-linear terms and as an example, consider one term coming from the divergence term in the density equation $\rho u_i = \overline{\rho}\ \overline{u_i} + \overline{\rho} u_i' + \overline{u_i}\rho' + \rho' u_i'$. Then, taking the mean of the density equation leads to an extra term to model: $\frac{\partial \overline{\rho}}{\partial t} + \nabla \cdot \left(\overline{\rho}\ \overline{\vec{u}} + \underbrace{\overline{\rho' \vec{u}'}}_{\text{new term}} \right) = 0.$

As a consequence, the transformed equation does not look like the initial one: it contains a new term related to density / velocity fluctuations to model. The average procedure dedicated to compressible flow effects was proposed first by Reynolds in 1901 [121] and the theory has finalised by Favre [44] in 1976. The principle is to keep ensemble average (classical Reynolds averaging) for density and pressure and to introduce mass-weighted average for other quantities. The mass-weighted average and the deviation from the instantaneous quantity (fluctuations) are denoted with the symbols $\widetilde{}$ and $''$. The mass-weighted average is defined by $\widetilde{u_i} = \overline{\rho u_i}/\overline{\rho}$ and $u_i'' = u_i - \widetilde{u}_i$. After algebraic simplifications, the final system of the mass-weighted averaged Navier-Stokes equations is:

$$\left\{\begin{array}{lcl} \partial_t \overline{\rho} + \nabla \cdot (\overline{\rho}\widetilde{\vec{u}}) & = & 0 \\ \partial_t (\overline{\rho}\,\widetilde{\vec{u}}) + \nabla \cdot (\overline{\rho}\widetilde{\vec{u}} \otimes \widetilde{\vec{u}}) & = & -\nabla \cdot (\overline{\rho \vec{u}'' \otimes \vec{u}''}) - \nabla \overline{p} + \nabla \cdot (\mu \overline{S}) \\ \partial_t (\overline{\rho}\,\widetilde{E}) + \nabla \cdot (\overline{\rho}\widetilde{E}\widetilde{\vec{u}}) & = & \nabla \cdot \left(\widetilde{\vec{u}}(\mu \widetilde{S} - \overline{\rho \vec{u}'' \otimes \vec{u}''}) - \widetilde{\vec{u}}\,\overline{p} \right) - \nabla \cdot (\lambda \nabla \widetilde{T} + \overline{\rho h'' \vec{u}''}) \\ & & +\nabla \cdot \left(\mu(\overline{S''}\,\widetilde{\vec{u}} + \overline{S''\,\vec{u}''} + \widetilde{S}\,\overline{\vec{u}''}) - \frac{1}{2}\overline{\rho \|\vec{u}''\|^2 \vec{u}''} \right) \end{array}\right. \tag{3.2}$$

where $\tau = \mu S$ and $S = \nabla \vec{u} + \nabla \vec{u}^\top - \frac{2}{3}(\nabla \cdot \vec{u}),\mathbf{I}$. With this average, new terms appear:

- $\overline{S'' \vec{u}''}$, $\overline{S''}\,\widetilde{\vec{u}}$ and $\widetilde{S}\,\overline{\vec{u}''}$ are dissipation terms linked with viscous friction dissipation,
- $R = -\overline{\rho \vec{u}'' \otimes \vec{u}''}$ characterises the turbulent friction,
- $H = -\overline{\rho \vec{u}'' h''}$ represents the diffusion of enthalpy due to turbulence,
- $\frac{1}{2}\overline{\rho \|\vec{u}''\|^2 \vec{u}''}$ is a third-level correlation.

The system of equations Eq. 3.2 contains too many unknowns and the system closure is actually *"The Question"* for the modelling of turbulence with both ensemble and mass-weighted averages.

3.3 The Navier-Stokes closure: RANS equations

The modelling for the mean equations is the main question for RANS turbulence modelling and many closures of varying complexity have been proposed. They can be distinguished using the following criteria:
− *First-order models* will express correlations in terms of state variable using algebraic expressions (such as the Baldwin/Lomax model). Further advances considered several transport equations for the mean effects of turbulence movement, leading to a coupling with RANS equations (see [6, 124] for a review of some models dedicated to hypersonic flows). Algebraic turbulence models are easier to implement but their efficiency is limited. These models are generally adapted following the kind of configuration to treat. Transport-equation turbulence models induce a larger CPU and memory usage. Their validity domain seems to be broader than the one for algebraic models.
−*Second-order turbulence models* are obtained formally from exact equations of Reynolds tensor terms and by modelling correlations with an order higher than or equal to 3. The CPU cost is the largest and for flows with a weak anisotropy, their interest is quite limited.

In complement to the first criterion dedicated to turbulence model closure, another criterion can be defined from the technique to close the system. In a schematic view, the closure can be done by:

- diminishing the number of unknowns,
- adding new equations,
- considering a blending procedure with new equations and less unknowns.

3.3.1 Gradient for closure: the Boussinesq hypothesis

Two-term correlations $\widetilde{\overline{\rho} u'' \otimes u''}$ are expressed following the Boussinesq hypothesis [15]. The Boussinesq hypothesis is written by an analogy with the kinetic theory of gases. The relation, obtained for incompressible flows (the Reynolds average procedure) is extended to compressible flows by a simple change of the average symbol.

The Reynolds stress tensor for incompressible flows is modelled easily and the turbulent viscosity is introduced as a product of the square root of the turbulent kinetic energy and a turbulent length scale. Basing the behaviour of the kinetic viscosity ν_t upon k^2/ε is preferred since it is much more difficult to build an equation on length scales than on the turbulent dissipation scale ε. For compressible flows, one finally obtains:

$$-\overline{\rho u_i'' u_j''} = -\overline{\rho}\widetilde{u_i'' u_j''} = -\frac{2}{3}\overline{\rho} k \delta_{ij} + \mu_t \left(\frac{\partial \widetilde{u_i}}{\partial x_j} + \frac{\partial \widetilde{u_j}}{\partial x_i} - \frac{2}{3} \frac{\partial \widetilde{u_l}}{\partial x_l} \delta_{ij} \right) , \tag{3.3}$$

with

$$\mu_t \sim \overline{\rho} \frac{k^2}{\varepsilon} . \tag{3.4}$$

Remark 3.3.1 *The term $2/3\overline{\rho}k$ in Eq. 3.3 represents a turbulent pressure to add to the fluid static pressure.*

3.3.2 Modelling thermal turbulence

Thermal instability can lead to dynamic instabilities in some situations and finally, the flow becomes turbulent. Turbulence increases the mixing of thermal scales, leading to a heat transfer greater than when the flow is laminar [81]. Turbulent heat transfer exchanges are characterised by the turbulent diffusivity coefficient λ_t. Even if they are introduced in the same manner, laminar and turbulent heat transfers represent different physical process. The standard approach for the turbulent heat transfer lies on transport with gradient, as the Boussinesq hypothesis: the turbulent heat flux is defined as the product of the temperature gradient and the turbulent thermal diffusion coefficient:

$$-\overline{\rho \vec{u}'' h''} = \lambda_t \nabla \widetilde{T}. \tag{3.5}$$

Remark 3.3.2 *If one exactly follows the Boussinesq approach for thermal turbulence, the closure would be based on enthalpy gradient rather than on the temperature gradient. In fact, the turbulent thermal diffusivity λ_t is defined with the temperature gradient. Eq. 3.5 for temperature or enthalpy is written in a similar manner for a perfect gas since there is a linear relation between temperature and enthalpy, leading to a linear relation between their gradients:*

$$\nabla \widetilde{h} = C_p \nabla \widetilde{T} \,,$$

and therefore a new coefficient α_t is introduced:

$$-\overline{\rho u'' h''} = \lambda_t \nabla \widetilde{T} = \alpha_t \nabla \widetilde{h}.$$

The last modelling issue concerns the link between the thermal diffusivity and mean variables. This is done with the (strong) Reynolds analogy.

3.3.3 Strong Reynolds analogy

Solving thermal transport by convection for a turbulent flow follows the Reynolds analogy concept [119]. Reynolds suggested that (thermal or mass) diffusion by turbulence varies linearly with the turbulent viscosity:

$$C_p \frac{\mu_t}{\lambda_t} = Pr_t \tag{3.6}$$

where Pr_t is called the turbulent Prandtl number (by analogy with the Prandtl number) and it is assumed to be equal to 1.

Following this analogy, only the knowledge of momentum transport mechanism is necessary to quantify turbulence effects. This is true for a wide variety of applications, provided that any quantity introduced in the fluid follows the flow, which is true at moderate molecular diffusion. Even if this approach is considered for turbulence modelling in most of industrial applications, it must be upgraded for several reasons. First, temperature is a scalar while velocity is a vector. Moreover, any quantity transported by the flow is considered as a passive scalar since it does not have any effects on the velocity field. Low levels of heating can be assumed to behave passively, while large temperature variations are no longer passive and so can induce strong density variations. Finally, Eq. 3.6 introduces a constant unit turbulent Prandtl number, although experiences have shown that Pr_t does vary witnin the boundary layer [77, 4]:

- $Pr_t \sim 0.85$ in the fully developed turbulence area, far from the wall.
- Near the wall, the problem remains open.
- The value of Pr_t depends on boundary conditions. If the velocity and temperature fields have Dirichlet boundary conditions, one can introduce Pr_t as a means to link the velocity and temperature turbulent diffusions. The situation is more complex if velocity and temperature fields have different boundary conditions (Dirichlet condition for velocity and Neumann condition for temperature).

In the following, a constant turbulent Prandtl number Pr_t is assumed. But, it can be concluded that the modelling of thermal turbulence effects for RANS computations seems to be a future way to increase the accuracy of the computations. In particular, new turbulence models dedicated to heat transfer in compressible flows will be described in Chapter 4.

3.3.4 Dissipation by viscous friction

The terms $\overline{S'' \vec{u}''}$, $\overline{S''}\,\widetilde{\vec{u}}$ and $\widetilde{S}\,\overline{\vec{u}''}$ model dissipation by viscous friction. They are neglected, following Morkovin's hypothesis and they vary as the inverse of the Reynolds number. Remember that for the considered turbulent flows, the Reynolds number per meter is about 10^6 to $10^7\,m^{-1}$.

3.3.5 Final version of the Navier-Stokes equations

The final form of the RANS equations, including modelling of the extra terms, is:

$$\left\{\begin{array}{ll}
\dfrac{\partial \overline{\rho}}{\partial t} + \nabla \cdot (\overline{\rho}\widetilde{\vec{u}}) & = 0\,, \\
\dfrac{\partial \overline{\rho}\widetilde{\vec{u}}}{\partial t} + \nabla \cdot (\overline{\rho}\widetilde{\vec{u}} \otimes \widetilde{\vec{u}}) + \nabla(\overline{p} + \dfrac{2}{3}\overline{\rho}k) & = \nabla \cdot \Big((\mu + \mu_t)(\nabla\widetilde{\vec{u}} + \nabla\widetilde{\vec{u}}^{\top} - \tfrac{2}{3}\nabla \cdot \widetilde{\vec{u}}\,\mathbf{I}) \Big) \\
\dfrac{\partial \overline{\rho}\widetilde{E}}{\partial t} + \nabla \cdot \Big(\widetilde{\vec{u}}(\overline{\rho}\widetilde{E} + \overline{p} + \dfrac{2}{3}\overline{\rho}k) \Big) & = \nabla \cdot \Big((\lambda + \lambda_t)\nabla\widetilde{T} \Big) + \\
 & \quad \nabla \cdot \Big(\widetilde{\vec{u}}(\mu + \mu_t) \Big(\nabla\widetilde{\vec{u}} + \nabla\widetilde{\vec{u}}^{\top} - \tfrac{2}{3}\nabla \cdot \widetilde{\vec{u}}\,\mathbf{I} \Big) \Big)
\end{array}\right. \tag{3.7}$$

The mean total energy $\widetilde{E}$ can be split into three contributions $\widetilde{E} = \widetilde{e} + 0.5\,\widetilde{\vec{u}}^{2} + k$, where $\widetilde{e}$ is the averaged internal energy. In Eq. 3.7, the extra term $2/3\overline{\rho}k$ is assumed to be a turbulent pressure to add to the static pressure. Of course, accounting for this term is possible only with turbulence models based on k plus a quantity to account for the dissipation of k.

The final closure needs supplementary relations for the turbulent kinetic energy k and the turbulent viscosity μ_t.

3.4 Turbulence model for RANS equations

There DOES NOT exist any perfect turbulence model, capable of accurately representing the mean effects of turbulence on the flow. This can be explained from a physical point of view by recognising that the high order moments in the equations must be neglected, which may be a poor assumption in some configurations. Modelled terms do not completely represent higher-order terms in the true flow and therefore the final system is NOT the mean of the initial version of the equations. Many turbulence models were built, tested, modified over the past few decades and because an exhaustive description of all RANS turbulence models is not the topic of this dissertation, it is decided to focus the attention upon turbulence models used in industry and on those that will be useful in next chapters.

3.4.1 RANS turbulence models for industry

Currently, the CFD code *elsA* [1] is used for both research and design in Airbus Group and Safran and is being used for flows around aircrafts, inside turbomachinery and flows around helicopters. This code has been under development by ONERA since 1997 with Cerfacs participation since 2001. In particular, *elsA* contains about 18 turbulence models for RANS equations, ranging in complexity from the zero-equation Baldwin-Lomax turbulence model [9], to Reynolds Stress Models (RSM).

In an industrial context, the choice of a turbulence model typically comes after several years of tests / validation and requires expertise in mesh generation. In fact, it is very easy to produce very bad results with a turbulence model and therefore to put discredit on it, while the problem comes from a mesh too coarse near the wall or from a specific way to initialise the computation. It seems that the preferred model for Airbus was the Spalart-Allmaras turbulence model 10 years ago, but it is nowadays the $k-\omega$ two-equation turbulence model, especially for flows with recirculation. In the later case, two versions are essentially considered, the latest Wilcox version [144] and Menter approach with Shear Stress Transport correction term [94]. For Safran group, many turbulence models are chosen, following their specificity and their capability in computing flows at certain conditions (compressor, turbine, guide-vane...). Among them, there are the Spalart-Allmaras turbulence model, Smith's $k-L$ turbulence model [132], several versions of $k-\varepsilon$ and $k-\omega$ turbulence models. For reentry at CEA/CESTA, the preferred turbulence models were Chien's [25] $k-\varepsilon$ and $k-\omega$ turbulence models up-to 2005.

3.4.2 Two-equation $k-\varepsilon$ turbulence model

Without entering into details, $k-\varepsilon$ models are a class of turbulence models. The equation on k can be directly obtained from the equations on the Reynolds stress tensor components, while the equation on ε is generally issued from modelling. As a consequence, there exist a lot of models based on these two quantities. One famous $k-\varepsilon$ turbulence model is the Chien's model [25] and it contains damping terms to be valid up to the wall. It was the preferred turbulence model at CEA/CESTA during my PhD thesis and gave reference solutions in the past.

Chien's $k-\varepsilon$ turbulence model

This model contains damping terms to account for the boundary layer and it is designed for a zero boundary condition on both k and ε at the wall. This leads to an implementation easier than for standard $k-\varepsilon$ models for which the condition on ε depends on gradient of k in the direction normal to the wall, a quantity that can only be computed by introducing the values of k in some cells above the wall (non local approach). Chien's turbulence model equations are:

$$\frac{\partial \overline{\rho} k}{\partial t} + \nabla \cdot (\overline{\rho} \tilde{u} k) + \nabla \cdot \left((\mu + \frac{\mu_t}{\sigma_k}) \nabla k \right) = P - \frac{2}{3} \overline{\rho} k \nabla \cdot \tilde{u} - \overline{\rho} \varepsilon^* - 2\mu \frac{k}{y^2} \tag{3.8}$$

and

$$\frac{\partial \overline{\rho}\varepsilon^*}{\partial t} + \nabla \cdot (\overline{\rho}\widetilde{u}\varepsilon^*) + \nabla \cdot \left((\mu + \frac{\mu_t}{\sigma_\varepsilon})\nabla\varepsilon^* \right) = \frac{\varepsilon^*}{k}(C_{\varepsilon_1}P - \frac{2C_{\varepsilon_1}}{3}\overline{\rho}k\nabla \cdot \tilde{u} - C_{\varepsilon_2}F_\varepsilon\overline{\rho}\varepsilon^*) + W_\varepsilon \, ,$$

with

$$F_\varepsilon = 1 - \frac{0.4}{1.8}exp\left(-(\frac{R_t}{6})^2\right) \, , \quad W_\varepsilon = C_{\varepsilon 3}\mu\frac{\varepsilon^*}{y^2}\exp(C_{\varepsilon 4}y^+) \, ,$$

$$R_t = \frac{\overline{\rho}k^2}{\mu\varepsilon^*} \, , \quad y^+ = \frac{\overline{\rho}_w u_\tau y}{\mu_w} \, ,$$

and

$$P = \mu_t\left((\nabla\widetilde{u} + \nabla\widetilde{u}^\top - \frac{2}{3}\nabla \cdot \widetilde{u}\,\mathbf{I})\right) : \nabla\widetilde{u} \tag{3.9}$$

is called the production term for the turbulence. In all previous relations, y is the minimum distance to the wall and y^+ is a dimensionless distance called the local Reynolds number. It will play a central role in the definition of the boundary layer. Variables with subscript w represent the variable computed at the wall and the friction velocity u_τ is:

$$u_\tau = \left(\frac{\mu_w}{\overline{\rho}_w}\frac{\partial U}{\partial y}\right)^{0.5} \, , \tag{3.10}$$

where U is the tangential component of the velocity vector and y is the distance to the wall. $u^+ = U/u_\tau$ is a dimensionless velocity useful to define quantities inside the boundary layer. μ_t is the turbulent viscosity computed from an algebraic relation depending on both k and ε:

$$\mu_t = C_\mu\overline{\rho}\frac{k^2}{\varepsilon^*}\left(1 - exp(-C_{\mu 2}y^+)\right) \, .$$

The model constants are summarised in Tab. 3.1.

σ_k	σ_ε	C_{ε_1}	C_{ε_2}	$C_{\varepsilon 3}$	$C_{\varepsilon 4}$	C_μ	$C_{\mu 2}$
1	1.3	1.35	1.8	0.0115	0.5	0.09	0.0115

Table 3.1: *Constants for Chien's $k - \varepsilon$ turbulence model.*

Remark 3.4.1 *Chien's $k - \varepsilon$ is expressed as a function of the pseudo-dissipation ε^* (following [84]) in order to implement a homogenous Dirichlet condition on ε^* at the wall: $\varepsilon^* = 0$. The modified quantity ε^* depends on ε:*

$$\varepsilon = \varepsilon^* + 2\mu\frac{k}{y^2}.$$

Two-layer approach

In this section, a two-layer version of the $k-\varepsilon$ turbulence model [96] is introduced. This is necessary to define some notations that will be used in the following sections.

Before entering into some details of the model, it is of great importance to recall some results for the turbulent boundary layer. We consider a turbulent boundary layer with a negligible longitudinal pressure gradient. In this case, the boundary layer is composed of three main regions (Fig. 3.1):

- Near the wall, for $y^+ < 5$, $u^+ = y^+$ and this region is called the viscous sub-layer.
- For $y^+ > 50$ and $y < 0.1h$ where h represents the boundary layer height, the turbulent production is counter-balanced by its dissipation. It is the fully-developed turbulent area. In this area, u^+ and y^+ follows a global dimensionless law:

  $$u^+ = \frac{1}{\kappa}\log(y^+) + C.$$

  C is a constant and it is assumed to have a universal value: $C \simeq 5$. κ is called the von Kármán constant and for air:

  $$\kappa \simeq 0.41\,. \tag{3.11}$$

- Between both areas, both linear and logarithmic profiles must be extrapolated in a continuous way. There are several ways to proceed.

The interest of the two-layer turbulence models is the following:

- "Far from the wall" (from the log layer), a standard $k-\varepsilon$ turbulence model without damping terms is considered. The idea is therefore to consider a "universal" form of the (considered) turbulence model.
- "Near the wall", the equation on k is conserved while the second unknown is deduced from k with algebraic expressions based on k and turbulence length scale(s). Therefore, the numerical stiffness of the initial model with two transport equations and strong variations of k and ε is reduced. Such strong variations near the wall are analysed by Kalitzin *et al.* in [75].

The two-layer technique is based on the resolution of a single transport equation near the wall. For $k-\varepsilon$ turbulence models and incompressible flows, the one-equation transport equation was introduced first by Wolfshtein [145] and then modified by Chen and Patel [23]. It was extended to compressible flows by Mohammadi and other authors [96, 98, 103]. The two-layer $k-\varepsilon$ turbulence model is easy to implement for (local) low-Reynolds number area, the region with high (local) Reynolds number being computed with a two-equation $k-\varepsilon$ turbulence model. Obtaining the low-Reynolds relations is not a complex task and it is presented below. In this section, constants have same meaning and values as for Chien's turbulence model.

First, the dynamic diffusivity is defined as the product of the turbulence scales $\mu_t \sim \overline{\rho}\Delta u_d L_d$, where Δu_d is the turbulence velocity scale and L_d is the turbulence length scale. Within the two-layer approximation, $\Delta u_d = \sqrt{k}$ and $L_d = L_\mu$, leading to:

$$\mu_t = C_\mu \overline{\rho}\sqrt{k} L_\mu\,. \tag{3.12}$$

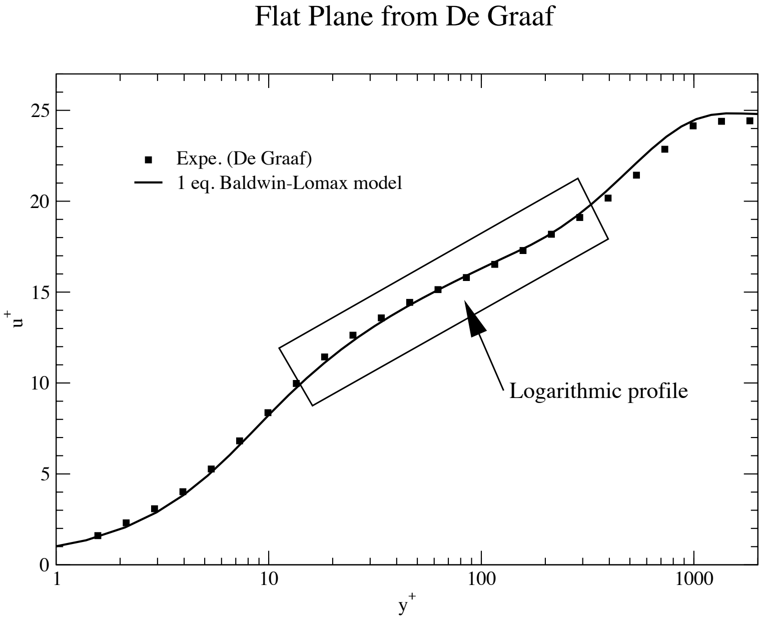

Figure 3.1: *Example of the turbulent boundary layer over De Graff and Eaton flat plate [32]. The turbulent simulation was performed by Y. Colin [27] with elsA.*

The length scale L_μ contains a damping terms to account for the wall [23] $L_\mu = C_d y\,(1 - \exp[-R_y/A_\mu])$, where $R_y = \overline{\rho}\sqrt{k}y/\mu$. This definition of the Reynolds number R_y does not contain the wall friction and the local velocity scale is $\sqrt{k}$.

In the equilibrium area between production and dissipation, the turbulent viscosity is still obtained from both unknowns k and ε of the full turbulence model (valid up to the wall). Moreover, other expressions are derived from the models in the logarithmic layer under boundary layer hypothesis:

$$k_{eq} = \frac{u_\tau^2}{\sqrt{C_\mu}}\,. \tag{3.13}$$

and

$$\varepsilon = u_\tau^2 \nabla u = \frac{u_\tau^3}{\kappa y}\,, \tag{3.14}$$

where κ is called the von Kármán constant (Eq. 3.11) and u_τ is the friction velocity (Eq. 3.10). Finally, since the behaviour of k and ε is known in the logarithmic layer (Eq. 3.13 and Eq. 3.14), it comes:

$$\mu_t = C_\mu \overline{\rho}\frac{k^2}{\varepsilon} = C_\mu \overline{\rho}\frac{u_\tau^4}{C_\mu}\frac{\kappa y}{u_\tau^3} = \overline{\rho} u_\tau \kappa y\,.$$

Linking both expressions leads to $\overline{\rho} C_\mu \sqrt{k} C_d y = \overline{\rho} C_\mu \frac{u_\tau}{C_\mu^{1/4}} C_d y = \overline{\rho} u_\tau \kappa y$, and therefore:

$$C_d = \kappa C_\mu^{-3/4}\,. \tag{3.15}$$

The choice of A_μ follows numerical experiments [23]: its value is chosen to recover the logarithmic law.

It was already explained that a transport equation for k is necessary to compute μ_t (Eq. 3.12) :

$$\partial_t \overline{\rho} k + \nabla \cdot (\overline{\rho} \widetilde{u} k) - \nabla \cdot \left((\mu + \frac{\mu_t}{\sigma_k}) \nabla k \right) = P - \overline{\rho} \varepsilon \,,$$

where P is the production term for k: $P = \left(\mu_t (\nabla \widetilde{u} + \nabla \widetilde{u}^\top - \frac{2}{3} \nabla \cdot \widetilde{u} \, \mathbf{I}) - \frac{2}{3} \overline{\rho} k \, \mathbf{I} \right) : \nabla \widetilde{u}$. ε appears in the k equation and it is defined with the following expression:

$$\varepsilon = \frac{k^{3/2}}{L_\varepsilon} \,. \tag{3.16}$$

The length scale L_ε contains a damping term near the wall that helps reproducing the kinetic energy dissipation rate variations near solid wall [23] :

$$L_\varepsilon = C_d y \left(1 - \exp[-R_y / A_\varepsilon] \right) .$$

The constant C_d is the same as for the turbulent viscosity. The last constant is therefore A_ε. Near the wall, the damping term L_ε is estimated from a Taylor expansion in y and the first order approximation leads to:

$$1 - exp \left(- \frac{R_y}{A_\varepsilon} \right) = \frac{R_y}{A_\varepsilon} \,.$$

Finally, L_ε is:

$$L_\varepsilon = \frac{\overline{\rho} \kappa \, C_\mu^{-3/4} \, y^2 \, \sqrt{k}}{\mu A_\varepsilon} \,. \tag{3.17}$$

Once L_ε expression is introduced in Eq. 3.16, it comes:

$$\varepsilon = \frac{\mu k A_\varepsilon}{\overline{\rho} y^2 \kappa \, C_\mu^{-3/4}} \,. \tag{3.18}$$

But, the behaviour of ε near the wall can be estimated from Chien turbulence model:

$$\varepsilon = 2 \mu \frac{k}{\overline{\rho} y^2} \,,$$

which leads to:

$$A_\varepsilon = 2 \kappa \, C_\mu^{-3/4} = 2 C_d \,.$$

Finally, the complete form of the turbulence model is:
– *In high-Reynolds regions (typically* $y^+ > 200$*)*

$$\left\{ \begin{array}{l} \dfrac{\partial \overline{\rho} k}{\partial t} + \nabla \cdot (\overline{\rho} \tilde{u} k) - \nabla \cdot ((\mu + \mu_t) \nabla k) = P - \dfrac{2}{3} \overline{\rho} k \nabla \cdot \tilde{u} - \overline{\rho} \varepsilon \\ \dfrac{\partial \overline{\rho} \varepsilon}{\partial t} + \nabla \cdot (\overline{\rho} \tilde{u} \varepsilon) - \nabla \cdot ((\mu + c_\varepsilon \mu_t) \nabla \varepsilon) = \dfrac{\varepsilon}{k} \left(\dfrac{c_1}{C_\mu} P + \dfrac{2 c_1}{3 C_\mu} \overline{\rho} k \nabla \cdot \tilde{u} - c_2 \overline{\rho} \varepsilon \right) \end{array} \right. \tag{3.19}$$

The eddy viscosity is given by $\mu_t = C_\mu \bar{\rho} \dfrac{k^2}{\varepsilon}$.

$-$In Low-Reynolds regions (typically $y^+ < 200$)
The eddy viscosity is given by:

$$\mu_t = C_\mu \bar{\rho} \sqrt{k} L_\mu \,, \text{ with } L_\mu = \kappa C_\mu^{-3/4} y \left(1 - exp(\frac{-y^+}{0.0142}) \right) .$$

The equation on k is kept as introduced in Eq. 3.19 and ε is deduced from $\varepsilon = \dfrac{k^{3/2}}{L_\varepsilon}$ with $L_\varepsilon = \kappa C_\mu^{-3/4} y \left(1 - exp(\dfrac{-y^+}{2\kappa C_\mu^{-3/4}}) \right)$. The model constants are summarised in Tab. 3.2.

c_ε	c_1	c_2	C_μ
1/1.4245	0.1296	11/6	0.09

Table 3.2: *Constants for the two-layer $k - \varepsilon$ turbulence model.*

Remark 3.4.2 *The key point is the switch between the two parts of the model. Starting a computation with a uniform flow leads to small values of y^+ inside the whole computational domain and the high-Reynolds version of the model is never activated. It leads to bad-quality results. Following our experience, the switch parameter must account for two contributions. The high-Reynolds version of the model must be applied for the condition:*

$$y^+ > 200 \textbf{ or } y > Y_L .$$

Y_L is a length chosen by the user, it depends on the estimated boundary layer height. The choice of Y_L is such that at convergence, the switch parameter is in practice given by $y^+ > 200$.

3.5 Conclusion

The principle of RANS modelling was introduced in this chapter and the derivation of a two-layer $k - \varepsilon$ turbulence model was presented. The same kind of approach will be considered to define a two-layer thermal turbulence model. In next chapter, we will see that the algebraic expression for ε issued from the two-layer $k - \varepsilon$ (dynamic) turbulence model defines a boundary condition for wall functions.

Chapter 4

Thermal turbulence

4.1 Introduction

Turbulent models applied to industrial flows account for the mean effects of turbulence. With these models, turbulent Reynolds stress tensor and heat flux are linearly depending on velocity and temperature[1] gradients respectively. In fact, turbulent dynamic diffusivity μ_t and turbulent thermal diffusivity λ_t follow the Boussinesq approximation. Both diffusivities are finally linked together through the turbulent Prandtl number, defined by analogy with the laminar consideration.

The key point for modelling the turbulent convection-induced heat flux under the turbulent regime follows the Reynolds analogy [119]. The idea is to link turbulent heat flux contribution with the temperature gradient and a turbulent thermal diffusivity. Finally, the turbulent thermal diffusivity is linked with the turbulent viscosity assuming a constant turbulent Prandtl number Pr_t. Therefore, only two independent scales need to be transported by the turbulence. In practice, scales for the dynamic turbulence are transported and thermal diffusion is assumed proportional to the dynamic diffusion. As a consequence, simply knowing turbulent momentum transport is necessary to quantify diffusion by turbulence.

This analogy is false in many configurations. First of all, it was measured or computed (as a post-treatment of DNS) that the turbulent Prandtl number Pr_t varies in the boundary layer: $Pr_t \simeq 0.85$ in the region of fully developed turbulence and near the wall, the question of the value of Pr_t is still open. Moreover, it is about 0.9 in the heated wake, but about 0.5 in a heated mixing layer. As a consequence, assuming $Pr_t = 0.9$ in the last example leads to an underestimation of the heat flux by 40%. Some DNS confirm this result [4], but the corresponding Reynolds numbers are quite limited and in general, far from the ones for industrial configurations. A database on Pr_t was built during the last decades [120, 76]. But it is limited to boundary layer, parallel plates and pipes. There is a lack of data for more complex geometries. Finally, obtaining accurately these values from experiments is a complex task because Pr_t is estimated from measures on several basic quantities:

$$Pr_t = \frac{\widetilde{u''v''}}{\widetilde{u''T''}} \frac{\frac{\partial \widetilde{T}}{\partial y}}{\frac{\partial \widetilde{u}}{\partial y}}. \tag{4.1}$$

In Eq. 4.1, errors in measures can be of great importance. As an example, error can be larger than 10% for $\widetilde{u''T''}$ [130, 8]. Therefore, it seems that the idea of a universal value for Pr_t is false

---

[1] It was seen in Chapter 3 that the "true" variable to consider is enthalpy. For a perfect gas, both approaches (based on temperature or enthalpy gradients) are equivalent.

[73]. A good way to overcome these theory limitations is to assume that λ_t must be estimated without knowing Pr_t *a priori*. The technique consists in modelling the turbulent heat diffusion, as it was done for the dynamic diffusion of turbulence [28]. This approach was presented in Chapter 3 but it is possible to go further in the thermal modelling, considering four-equation transport models (two equations for dynamic turbulence and the last two equations for thermal turbulence). For the dynamic part, some models were already considered. For the thermal counterpart, models generally consist in the transport of the thermal energy of turbulence k_h and the dissipation scale of this quantity ε_h [84]. Turbulence models based on $k - \varepsilon \,/\, k_h - \varepsilon_h$ quantities are generally not built for boundary layer effects and damping terms are added to correct the behaviour near solid walls. This approach is generally considered for low-Reynolds extension of turbulence models [111, 64, 110, 112, 147, 67].

The work on thermal RANS turbulence models is motivated by the need to increase accuracy of the heat flux computed on the thermal protection of a reentry object. In particular, many results were obtained during the PhD thesis of S. Galera [47] at CEA/CESTA and the most important results are summarised below.

4.2 Analysis of thermal turbulence models

The way to build a turbulence model for thermal effects follows the technique used for dynamic turbulence. The first thermal model for RANS was proposed by Nagano and Kim in 1988 [111]. It is a low-Reynolds turbulence model (valid up to the wall) that was considered to predict turbulent convection near the wall. Authors show impressive results in very close agreement with experiments. The underlying method to build the model remains the Boussinesq approach for the turbulent thermal transfer:

$$-\overline{\rho u'' h''} = \alpha_t \nabla \tilde{h} \tag{4.2}$$

The thermal diffusivity λ_t is not introduced in Eq. 4.2: it is replaced by a new coefficient α_t.

Remark 4.2.1 *α_t has not any name for physicists. It will be called turbulent thermal diffusivity (or simply thermal diffusivity) in the following, even if the "true" turbulent thermal diffusivity is of course λ_t.*

Remark 4.2.2 *Eq. 4.2 means that the total heat flux for RANS modelling is written under the form:*

$$q = -(\lambda \nabla \widetilde{T} + \alpha_t \nabla \widetilde{h})\,.$$

α_t can be defined by a dimensional analysis in which integral scales of turbulence are introduced:

$$\alpha_t \sim \overline{\rho}\, \Delta u_h L_h\,, \tag{4.3}$$

where $\overline{\rho}$, l_h and Δu_h are the averaged density, a mixing length and a velocity scale to represent thermal turbulence activity.

The choice of both scales Δu_h and L_h is much more complex than for a pure dynamic model since there are a lot of combinations to build these scales.

The thermal velocity scale must be established by turbulence convection considerations. Iritani *et al.* [68] showed that the structures with the maximum of dynamic and thermal energies are the same. A choice for the velocity scale is therefore the dynamic turbulence velocity

$$\Delta u_h \sim \sqrt{k}\,,$$

and new corrections must be introduced in the time scale τ_h.

Remark 4.2.3 *With a pure dynamic approach, the dynamic and thermal time scales are the same* $\tau_d = \tau_h = k/\varepsilon$ *and Reynolds' analogy is recovered.*

The time scale τ_h is generally assumed to be a function of dynamic dissipation time $\tau_d = k/\varepsilon$ and thermal dissipation time $\tau_{th} = 2k_h/\varepsilon_h$, where $k_h = 1/2\ \widetilde{h''^2}$ represents enthalpy fluctuations and ε_h appears in the transport equation for k_h as its dissipation rate:

$$\varepsilon_h = \alpha\overline{(\nabla h'')^2}\,. \tag{4.4}$$

As a consequence

$$\tau_h \ = \tau_d^m \times \tau_{th}^n \text{ with } m+n=1 \text{ and } m,n \in \mathbb{R}.$$

The thermal diffusivity of turbulence is finally given by the following general relation:

$$\alpha_t = \overline{\rho} C_\alpha \left(\frac{k}{\varepsilon}\right)^m \left(\frac{\widetilde{h''^2}}{\varepsilon_h}\right)^n = \overline{\rho} C_\alpha \left(\frac{k}{\varepsilon}\right)^m \left(\frac{2\,k_h}{\varepsilon_h}\right)^n\,,$$

where C_α is a constant (which value is still unknown).

Another way to proceed consists in introducing the ratio R of thermal and dynamic time scales:

$$R = \frac{k_h/\varepsilon_h}{k/\varepsilon}\,. \tag{4.5}$$

This parameter plays an important role in turbulence modelling. It is generally considered constant, following the constant turbulent Prandtl number assumption. However, experiments show that R has large variations: they depend on the case itself and for a given case, there are also variations inside the flow [143]. The time scale can be written

$$\tau_h = \tau_d^n\,(2\tau_{th})^m = \tau_d\,(2R)^m\ ,$$

and the final definition of α_t is:

$$\alpha_t = \overline{\rho} C_\alpha k \tau_d\,(2R)^m\ . \tag{4.6}$$

The case $m = 0$ means $\tau_h = \tau_d$. The case $m = 1$ makes the thermal scale τ_{th} appear. Any value of m is possible but the values of m will be chosen such as:

$$|m| < 2\,.$$

The choice of the time scale is transformed in the choice of the parameter m**.**

4.2.1 Transport equation for enthalpy fluctuations and their rate of dissipation

Without entering into details (the reader can analyse [47, 65] for all details in the derivation of both equations) and introducing $k_h = \frac{1}{2}\widetilde{h''h''}$, the equation for the mean of squared thermal energy fluctuations is:

$$\frac{\partial(\overline{\rho}k_h)}{\partial t} + \frac{\partial(\overline{\rho}\tilde{u}_i k_h)}{\partial x_i} = \frac{\partial}{\partial x_i}\left((\alpha + d_h)\frac{\partial k_h}{\partial x_i}\right) + H_i\frac{\partial \tilde{h}}{\partial x_j} - \overline{\rho}\varepsilon_h\,, \tag{4.7}$$

with $d_h = \dfrac{\alpha_t}{\sigma_h}$, $H_i = \alpha_t\dfrac{\partial \tilde{h}}{\partial x_i}$ and σ_h is the turbulent Prandtl-Schmidt number for thermal energy.

Deriving an equation for ε_h is much more complex and all details are in [65]. The final form of the equation is:

$$\begin{aligned}\frac{\partial}{\partial t}(\overline{\rho}\varepsilon_h) + \frac{\partial}{\partial x_i}(\overline{\rho}\tilde{u}_i\varepsilon_h) = \;& \frac{\partial}{\partial x_i}\left((\alpha + d_{\varepsilon_h})\frac{\partial \varepsilon_h}{\partial x_i}\right)\\ &+\frac{\varepsilon_h}{k_h}\left(C_{\varepsilon_{h_1}}H_i\frac{\partial \tilde{h}}{\partial x_j} - C_{\varepsilon_{h3}}\overline{\rho}\varepsilon_h\right)\\ &+\frac{\varepsilon_h}{k}\left(C_{\varepsilon_{h_2}}R_{ij}\frac{\partial \tilde{u}_i}{\partial x_j} - C_{\varepsilon_{h_4}}\overline{\rho}\varepsilon\right),\end{aligned}$$

in which $d_{\varepsilon_h} = \alpha_t/\sigma_{\varepsilon_h}$, and σ_{ε_h} is the turbulent Prandtl-Schmidt number for thermal energy dissipation rate.

4.2.2 Turbulence model closure

The final form of the turbulence model is obtained once the coefficients are fixed. Several simplified configurations are considered, namely the local equilibrium assumption, the turbulence decrease after a grid and a flow in rapid distortion (shear layers).

4.2.3 Extension for low-Reynolds modelling

In practice, any author calibrates his model with his own coefficients (see Tab. 4.1 and Tab. 4.2). All authors have their own formulation to extend the proposed equations near the wall, using damping terms. These formulations are defined in Tab. 4.1 and Tab. 4.2.

The equations are finally modified and a generic low-Reynolds version of the $k - \varepsilon \,/\, k_h - \varepsilon_h$ model for both thermal and dynamic turbulences is:

$$\left\{\begin{array}{ll}\partial_t\overline{\rho}k + \nabla.(\overline{\rho}\tilde{u}k) - \nabla.\left((\mu + \dfrac{\mu_t}{\sigma_k})\nabla k\right) & = P_k - \overline{\rho}\varepsilon^* - D_k\\ \partial_t\overline{\rho}\varepsilon^* + \nabla.(\overline{\rho}\tilde{u}\varepsilon^*) - \nabla.\left((\mu + \dfrac{\mu_t}{\sigma_\varepsilon})\nabla \varepsilon^*\right) & = \dfrac{\varepsilon^*}{k}(f_{\varepsilon_1}C_{\varepsilon_1}P_k - f_{\varepsilon_2}C_{\varepsilon_2}\overline{\rho}\varepsilon^*) + E_k\\ \partial_t\overline{\rho}k_h + \nabla.(\overline{\rho}\tilde{u}k_h) - \nabla.\left((\alpha + \dfrac{\alpha_t}{\sigma_{k_h}})\nabla k_h\right) & = P_{k_h} - \overline{\rho}\varepsilon_h^* - D_h\\ \partial_t\overline{\rho}\varepsilon_h^* + \nabla.(\overline{\rho}\tilde{u}\varepsilon_h^*) - \nabla.\left((\alpha + \dfrac{\alpha_t}{\sigma_{\varepsilon_h}})\nabla \varepsilon_h^*\right) & = \dfrac{\varepsilon_h^*}{k_h}(f_{\varepsilon_{h_1}}C_{\varepsilon_{h_1}}P_{k_h} - f_{\varepsilon_{h_3}}C_{\varepsilon_{h_3}}\overline{\rho}\varepsilon_h^*)\\ & \quad +\dfrac{\varepsilon_h^*}{k}(f_{\varepsilon_{h_2}}C_{\varepsilon_{h_2}}P_k - f_{\varepsilon_{h_4}}C_{\varepsilon_{h_4}}\overline{\rho}\varepsilon^*) + E_h\end{array}\right.$$

Remark 4.2.4 *For numerical stability, equations are written with a pseudo-dissipation assumption, as in Remark 3.4.1. The transformation leads to homogeneous Dirichlet condition on* ε^* *and* ε_h^*.

Remark 4.2.5 *In the following, the star will be removed from expressions.*

Thermal and dynamic diffusivities are finally given by:

$$\mu_t = \overline{\rho} f_\mu C_\mu \frac{k^2}{\varepsilon} \,, \tag{4.8}$$

$$\alpha_t = \overline{\rho} f_\alpha C_\alpha \frac{k^2}{\varepsilon} \left(2\,R\right)^m \,, \tag{4.9}$$

where R is the time scale ratio from Eq. 4.5. Compared with their high-Reynolds version, the new models contain diffusion term and damping terms to account for the wall effects on turbulence (f_μ, f_{ε_1}, f_{ε_2}, f_α, $f_{\varepsilon_{h_1}}$, $f_{\varepsilon_{h_2}}$, $f_{\varepsilon_{h_3}}$ and $f_{\varepsilon_{h_4}}$). New terms (D_k, E_k, D_h, E_h) increase the model accuracy near the wall.

Damping terms, constants and supplementary terms for some models are summarised in Tab. 4.1 and 4.2. In these tables, the following definitions are used:

$$R_t = \frac{\overline{\rho} k^2}{\mu\varepsilon}, \;\; R_y = \frac{\overline{\rho}\sqrt{k} y}{\mu}, \;\; y^+ = \frac{\overline{\rho} u_\tau y}{\mu}.$$

	Hattori & Nagano & Tagawa	Nagano & Kim	Chien
C_μ	0.09	0.09	0.09
C_{ε_1}	1.45	1.45	1.35
C_{ε_2}	1.9	1.9	1.8
σ_k	1.4	1.0	1.0
σ_ε	1.3	1.3	1.3
f_μ	$[1-\exp(-y^+/30)]^2$ $\times[1+(20/R_t^{3/4})\exp\{-(R_t/120)^2\}]$	$[1-\exp(-y^+/26.5)]^2$	$1-\exp(-0.0115y^+)$
f_{ε_1}	1.0	1.0	1.0
f_{ε_2}	$1-0.3\exp(-R_t^2)$	$1-0.3\exp(-R_t^2)$	$1-\dfrac{0.4}{1.8}\exp(-R_t^2/36)$
$\lim\limits_{y=0}\varepsilon$	0.0	0.0	0.0
D_k	$2\mu\left(\dfrac{\partial\sqrt{k}}{\partial y}\right)^2$	$2\mu\left(\dfrac{\partial\sqrt{k}}{\partial y}\right)^2$	$2\mu\dfrac{k}{y^2}$
E_k	$\dfrac{\mu\mu_t}{\overline{\rho}}(1-f_{w1})\left(\dfrac{\partial^2\tilde{u}}{\partial y^2}\right)^2$ with $f_{w1}=\{1-\exp(-y^+/30)\}^2$	$\dfrac{\mu\mu_t}{\overline{\rho}}(1-f_\mu)\left(\dfrac{\partial^2\tilde{u}}{\partial y^2}\right)^2$	$2\mu\dfrac{\varepsilon}{y^2}\exp(-y^2/2)$

Table 4.1: *Dynamic characteristics of Hattori - Nagano - Tagawa (HNT), Nagano - Kim (NK) and Chien turbulence models.*

	Hattori & Nagano & Tagawa	Nagano & Kim
C_α	0.1	0.11
$C_{\varepsilon_{h_1}}$	0.85	0.9
$C_{\varepsilon_{h_2}}$	0.64	0.72
$C_{\varepsilon_{h_3}}$	1.0	1.1
$C_{\varepsilon_{h_4}}$	0.9	0.8
σ_{k_h}	1.0	1.0
σ_{ε_h}	1.0	1.0
f_α	$[1-\exp(-y^+/30)]$ $\times[1-\exp(-y^+/(30/Pr^{1/3}))]$ $\times[1+(7.9/R_t^{3/4})\exp\{-(R_t/120)^2\}]$	$[1-\exp(-\frac{\sqrt{Pr}y^+}{30.5}\frac{2S_t}{C_f})]^2$
$f_{\varepsilon_{h_1}}$	1.0	1.0
$f_{\varepsilon_{h_2}}$	1.0	1.0
$f_{\varepsilon_{h_3}}$	1.0	1.0
$f_{\varepsilon_{h_4}}$	$(1/C_{\varepsilon_{h_4}})(C_{\varepsilon_2}f_{\varepsilon_2}-1)$	1.0
$\lim_{y=0}\varepsilon_h$	0.0	0.0
D_h	$2\alpha\left(\frac{\partial\sqrt{k_h}}{\partial y}\right)^2$	$2\alpha\left(\frac{\partial\sqrt{k_h}}{\partial y}\right)^2$
E_h	$\frac{\alpha\alpha_t}{\overline{\rho}}(1-f_{w2})\left(\frac{\partial^2\tilde{h}}{\partial y^2}\right)^2$ with $f_{w2}=\{1-\exp(-y^+/(30/Pr^{1/3}))\}^2$	$\frac{\alpha\alpha_t}{\overline{\rho}}(1-f_\alpha)\left(\frac{\partial^2\tilde{h}}{\partial y^2}\right)^2$
R_{eq}, m	0.5, 0.5	0.44, 0.5

Table 4.2: *Thermal characteristics of Hattori - Nagano - Tagawa (HNT) and Nagano - Kim (NK) turbulence models.*

4.2.4 Effects of thermal turbulence models on RANS results

Following asymptotic analysis (in the equilibrium region and near the wall), Galera showed that the model with the best properties is Nagano - Kim turbulence model [47]. This choice is also driven by computational considerations, analysing the flow over an isothermal flat plate at $Ma = 5$. The main conclusions are:

- The dynamic boundary layer is weakly influenced by the thermal boundary layer on isothermal wall,
- The temperature profile computed with a thermal turbulence model differs with the one from a pure dynamic turbulence model,
- The thermal boundary layer height is not influenced by the thermal turbulence model,
- The turbulent Prandtl number computed as a post-treatment of the thermal turbulence model varies inside the boundary layer: Fig.4.1 represents the evolution of $Pr_t = \mu_t/\alpha_t$.
- The wall heat flux decreases with a thermal turbulence model (Fig. 4.2). This is due to the fact that α_t computed from the thermal model is lower than μ_t/Pr_t.
- For $y^+ > y^+_{eq}$ (fully turbulent zone), the ratio μ_t/α_t tends to a constant value, the turbulent Prandtl number obtained with a pure dynamic analysis of the boundary layer (following the Reynolds analogy).
- Switching from a coupled dynamic / thermal turbulence model near the wall to a pure dynamic turbulence model inside the equilibrium region has not strong effects on wall friction and wall heat flux, as shown in Fig. 4.3. This is a key point to introduce thermal model corrections locally and not inside the whole computational domain.

As a consequence, the thermal boundary layer modelling has only a local effect and enables a dedicated temperature distribution inside the boundary layer.

4.2.5 Conclusion

Most of RANS CFD codes used in industry consider the strong Reynolds analogy to link temperature fluctuations effects with temperature gradients through the introduction of a constant turbulent Prandtl number. Experiments showed that such hypothesis is false in the boundary layer. Nagano *et al.* were the first authors to propose, develop and analyse new thermal turbulence models. Their work was motivated by the desire to analyse thermal turbulence effects in metal casting. Their models are based on four transport equations. The standard $k - \varepsilon$ equations treat the dynamic part of the turbulence, while thermal effects are represented by k_h and ε_h.

Their models were extended to account for compressibility effects and they were applied to hypersonic flows over isothermal flat plate. It is clear that including thermal modelling for the boundary layer has an effect on wall heat flux, especially at high speed, such as during reentry. This aspect of the modelling cannot be neglected, even if the overall effect of the thermal turbulence model depends on areas in the flow. For reentry, the local modification of the heat flux can be forgotten since there remains thermal protection on the body and the overall change in heat flux is easily accounted for through margins of the heat protection system. The

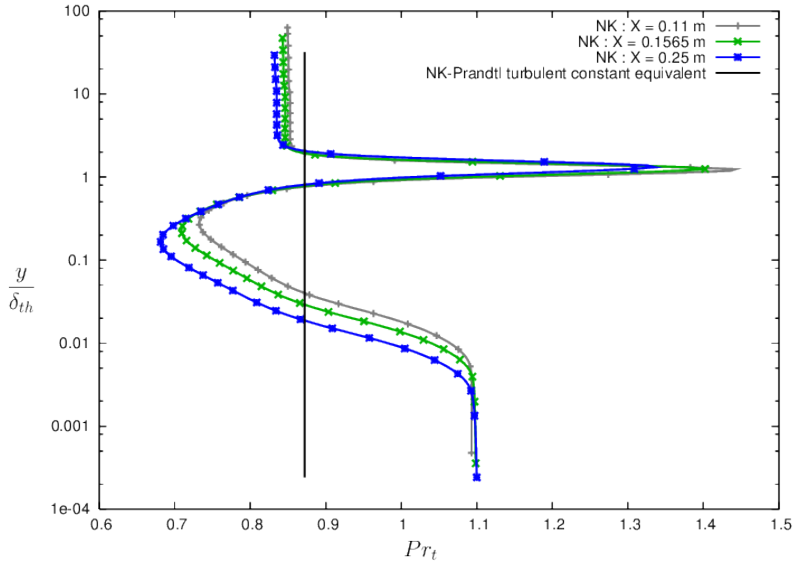

Figure 4.1: *Nagano - Kim turbulence model: turbulent Prandtl number inside the thermal boundary layer for 3 abscissa ($x = 0.11m$, $x = 0.1565m$, $x = 0.25m$)*

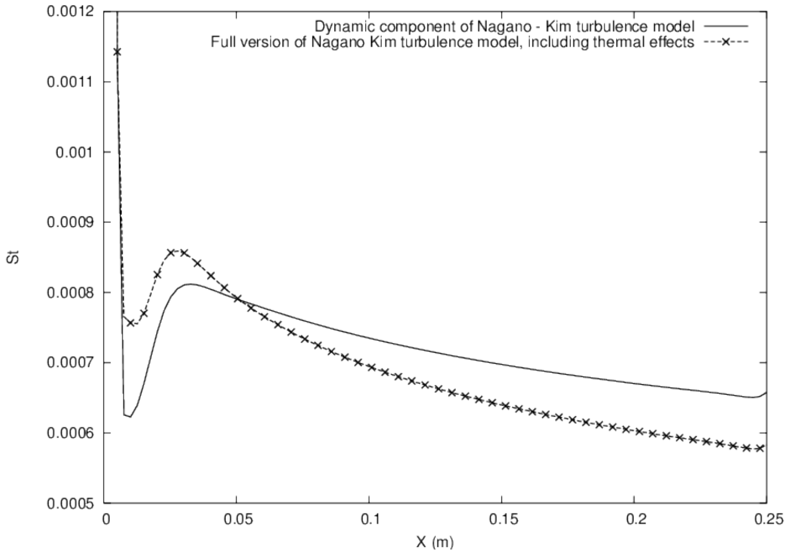

Figure 4.2: *Stanton number (dimensionless heat flux) along an isothermal flat plate at $Ma = 5$. Comparison of results obtained with the full version of Nagano - Kim model with the ones computed considering only the dynamic part of the model (and therefore linking explicitly α_t to μ_t).*

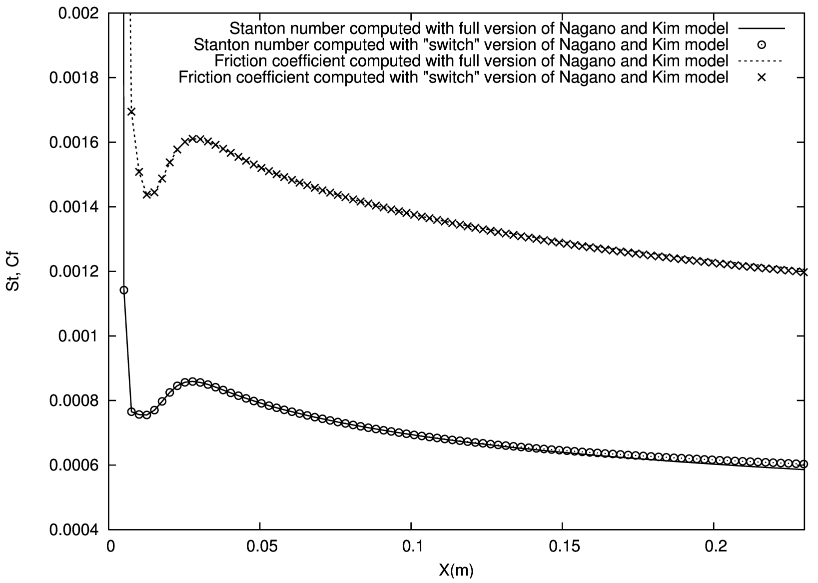

Figure 4.3: *Comparison of friction coefficient and Stanton number obtained with the full turbulence model or the switch version.*

situation is not so favourable for the reentry object bottom where heat flux is lower, leading to less thermal protection. The computation of large recirculation bubbles downstream the reentry object is a challenging computation since the size of the recirculation bubble can be very large compared to the reference length of the object.

This work on thermal turbulence models was presented during a conference [49] and fully described in S. Galera PhD thesis [47]. Moreover, the comparison of thermal turbulence models is also available in [48].

The procedure for dynamic turbulence consists in deriving wall functions from a two-layer turbulence model that helps in defining Dirichlet boundary condition for turbulence quantities. Following this procedure, we derive in next section a new two-layer thermal turbulence model.

4.3 A two-layer turbulence model with dynamic and thermal effects

The key point regarding thermal turbulence is to account for its effects near the wall, up to the equilibrium region. It can be less CPU consuming to split the computational domain dynamically into two parts: near the wall, a turbulence model that includes two different scales for dynamic and thermal turbulence is considered, while a pure dynamic model is suitable far from the wall. In practice, a standard $k - \varepsilon$ model without damping terms can be chosen far from the wall. This kind of model was basically chosen for the two-layer approach for dynamic turbulence. The way to separate scales is the key point.

A first way to account for thermal turbulence effects with a low additional cost is to develop a two-layer turbulence model. A two-layer dynamic model uses a standard equation for k and links ε with k through an algebraic relation. If the same approach can be applied to k_h, one would finally obtain a two-equation turbulence model near the wall, with an equation for k and the second one for k_h plus two algebraic expressions for ε and ε_h. Far from the wall, the equation for k_h would be replaced by the equation on ε. The boundary condition for ε would simply be defined from the algebraic expression needed to introduce ε near the wall.

4.3.1 Two-layer technique for the temperature

Thermal diffusivity can be defined as the product of its internal scales:

$$\alpha_t \sim \overline{\rho} \Delta u_h L_h,$$

where Δu_h and L_h are a velocity scale and a thermal turbulence scale respectively.

There are many choices regarding Δu_h but a first approach consists in taking the scale associated with dynamic turbulence, as Iritani [68] does:

$$\Delta u_h = \Delta u_d \simeq \sqrt{k}\,.$$

It is therefore mandatory to include thermal corrections in L_h. If one follows the same procedure as for the dynamic two-layer turbulence model, α_t becomes:

$$\alpha_t = \overline{\rho} C_\alpha \sqrt{k} L_\alpha\,,$$

where C_α is a constant from Nagano et Kim turbulence model. L_α contains damping effects near the wall and thermal corrections due to the choice of the reference velocity Δu_h:

$$L_\alpha = C_{th} y \left(1 - \exp[-R_y/A_\alpha]\right),$$

where $R_y = \overline{\rho}\sqrt{k} y/\mu$.

The system is closed once values are defined for both C_{th} and A_α.

4.3.2 Constant C_{th}

Before entering into details, do not forget that dynamic and thermal scales are linked together with R (Eq. 4.5):

$$\alpha_t = \frac{C_\alpha}{C_\mu} \mu_t (2R)^m, \tag{4.10}$$

Since μ_t was already introduced for the dynamic version of the two-layer model (Eq. 3.12), Eq. 4.10 comes easily:

$$\alpha_t = \frac{C_\alpha}{C_\mu} \rho C_\mu \sqrt{k} L_\mu (2R)^m. \tag{4.11}$$

First, let us define L_α. Far from the wall, thermal and dynamic turbulence scales are closed and a full four equation coupled turbulence model is not necessary for a pure aerodynamic problem for which the main parameter is heat flux. But, near the wall, a four-equation model is mandatory. A continuous transition between both models is required and it comes:

$$\overline{\rho}\sqrt{k} C_\alpha C_{th} y = \alpha_t = C_\alpha \overline{\rho} \sqrt{k} \kappa C_\mu^{-3/4} y (2R_{eq})^{m_{eq}}\,,$$

and therefore

$$C_{th} = \kappa C_\mu^{-3/4} (2R_{eq})^{m_{eq}} \,. \tag{4.12}$$

In the equilibrium area, a good choice is $R_{eq} = 0.5$ and $m_{eq} = 1$ (from Eq. 4.6). Finally:

$$C_{th} = \kappa C_\mu^{-3/4} \,. \tag{4.13}$$

4.3.3 Constant A_α

The system closure needs to define A_α. Near the wall, L_α can be expanded following Taylor expansion rule:

$$L_\alpha = \frac{(2R_{eq})^{m_{eq}} \overline{\rho} \kappa C_\mu^{-3/4} y^2 \sqrt{k}}{\mu A_\alpha} \,.$$

Using Eq. 4.11 in which L_μ and L_α are replaced by their limited developments, one obtains:

$$A_\alpha = \frac{(2R_{eq})^{m_{eq}}}{(2R_w)^{m_w}} A_\mu .$$

4.3.4 Consequences

The new thermal two-layer turbulence model does not need to solve an equation for k_h. This is due to the fact that our way to close relations, and especially A_α does not depend directly on k_h.

4.3.5 Summarising the model

Near the wall, for $y^+ < y^+_{eq}$, the boundary layer is computed with the following thermal two-layer turbulence model.

Dynamic part

Dynamic diffusivity of turbulence is modelled by:

$$\mu_t = \overline{\rho} C_\mu \sqrt{k} L_\mu \,, \tag{4.14}$$

with

$$L_\mu = C_d y \left(1 - \exp[-R_y / A_\mu]\right) , \tag{4.15}$$

where $C_d = \kappa C_\mu^{-3/4}$ and $A_\mu = 70$. The turbulent kinetic energy is solution of a partial differential equation:

$$\partial_t \overline{\rho} k + \nabla.(\overline{\rho} \tilde{u} k) - \nabla. \left((\mu + \frac{\mu_t}{\sigma_k}) \nabla k \right) = P_k - \overline{\rho} \frac{k^{3/2}}{L_\varepsilon} \,, \tag{4.16}$$

where

$$L_\varepsilon = \kappa C_\mu^{-3/4} y \left(1 - \exp[-R_y / A_\varepsilon]\right) \,,$$

and $A_\varepsilon = 2\kappa C_\mu^{-3/4}$.

Thermal part

Thermal turbulent diffusivity is estimated from:

$$\alpha_t = \overline{\rho} C_\alpha \sqrt{k} L_\alpha \,, \tag{4.17}$$

where L_α is a length scale:

$$L_\alpha = C_{th} y \left(1 - \exp[-R_y / A_\alpha]\right) , \tag{4.18}$$

with $C_{th} = \kappa C_\mu^{-3/4} (2R_{eq})^{m_{eq}}$. A_α is a correction at the wall:

$$A_\alpha = \frac{(2R_{eq})^{m_{eq}}}{(2R_w)^{m_w}} A_\mu \,. \tag{4.19}$$

In Eq. 4.17-4.19, new constants to define behaviour of quantities at the limit are necessary and their values are summarised in Tab. 4.3.

m_{eq}	R_{eq}	R_w
1.0	0.5	Pr

Table 4.3: *New constants for the thermal model.*

4.3.6 Final closure

The value of m at the wall is still unknown. This parameter plays an important role in modelling thermal turbulence since the power m acts on the "unbalanced turbulence scales" through the coefficient R. For a 4-equation thermal turbulence model, a theoretical (judicious!) choice is $m_w = 0.5$ but this choice cannot be applied to the reduced model that needs to include turbulence time scale corrections. In practice, m_w cannot be computed from asymptotic developments of previous relations near the wall.

The value of m is in practice strongly coupled with the value of the turbulent Prandtl number at the wall:

$$Pr_{t_w} = \lim_{y^+ \to 0} \frac{\mu_t}{\lambda_t} = Pr_{t_{eq}} \frac{(2R_{eq})^{m_{eq}}}{(2R_w)^{m_w}} = \frac{Pr_{t_{eq}}}{(2Pr)^{m_w}} \,. \tag{4.20}$$

All numerical solutions and experimental data show that $Pr_{t_w} > 1$ at the wall, from which one can deduce

$$m_w < \frac{\ln(Pr_{t_{eq}})}{\ln 2Pr} < 0. \tag{4.21}$$

Our final choice for m_w follows the one proposed by Horiuti [66]:

$$m_w = -1. \tag{4.22}$$

It is important to remark that the value of Pr_t at the wall depends on Pr, which is in agreement with experiments [110].

Our two-layer thermal turbulence model is validated on the same boundary layer over a flat plate as previously. The Stanton number distribution on the wall is compared with experimental results [34] on Fig. 4.4. It is shown that the thermal correction of the two-layer turbulence model leads to an increase of the dimensionless heat flux by 18%. Results are improved with the correction.

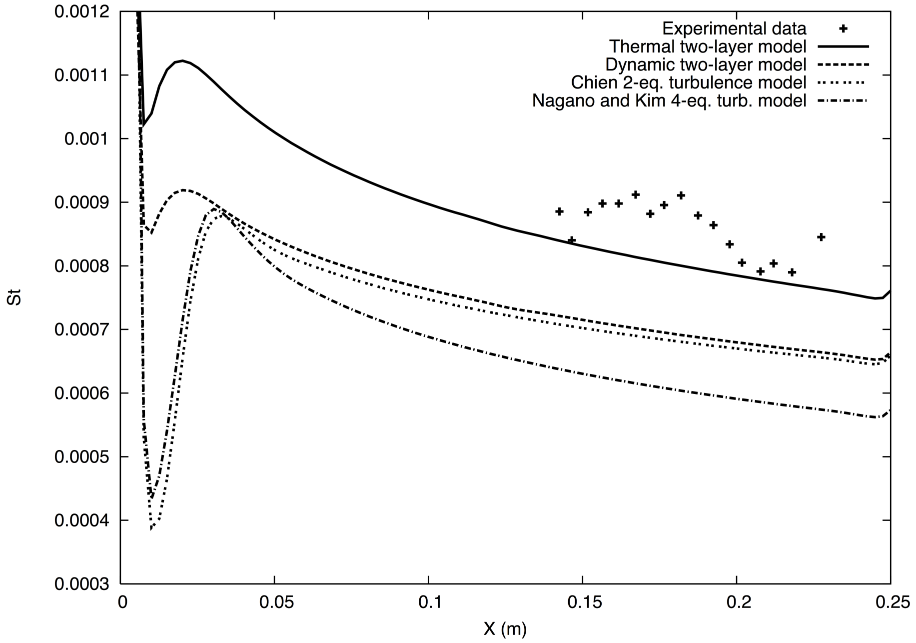

Figure 4.4: *Stanton number obtained with different turbulence models and comparison with experimental data.*

4.4 Conclusion

This chapter addresses the specific problem of not linking algebraically thermal and dynamic turbulence effects. To do so, a four-equation $k - \varepsilon - k_h - \varepsilon_h$ was extended to compressible flows and its physical behaviour was analysed on a simple flat plate configuration. Numerical results showed that dynamic and thermal boundary layers do not share identical scales and accounting for thermal turbulence has an impact on the wall heat flux.

In a second step, we developed a two-layer dynamic turbulence model that includes thermal turbulence corrections.

It is now possible to focus attention on the development of wall functions and including thermal effects in wall functions will be based on the two-layer thermal model.

Chapter 5

Wall functions

5.1 Introduction and principle

The basic idea in wall functions is to remove the stiff part of the boundary layer: the no-slip boundary condition is replaced by more sophisticated relations between the variables and their derivatives. Mathematically, wall functions are based on a scale reduction of original models. Following physical assumptions, the full version of RANS equations are simplified using directions parallel and normal to the wall.

Historically, many wall functions were defined during the last 30 years because they can help to minimise the effort on the discretisation of the boundary layer. Instead of solving the whole boundary layer as usual with a turbulence model valid up to the wall, a less refined mesh is considered and the inherent loss of accuracy is counterbalanced by physical models introduced in the discretisation. We have also considered wall function as a way to account for rough boundary (in 2003) and a general strategy to extend standard turbulence models to rough wall was published recently [7]. Our computations also showed that wall functions induced a better-conditioned problem that was easier to solve.

Some researchers see in wall functions a “miraculous” technique for which good results are more due to chance rather than physical analysis. But, our wall functions are based on physical and mathematical closure and of course, their use needs best practices, as for any numerical ingredient. In particular, independence of results with respect to mesh is a key point to address.

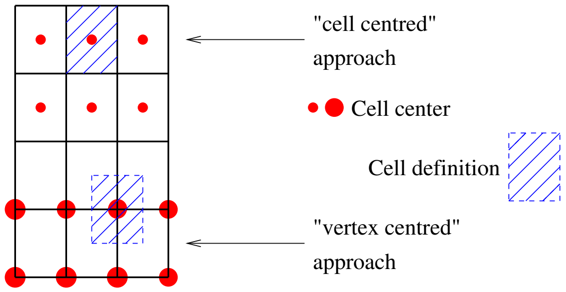

Figure 5.1: *Principles of control volume / cells associated with cell-centred and vertex-centred formulations.*

Wall functions can be implemented in any CFD solver, for structured or unstructured grids and for any mathematical formulation. This means that once a discretisation technique is chosen (finite volume and finite element are the two discretisation formalisms considered here, but an extension to finite difference may be built), implementation of wall functions follows the mathematical procedure to solve the partial differential equation. Finally, wall functions can be applied on any formulation, either cell-centred or vertex-centred, as introduced in Fig. 5.1.

The vertex-centred formulation was considered for developments inside NSC2KE, a research code developed by B. Mohammadi [97]. NSC2KE was used during PhD of S. Galera and myself. At CEA/CESTA and for the French civil aeronautic industries (Airbus Group and Safran) or research centres (ONERA), codes are essentially block-structured and based on a cell-centred formalism. A good overview of results obtained with wall laws can be found in [54] for transonic flows and in [113, 47] for supersonic flows.

The principle of wall functions is to remove the computation of the part of the boundary layer near the wall, even if this part contains most of the flow physics. In term of implementation, there are two ways to proceed, as introduced in the following picture.

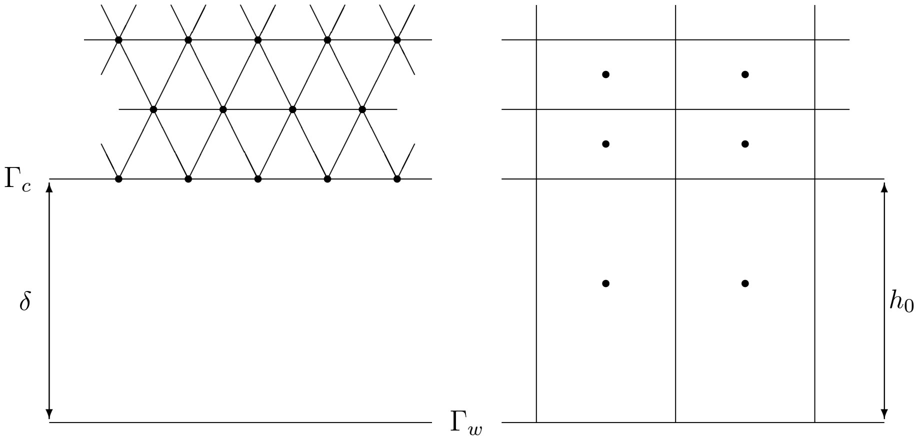

Wall law with fictitious wall on an unstructured triangular mesh

Wall laws with cell clustering for a structured mesh (Onera method [54])

For the first method (left), Γ_w is the true solid boundary and Γ_c is a fictitious boundary, obtained as a translation of a distance δ in the direction $\vec{n}$ normal to the wall and directed in the flow. The wall treatment is applied on Γ_c. The parameter δ is the shift between true and computational boundaries. This approach is implemented in CEA/CESTA CFD codes and it is also introduced in *elsA*. In practice, the shift δ is very small, compared to the reference length scale introduced in the Reynolds number. This fact explains why, in practice, the shift is not accounted for in the mesh generation and $\Gamma_w = \Gamma_c$. In the same way, the reference length needs to be corrected to define the Reynolds number:

$$Re' = Re\frac{L+\delta}{L}\,. \tag{5.1}$$

but for the considered Reynolds numbers (about 5×10^6) and with $\delta = 10^{-4}m$ for a reference length of several meters, the Reynolds number modification Eq. 5.1 is neglected.

In practice, one only needs to define a mesh not refined enough to capture accurately the turbulent boundary layer. The main parameter is therefore the height h of the cell above the wall and one generally chooses:

$$\frac{\delta}{3} < h < \frac{\delta}{2}$$

The second approach (right) consists in applying wall functions in the centre of the first cell above the wall. With this approach, gradients computed for the face of the first cell parallel to the wall need a correction since their value can be false. This last approach was implemented in CANARI[1] and *elsA* [17]. This approach presents several drawbacks:

- Mesh generation: one needs to create a grid as usual and then several rows must be clustered in the direction normal to the wall. After the computation, it is necessary to check that the mesh coarsening is in agreement with physical considerations introduced by the wall functions. If the local Reynolds number y^+ is too large, too many cells are clustered and the clustering procedure must be performed again.

- Compatibility with advanced techniques for convergence speed-up: This technique is difficult to couple with multigrid or grid sequencing approaches. Grid sequencing differs from multigrid: with grid sequencing, the computation begins on very coarse grid and the result is then interpolated on a refined one, etc. up to the initial mesh. At each level, it is possible to use a multigrid technique taking into account the previous meshes as sub grids.

Once these considerations regarding implementation are established, one can work on the wall function itself. Our choices follow the following rules:

1. Global formulation in y^+: validity up to the wall.
2. Mathematical formulation: the chosen formulation implies boundary integrals that need to be computed with the wall function.
3. Choice of the shift parameter δ: δ must not be too high.
4. Mesh refinement: one needs to take care of mesh refinement in order to get mesh-converged results.
5. Large validity domain: this point is important for compressibility effects.
6. Thermal effects: adiabatic and isothermal walls.

5.2 Boundary integrals

The RANS version of the Navier-Stokes equations is coupled with a turbulence model. Here, for the sake of clarity, the $k - \varepsilon$ turbulence model is considered but our approach can be adapted easily to any (standard) turbulence model associated with one or two partial differential equations. The conservative Navier-Stokes equations can be written in the following compact form:

$$\frac{\partial W}{\partial t} + \nabla.(F(W) - N(W)) = S(W), \tag{5.2}$$

where $W = (\rho, \rho\vec{u}, \rho E, \rho k, \rho\varepsilon)^\top$ are conservative fields, F and N are convection and diffusion operators respectively and $S = (0, ..., 0, S_k, S_\varepsilon)$ contains source terms from the turbulence

---

[1] CANARI is one of ONERA CFD codes developed before *elsA*.

model. Introducing a finite volume approach, the following boundary integrals are obtained from Eq. 5.2:

$$\int_{\Gamma_c} W(\vec{u}\cdot\vec{n})d\sigma,\ \int_{\Gamma_c} p\vec{n}d\sigma,\ \int_{\Gamma_c} p(\vec{u}\cdot\vec{n})d\sigma, \tag{5.3}$$

$$\int_{\Gamma_c} \tau\cdot\vec{n}d\sigma, \tag{5.4}$$

$$\int_{\Gamma_c} \Big((\lambda+\lambda_t)\frac{\partial T}{\partial n} - (\vec{u}\tau)\cdot\vec{n}\Big)d\sigma, \tag{5.5}$$

$$\int_{\Gamma_c} (\mu+\mu_t)\frac{\partial k}{\partial n}d\sigma \text{ and } \int_{\Gamma_c}\left(\mu+\frac{\mu_t}{\sigma_\varepsilon}\right)\frac{\partial \varepsilon}{\partial n}d\sigma \tag{5.6}$$

where p is the pressure, $\sigma = -p\mathbf{I} + \tau$ with τ the Reynolds stress tensor. μ_t is the turbulent viscosity, λ_t thermal conductivity. $(\vec{t}, \vec{t'}, \vec{n})$ is an orthogonal normalised local basis with $\vec{n}$ unit normal vector at the wall and $(\vec{t}, \vec{t'})$ is a basis of the tangential space.

5.3 How to build wall functions?

In this section, the goal is not to explicitly recall all developments of wall functions but it is of great interest to put the focus on several key points, in particular on the closure for turbulence equations.

5.3.1 Key point 1: variables variation and local reference frame

Wall functions are based on the resolution of 1D equations in the direction normal to the wall. To do so, the first step consists in projecting equations in the local normal direction at the wall and in neglecting transverse quantities. Mathematically, this means that the flow is fully anisotropic and variations of the tangential component of the velocity in the normal direction are the most important phenomena to capture.

5.3.2 Key point 2: recovering theory and standard laws of the wall

For incompressible flows, the boundary layer can be divided in several parts and the standard laws were introduced in Sec. 3.4.2.

For the use of wall functions in a Navier-Stokes solver, it is needed to model the velocity and the friction from the wall ($y^+ = 0$) up to $y^+ \simeq 300$. An extension of the linear and logarithmic laws is suitable ($5 \leq y^+ \leq 50$). The easiest model is the following:

$$\begin{aligned} u^+ &= y^+ && \text{if} \quad y^+ < 11,13\,, \\ u^+ &= \frac{1}{\kappa}\log y^+ + C_1 && \text{if} \quad y^+ > 11,13\,. \end{aligned} \tag{5.7}$$

The constant 11.13 is obtained as intersection of linear and logarithmic profiles. Eq. 5.7 represents an extrapolation of profiles according to continuity of expressions but the derivative is not continuous. A way to overcome this problem is to consider Reichardt function. Reichardt function f_r accounts for both linear and logarithmic profiles:

$$f_r(y^+) = 2.5\log(1+\kappa y^+) + 7.8\Big(1 - \exp\left(-\frac{y^+}{11}\right) - \frac{y^+}{11}\exp(-0.33y^+)\Big).$$

In our implementations, Reichardt function is the preferred profile.

5.3.3 Key point 3: compressibility corrections

For compressible flows, corrections of the velocity profile must be implemented. Van Driest [138] showed that the logarithmic law remains valid for compressible flows if the tangential component U of the velocity is replaced by the transformed velocity $\overline{U}$, which is defined as a mean quantity depending on the density:

$$u^+ = \frac{\overline{U}}{u_\tau} \quad ; \quad u_\tau = \sqrt{\tau_w/\rho_w} \quad ; \quad y^+ = \frac{y u_\tau}{\nu_w} \,. \tag{5.8}$$

$$\overline{U} = \int_0^U \sqrt{\frac{\rho}{\rho_w}} \, \mathrm{d}U \,. \tag{5.9}$$

This correction of the velocity profile works fine for transonic flows. For supersonic flows, we proposed and validated a modification of Van Driest correction [99, 48, 102].

5.3.4 Key point 4: closure of energy equation

Writing the conservation of the total enthalpy in the local basis $(\vec{t}, \vec{n})$ and neglecting the convection effects leads to:

$$\frac{\partial}{\partial n}(U\tau_{nt} - \phi_n) = 0. \tag{5.10}$$

Assuming friction constant near the wall, Eq. 5.10 gives an expression for the evolution of the normal component of the heat flux near the wall:

$$\phi_n - U\tau_w = \phi_w, \tag{5.11}$$

where U is the tangential component of the velocity. Remarking that Eq. 5.11 is integrated in Eq. 5.5, a very simple closure of the energy equation for an adiabatic wall is found: it is 0. For an isothermal wall, the situation is more complex but the closure is based on the same relation.

5.3.5 Key point 5: closure of turbulence equations

Turbulence equations are weakly coupled with the wall function for the mean flow. Once the boundary conditions for the mean flow are established, the turbulent quantities boundary conditions are linked with the friction velocity. For a standard $k - \varepsilon$ turbulence model, a Dirichlet condition on k that is directly extrapolated from the analysis of k behaviour near the wall is applied. ε is simply obtained from the two-layer turbulence model introduced in Sec. 3.4.2.

5.4 Extension of wall functions

Three extensions are summarised in this section. The first one deals with the extension of wall functions to handle rough walls. The second extension concerns the coupling between wall functions and a thermal turbulence model. The last extension concerns the simulations of pitching airfoil with mesh deformation.

5.4.1 Wall functions and rough walls

Wall roughness introduces significant changes in heat and strain transfers between the wall and the flow with respect to the corresponding quantities for a smooth wall. From an industrial point of view, it is therefore important to efficiently account for the presence of wall roughness in numerical methods.

The first approach to introduce wall roughness is to account for it directly in the mesh. Of course, this is not feasible for standard roughness encountered in reentry flows: their typical dimension is about $100\mu m$ and the reentry object measures more than 1 meter. A second approach consists in introducing a correction in the turbulence model (valid up to the wall) such as performed by Durbin *et al.* [40] or Aupoix [7]. For incompressible flows, there are many articles or parts of books about rough boundaries. Usually, to take rough elements into account, a new coefficient, that vanishes on smooth boundaries, is added to the log-relation to modify the evaluation of the friction velocity u_τ that helps closing boundary integral for momentum and energy equations. As an example, one can consider the sand grain theory due to Schlichting [127]. But such an approach issued from experiments cannot be extended easily to any roughness element shape since there is no perfect law to find the equivalent sand-grain parameters in agreement with a general rough element shape. This is especially true for reentry flows where rough element are mainly a consequence of thermal protection ablation.

Our approach is different. A sensitivity analysis with CFD computations is performed and a general law to account for rough elements is deduced from the sampling. This approach has several advantages:

1. It is simple to analyse and to implement since it is based on numerical solutions and not on experiments.

2. The sensitivity of the flow with respect to roughness shape is large and up to now, no one has found a universal adaptation of the near wall behaviour of velocity and temperature. With this approach, it is possible to define the parameters of the roughness and to adapt the treatment according to the kind of material considered during reentry.

With this approach, the sensitivity analysis leads to the definition of a polynomial approximation and the polynomial coefficients are computed solving an optimisation problem using least-square method. Two correction polynomials (to link the increase in friction and in heat flux due to roughness at the wall with the same quantity on smooth wall) were found. Without entering into details, one key point of our procedure is that it enables to find a generic law that produces results in quite close agreement with PANT law.

PANT method (PAssive Nosetip Technology) is an engineering method to evaluate the heat flux on rough boundaries. The principle of PANT method (described in [38]) is to give a correlation between the heat transfer flux on smooth walls (C_{h_0}) and the one on rough boundaries (C_{h_r}). This correlation is validated by experimental results. Let P_t be defined as

$$P_t = \frac{\rho_\infty u_\infty h}{\mu_\infty}\sqrt{\frac{C_{h_0}}{1.24}\frac{T_\infty}{T_w}\frac{1+110.4/T_w}{1+110.4/T_\infty}}\,,$$

with C_{h_0} the Stanton number on the smooth boundary and h the sand-grain roughness parameter. The following relations link P_t with the heat flux on rough boundaries:

$$\begin{cases} \dfrac{C_{h_r}}{C_{h_0}} = 1 \text{ if } P_t \leq 10\,, \\ \dfrac{C_{h_r}}{C_{h_0}} = 1 + \dfrac{2}{3}\left(log_{10}(P_t) - 1\right) \text{ if } 10 < P_t < 10^4\,, \\ \dfrac{C_{h_r}}{C_{h_0}} = 3 \text{ if } 10^4 \leq P_t\,. \end{cases} \tag{5.12}$$

Fig. 5.2 represents the behaviour of C_{h_r}/C_{h_0} as function of $log_{10}(P_t)$. This figure comes from [38]. An interesting point is the fact that the error between the experimental data and C_{h_r}/C_{h_0} defined in Eq. 5.12 is less than 30%.

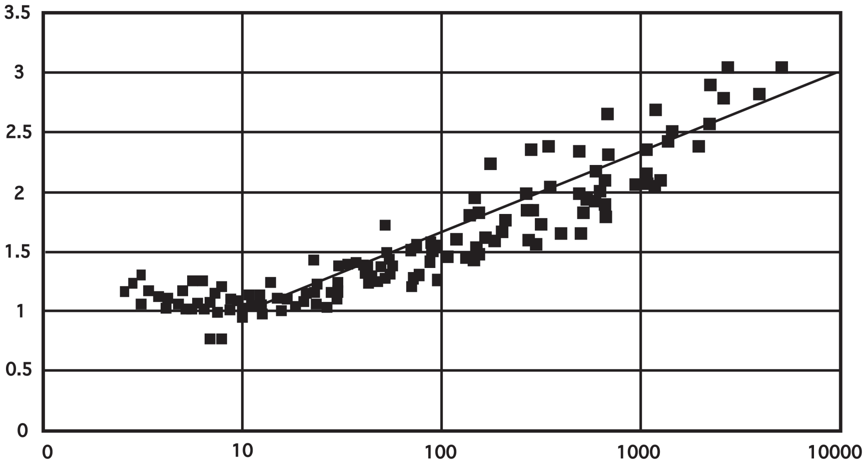

Figure 5.2: *Influence of rough elements on the heat flux for high speed turbulent flows, figure extracted from [38]. Each black square represents data extracted from experiences and the line represents Eq. 5.12.*

In Fig. 5.3, numerical solutions are compared with experimental results from PANT. The results are in good agreement with the PANT formulation since, like in Fig. 5.2, the results from numerical simulation are distributed around the graph of the correction C_{hr}/C_{h0} (Eq. 5.12).

For practical use, two correction polynomials were obtained [101]: one for the integral for momentum equation closure and one for the energy equation closure. They were validated on supersonic configurations. One drawback of the current formulation lies on the fact that it cannot account for pressure effects due to the presence of rough elements. In particular, following results obtained during the training period of O. Frayssinet [46], there can be strong variations of the pressure due to the presence of the rough elements, especially at high Mach number (flow of air at $Ma \simeq 7$, rough elements characterised by a size of about $100\mu m$, hypotheses of chemical equilibrium, isothermal wall at temperature about $750K$).

5.4.2 Wall functions and thermal turbulence

The development of wall functions including thermal turbulence follows the same procedure as for the dynamic turbulence. The main difference occurs in the integration procedure of the

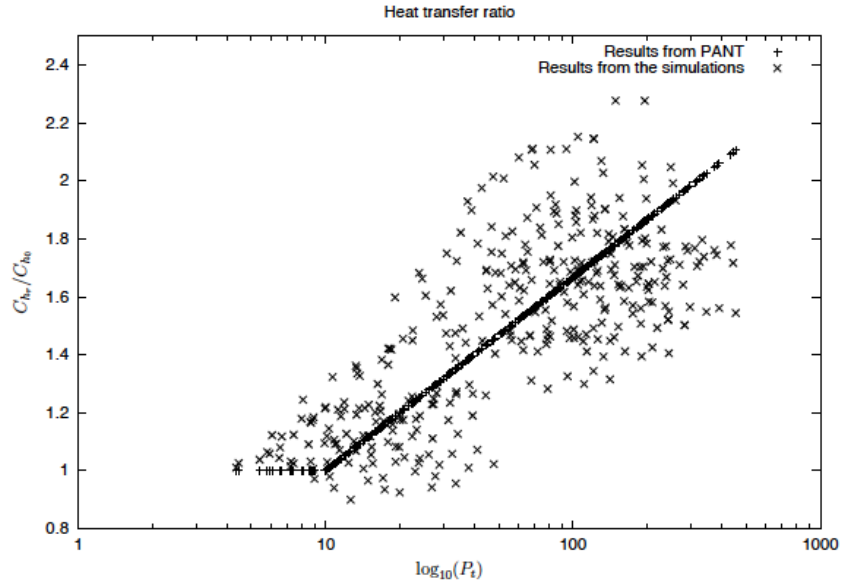

Figure 5.3: *Influence of rough elements on the heat flux for turbulent flows, comparison of the results of the simulations with the ones from PANT method. The distribution of numerical solutions follows experimental data distribution shown in Fig. 5.2.*

simplified energy equation and an approach similar to the one performed by Goncalves and Houdeville [55] has proved to be efficient. The thermal correction is introduced through the definition of α_t for the integration of the energy equation. These wall functions are coupled with a dynamic turbulence model (high-Reynolds version of $k-\varepsilon$ turbulence model) with two prescribed Dirichlet boundary conditions: a standard condition for k is chosen while the condition on ε follows the expression for ε in the two-layer $k-\varepsilon$ turbulence model.

5.4.3 Wall functions and mesh deformation

When the mesh is moving or is deformable, the no-slip boundary condition is replaced by a continuity condition: the flow velocity at the wall is the boundary velocity. And of course, standard velocity profile cannot be applied in the reference frame since $\vec{u}_w \neq \vec{0}$.

The only way to use the standard wall-laws is to express wall functions in the relative frame associated with wall boundary. In this case, the no-slip condition is recovered at the wall. But the geometry movement generally induces a longitudinal component of the pressure gradient and the standard logarithmic law with $C \simeq 5$ becomes false: the constant depends on many physical effects including potential negative or positive pressure gradients. In our implementation, the modification of C according to longitudinal pressure gradient is not accounted for: the simple formulation for stationary walls is recovered.

The wall heat flux is independent of the frame used for the computation. However, the change in the basis has an impact on the shear stress tensor τ_w. All the complexity is hidden in the transformation back to the original frame.

Using the velocity law composition, the true velocity $\vec{u}$ is the sum of a component in the reference frame $\vec{u}_r$ and a velocity associated with mesh movement $\vec{s}$:

$$\vec{u} = \vec{u}_r + \vec{s}.$$

Let $\overline{\mu}$ represent the sum of dynamic and turbulent viscosities. Using the linearity of τ, it comes $\tau = \tau_r + \tau_m$, where $\tau_r = \overline{\mu}(\nabla\vec{u}_r + \nabla\vec{u}_r^\top - \frac{2}{3}\nabla \cdot \vec{u}_r\mathbf{I})$ represents the shear stress contribution due to the relative velocity $\vec{u_r}$ of the fluid and $\tau_m = \overline{\mu}(\nabla\vec{s} + \nabla\vec{s}^\top - \frac{2}{3}\nabla \cdot \vec{s}\mathbf{I})$ is the shear stress contribution due to the mesh velocity $\vec{s}$. Wall functions enable to compute $\tau_r\vec{n}$. To obtain the correct shear stress, one has to add $\tau_m\vec{n}$ to $\tau_r\vec{n}$.

This approach of wall functions was developed during the European Project SimSAC in 2008 [114] and the implementation was performed in *elsA*. Some results regarding 2D computations of NACA0012 airfoil are included below.

Experimental data were summarised by Landon [82]. In order to compare numerical data from *elsA* and experimental data, a post-treatment of experimental data was performed. It consists in casting Landon results back to the dimensionless pressure p (defined as computational pressure over inflow pressure), using the non-dimensional variables used for the computations. The flow incidence follows a sinus law: $\alpha(t) = \alpha_0 + \alpha_m \sin(\omega t)$. Four configurations are considered and are summarised in Tab. 5.1. The reduced frequency is the non-dimensional oscillation frequency $\bar{\omega} = \omega c/2V$ where c is the chord and V the velocity norm at inflow.

	α_m (deg)	α_0 (deg)	R_e ($\times 10^6$)	f (Hz)	$\bar{\omega}$	Ma
CT1	2.89	2.41	4.8	50.32	0.0808	0.6
CT2	3.16	4.59	4.8	50.32	0.0811	0.6
CT3	4.86	2.44	4.8	50.32	0.0810	0.6
CT5	0.016	2.51	5.5	62.5	0.0814	0.755

Table 5.1: *Parameters for NACA0012 test cases.*

For all test cases, the agreement between low-Reynolds simulation (referred AEL LR for AeroELastic - Low-Reynolds modelling), wall laws simulation (referred AEL WL for AeroELastic - Wall-Laws approach, fictitious wall approach), and experimental data is quite good (Fig. 5.4, Fig. 5.5, Fig. 5.6, Fig. 5.7). Actually, we recover a general property of wall functions: wall functions perform quite well even in situations for which they were not designed for. Here, the angle of attack for CT5 is sufficiently high to induce a strong recirculation bubble coupled with a high displacement of the shock and our formulation is only valid for attached flow.

5.5 Conclusion

This chapter addresses the last step of the turbulence modelling. The development of wall functions is motivated by the possible decrease in restitution time. This is possible by replacing the no-slip condition by more sophisticated relations involving *a priori* knowledge of the boundary layer. Wall function lead to a better problem conditioning since most of the stiff part of the boundary layer is integrated in the formulation of wall functions.

We showed that wall functions can include complex physical phenomena, such as wall roughness, thermal effects or mesh movement. For aircraft computations (for instance drag coefficient), results obtained with wall functions differ with the ones using turbulence models valid up-to the wall. For industry, it does not mean that wall functions lead to bad results, it

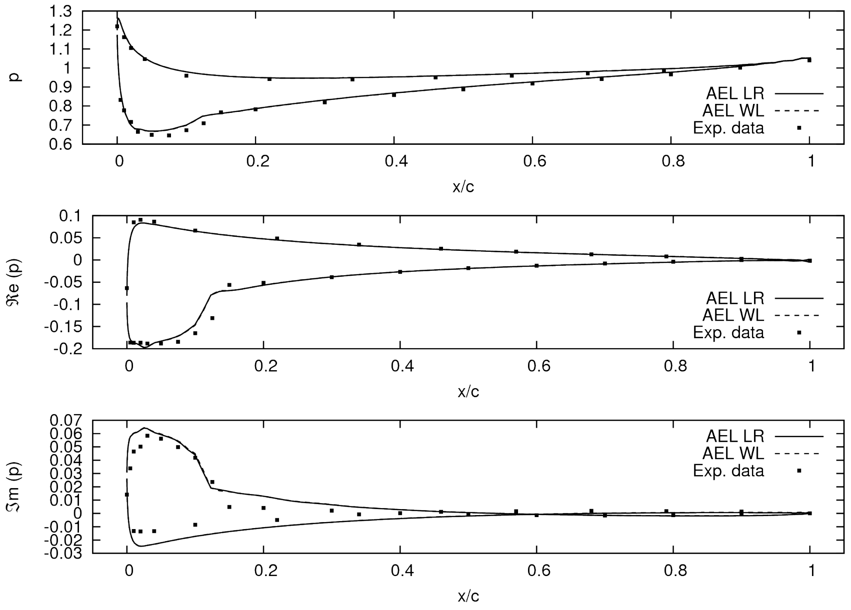

Figure 5.4: *Dimensionless wall pressure distribution for NACA0012. CT1 test case.*

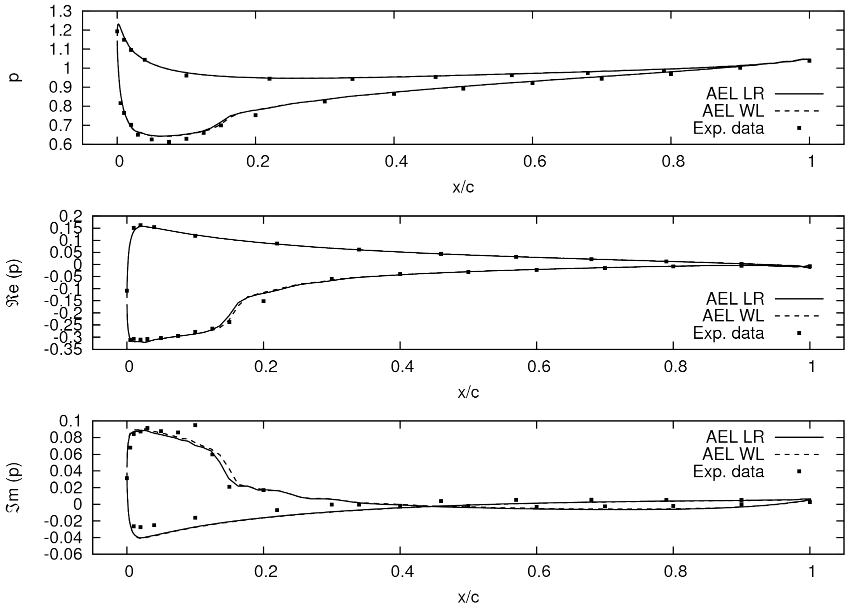

Figure 5.5: *Dimensionless wall pressure distribution for NACA0012. CT2 test case.*

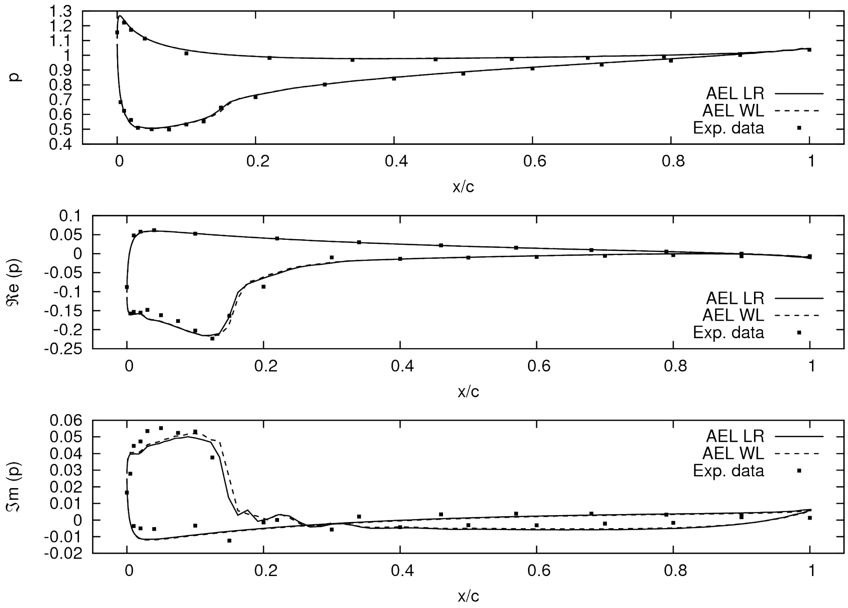

Figure 5.6: *Dimensionless wall pressure distribution for NACA0012. CT3 test case.*

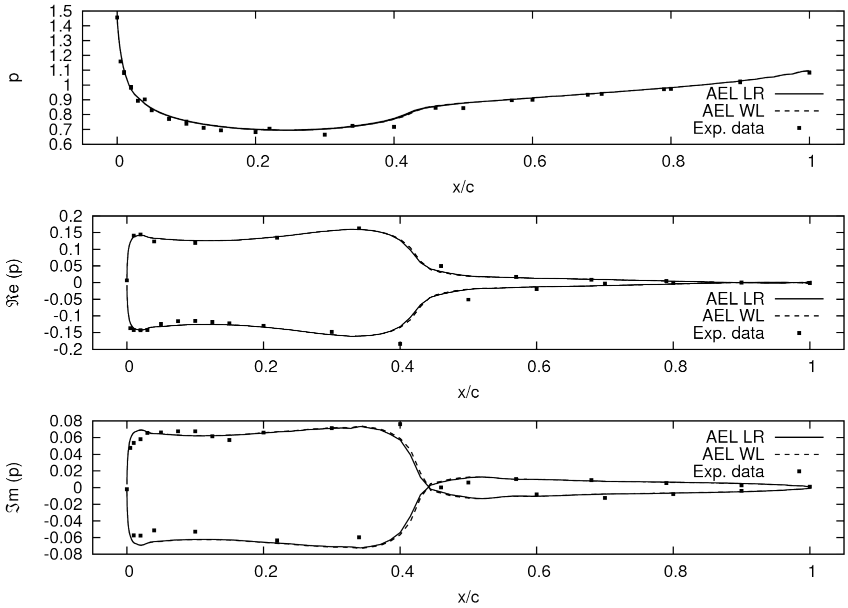

Figure 5.7: *Dimensionless wall pressure distribution for NACA0012. CT5 test case.*

simply means that the way to include margins has to be adapted. Wall functions must be seen as a reduced-order model that enables to capture a complex flow at a moderate CPU cost.

We also demonstrated that wall functions can include complex physical phenomena as wall roughness for supersonic flows at reentry conditions. In this case, our approach consists in defining corrections to account for wall roughness directly in wall functions for smooth boundary. The correction is defined with a sensitivity analysis on numerical simulations.

Finally, we adapted wall functions to account for mesh movement and the validation was performed on a pitching airfoil case. We saw that wall functions performed quite well, even if the flow could contain recirculation areas where wall functions were not optimised to lead to accurate results.

Part II

Mathematical analysis of turbulence models

It is generally accepted that, even if implementing a turbulence model in a CFD code can be a tedious work due to its impact on all schemes, validation and best practices are the bottleneck. In particular, turbulence models are built using physical considerations and are generally not analysed in term of mathematical behaviour. As an example, many turbulence models like $k-\varepsilon$ or $k-\omega$ turbulence models need to remain positive and bounded during all steps of the computational loop because these quantities are positive and bounded by nature. This is not always the case and researchers established several corrections. An example regarding the $k-\varepsilon$ turbulence model is presented in [87]. In this part, the goal is not to present all possible corrections because they depend on the model and potentially on the application to treat, but to work towards a new formulation of the model with improved mathematical properties. This part is a tentative to make a bridge between physical turbulence models and turbulence models defined from mathematical considerations with good numerical properties.

This part is issued from my PhD thesis and from a work performed with V. Arrecgros during a training period at CEA/CESTA. It is a “mathematical” work on the numerical stability of the equations and on the demonstration of existence and unicity of the solution of “isolated” turbulence equations. The present work concerns properties established for the incompressible version of the Navier-Stokes equations.

This topic is nowadays far from my current activities and I will not be able to work on it in the next years.

Associated paper:

− Mathematical and Numerical Analysis of an Alternative Well-Posed Two-Layer Turbulence Model, B. Mohammadi and G. Puigt. *ESAIM: Mathematical Modelling and Numerical Analysis - Modélisation Mathématique et Analyse Numérique*, 35(6), pp. 1111-1136, 2001.

Master thesis:

− Mise en œuvre et validation d’un nouveau modèle de turbulence mathématiquement bien posé, V. Arrecgros. Master thesis, Université de Bordeaux 1.

People I worked directly with:

− Prof. Bijan Mohammadi

− Vincent Arrecgros (training period at CEA/CESTA)

Chapter 6

Mathematical models for incompressible turbulent flows

6.1 Introduction

The mathematical analysis of RANS equations, even if it is of strong interest for industry, has been generally neglected by the mathematician community. For compressible flows, this is due to the high complexity to solve the Navier-Stokes equations without adding any modelling: this is one of the Millennium Problems[1] related to three dimensional turbulence.

This topic was addressed by physicists in a different way: for some turbulence models, their simulations were leading to unphysical behaviour (negativity of kinetic energy for instance) and they proposed and implemented several techniques to maintain realizability.

Here, the goal is to correct the bad numerical behaviour of a turbulence model based on k and ε quantities in order to:

1. Maintain **positivity** during the computational loop. This is to keep physical properties of the turbulent variables. Spalart and Allmaras recently summarised in [3] the modifications of their turbulence model in order to keep positivity of the turbulent variable.

2. Maintain **bounded** variables during the computational loop. This it to avoid an increase of turbulence quantities up-to an “overflow”.

3. Maintain a global numerical **stability**, allowing an easier implicit formulation (for time integration) and larger physical or pseudo time steps. Even if the computation of the time step accounts for turbulent viscosity and turbulent diffusivity explicitly, the maximum CFL number for stability is never possible due to turbulence equations. For implicit time integration (as for steady flows), the linearisation of turbulent equations is generally not performed rigorously and artificial “corrections” based on user experience are generally introduced.

After introducing the technique developed by Mohammadi [95], some results obtained for the equation alone and for the coupled RANS equations in 2D are recalled. Then, our work on the two layer $k-\varepsilon$ turbulence model is summarised.

---

[1] `http://www.claymath.org/millennium-problems`

6.2 A change in variables for the turbulence

The first point to remember is Eq. 3.19 where P represents the production term (Eq. 3.9). Let us introduce $\mathcal{P}$:

$$P = \mu_t \mathcal{P}. \tag{6.1}$$

It is clear that $\mathcal{P}$ has a strong mathematical property: $\mathcal{P}$ is always positive. Actually, in 2D, if $\vec{u} = (U, V)$, one has $\mathcal{P} = \frac{2}{3}(\partial U/\partial x - \partial V/\partial y)^2 + (\partial U/\partial y + \partial V/\partial x)^2 \geq 0$ and in 3D, if $\vec{u} = (U, V, W)$, the expression for P is:

$$\begin{aligned} \mathcal{P} \quad = \quad & \frac{2}{3}\left\{ \left(\frac{\partial U}{\partial x} - \frac{\partial V}{\partial y}\right)^2 + \left(\frac{\partial U}{\partial x} - \frac{\partial W}{\partial z}\right)^2 + \left(\frac{\partial V}{\partial y} - \frac{\partial W}{\partial z}\right)^2 \right\} + \\ & \left(\frac{\partial U}{\partial y} + \frac{\partial V}{\partial x}\right)^2 + \left(\frac{\partial U}{\partial z} + \frac{\partial W}{\partial x}\right)^2 + \left(\frac{\partial V}{\partial z} + \frac{\partial W}{\partial y}\right)^2 \geq 0. \end{aligned}$$

With the present form of the equation, no classic technique from theory of variations is able to give an upper bound of the left hand side of the high-Reynolds version of the two-layer $k - \varepsilon$ turbulence model.

Mohammadi proposed in [95] to define a new turbulence model using equations from k and ε for incompressible flows. The first variable is called θ and it was proposed for the first time by Cardot, Mohammadi and Pironneau [19]. For an incompressible flow, their choice is $\theta = k/\varepsilon$. The high-Reynolds version of the turbulence model needs a second turbulent quantity. For an incompressible flow, Lewandowski and Mohammadi [88] proposed to choose $\phi = \varepsilon^2/k^3$. Exponents in ϕ expression are chosen according to mathematical analysis. Taking k and ε equations and neglecting the viscous terms, one looks for $\phi = k^\alpha \varepsilon^\beta$ such that:

$$\frac{d\phi}{dt} = \frac{\partial \phi}{\partial t} + \vec{u} \cdot \nabla \phi \leq 0.$$

For a compressible flow ($\nabla \cdot \vec{u} \neq 0$), a single choice is proposed $\alpha = -C_{\varepsilon_1}/C_\mu$ and $\beta = 1$ but for an incompressible flow, several choices are possible. The classical choice is $\alpha = -3$ and $\beta = 2$ and it leads to $\phi \sim m^{-2}$: ϕ behaves as the square of the length scale L.

Remark 6.2.1 *Such a length scale L is introduced to recover the theoretical value $C_{\varepsilon_1} = 3/2$ that is slightly modified in the model equations.*

Remark 6.2.2 *The new variables θ and ϕ for incompressible flow have a physical meaning: θ (in s) represents a characteristic time and ϕ (in m^{-2}) is linked with a characteristic turbulent length scale. This is of course a consequence of the power considered to define θ and ϕ.*

As explained in the following sections, the constraint on the sign of the right hand side can be diminished, leading to other choices of the coefficient. This is indeed the case for the compressible version of the model discussed in Chap. 7.

6.2.1 The turbulence model based on new quantities

For the sake of clarity, the way to obtain the form of the new turbulence model is summarised here. In particular, attention is paid on the treatment of the diffusion term. Using the definition of θ, one finds:

$$\frac{\partial \theta}{\partial t} = \frac{\partial \frac{k}{\varepsilon}}{\partial t} = \frac{1}{\varepsilon}\frac{\partial k}{\partial t} - \frac{k}{\varepsilon^2}\frac{\partial \varepsilon}{\partial t} \tag{6.2}$$

and

$$\vec{u} \cdot \nabla\theta = \frac{1}{\varepsilon}\vec{u} \cdot \nabla k - \frac{k}{\varepsilon^2}\vec{u} \cdot \nabla\varepsilon. \tag{6.3}$$

Using Eq. 6.2 and Eq. 6.3 and the same kind of relation for ϕ, the turbulence model equations can be easily found but the expressions for diffusion terms of θ and ϕ are complex since they involve gradient of θ, ϕ, ν and ν_t.

The key point proposed in [95, 88] is to simplify diffusion terms: the diffusion term is modelled as usual, including Prandtl-Schmidt numbers C_θ and C_ϕ:

$$\left\{\begin{aligned} &\frac{\partial \theta}{\partial t} + \vec{u} \cdot \nabla\theta - \nabla \cdot \Big((\nu + C_\theta \nu_t)\nabla\theta\Big) = -C_3 \mathcal{P}\theta^2 + C_5 \\ &\frac{\partial \phi}{\partial t} + \vec{u} \cdot \nabla\phi - \nabla \cdot \Big((\nu + C_\phi \nu_t)\nabla\phi\Big) = -C_6 \mathcal{P}\theta\phi - C_8\frac{\phi}{\theta} \end{aligned}\right. \tag{6.4}$$

Such a modelling of the diffusion change the properties of the turbulence model. The new positive constants C_3, C_5, C_6 and C_8 depend explicitly on the initial $k - \varepsilon$ turbulence model constants through algebraic expressions. Finally, ν_t is computed from θ and ϕ:

$$\nu_t = C_\mu \frac{1}{\theta\phi}.$$

6.3 Mathematical results

In this section, the goal is to present (for consistency) the mathematical properties of the $\theta - \phi$ turbulence model. This part summarises most of the results presented in [52] for the incompressible version of the Navier-Stokes equations.

6.3.1 Notations

First, let us introduce mathematical definitions from the theory of distributions. Let $\Omega \subset \mathbb{R}^n$ be a bounded set with $\partial\Omega$ the lipschitzian boundary and n the space dimension ($n \geq 2$). Q is the cylinder $\Omega \times (0, T')$ where T' is the final time ($T' > 0$). Let $D(\Omega)$ be the space of C^∞ functions with a compact support in Ω. For an integer $m \geq 0$ and $1 \leq p \leq +\infty$, let us introduce:

$$W^{(m,p)}(\Omega) = \left\{ v \in L^p(\Omega) \mid \frac{\partial^{|\alpha|} v}{\partial^{\alpha_1} x_1 ... \partial^{\alpha_l} x_l} \in L^p(\Omega) \mid \forall \alpha = (\alpha_1, .., \alpha_l) \in \mathbb{Z}^l_+, |\alpha| = \sum_{k=1}^{l} \alpha_k \leq m \right\}.$$

In the same way, for $s > 0$ and $1 \leq p \leq +\infty$, one can introduce $W^{(s,p)}(\Omega)$ by interpolation. Moreover, $W_0^{(s,p)}(\Omega)$ is the closed space of $D(\Omega)$ with respect to the standard norm of $W^{(s,p)}(\Omega)$ and $W^{(-s,p')}(\Omega)$ the dual space of $W_0^{(s,p)}(\Omega)$ where $1/p + 1/p' = 1$ and $1 \leq p \leq +\infty$.

Let us also introduce usual notations: $H^1(\Omega) = W^{(1,2)}(\Omega)$, $H_0^1(\Omega) = W_0^{(1,2)}(\Omega)$ and $H^{-1}(\Omega) = W^{(-1,2)}(\Omega)$. Moreover, let $V = \left\{v \in H_0^1(\Omega)^n | \nabla \cdot v = 0\right\}$ and V' its dual space. Introducing $\vec{n}(x)$ as unit vector normal to $\partial\Omega$ and directed out of Ω, let us define:

$$H = \left\{\vec{v} \in L^2(\Omega)^n | \nabla \cdot \vec{v} = 0 \text{ and } \vec{v} \cdot \vec{n} = 0 \text{ on } \partial\Omega\right\} .$$

For any Banach space X with $\| \cdot \|_X$ its norm and $1 \leq p \leq +\infty$, let $\mathbf{L}^p(X)$ represent the space $L^p([0,T'];X)$ of measurable functions $f : [0,T'] \to X$ such that $t \in [0,T'] \to \|f(t)\|_X$ is a member of $L^p(0,T')$. For $f \in \mathbf{L}^p(X)$, one defines:

$$\|f(t)\|_{\mathbf{L}^p(X)} = \left(\int_0^{T'} \|f(t)\|_X^p dt\right)^{1/p} , 1 \leq p \leq +\infty \, , \|f\|_{\mathbf{L}^\infty(X)} = ess \sup_{t\in[0,T']} \|f(t)\|_X \, .$$

ess sup is a generalisation of the supremum and details can be found on `http://en.wikipedia.org/wiki/Essential_supremum_and_essential_infimum`.

It is well known that $(\mathbf{L}^p(X), \|.\|_{\mathbf{L}^p(X)})$ is a Banach space and with Funibi's theorem, $\mathbf{L}^p(L^p(\Omega))$ can be identified with $L^p(Q)$. Finally, let:

$$\mathbf{W}_1 = \left\{v \in \mathbf{L}^2(V) \mid \frac{\partial v}{\partial t} \in \mathbf{L}^2(V')\right\} ,$$

$$\mathbf{W}_2^{(q)} = \left\{v \in \mathbf{L}^2(H_0^1(\Omega)) \mid \frac{\partial v}{\partial t} \in \mathbf{L}^2(W^{(-1,q)}(\Omega))\right\} , \; 1 \leq q \leq +\infty \, ,$$

$$\mathbf{W}_3^{(q)} = \left\{v \in \mathbf{L}^q(W_0^{(1,q)}(\Omega)) \mid \frac{\partial v}{\partial t} \in \mathbf{L}^1(W^{(-1,q)}(\Omega))\right\} , \; 1 \leq q \leq +\infty \, .$$

For all these definitions, the derivative notation is not classic and derivatives are understood in the distribution sense.

6.3.2 System of interest

Let r be a strictly positive constant. Consider the following system of equations:

$$\left\{\begin{array}{lll}
\dfrac{\partial \vec{u}}{\partial t} + (\vec{u} \cdot \nabla)\vec{u} - \nabla \cdot (A_1(\theta,\phi)\nabla\vec{u}) + \nabla p = f \, , \; \nabla \cdot u = 0 & \text{in} & Q \\
\dfrac{\partial \theta}{\partial t} + \vec{u} \cdot \nabla\theta - \nabla \cdot (A_2(\theta,\phi)\nabla\theta) = -C_3\theta^2\|\nabla\vec{u}\|^2 + C_5 & \text{in} & Q \\
\dfrac{\partial \phi}{\partial t} + \vec{u} \cdot \nabla\phi - \nabla \cdot (A_3(\theta,\phi)\nabla\phi) = \phi\left(-C_6\theta\|\nabla\vec{u}\|^2 + \dfrac{C_8}{\theta + r}\right) & \text{in} & Q \\
u(x,0) = u_0(x) \, , \; \theta(x,0) = \theta_0(x) \, , \; \phi(x,0) = \phi_0(x) & \text{in} & Q \\
u(x,t) = 0 \, , \; \theta(x,t) = a \, , \; \phi(x,t) = b & \text{in} & \partial\Omega \times (0,T')
\end{array}\right. \tag{6.5}$$

where a and b are boundary conditions for θ and ϕ respectively and

$$A_i(\theta,\phi) = \left(\nu + \frac{1}{\sigma_i\theta\phi + r}\right)\mathbf{I} \text{ for } 1 \leq i \leq 3$$

with

$$(\sigma_1, \sigma_2, \sigma_3) = (1, \sigma_\theta, \sigma_\phi) \, .$$

The constant values C_3, C_5, C_6 and C_8 are left free, but the sign for all of them is positive. The mathematical system considered is obtained by taking the weak formulation of Eq. 6.5. The system Eq. 6.5 is of course closely related to Eq. 6.4. Note that in order to "simplify the expressions", the positive term $\mathcal{P}$ is replaced by $\|\nabla\vec{u}\|^2$ in the original article. In practice, this choice has many consequences on the different steps to prove Theorem 6.3.1.

6.3.3 Existence of solution

The existence of the solution was proved in [52] and we simply recall the hypothesis and the conclusion:

Theorem 6.3.1 We assume to be in two dimensions: $n = 2$.
Let us consider the definitions introduced in Sec. 6.3.1 and Sec. 6.3.2. Let us add the following hypotheses:
- *(H1)* $f \in \mathbf{L}^2(H^{-1}(\Omega)^n)$ *(exterior forces),* $u_0 \in H$,
- *(H2)* $a \geq 0$ *and* $b \geq 0$ *are real constants,*
- *(H3)* $\theta_0 \geq 0$ *and* $\phi_0 \geq 0$,
- *(H4)* $A_i : \Omega \times \mathbb{R} \times \mathbb{R} \mapsto \mathbb{R}^{n\times n}$ *is a continuous function and there exists a constant* $\psi > 0$ *such that:*

$$A_i(s_1, s_2)\eta\eta \geq \psi|\eta|^2\,,\ \forall s_1, s_2 \in \mathbb{R}\,,\ \eta \in \mathbb{R}^n\,,$$

then:

1. *If* $\theta_0, \phi_0 \in L^\infty(\Omega)$, *then there exists at least one solution* $(\vec{u}, \theta, \phi)$ *of the initial system such that:*
   - $\vec{u} \in \mathbf{W}_1$, $\theta - a, \phi - b \in \mathbf{W}_2^{(q)} \cap L^\infty(\Omega)$, $\forall q \in \left[1, \frac{n}{n-1}\right)$,
   - $0 \leq \theta(x,t) \leq \max\left(\|\theta_0\|_{L^\infty(\Omega)}, a\right) + t$, *a.e. in* $\Omega \times (0, T')$,
   - $0 \leq \phi(x,t) \leq \max\left(\|\phi_0\|_{L^\infty(\Omega)}, b\right) + t$, *a.e. in* $\Omega \times (0, T')$.
2. *If moreover, we have hypothesis (H5):*

- *(H5) There exists a constant* $\zeta > 0$ *such that* $\|A_i(s_1, s_2)\| \leq \zeta$ *for all* $s_1, s_2 \in \mathbb{R}$ *where* $\|.\|$ *is a matrix norm*

and if $\theta_0 \in L^1(\Omega)$ *and* $\phi_0 \in L^1(\Omega)$, *then, there exists at least one solution* $(\vec{u}, \theta, \phi)$ *such that:*
   - $\vec{u} \in \mathbf{W}_1$, $\theta - a, \phi - b \in \mathbf{W}_3^{(q)} \cap \mathbf{L}^\infty(L^\infty(\Omega))$, $\forall q \in \left[1, \frac{n+2}{n+1}\right)$,
   - $0 \leq \theta(x,t)$, *a.e. in* $\Omega \times (0, T')$,
   - $0 \leq \phi(x,t)$, *a.e. in* $\Omega \times (0, T')$,
   - $\theta^2\|\nabla\vec{u}\|^2 \in L^1(\Omega \times (0, T'))$, $\theta\Phi\|\nabla\vec{u}\|^2 \in L^1(\Omega \times (0, T'))$.

From the numerical point of view, we are mainly interested by the first part of the theorem since initial values of θ and ϕ must be bounded by nature. Of course, hypotheses (H1), (H2), (H3) and (H4) are verified by the $\theta - \phi$ turbulence model proposed in [88]. Finally, if the turbulent quantities are initialised by constant values over the whole computational domain, then both parts of the theorem are true ($\theta_0, \phi_0 \in L^\infty(\Omega)$ and $\theta_0, \phi_0 \in L^1(\Omega)$).

Remark 6.3.2 *Demonstration of Theorem 6.3.1 needs the introduction of a list of approximated problems. In practice, the truncation function T_M of height M is introduced:*

$$T_M(s) = \begin{cases} s & \text{if } |s| \leq M \\ M sign(s) & \text{if } |s| \geq M \end{cases} \quad \text{where } sign(s) = \begin{cases} s/|s| & \text{if } |s| \neq 0 \\ 0 & \text{if } s = 0 \end{cases}$$

and it is applied to the production term in $\|\nabla \vec{u}\|^2$ (so replaced by $T_M(\|\nabla \vec{u}\|^2)$). With the use of $T_M(\|\nabla \vec{u}\|^2)$, the problem has a solution u_M and it is necessary to pass to the limit. At this level, the demonstration in dimension 3 is impossible since the strong convergence of $\|\nabla \vec{u}_M\|^2$ to $\|\nabla \vec{u}\|^2$ in $L^2(Q)$ cannot be established. Moreover, this strong convergence is a consequence of the convergence of u_M to u strongly in $\mathbf{L}^2(H_0^1(\Omega)^n)$ obtained with the weak (integral) form of the equation and the choice of u_M as test function.

Remark 6.3.3 *For steady flow (lack of derivative in time), M. Gómez Mármol and F. Ortegón Gallego [53] succeeded in demonstrating the result with the full symmetric production term under an incompressible flow assumption. The key points are to write the production term of θ as the product of θ and a function $g_\theta(\theta, \phi, \nabla \vec{u})$ and the production of ϕ as the product of ϕ and a function $g_\phi(\theta, \phi, \nabla \vec{u})$. Moreover, hypothesis $(H4)$ must hold for $g_\theta(\theta, \phi, \nabla \vec{u})$ and $g_\phi(\theta, \phi, \nabla \vec{u})$.*

6.4 Author's involvement in the demonstration of existence of the solutions

In [100], the work presented in previous sections and dedicated to high-Reynolds version of the $k - \varepsilon$ turbulence model was extended to the treatment near the wall. To do so, the incompressible version of the Navier-Stokes equations coupled with the one equation turbulence model issued from the two-layer $k - \varepsilon$ model was considered and analysed. It was shown that far from the wall, results presented before remain valid while a new theoretical development was performed for the turbulence model near the wall. The key points are summarised in the following sections.

6.4.1 The new equation

The same approach as before is considered to define the equation for θ and the same change of variable is considered. It leads to $\theta = L_\varepsilon/\sqrt{k}$ and $\phi = 1/L_\varepsilon^2$. Of course, it is not possible to define a transport equation on the length scale for ε and only the equation on θ is considered. Using the modelling of the diffusion term in θ equation, one obtains:

$$\frac{\partial \theta}{\partial t} + \vec{u} \cdot \nabla \theta - \nabla \cdot \Big((\nu + C_\theta \nu_t) \nabla \theta \Big) = -C_\mu \frac{L_\mu}{L_\varepsilon} \mathcal{P} \theta^2 + \frac{1}{2} \tag{6.6}$$

6.4.2 Analysis of a simplified θ model alone

First, a model problem considering θ equation alone and assuming a constant diffusivity is analysed:

$$\begin{cases} \dfrac{\partial \theta}{\partial t} + \vec{u} \cdot \nabla \theta - \nu \triangle \theta = -C_\mu \dfrac{L_\mu}{L_\varepsilon} \mathcal{P} \theta |\theta| + \dfrac{1}{2} \\ \theta(t=0) = \theta_0 \geq 0 \\ \theta_{\partial \Omega} = 0 \end{cases} \tag{6.7}$$

Eq. 6.7 must be understood in the distribution sense.

Theorem 6.4.1 *Let* $\vec{u} \in L^\infty([0,T'), L^\infty(\Omega))$, *and* $\mathcal{P} \in L^\infty([0,T'), L^\infty(\Omega))$, *and suppose* $\theta_0 \in L^\infty(\Omega) \cap H^1_0(\Omega)$, *with* $\theta_0 \geq 0$. *Then, the problem (6.7) has a unique solution* θ *such that:*

$$\theta \in L^\infty([0,T'), L^\infty(\Omega)) \cap L^2([0,T'); H^1_0(\Omega))$$

and

$$\theta \geq 0 \textit{ in } \Omega \times [0,T)\,.$$

It means that θ is positive and bounded.

6.4.3 Analysis of the θ model alone

Compared with Eq. 6.7, the key point concerns the introduction of θ in the definition of the dynamic viscosity, and in the denominator of ν_t. The new problem $(\mathcal{Q})$ is the following:

$$(\mathcal{Q}) \begin{cases} \dfrac{\partial \theta}{\partial t} + \vec{u}\cdot\nabla\theta - \nabla\cdot\left\{\left(\nu + C_\theta \dfrac{C_\mu L_\mu L_\varepsilon}{\theta}\right)\nabla\theta\right\} = -C_\mu \dfrac{L_\mu}{L_\varepsilon}\mathcal{P}\theta|\theta| + \dfrac{1}{2}\,, \\ \theta(x,0) = \theta_0 \geq 0\,, \\ \nabla\theta\cdot\vec{n} = 0 \text{ on } \Gamma_1, \\ \theta = 0 \text{ on } \Gamma_0\,. \end{cases} \tag{6.8}$$

Eq. 6.8 involves a part Γ_0 of the boundary where a Dirichlet condition is applied on θ: it corresponds to the wall. On the second part of the boundary Γ_1, a Neumann boundary condition on θ is applied. This is a kind of “weak” condition in the sense that it does not give information on the bounds of θ.

From now on, let $H(\Omega)$ be the space:

$$H(\Omega) = \{u \in H^2(\Omega), \quad u = 0 \text{ on } \Gamma_0 \text{ and } \nabla\vec{u}\cdot\vec{n} = 0 \text{ on } \Gamma_1\}$$

$H(\Omega)$ is mandatory for the following results.

When θ is small, there is a potential risk that the diffusivity blows up and the computation stops. This is the reason why a sequence of problems is introduced and let $(\mathcal{Q}_s)$ represent the following alternative problem:

$$(\mathcal{Q}_s) \begin{cases} \dfrac{\partial \theta_s}{\partial t} + \vec{u}\cdot\nabla\theta_s - \nabla\cdot\left\{\left(\nu + C_\theta \dfrac{L_\mu L_\varepsilon}{\sqrt{\theta_s^2 + s^2}}\right)\nabla\theta_s\right\} = -C_\mu \dfrac{L_\mu}{L_\varepsilon}\mathcal{P}\theta_s|\theta_s| + \dfrac{1}{2}\,, \\ \theta_s(x,0) = \theta_0 \geq 0\,, \\ \nabla\theta_s\cdot\vec{n} = 0 \text{ on } \Gamma_1, \\ \theta_s = 0 \text{ on } \Gamma_0, \end{cases} \tag{6.9}$$

where s is a small parameter to prevent division by 0. The demonstration of the existence of the solution of $(\mathcal{Q}_s)$ looks like the case for a constant diffusivity and the solution θ_s is positive.

The last step consists in going to the limit to have results directly on θ. In order to prove the convergence of θ_s to θ, solution of problem $(\mathcal{Q})$, one has to demonstrate that $L_\mu L_\varepsilon/\theta$ is bounded, and in particular in the neighbourhood of the wall. Coming back to the $k-\varepsilon$ variables, $L_\mu L_\varepsilon/\theta = L_\mu\sqrt{k}$ which is bounded near the wall since k vanishes at the wall. Moreover, a local analysis of the flow shows that the behaviour of L_ε is of order $d^2\sqrt{k}$ in the near-wall region, where d is the distance to the wall. Therefore, θ behaviour must be the same as a second degree polynomial.

In order to simplify the proof, it is assumed that $\Omega = \prod_{i=1}^{3}]0, a_i[$, $a_i > 0$ for $i = 1, 3$ and $\Gamma_0 =]0, a_1[\times\{0\}\times]0, a_3[\subset \partial\Omega$ the wall boundary with $\vec{n}$ the inward unit vector normal to Γ_0. With these considerations, the use of theoretical results involving the distance to the wall is simplified since the distance to the wall at a point M defined by its components (x, y, z) is simply y.

Lemma 6.4.2 *Let* $\Omega = \prod_{i=1}^{3}]0, a_i[$, $a_i > 0$ *for* $i = 1, 3$ *and* $\Gamma_0 =]0, a_1[\times\{0\}\times]0, a_3[\subset \partial\Omega$ *the wall boundary with* $\vec{n}$ *the inward unit vector normal to* Γ_0*. Let* $\vec{u} \in L^\infty([0, T']; L^\infty(\Omega))$, $\mathcal{P} \in L^\infty([0, T']; L^\infty(\Omega))$ *and* $\theta_0 \in H(\Omega) \cap L^\infty(\Omega)$*. We suppose that there exists a constant* C *such that* $\theta_0 \geq Cy^2 \geq 0$ *and:*

$$CC_\mu \frac{C_1}{C_2} M_1 M_2 b^2 - \frac{1}{2} < 0\,,$$

where $M_1 = \|\mathcal{P}\|_{L^\infty([0,T'];L^\infty(\Omega))}$, M_2 *the uniform upper bound of* θ_s *in* $L^\infty([0, T']; L^\infty(\Omega))$*, and* b *an upper bound of the distance* y *to the wall.*

Then, if θ_0 *is such that* $\theta_0 - Cy^2 \geq 0$ *a.e. on* Ω*, we have:*

$$\theta_s \geq Cy^2 \ \text{a.e. } x, t\,,$$

where θ_s *is solution of the following problem:*

$$\begin{cases} \dfrac{\partial\Phi}{\partial t} - \nu\triangle\Phi = -C_\mu \dfrac{L_\mu}{L_\varepsilon}\mathcal{P}|\Phi|\Phi + \dfrac{1}{2}\,, \\ \Phi_0 = \Phi(t = 0) = \theta_0 - Cy^2 \geq 0 \ \text{a.e. } x\,, t\,, \\ \Phi = 0 \ \text{on } \Gamma_0 \\ \nabla\Phi \cdot \vec{n} = 0 \ \text{on } \Gamma_1 \end{cases}$$

Remark 6.4.3 *We did not succeed in demonstrating the same result in the case of a non constant diffusivity and with convection term. But for the following, we will assume the existence of such a constant* C*.*

Finally, next theorem is the main result for the turbulent equation alone:

Theorem 6.4.4 *Let* $\Omega = \prod_{i=1}^{3}]0, a_i[$, $a_i > 0$ *for* $i = 1, 3$ *and* $\Gamma_0 =]0, a_1[\times\{0\}\times]0, a_3[\subset \partial\Omega$ *the wall boundary with* $\vec{n}$ *the inward unit vector normal to* Γ_0*. Let* $\vec{u} \in L^\infty([0, T']; L^\infty(\Omega))$, $\mathcal{P} \in L^\infty([0, T']; L^\infty(\Omega))$ *and* $\theta_0 \in H(\Omega) \cap L^\infty(\Omega)$*. Suppose that there exists a constant* C *such that* $\theta_0 \geq Cy^2 \geq 0$ *and:*

$$CC_\mu \frac{C_1}{C_2} M_1 M_2 b^2 - \frac{1}{2} < 0\,,$$

where $M_1 = \|\mathcal{P}\|_{L^\infty([0,T'];L^\infty(\Omega))}$, M_2 *the uniform upper bound of* θ_s *in* $L^\infty([0, T']; L^\infty(\Omega))$*, and* b *an upper bound of the distance* y *to the wall.*

Then, there exists a solution θ *of the problem* $(\mathcal{P})$ *and* θ *is such that:*

$$\theta \in L^\infty([0, T']; L^\infty(\Omega)) \cap L^2([0, T']; H(\Omega))\,,\ \theta' \in L^2([0, T']; H^{-1}(\Omega))$$

and

$$\theta \geq Cy^2 \geq 0\,.$$

6.4.4 Coupling the θ equation with the steady-state incompressible Navier-Stokes problem

In this section, we are interested in the coupling between the steady-state Navier-Stokes system and our $\theta-$ or θ_s- turbulence model. Here, we do not apply any assumption on the space dimension and we can choose $n = 2$ or $n = 3$. Let us consider the following system:

$$\begin{cases} (\vec{u}\cdot\nabla)\vec{u} - \nabla\cdot((\nu + C_\theta\nu_t)\nabla\vec{u}) + \nabla p = f \text{ on } \Omega\,, \\ \nabla\cdot\vec{u} = 0 \text{ on } \Omega\,, \\ \vec{u}\cdot\nabla\theta - \nabla\cdot((\nu + C_\theta\nu_t)\nabla\theta) = -C_\mu\dfrac{L_\mu}{L_\varepsilon}\mathcal{P}\theta + \dfrac{1}{2} \text{ on } \Omega\,, \\ \vec{u} = \vec{0} \text{ and } \theta = 0 \text{ on } \partial\Omega\,, \end{cases} \tag{6.10}$$

where the turbulent kinematic viscosity ν_t is:

$$\nu_t = C_\mu\frac{L_\mu L_\varepsilon}{\theta} \text{ or } \nu_t = C_\mu\frac{L_\mu L_\varepsilon}{\sqrt{\theta^2 + s^2}}\,.$$

Our aim is to prove, if possible, the existence of a solution to this system. We will begin by demonstrating the existence in a more general situation, as in [52]. In practice, we consider the following system:

$$\begin{cases} (\vec{u}\cdot\nabla)\vec{u} - \nabla\cdot(A(\theta)\nabla\vec{u}) + \nabla p = f \text{ on } \Omega\,, \\ \nabla\cdot\vec{u} = 0 \text{ on } \Omega\,, \\ \vec{u}\cdot\nabla\theta - \nabla\cdot(A(\theta)\nabla\theta) = -g(\theta,\nabla\vec{u})\theta + \dfrac{1}{2} \text{ on } \Omega\,, \\ \vec{u} = \vec{0} \text{ and } \theta = a \text{ on } \partial\Omega\,. \end{cases} \tag{6.11}$$

We make the following hypotheses on the data:
(H_1) $f \in H^{-1}(\Omega)^n$;
(H_2) $a \geq 0$;
(H_3) $A : \Omega\times\mathbb{R} \to \mathbb{R}^{n\times n}$ is a Caratheodory mapping. This means that $x \to A(x,s)$ is measurable in Ω, $\forall s \in \mathbb{R}$ and $s \to A(x,s)$ is continuous in $\mathbb{R}$, a.e. in Ω. Moreover, let us suppose the existence of a scalar $\alpha > 0$ such that

$$A(x,s)\psi\psi \geq \alpha|\psi|^2\,,\ \forall s \in \mathbb{R},\ \forall\psi \in \mathbb{R}^n \text{ and a.e. } x \in \Omega\,;$$

(H_4) There exists a continuous function $d : \mathbb{R} \to \mathbb{R}^+$ such that

$$A(x,s)\psi\psi \leq d(s)|\psi|^2\,,\ \forall s \in \mathbb{R},\ \forall\psi \in \mathbb{R}^n \text{ and a.e. } x \in \Omega\,;$$

(H_5) $g : \Omega\times\mathbb{R}\times\mathbb{R}^{n\times n} \to \mathbb{R}$ is a Caratheodory function and there exists $c \in L^1(\Omega)$ such that

$$0 \leq g(x,s,B) \leq d(s)(c(x) + |B|^2)\,,\ \forall s \in \mathbb{R},\ \forall B \in \mathbb{R}^{n\times n} \text{ and a.e. } x \in \Omega\,.$$

Theorem 6.4.5 *Under hypotheses (H_1-H_5), there exists $(\vec{u}, \theta)$ solution of (6.11) such that:*

$$0 \leq \theta \leq a + \frac{C(n,\Omega)}{\alpha}\,, \ a.e. \ in\, \Omega\,,$$

where $C(n, \Omega)$ is a constant value that depends only on the space dimension n and on the domain of interest Ω.

It is clear that Theorem 6.4.5 can be applied without modification to each steady-state version of the θ_s equation (from problem $(\mathcal{Q}_s)$) coupled with the steady-state Navier-Stokes equations, as all the hypotheses (H_1)-(H_5) are true (we take $A = (\nu + C_\theta C_\mu L_\mu L_\varepsilon/\sqrt{\theta^2+s^2})I$).

Actually, the application of the method to the original problem Eq. 6.10 for the θ turbulence model raises some difficulties. This is due to the fact that we must demonstrate that $\mathcal{P}$ (assumed to be $\|\nabla\vec{u}\|^2$) is bounded uniformly (in $L^\infty(\Omega)$) with respect to s, and the inequality $\theta_s \geq Cd^2$ is mandatory with a constant C independent of s. d represents the distance to the wall.

6.5 Towards a usable turbulence model

The θ turbulence model is still not complete: coefficients on right hand side of Eq. 6.8 are obtained algebraically from the constants of the two-layer turbulence model. But the Prandtl-Schmidt diffusivity coefficient C_θ is still unknown. We have tried to find a value of C_θ that respects the physics of the boundary layer.

We suppose that $\Omega = \prod_{i=1}^{3}]0, a_i[$, $a_i > 0$ for $i = 1,\ 3$, with a solid boundary on the flat surface $\Gamma_0 =]0, a_1[\times\{0\}\times]0, a_3[$. As previously, this domain is interesting as the distance between a point M of coordinates (x, y, z) in the flow and the wall boundary Γ_0 is y. Moreover, physicists have shown that in the boundary layer over a flat plate, one can neglect the variations of the variables in the longitudinal directions. This means that $\partial/\partial x \ll \partial/\partial y$ and $\partial/\partial z \ll \partial/\partial y$. We assume that the velocity field is parallel to the wall boundary ($\vec{u} = (0, U, 0)$ and that θ is stationary. As a consequence, one has:

$$\vec{u}\cdot\nabla\theta = 0\,,$$
$$\nabla\cdot\left((\nu + C_\theta\frac{C_\mu L_\mu L_\varepsilon}{\theta})\nabla\theta\right) = \frac{\partial}{\partial y}\left((\nu + C_\theta\frac{C_\mu L_\mu L_\varepsilon}{\theta})\frac{\partial\theta}{\partial y}\right)\,,$$
$$\mathcal{P} = \left(\frac{\partial u}{\partial y}\right)^2$$

Near solid walls, there may be a boundary layer, for which experimental observations showed logarithmic profile for the longitudinal component U of the fluid velocity [29]:

$$\frac{U}{u_\tau} = \frac{1}{\kappa}\log(y^+) + 5.5\,, \tag{6.12}$$

where κ, y^+ and u_τ are defined in Chap. 3. Moreover, experimental studies also showed that relation (6.12) was valid when $50 \leq y^+ \leq 200$ [29]. As a consequence, the θ model equation becomes:

$$-\frac{\partial}{\partial y}\left(C_\theta\frac{C_\mu L_\mu L_\varepsilon}{\theta}\frac{\partial\theta}{\partial y}\right) = -C_\mu\frac{L_\mu}{L_\varepsilon}\mathcal{P}\theta^2 + \frac{1}{2}\,. \tag{6.13}$$

Physical studies enable us to admit that the k equation is satisfied by the following variable in the logarithmic layer:

$$k = \frac{u_\tau^2}{\sqrt{C_\mu}}$$

We deduce that the θ equation is satisfied by:

$$\theta = \frac{L_\varepsilon}{\sqrt{k}} = \frac{L_\varepsilon \sqrt[4]{C_\mu}}{u_\tau} \text{ and } \mathcal{P} = \frac{u_\tau^2}{\kappa^2 y^2}\,.$$

Following [100] and assuming $50 \leq y^+ \leq 200$, the θ equation becomes:

$$-C_\theta C_\mu \frac{u_\tau}{\sqrt[4]{C_\mu}} \left(\frac{\partial L_\mu}{\partial y} \frac{\partial L_\varepsilon}{\partial y} + L_\mu \frac{\partial^2 L_\varepsilon}{\partial y^2} \right) = -C_\mu^{5/4} \frac{L_\mu L_\varepsilon}{\kappa^2 y^2} + \frac{1}{2}\,. \tag{6.14}$$

This relation expresses that C_θ is not constant and is a positive function of y^+. But the expression was obtained assuming that C_θ is not a function of y in order to pull C_θ out of the derivative between Eq. 6.13 and Eq. 6.14. Therefore, this approach is not mathematically consistent.

But, assuming that y^+ is large enough to drop the damping terms in L_μ and L_ε, it is easy to show that the right hand side of Eq. 6.13 is simply $-1/2$. For the left hand side, we have $\partial\theta/\partial y \simeq \kappa/(\sqrt{C_\mu} u_\tau)$ and $C_\mu L_\mu L_\varepsilon/\theta = C_\mu^{3/4} L_\mu u_\tau \simeq \kappa u_\tau y$. Assuming that C_θ is constant, it comes:

$$\frac{\partial}{\partial y} \left\{ \frac{C_\mu L_\mu L_\varepsilon}{\theta} \frac{\partial \theta}{\partial y} \right\} = \frac{\partial}{\partial y} \left\{ \kappa u_\tau y \frac{\kappa}{\sqrt{C_\mu} u_\tau} \right\} = \frac{\kappa^2}{\sqrt{C_\mu}}. \tag{6.15}$$

Using the value of the right hand side and Eq. 6.15, it comes finally:

$$C_\theta = \frac{\sqrt{C_\mu}}{2\kappa^2} \simeq 0.8923.$$

6.6 Conclusion

In this chapter, the main results on the positivity and upper bound of an alternative family of turbulence models was introduced. This chapter shows how mathematics can help stabilising turbulence simulations for incompressible flows.

Up-to now, such results were essentially ignored by the community of RANS turbulence models. But mathematicians continued to work on this topic. They continued on the high Reynolds version of the model, far from the wall. In particular, Dreyfus studied in [36] the diffusion term of the $\theta - \phi$ turbulence model and he showed that the hypothesis of bounded turbulent viscosity (the term in $(\theta\phi)^{-1}$) could be overcome. This paper follows the first theoretical (mathematical) paper with a single “turbulent-like” equation [51]. Very recently, Dreyfus [37] succeeded in extending this result to the full version of the incompressible high-Reynolds $\theta - \phi$ turbulence model (in their stationary form). His recent results also include the true production term on turbulent equations but neglects the strong link with the momentum equation.

Chapter 7

Mathematical models for compressible turbulent flows

7.1 Introduction

In Chap. 6, attention was focused on mathematical results regarding incompressible RANS turbulence models based on two equations and on the two-layer approach. However, for the application of interest considered in this thesis, compressibility must be accounted for and dedicated turbulence models must be defined.

For compressible flows, no proof of existence of the solution of any compressible RANS model is available and the approach considered is different. In practice, one can expect a compressible turbulence model to recover its incompressible version when one assumes incompressibility ($\nabla \cdot \vec{u} = 0$). Following this consideration, our work consisted in:

1. Taking mathematical papers regarding positivity and boundedness of variables, extract the main hypothesis for the proof.

2. Apply the transformation from $k-\varepsilon$ to $\theta-\phi$ turbulence models and check the hypothesis from 1.

3. If necessary, change the variable definitions.

This work was performed during the training period of V. Arrecgros and has never been published.

7.2 Initial status

In their original article, Lewandowski and Mohammadi [88] proposed several new couples of variables and their choices depended on compressibility. Incompressible change of variable and results are summarised in Chap. 6. For compressible flows, the new variables are:

$$\theta = \frac{k}{\varepsilon} \text{ and } \phi = \frac{\varepsilon}{k^{C_{\varepsilon 1}/C_\mu}}. \tag{7.1}$$

In this chapter and up-to a new definition, we introduce $\alpha = C_{\varepsilon 1}/C_\mu$ in order to simplify expressions.

7.2.1 Transport equation for θ

From the definition of θ, it comes:

$$\frac{\partial(\rho\theta)}{\partial t} = \frac{\partial\left(\rho\frac{k}{\varepsilon}\right)}{\partial t} = \frac{k}{\varepsilon}\frac{\partial\rho}{\partial t} + \frac{\rho}{\varepsilon}\frac{\partial k}{\partial t} - \frac{\rho k}{\varepsilon^2}\frac{\partial\varepsilon}{\partial t},$$

and

$$\nabla\cdot(\rho\vec{u}\theta) = \frac{k}{\varepsilon}\nabla\cdot(\rho\vec{u}) + \frac{\rho\vec{u}}{\varepsilon}\cdot\nabla k - \frac{\rho\vec{u}k}{\varepsilon^2}\cdot\nabla\varepsilon,$$

and finally:

$$\begin{aligned}\partial_t(\rho\theta) + \nabla\cdot(\rho u\theta) &= \frac{k}{\varepsilon}(\partial_t\rho + \nabla\cdot(\rho\vec{u})) \quad + \frac{\rho}{\varepsilon}(\partial_t k + \vec{u}\cdot\nabla k) - \frac{\rho k}{\varepsilon^2}(\partial_t\varepsilon + \vec{u}\cdot\nabla\varepsilon)\\ &= \qquad 0 \qquad\qquad + \frac{\rho}{\varepsilon}(\partial_t k + \vec{u}\cdot\nabla k) - \frac{\rho k}{\varepsilon^2}(\partial_t\varepsilon + \vec{u}\cdot\nabla\varepsilon)\,,\end{aligned}$$

with the density equation. Using density equation, we also have:

$$\rho(\partial_t k + \vec{u}\cdot\nabla k) = \partial_t(\rho k) + \nabla\cdot(\rho\vec{u}k)\,,$$

$$\rho(\partial_t\varepsilon + \vec{u}\cdot\nabla\varepsilon) = \partial_t(\rho\varepsilon) + \nabla\cdot(\rho\vec{u}\varepsilon)\,,$$

which leads to:

$$\partial_t(\rho\theta) + \nabla\cdot(\rho\vec{u}\theta) = \frac{1}{\varepsilon}\Big(\partial_t(\rho k) + \nabla\cdot(\rho\vec{u}k)\Big) - \frac{k}{\varepsilon^2}\Big(\partial_t(\rho\varepsilon) + \nabla\cdot(\rho\vec{u}\varepsilon)\Big)\,.$$

Let $Diff_k$ and $Diff_\varepsilon$ be the diffusion terms for k and ε equation respectively. Using k and ε equations and the definition of μ_t , one finds:

$$\partial_t(\rho\theta) + \nabla\cdot(\rho\vec{u}\theta) = S_\theta + Diff_\theta\,,$$

where

$$S_\theta = C_\mu C_4\rho\theta^2\mathcal{P} + C_5\rho\theta\nabla\cdot\vec{u} + \frac{2}{3}C_6\rho\,,$$

$\mathcal{P}$ is defined in Eq. 6.1 and μ_t is transformed using the change of variable on:

$$\mu_t = C_\mu\rho\frac{k^2}{\varepsilon}. \tag{7.2}$$

Moreover

$$Diff_\theta = \frac{1}{\varepsilon}Diff_k - \frac{k}{\varepsilon^2}Diff_\varepsilon\,.$$

Constants C_4, C_5 and C_6 are algebraically expressed from the original $k-\varepsilon$ turbulence model:

$$C_4 = 1 - \frac{C_{\varepsilon_1}}{C_\mu} = -0.44,\ C_5 = \frac{C_{\varepsilon_1}}{C_\mu} - 1 = 0.44 \text{ and } C_6 = C_{\varepsilon_2} - 1 = 0.88.$$

θ equation is fully defined once the diffusion term is expressed. Remembering the expression for $\alpha = C_{\varepsilon_1}/C_\mu$ and using the inverse change of variable:

$$k = \theta^{\frac{1}{1-\alpha}}\phi^{\frac{1}{1-\alpha}} \text{ and } \varepsilon = \theta^{\frac{\alpha}{1-\alpha}}\phi^{\frac{1}{1-\alpha}}\,, \tag{7.3}$$

$Diff_\theta$ is:

$$\begin{aligned}
Diff_\theta &= \frac{1}{1-\alpha}\Delta\theta\Big[\mu_k - \alpha\mu_\varepsilon\Big] + \frac{\theta}{(1-\alpha)\phi}\Delta\phi\Big[\mu_k - \mu_\varepsilon\Big] \\
&+ \frac{\alpha}{(1-\alpha)^2\theta}\|\nabla\theta\|^2\Big[\mu_k - (2\alpha-1)\mu_\varepsilon\Big] + \frac{\alpha\theta}{(1-\alpha)^2\phi^2}\|\nabla\phi\|^2\Big[\mu_k - \mu_\varepsilon\Big] \\
&+ \frac{\theta}{(1-\alpha)\phi}\nabla\phi\cdot\Big[\nabla\mu_k - \nabla\mu_\varepsilon\Big] + \frac{1}{1-\alpha}\nabla\theta\cdot\Big[\nabla\mu_k - \alpha\nabla\mu_\varepsilon\Big] \\
&+ \frac{2}{(1-\alpha)^2\phi}\Big[\mu_k - \alpha\mu_\varepsilon\Big]\nabla\theta\cdot\nabla\phi\,,
\end{aligned}$$

with

$$\mu_k = \mu + \frac{\mu_t}{\sigma_k} \text{ and } \mu_\varepsilon = \mu + \frac{\mu_t}{\sigma_\varepsilon}\,. \tag{7.4}$$

$Diff_\theta$ expression is fully non-linear and its form must not be considered for numerical implementation. Indeed, classic two-equation RANS turbulence models share many complex terms and the treatment established for one model can be easily extended to another one. Here, the use of the full version of the diffusion term involves many gradients that are not classically computed. Therefore, following the approach introduced for incompressible flows, we define the diffusion term by:

$$Diff_\theta = \nabla\cdot\left\{\left(\mu + \frac{\mu_t}{\sigma_\theta}\right)\nabla\theta\right\} = \nabla\cdot\Big((\mu + C_\theta\mu_t)\nabla\theta\Big)$$

where σ_θ is the Prandtl-Schmidt number relative to θ and its value must be defined. In the following, we will use σ_θ or its inverse C_θ without ambiguity.

Remark 7.2.1 *The modification of the diffusion term has many consequences on the behaviour of the turbulence model. It has been demonstrated by Catris and Aupoix [21] that the diffusion term contains a large part of the physical answer to density gradient and modifications of the diffusion term can lead to improvement of the boundary layer representation.*

7.2.2 Transport equation for ϕ

Transport equation for ϕ is deduced using the same approach as for the θ equation. Using the fact that:

$$\partial_t(\rho\phi) = \partial_t(\rho\frac{\varepsilon}{k^\alpha}) = \frac{\varepsilon}{k^\alpha}\partial_t\rho + \frac{\rho}{k^\alpha}\partial_t\varepsilon - \frac{\alpha\rho\varepsilon}{k^{\alpha+1}}\partial_t k\,,$$

and

$$\nabla\cdot(\rho\vec{u}\phi) = \nabla\cdot(\rho\vec{u}\frac{\varepsilon}{k^\alpha}) = \frac{\varepsilon}{k^\alpha}\nabla\cdot(\rho\vec{u}) + \frac{\rho\vec{u}}{k^\alpha}\cdot\nabla\varepsilon - \frac{\alpha\rho\vec{u}\varepsilon}{k^{\alpha+1}}\cdot\nabla k\,,$$

it comes easily, using the density equation:

$$\begin{aligned}
\partial_t(\rho\phi) + \nabla\cdot(\rho\vec{u}\phi) &= \frac{\varepsilon}{k^\alpha}(\partial_t\rho + \nabla\cdot(\rho\vec{u})) && +\frac{\rho}{k^\alpha}(\partial_t\varepsilon + \vec{u}\cdot\nabla\varepsilon) - \frac{\alpha\rho\varepsilon}{k^{\alpha+1}}(\partial_t k + \vec{u}\cdot\nabla k) \\
&= \qquad 0 && +\frac{\rho}{k^\alpha}(\partial_t\varepsilon + \vec{u}\cdot\nabla\varepsilon) - \frac{\alpha\rho\varepsilon}{k^{\alpha+1}}(\partial_t k + \vec{u}\cdot\nabla k) \\
&= \qquad 0 && +\frac{1}{k^\alpha}\Big(\partial_t(\rho\varepsilon) + \nabla\cdot(\rho\vec{u}\varepsilon)\Big) - \\
& && \qquad \frac{\alpha\varepsilon}{k^{\alpha+1}}\Big(\partial_t(\rho k) + \nabla\cdot(\rho\vec{u}k)\Big)\,.
\end{aligned}$$

Using again equations for k and ε (Eq. 7.3) and expression for μ_t (Eq. 7.2), the final form of ϕ equation is:

$$\partial_t(\rho\phi) + \nabla\cdot(\rho\vec{u}\phi) = S_\phi + Diff_\phi\,,$$

where

$$S_\phi = C_\mu C_8 \rho\phi\theta\mathcal{P} + \frac{2}{3}C_9\rho\phi\nabla\cdot\vec{u} + C_{10}\rho\frac{\phi}{\theta}$$

and

$$Diff_\phi = \frac{1}{k^\alpha}Diff_\varepsilon - \frac{\alpha\varepsilon}{k^{\alpha+1}}Diff_k\,.$$

Constants C_8, C_9 and C_{10} are deduced from the ones of the initial $k-\varepsilon$ model:

$$C_8 = \frac{C_{\varepsilon_1}}{C_\mu} - \alpha = 0,\; C_9 = \alpha - \frac{C_{\varepsilon_1}}{C_\mu} = 0 \text{ and } C_{10} = \alpha - C_{\varepsilon_2} = -0.44\,.$$

Remark 7.2.2 *The same results as in Remark 7.2.1 hold for the diffusion term on ϕ.*

Remark 7.2.3 *The theoretical development is not presented in the right way and this choice is motivated by the fact that it is easier to derive the equation first. But, in practice, it is the choice of $C_8 = 0$ that drives the value of α in order to make the total derivative of ϕ negative.*

It is possible to define $Diff_\phi$ with the change of variables $k = f(\theta,\phi)$ and $\varepsilon = g(\theta,\phi)$:

$$\begin{aligned}
Diff_\phi &= \frac{\alpha\phi}{(1-\alpha)\theta}\Delta\theta\Big[\mu_\varepsilon - \mu_k\Big] + \frac{1}{(1-\alpha)}\Delta\phi\Big[\mu_\varepsilon - \alpha\mu_k\Big] \\
&+ \frac{\alpha\phi}{(1-\alpha)^2\theta^2}\|\nabla\theta\|^2\Big[(2\alpha-1)\mu_\varepsilon - \alpha\mu_k\Big] + \frac{\alpha}{(1-\alpha)^2\phi}\|\nabla\phi\|^2\Big[\mu_\varepsilon - \alpha\mu_k\Big] \\
&+ \frac{1}{1-\alpha}\nabla\phi\cdot\Big[\nabla\mu_\varepsilon - \alpha\nabla\mu_k\Big] + \frac{\alpha\phi}{(1-\alpha)\theta}\nabla\theta\cdot\Big[\nabla\mu_\varepsilon - \nabla\mu_k\Big] \\
&+ \frac{2\alpha}{(1-\alpha)^2\theta}\Big[\mu_\varepsilon - \mu_k\Big]\nabla\theta\cdot\nabla\phi\,,
\end{aligned}$$

where μ_k and μ_ε are defined in Eq. 7.4. But, as for θ equation, modelling the diffusion term is considered and

$$Diff_\phi = \nabla\cdot\left\{\left(\mu + \frac{\mu_t}{\sigma_\phi}\right)\nabla\phi\right\} = \nabla\cdot\Big((\mu + C_\phi\mu_t)\nabla\phi\Big),$$

with σ_ϕ a non negative constant called Prandtl-Schmidt number for ϕ equation. In the following, we will use σ_ϕ or its inverse C_ϕ without ambiguity.

7.2.3 Consequences

At the present time, the turbulent Prandtl-Schmidt numbers σ_θ and σ_ϕ are positive constants and their values are still unknown: they must be established from physical considerations. The process follows the one introduced for the two-layer turbulence model based on θ. This is explained by the fact that a two-equation turbulence model is first defined from the equilibrium region and then extended up-to the wall using damping functions to reproduce the "good" behaviours of all variables near the wall.

As before, the computation of the constant is performed under a stationary incompressible flow assumption. In order to simplify the development and to agree with the theorem assumption, the flow is assumed 2D. As a consequence, we have:

- $\nabla \cdot \vec{u} = 0$ and $\rho = Cst$,
- $\vec{u}$ is parallel to the wall $\vec{u} = (U, 0)$,
- variables mainly vary in the direction normal to the wall,
- a fully turbulent boundary layer is assumed and attention is focused on the logarithmic region:
$$\theta = \frac{\kappa y}{u_\tau \sqrt{C_\mu}},\ \phi = \frac{u_\tau^{3-2\alpha} \sqrt{C_\mu}^{\alpha}}{\kappa y},\ \frac{\mu_t}{\rho} = u_\tau \kappa y,\ \partial_y U = \frac{u_\tau}{\kappa y} \text{ and } \mu_t >> \mu\,.$$

We deduce from θ equation:

$$-\partial_y \left(\frac{\mu_t}{\rho \sigma_\theta} \partial_y \theta \right) = (1-\alpha) C_\mu \theta^2 (\partial_y U)^2 + (C_{\varepsilon_2} - 1)\,.$$

But

$$-\partial_y \left(\frac{\mu_t}{\rho \sigma_\theta} \partial_y \theta \right) = -\frac{\kappa^2}{\sigma_\theta \sqrt{C_\mu}}\,,$$

and

$$(1-\alpha) C_\mu \theta^2 (\partial_y u_1)^2 + (C_{\varepsilon_2} - 1) = (1-\alpha) + (C_{\varepsilon_2} - 1) = C_{\varepsilon_2} - \alpha\,.$$

And, as a consequence:

$$\sigma_\theta = -\frac{\kappa^2}{\sqrt{C_\mu}(C_{\varepsilon_2} - \alpha)}\,.$$

Since $C_{\varepsilon_2} - \alpha > 0$, we have:

$$\sigma_\theta < 0\,. \tag{7.5}$$

The Prandtl-Schmidt number σ_θ cannot be negative for physical reasons and in order to cope with mathematical assumptions. Eq. 7.5 shows that the change of variable for compressible flows is not valid to represent accurately flow physics.

The same approach for σ_ϕ leads to:

$$\sigma_\phi = -\frac{\kappa^2}{\sqrt{C_\mu}(\alpha - C_{\varepsilon_2})} = 1.27348 > 0\,.$$

Finally, a new change of variable must be found in order to try to cope with both mathematical assumptions and physics of the boundary layer. This point is addressed in the next section.

7.3 A general framework for the change of variable

The general definition for the change of variable is:

$$\theta = \frac{k^\gamma}{\varepsilon^\beta}, \quad \phi = \frac{\varepsilon^\omega}{k^\delta}\,,$$

where the powers γ, β, ω and δ can be chosen in order to satisfy both physical and mathematical assumptions. Let α be as before:

$$\alpha = \frac{C_{\varepsilon_1}}{C_\mu}$$

7.3.1 Equation for θ depending on γ and β

It comes from the definition of θ:

$$\partial_t(\rho\theta) + \nabla\cdot(\rho\vec{u}\theta) = \frac{\gamma k^{\gamma-1}}{\varepsilon^\beta}(S_k + Diff_k) - \frac{\beta k^\gamma}{\varepsilon^{\beta+1}}(S_\varepsilon + Diff_\varepsilon)\,, \tag{7.6}$$

and:

$$\partial_t(\rho\theta) + \nabla\cdot(\rho\vec{u}\theta) - Diff_\theta = S_\theta\,,$$

where

$$S_\theta = C_\mu(\gamma - \beta\alpha)\rho\theta\frac{k}{\varepsilon}\mathcal{P} + \frac{2}{3}(\gamma-\beta\alpha)\rho\theta\nabla\cdot\vec{u} + (\beta C_{\varepsilon_2} - \gamma)\rho\theta\frac{\varepsilon}{k}\,,$$

and

$$Diff_\theta = \frac{\gamma k^{\gamma-1}}{\varepsilon^\beta}(Diff_k) - \frac{\beta k^\gamma}{\varepsilon^{\beta+1}}(Diff_\varepsilon)\,.$$

7.3.2 Equation for ϕ depending on ω and δ

Equation for ϕ is found using the same approach:

$$\partial_t(\rho\phi) + \nabla\cdot(\rho\vec{u}\phi) = \frac{\omega\varepsilon^{\omega-1}}{k^\delta}(S_\varepsilon + Diff_\varepsilon) - \frac{\delta\varepsilon^\omega}{k^{\delta+1}}(S_k - Diff_k)\,, \tag{7.7}$$

which leads to:

$$\partial_t(\rho\phi) + \nabla.\cdot(\rho\vec{u}\phi) - Diff_\phi = S_\phi\,,$$

where

$$S_\phi = C_\mu(\omega\alpha - \delta)\rho\frac{k}{\varepsilon}\phi\mathcal{P} + \frac{2}{3}(\delta - \alpha\omega)\rho\phi\nabla\cdot\vec{u} + (\delta - C_{\varepsilon_2}\omega)\rho\phi\frac{\varepsilon}{k}$$

and

$$Diff_\phi = \frac{\omega\varepsilon^{\omega-1}}{k^\delta}Diff_\varepsilon - \frac{\delta\varepsilon^\omega}{k^{\delta+1}}Diff_k\,.$$

7.3.3 Closed form of equations

k and ε can be expressed from θ and ϕ using inverted variable change:

$$k = \theta^{\frac{\omega}{\gamma\omega-\delta\beta}} \phi^{\frac{\beta}{\gamma\omega-\delta\beta}} , \quad \varepsilon = \theta^{\frac{\delta}{\gamma\omega-\delta\beta}} \phi^{\frac{\gamma}{\gamma\omega-\delta\beta}} . \tag{7.8}$$

In the same way, we have:

$$\frac{\varepsilon}{k} = \theta^{\frac{\delta-\omega}{\gamma\omega-\delta\beta}} \phi^{\frac{\gamma-\beta}{\gamma\omega-\delta\beta}} ,$$

$$\frac{k}{\varepsilon} = \theta^{\frac{\omega-\delta}{\gamma\omega-\delta\beta}} \phi^{\frac{\beta-\gamma}{\gamma\omega-\delta\beta}}$$

and

$$\frac{k^2}{\varepsilon} = \theta^{\frac{2\omega-\delta}{\gamma\omega-\delta\beta}} \phi^{\frac{2\beta-\gamma}{\gamma\omega-\delta\beta}} .$$

Using all these expressions, terms in k and ε can be dropped out from equations for θ (Eq. 7.6) and ϕ (Eq. 7.7):

$$\partial_t(\rho\theta) + \nabla \cdot (\rho\vec{u}\theta) - Diff_\theta = S_\theta , \tag{7.9}$$

where

$$S_\theta = C_\mu(\gamma - \beta\alpha)\rho\theta^{\frac{\omega(\gamma+1)-\delta(\beta+1)}{\gamma\omega-\beta\delta}} \phi^{\frac{\beta-\gamma}{\gamma\omega-\beta\delta}} \mathcal{P} + \frac{2}{3}(\beta\alpha - \gamma)\rho\theta\nabla \cdot \vec{u} + \\ (\beta C_2 - \gamma)\rho\theta^{\frac{\omega(\gamma-1)-\delta(\beta-1)}{\gamma\omega-\beta\delta}} \phi^{\frac{\gamma-\beta}{\gamma\omega-\beta\delta}}$$

and

$$Diff_\theta = \frac{\gamma k^{\gamma-1}}{\varepsilon^\beta}(Diff_k) - \frac{\beta k^\gamma}{\varepsilon^{\beta+1}}(Diff_\varepsilon) .$$

In the same way:

$$\partial_t(\rho\phi) + \nabla.(\rho u\phi) - Diff_\phi = S_\phi , \tag{7.10}$$

where

$$S_\phi = C_\mu(\omega\alpha - \delta)\rho\theta^{\frac{\omega-\delta}{\gamma\omega-\beta\delta}} \phi^{\frac{\gamma(\omega-1)-\beta(\delta-1)}{\gamma\omega-\beta\delta}} \mathcal{P} + \frac{2}{3}(\delta - \alpha\omega)\rho\phi\nabla \cdot \vec{u} + \\ (\delta - C_2\omega)\rho\theta^{\frac{\delta-\omega}{\gamma\omega-\beta\delta}} \phi^{\frac{\gamma(\omega+1)-\beta(1+\delta)}{\gamma\omega-\beta\delta}}$$

and

$$Diff_\phi = \frac{\omega\varepsilon^{\omega-1}}{k^\delta} Diff_\varepsilon - \frac{\delta\varepsilon^\omega}{k^{\delta+1}} Diff_k .$$

Moreover, the new expression for the turbulent viscosity is:

$$\mu_t = C_\mu\rho\theta^{\frac{2\omega-\delta}{\gamma\omega-\delta\beta}} \phi^{\frac{2\beta-\gamma}{\gamma\omega-\delta\beta}} .$$

Expressions for σ_θ and σ_ϕ

Constants σ_θ and σ_ϕ are found using the same approach as before, using the modelled diffusion term:

$$\sigma_\theta = -\frac{\beta\kappa^2}{(C_{\varepsilon_2} - \alpha)\sqrt{C_\mu}} \text{ and } \sigma_\phi = \frac{\omega\kappa^2}{(C_{\varepsilon_2} - \alpha)\sqrt{C_\mu}} .$$

7.3.4 A new system of relations to define γ, β, ω and δ

Using both mathematical relations and physical assumptions, the following conditions must be true:

1. Negativity on β leads to $\sigma_\theta > 0$

$$\beta < 0\,, \tag{7.11}$$

2. Positivity on ω leads to $\sigma_\phi > 0$

$$\omega > 0\,, \tag{7.12}$$

3. Negativity of the constant for the production term on θ equation:

$$\gamma - \beta\alpha < 0\,, \tag{7.13}$$

4. Negativity of the constant for the production term on ϕ equation:

$$\omega\alpha - \delta < 0\,, \tag{7.14}$$

5. Positivity of the constant for the dissipation on θ equation:

$$\beta C_{\varepsilon_2} - \gamma > 0 \tag{7.15}$$

6. Negativity of the constant for the dissipation on ϕ equation:

$$\delta - C_{\varepsilon_2}\omega < 0 \tag{7.16}$$

7. The condition for hypothesis (H4) and (H5) of the theorem 6.3.1 leads to negative power on θ and ϕ for the turbulent viscosity:

$$\frac{2\omega - \delta}{\gamma\omega - \delta\beta} < 0 \quad \text{and} \quad \frac{2\beta - \gamma}{\gamma\omega - \delta\beta} < 0 \tag{7.17}$$

8. Eq. 7.11 and Eq. 7.13 imply $\gamma < 0$,
9. Eq. 7.12 and Eq. 7.14 imply $\delta > 0$.

We look for integer powers for θ and ϕ. Let:

- N_1 be the power on θ for the production term of θ equation (Eq. 7.9);
- N_2 be the power on ϕ for the dissipation term of θ equation (Eq. 7.9);
- N_3 be the power on θ for the production term of ϕ equation (Eq. 7.10);
- N_4 be the power on ϕ for the dissipation term of ϕ equation (Eq. 7.10).

It leads to:

$$\begin{cases} \omega(\gamma+1) - \delta(\beta+1) = N_1(\gamma\omega - \delta\beta) \\ \beta - \gamma = N_2(\gamma\omega - \delta\beta)\,, \\ \omega - \delta = N_3(\gamma\omega - \delta\beta)\,, \\ \gamma(\omega - 1) + \beta(1-\delta) = N_4(\gamma\omega - \delta\beta)\,. \end{cases}$$

and a simplified version is:

$$\begin{cases} \omega - \delta = (N_1 - 1)(\gamma\omega - \delta\beta)\,, \\ \beta - \gamma = N_2(\gamma\omega - \delta\beta)\,, \\ \omega - \delta = N_3(\gamma\omega - \delta\beta)\,, \\ \beta - \gamma = (N_4 - 1)(\gamma\omega - \delta\beta)\,. \end{cases}$$

As a consequence, one can find relations linking N_1 and N_3 on one side and N_2 and N_4 on the other side:

$$N_1 = N_3 + 1 \quad \text{and} \quad N_4 = N_2 + 1\,.$$

The final system is composed of 10 inequalities and 3 equalities to define 8 unknowns N_1, N_2, N_3, N_4, δ, ω, β and γ:

$$\begin{cases} \beta < 0, \quad \gamma < 0, \quad \omega > 0, \quad \delta > 0, \\ \gamma - \beta\alpha < 0, \quad \omega\alpha - \delta < 0, \\ \beta C_{\varepsilon_2} - \gamma > 0, \quad \delta - C_{\varepsilon_2}\omega < 0, \\ \dfrac{2\omega - \delta}{\gamma\omega - \delta\beta} < 0, \quad \dfrac{2\beta - \gamma}{\gamma\omega - \delta\beta} < 0, \\ N_1 = N_3 + 1, \quad N_4 = N_2 + 1, \\ \omega - \delta = N_3(\gamma\omega - \delta\beta)\,, \\ \beta - \gamma = N_2(\gamma\omega - \delta\beta)\,. \end{cases} \tag{7.18}$$

The last two equations are non-linear and a change of variable will help to make them linear. Let:

$$\bar{\gamma} = \frac{\gamma}{\gamma\omega - \delta\beta}, \quad \bar{\beta} = \frac{\beta}{\gamma\omega - \delta\beta}, \quad \bar{\omega} = \frac{\omega}{\gamma\omega - \delta\beta} \quad \text{and} \quad \bar{\delta} = \frac{\delta}{\gamma\omega - \delta\beta}\,.$$

This choice has a meaning if $\gamma\omega - \delta\beta \neq 0$ but $\gamma\omega - \delta\beta = 0$ is impossible as in this case, definitions for θ and ϕ are mathematically linked and we only recover one equation for the turbulence model.

Finally:

$$\begin{cases} \bar{\omega} - \bar{\delta} = N_3\,, \\ \bar{\beta} - \bar{\gamma} = N_2\,. \end{cases} \tag{7.19}$$

Two inequalities are also modified. Two of them are always valid, whatever the sign of $\gamma\omega - \delta\beta$ is:

- Condition of negativity of the power on θ in μ_t expression:

$$2\bar{\omega} < \bar{\delta}$$

- Condition of negativity of the power on ϕ in μ_t expression:

$$2\bar{\beta} < \bar{\gamma}$$

From now on, it is necessary to split the problem into two parts, following the sign of $\gamma\omega - \delta\beta$:

- **Case 1:** $\gamma\omega - \delta\beta > 0$

$$\begin{cases} \bar{\beta} < 0, \quad \bar{\gamma} < 0, \quad \bar{\omega} > 0, \quad \bar{\delta} > 0, \\ \bar{\gamma} < \alpha\,\bar{\beta}, \quad \alpha\,\bar{\omega} < \bar{\delta}, \\ \bar{\beta}C_{\varepsilon_2} - \bar{\gamma} > 0, \quad \bar{\delta} - C_{\varepsilon_2}\bar{\omega} < 0, \\ 2\bar{\omega} \leq \bar{\delta}, \quad 2\bar{\beta} \leq \bar{\gamma}, \\ N_1 = N_3 + 1, \quad N_4 = N_2 + 1\,, \\ \bar{\omega} - \bar{\delta} = N_3\,, \\ \bar{\beta} - \bar{\gamma} = N_2\,, \end{cases} \tag{7.20}$$

- **Case 2:** $\gamma\omega - \delta\beta < 0$

$$\begin{cases} \bar{\beta} > 0, \quad \bar{\gamma} > 0, \quad \bar{\omega} < 0, \quad \bar{\delta} < 0, \\ \bar{\gamma} > \alpha\,\bar{\beta}, \quad \alpha\,\bar{\omega} > \bar{\delta}, \\ \bar{\beta}C_{\varepsilon_2} - \bar{\gamma} < 0, \quad \bar{\delta} - C_{\varepsilon_2}\bar{\omega} > 0, \\ 2\bar{\omega} \leq \bar{\delta}, \quad 2\bar{\beta} \leq \bar{\gamma}, \\ N_1 = N_3 + 1, \quad N_4 = N_2 + 1\,, \\ \bar{\omega} - \bar{\delta} = N_3\,, \\ \bar{\beta} - \bar{\gamma} = N_2\,. \end{cases} \tag{7.21}$$

7.3.5 Analysis of case 1

it is very easy to prove that Eq. 7.20 has no solution. In fact:

$$\bar{\delta} < C_{\varepsilon_2}\bar{\omega} = 1.88\bar{\omega}\,,$$

that is in contradiction with $2\bar{\omega} \leq \bar{\delta}$.

7.3.6 Analysis of case 2

One needs to choose 4 values to define the last 4 ones. We chose to define N_2, N_3, $\bar{\omega}$ and $\bar{\gamma}$ in order to compute N_1, N_4, β and δ. Inequalities are verified *a posteriori*. Once the values are defined, δ, γ, ω and β are computed:

$$\gamma = \frac{\bar{\gamma}}{\bar{\gamma}\bar{\omega} - \bar{\delta}\bar{\beta}}, \quad \omega = \frac{\bar{\omega}}{\bar{\gamma}\bar{\omega} - \bar{\delta}\bar{\beta}}, \quad \delta = \frac{\bar{\delta}}{\bar{\gamma}\bar{\omega} - \bar{\delta}\bar{\beta}} \text{ and } \beta = \frac{\bar{\beta}}{\bar{\gamma}\bar{\omega} - \bar{\delta}\bar{\beta}}\,.$$

The choice of N_2, N_3, $\bar{\omega}$ and $\bar{\gamma}$ is the key point to find (at least!) one solution. The definition of μ_t helps:

$$\begin{aligned} \mu_t &= C_\mu \rho \theta^{\frac{2\omega-\delta}{\gamma\omega-\delta\beta}} \phi^{\frac{2\beta-\gamma}{\gamma\omega-\delta\beta}} \\ &= C_\mu \rho \theta^{\frac{\omega-\delta}{\gamma\omega-\delta\beta}} \phi^{\frac{\beta-\gamma}{\gamma\omega-\delta\beta}} \; \theta^{\frac{\omega}{\gamma\omega-\delta\beta}} \phi^{\frac{\beta}{\gamma\omega-\delta\beta}} \\ &= C_\mu \rho \theta^{N_3} \phi^{N_2} \theta^{\bar{\omega}} \phi^{\bar{\beta}}\,. \end{aligned}$$

We search for integer powers in the definition of μ_t.

7.3.7 Final choice

The choice $N_2 = -2$, $N_3 = 1$, $\bar{\omega} = -2$ and $\bar{\beta} = 1$ is judicious. It leads to:

$$\gamma = -1, \beta = -1/3, \omega = 2/3 \text{ and } \delta = 1.$$

It is necessary to prove that hypotheses of Eq. 7.18 are true:

- $\beta = -\dfrac{1}{3} < 0$, $\gamma = -1 < 0$, $\omega = \dfrac{2}{3} > 0$ and $\delta = 1 > 0$;
- $\gamma - \beta\alpha = -0.52 < 0$ and $\omega\alpha - \delta = -0.04 < 0$;
- $\beta C_{\varepsilon_2} - \gamma = 0.37 > 0$ and $\delta - C_{\varepsilon_2}\omega = -0.253 < 0$;
- $\dfrac{2\omega - \delta}{\gamma\omega - \beta\delta} = -\dfrac{1/3}{1/3} = -1 < 0$ and $\dfrac{2\beta - \gamma}{\gamma\omega - \beta\delta} = -\dfrac{1/3}{1/3} = -1 < 0$;
- $N_2 = -2$ and $N_4 = -1 \Rightarrow N_4 = N_2 + 1$, $N_3 = 1$ and $N_1 = 2 \Rightarrow N_1 = N_3 + 1$;
- $\omega - \delta = -\dfrac{1}{3}$ and $N_3(\gamma\omega - \beta\delta) = -\dfrac{1}{3} \Rightarrow \omega - \delta = N_3(\gamma\omega - \beta\delta)$;
- $\beta - \gamma = \dfrac{2}{3}$ and $N_2(\gamma\omega - \beta\delta) = \dfrac{2}{3} \Rightarrow \beta - \gamma = N_2(\gamma\omega - \beta\delta)$.

This choice respects all constraints and it leads to:

$$\theta = \frac{\varepsilon^{1/3}}{k} \text{ and } \phi = \frac{\varepsilon^{2/3}}{k},$$

Finally, the system of equations for turbulence is:

$$\left\{ \begin{array}{lcl} \dfrac{\partial(\rho\theta)}{\partial t} + \nabla\cdot(\rho\vec{u}\theta) - \nabla\cdot\left((\mu + \dfrac{\mu_t}{\sigma_\theta})\nabla\theta\right) & = & C_\mu C_4 \rho \dfrac{\theta^2}{\phi^2}\mathcal{P} + \dfrac{2}{3}C_5\rho\theta\nabla\cdot\vec{u} + C_6\rho\phi^2 \\ \dfrac{\partial(\rho\phi)}{\partial t} + \nabla\cdot(\rho\vec{u}\phi) - \nabla\cdot\left((\mu + \dfrac{\mu_t}{\sigma_\phi})\nabla\phi\right) & = & C_\mu C_7 \rho \dfrac{\theta}{\phi}\mathcal{P} + \dfrac{2}{3}C_8\rho\phi\nabla\cdot\vec{u} + C_9\rho\dfrac{\phi^3}{\theta} \end{array} \right. \tag{7.22}$$

where the turbulent viscosity is expressed as in the initial system of equations [88, 52]:

$$\mu_t = C_\mu \rho \frac{1}{\theta\phi}.$$

Constants have the “good” sign:

$$C_4 = -0.52,\ C_5 = 0.52,\ C_6 = 0.37,\ C_7 = -0.04,\ C_8 = 0.04 \text{ and } C_9 = -0.253.$$

The Prandtl-Schmidt numbers are:

$$\sigma_\theta = \frac{\kappa^2}{3(C_{\varepsilon_2} - \alpha)\sqrt{C_\mu}} = 0.849 \quad \text{and} \quad \sigma_\phi = \frac{2\kappa^2}{3(C_{\varepsilon_2} - \alpha)\sqrt{C_\mu}} = 1.698.$$

7.4 Conclusions

In this chapter, we showed the current status of our work in order to define a compressible version of the $\theta-\phi$ turbulence model. The change of variable proposed initially by Lewandowski and Mohammadi was not able to capture the boundary layer since the Prandtl-Schmidt number of θ equation was negative. We proposed an alternative change of variables that lead to constants with the correct signs but there remains some work in order to prove the existence of a solution. This is due to the right hand side of Eq. 7.22 that does not cope with the right hand side of Eq. 6.5 introduced for the theorem 6.3.1 on k and ε.

Part III

Discrete analysis of Navier-Stokes equations - numerical schemes

Solving the Navier-Stokes equations involves three steps: time integration, convection and diffusion. In this part, we propose to analyse separately the time integration scheme and the diffusion scheme on multi element-shape meshes. Regarding convection scheme, our efforts are mainly focused on the numerical analysis of classic second order convection schemes in the presence of structured block interface with mismatched nodes.

First, we focus attention on the time integration procedure for time periodic flows and almost-periodic flows. In this part, our efforts were dedicated to the harmonic balance technique, a way to transform an unsteady (almost-) periodic simulation in several stationary simulations coupled by a source term. This activity was one of my main activities during the last 5 years at Cerfacs.

The second activity concerns diffusion. For any integral approach (finite element or finite volume), the diffusion term of the initial equation (volume integral) is transformed into a surface-integral flux computation. In the framework of cell-vertex approach, we proposed and analysed several diffusion schemes - way to compute the gradient for the surface flux integral - and proposed a new scheme with several good properties. This work was published in *Journal of Computational Physics*. Moreover, a recent work for diffusion scheme in cell-centred unstructured finite volume approach is summarised in this thesis. This part is extracted from a new article under preparation.

Our last activity concerns convection scheme. Indeed, in a near future, we will have to consider the coupling between structured and unstructured zones inside a single computational grid. This work is motivated by an industrial demand to handle structured grids in region where the geometry is quite simple and unstructured zones near complex geometry. At the interface between both kind of zones, it will be very difficult to impose the same discretisation of the interface and Block Interface with Mismatched Nodes (BIMN) can be encountered. Before studying BIMN with hybrid structured / unstructured grids, the effect of BIMN was analysed for unsteady flows with structured grids and a paper has been submitted to *Journal of Computational Physics*. The development of numerical schemes and integration techniques is one of my current activities and I wish to continue on this topic.

Associated papers:

− Non-uniform time sampling for multiple-frequency harmonic balance computations, T. Guédeney, A. Gomar, F. Gallard, F. Sicot, G. Dufour and G. Puigt, Journal of Computational Physics, 236(1), pp. 317-345, 2013.

− Contrasting the Harmonic Balance and Linearized Methods for Oscillating-Flap Simulations, G. Dufour, F. Sicot, G. Puigt, C. Liauzun, A. Dugeai, American Institute of Aeronautics and Astronautics Journal, 48(4): 788-797, 2010.

− Discretisation of diffusive fluxes on hybrid grids, G. Puigt, J.-D. Müeller and V. Auffray, Journal of Computational Physics, 229(5), pp.1425-1447, 2010.

− Block-Jacobi Implicit Algorithms for the Time Spectral Method, F. Sicot, G. Puigt and M. Montagnac. American Institute of Aeronautics and Astronautics Journal, 46(12): 3080-3089, 2008.

Articles in preparation:
– Theoretical and numerical analysis of nonconforming grid interface for unsteady flows, J. Vanharen, G. Puigt and M. Montagnac. Submitted to Journal of Computational Physics in August 2014.
– Analysis of a new finite volume scheme for diffusion flux on unstructured grids, P. Cayot and G. Puigt.
– A new family of convection schemes for Large Eddy Simulation, P. Cayot and G. Puigt.

Master thesis:
– Mise en œuvre d'une approche pour maillage hybride dans *elsA*. Etude des solveurs diffusifs, A. Fosso-Pouangue, master thesis, Université de Toulouse, 2007.
– Traitement des raccords entre blocs structurés et blocs non-structurés dans *elsA* hybride, M. Devilliers, master thesis, Université de Toulouse, 2008.
– Mise en oeuvre d'une approche multi-fréquentielle harmonique dans *elsA*, P. Rauschenberger, master thesis, SupAero, 2008.
– Etude et mise en œuvre de schémas cinétiques dans *elsA*, M. Boger, master thesis, SupAero, 2008. Co-advised with Hugues Deniau.
– Analyse des effets de clocking dans les turbomachines par approche d'équilibrage harmonique dans le domaine temporel avec *elsA*. W. Mahmoudi, Master thesis, Université Paris 6, 2009.
– Vers la LES sur maillage hybride avec *elsA*. P. Cayot, Master thesis, INSA Toulouse, 2011.
– Theoretical and numerical analysis of block interfaces with mismatched nodes. Emphasis on unsteady flows. J. Vanharen, Master thesis, SupAero, 2013.

People I worked directly with:
– Frédéric Sicot, Marc Montagnac and Guillaume Dufour (senior researchers at Cerfacs)
– Alain Dugeai and Cedric Liauzun (from ONERA)
– Valérie Auffray, Frédéric Sicot, Thomas Guedeney, Adrien Gomar, François Gallard, Pierre Cayot, Julien Vanharen (PhD students at Cerfacs)
– Arnaud Fosso-Pouangue, Marion Devilliers, Philipp Rauschenberger, Markus Boger, Wassim Mahmoudi, Pierre Cayot and Julien Vanharen (training period at Cerfacs)

Chapter 8

An efficient time integration procedure for periodic and almost-periodic flow

8.1 Introduction

Three-dimensional steady turbulent flow simulations are handled routinely in the industry, but unsteady turbulent flow simulations still require large computational times and an acceleration of the calculations is mandatory to reduce design cycles. In fact, many industrial applications involve flows periodic in time and a transient regime responsible of a large CPU time must be bypassed. In this chapter, we discuss a strategy to monitor better the convergence towards the periodic or almost-periodic solution.

Classic time integration techniques follow an hyperbolic approach: the future is influenced by the past and a retro action is not possible. An efficient time integration procedure for periodic flows must take in consideration all flow characteristics. In this chapter, we consider the Harmonic Balance Method (HBM). The HBM was introduced by Hall *et al.* [62] for blade cascades computations. Then Gopinath *et al.* presented the Time Spectral Method (TSM) [56] for external aerodynamic applications. Both methods are essentially the same and allow to capture the fundamental frequency of the flow and a given number of its harmonics. They cast the unsteady governing equations in a set of coupled steady equations corresponding to a uniform sampling of the flow within the time period. These steady equations can then be solved using standard steady RANS methods with convergence acceleration techniques such as local time stepping, multigrid and implicit time algorithm. The convergence of a steady computation is better monitored than the transient regime induced by an unsteady computation to reach the periodic state. This method proved to be efficient in periodic problem computations such as vortex shedding [57, 134], flutter [135] and turbomachinery applications [63, 137]. All these references use a classic Runge-Kutta explicit time integration procedure, leading to small pseudo-time steps and to a large number of iterations.

Remark 8.1.1 *The integration of harmonic representation of the solution inside Euler or Navier-Stokes equations is not a new idea. During the 70's, spectral approaches were first applied to the spatial terms of the equations. Following the work of Morchoisne [108], spectral representation of data have been extended to the time integration. C. Canuto, M.Y. Hussaini, A. Quarteroni and T.A. Zang published in 1987 a reference book on spectral methods for fluid dynamics [18].*

This chapter is organised as follows. After introducing the theoretical aspects of the HBM for the RANS equations, a focus is put on the implicit time treatment. Introduction of an implicit time integration is for sure the key point to achieve efficiently computations of periodic problems in industry since it provides a large CPU time saving. Then, the assessment of the method by comparison with classical time-marching integration techniques and linearised solutions is performed. Finally, the last section is devoted to the treatment of the HBM when several non-related frequencies are present in the flow.

8.2 Implicit treatment of the Harmonic Balance method

8.2.1 A new set of equations

The Navier-Stokes equations in Cartesian coordinates are written in semi-discrete form as

$$V\frac{\partial W}{\partial t} + R(W) = 0. \tag{8.1}$$

V is the volume of a cell, W is the vector of the mean conservative variables over the volume V: $W = (\rho, \rho\vec{u}, \rho E)^\top$, complemented with an arbitrary number of turbulent variables as within the RANS framework. $R(W)$ is the residual vector resulting from spatial discretisation of the convective and viscous fluxes.

If W is periodic with period $T = 2\pi/\omega$, so is $R(W)$ and the Fourier series of Eq. 8.1 is

$$\sum_{k=-\infty}^{\infty} (ik\omega V\hat{W}_k + \hat{R}_k)\exp(ik\omega t) = 0, \tag{8.2}$$

where $\hat{W}_k$ and $\hat{R}_k$ are the Fourier coefficients of W and R corresponding to mode k and $i^2 = -1$. The complex exponential family forming an orthogonal basis, the only way for Eq. 8.2 to be true is that the weight of every mode k is zero. An infinite number of steady equations in the frequency domain is obtained:

$$ik\omega V\hat{W}_k + \hat{R}_k = 0, \qquad \forall k \in \mathbb{Z}. \tag{8.3}$$

Remark 8.2.1 *McMullen* et al. *[93] solve a subset of these equations up to mode N, $-N \leq k \leq N$, yielding the Non-Linear Frequency Domain (NLFD) method.*

The HBM [56] uses an Inverse Discrete Fourier Transform (IDFT) to cast back in the time domain this subset of $2N+1$ equations from Eq. 8.3. The IDFT induces linear relations between Fourier's coefficients $\hat{W}_k$ and a uniform sampling of W within the period:

$$W_n = \sum_{k=-N}^{N} \hat{W}_k \exp(i\omega n\Delta t), \qquad 0 \leq n < 2N+1,$$

with $W_n \equiv W(n\Delta t)$ and $\Delta t = T/(2N+1)$. This leads to a time discretisation with a new time operator D_t:

$$R(W_n) + VD_t(W_n) = 0, \qquad 0 \leq n < 2N+1. \tag{8.4}$$

These steady equations correspond to $2N+1$ instants equally spaced within the period. The new time operator connects all time levels and can be expressed analytically by:

$$D_t(W_n) = \sum_{m=-N}^{N} d_m W_{n+m},$$

with

$$d_m = \begin{cases} \frac{\pi}{T}(-1)^{m+1} \csc\left(\frac{\pi m}{2N+1}\right) & , m \neq 0, \\ 0 & , m = 0. \end{cases}$$

Remark 8.2.2 *The same treatment can be performed for an even number of instants but it is proved in [137] that it can lead to an odd-even decoupling and the method can become unstable. In the following the number of instants is odd.*

A pseudo-time derivative τ_n is added to Eq. 8.4 in order to time march the equations to the steady-state solutions of all instants,

$$V\frac{\partial W_n}{\partial \tau_n} + R(W_n) + VD_t(W_n) = 0, \qquad 0 \leq n < 2N+1. \tag{8.5}$$

The term $VD_t(W_n)$ appears as a source term that represents a high order formulation of the initial time derivative in Eq. 8.1. For stability reasons, the computation of the local time step is modified [137] to take into account this additional source term,

$$\Delta\tau = CFL\frac{V}{\|\lambda\| + \omega NV}. \tag{8.6}$$

An extra term ωNV is added to the spectral radius $\|\lambda\|$ to restrict the time step. Equation 8.6 implies that a high frequency and/or a high number N of harmonics can considerably constrain the time step. Actually, it was observed [62] that the convergence of the method slows down for increasing N. All the cited references use explicit schemes, such as Runge-Kutta, to carry out the pseudo-time integration. Their limited stability criteria (low CFL number) is very sensitive to such a restriction. Conversely, implicit schemes are more stable and allow larger CFL numbers, reducing this sensitivity. In particular, we look for an integration procedure that overcomes the theoretical limitation (Eq. 8.6) and that leads to a large pseudo time step for any N and any frequency. Such schemes would have the same behaviour when the frequency of the unsteadiness increases. The following section describes the backward-Euler algorithm for the HBM.

8.2.2 Implicit treatment strategies

In this section, the full equations will not be derived but the key points will be introduced and the proposed solution explained.

Naive implicit algorithm

To introduce an implicit algorithm in the HBM, the first approach is to linearise only the residual $R(W_n)$ of Eq. 8.5 but not the source term $VD_t(W_n)$. This leads to the augmented system

$$\begin{pmatrix} \boxed{\frac{V}{\Delta\tau_0}I + J_0} & 0 & \cdots & 0 \\ 0 & \boxed{\frac{V}{\Delta\tau_1}I + J_1} & \ddots & \vdots \\ \vdots & \ddots & \ddots & 0 \\ 0 & \cdots & 0 & \boxed{\frac{V}{\Delta\tau_{2N}}I + J_{2N}} \end{pmatrix} \begin{pmatrix} \Delta W_0 \\ \Delta W_1 \\ \vdots \\ \Delta W_{2N} \end{pmatrix} = - \begin{pmatrix} R_{HBM}(W_0^q) \\ R_{HBM}(W_1^q) \\ \vdots \\ R_{HBM}(W_{2N}^q) \end{pmatrix}, \tag{8.7}$$

with $R_{HBM}(W_n^q) = R(W_n^q) + VD_t(W_n^q)$ the right-hand side of the HBM equations, and J_n the Jacobian of the standard residual operator at instant n, $J_n = \partial R(W_n)/\partial W_n$. The augmented matrix is block diagonal and a LU-SSOR algorithm[1] can be applied independently on each instant n. In other words, $2N+1$ steady flows are computed and they are only coupled through the explicit residuals. This is clearly an advantage since this implicit approach needs the same data exchange as the explicit formulation. It does not need any new development on the implicit side. However, we showed in [131] that convergence is not achieved easily with this technique and we proposed an alternative.

Full implicitation of the source term

In order to improve the performances, the source term of the HBM needs to be taken into account. The HBM equations with W considered at iteration $q+1$ read

$$V\frac{\Delta W_n}{\Delta \tau_n} = -\left(R\left(W_n^{q+1}\right) + VD_t\left(W_n^{q+1}\right)\right), \quad 0 \le n < 2N+1. \tag{8.8}$$

As the operator D_t is linear, applying it on W_n at iteration $q+1$ gives

$$D_t\left(W_n^{q+1}\right) = D_t(W_n^q) + D_t(\Delta W_n). \tag{8.9}$$

In the same manner as the HBM time operator D_t couples together the conservative variables at all instants, Eq. 8.9 leads to a coupling of the increments ΔW at all instants. Equation 8.8 turns into

$$\left(\frac{V}{\Delta \tau_n} I + J_n\right)\Delta W_n + VD_t(\Delta W_n) = -R_{HBM}(W_n^q), \quad 0 \le n < 2N+1.$$

As $d_0 = 0$, the diagonal terms are identical to the diagonal terms of Eq. 8.7. The matrix of the system becomes

$$A^\star = \begin{pmatrix} \boxed{\frac{V}{\Delta\tau_0}I + J_0} & Vd_1I & \dots & Vd_NI & Vd_{-N}I & \dots & Vd_{-1}I \\ Vd_{-1}I & \ddots & \ddots & \vdots & \ddots & \ddots & \vdots \\ \vdots & \ddots & \ddots & Vd_1I & \ddots & \ddots & \vdots \\ Vd_{-N}I & \dots & Vd_{-1}I & \boxed{\frac{V}{\Delta\tau_N}I + J_N} & Vd_1I & \dots & Vd_NI \\ \vdots & \ddots & \ddots & Vd_{-1}I & \ddots & \ddots & \vdots \\ \vdots & \ddots & \ddots & \vdots & \ddots & \ddots & Vd_1I \\ Vd_1I & \dots & Vd_NI & Vd_{-N}I & \dots & Vd_{-1}I & \boxed{\frac{V}{\Delta\tau_{2N}}I + J_{2N}} \end{pmatrix}.$$

The new matrix A^* is not block-sparse anymore and couples all the increments ΔW_n of all the instants n. This probably explains why the adapted LU-SSOR scheme (with the coupling operator on the explicit increment) fails to converge for a high number of harmonics [131]: the

---

[1] Such a LU-SSOR algorithm is currently implemented to converge steady solutions within the *elsA* code considered in this analysis.

linearisation error grows as the number of harmonics increases and so the convergence rate decays.

A^* could be decomposed as a sum of three matrices $A^\star = \mathcal{L}^\star + \mathcal{D}^\star + \mathcal{U}^\star$ with $\mathcal{L}^\star$ a lower block triangular matrix, $\mathcal{D}^\star$ a block diagonal matrix and $\mathcal{U}^\star$ an upper block triangular matrix. Then a classic SSOR algorithm could be applied on the whole system but it would necessitate to go all over the blocks and thus would break down code efficiency in term of CPU requirement. This is also a drawback for parallel computations. To remove this drawback, two algorithms based on the block-Jacobi method are now presented.

8.2.3 Block-Jacobi Strategies for Full Implicit HBM

Applied to the HBM, the iterative block-Jacobi method [126] allows to move the implicit coupling term $VD_t(\Delta W_n)$ to the right-hand side and yields $2N+1$ independent linear systems. A Jacobi step l reads

$$\left(\frac{V}{\Delta\tau_n} I + J_n\right) \Delta W_n^{l+1} = -R_{HBM}(W_n^q) - VD_t\left(\Delta W_n^l\right), \quad 0 \leq n < 2N+1, \tag{8.10}$$

with $l \geq 0$, $\Delta W_n^0 = 0$ and at the end of the l_{max} block-Jacobi iterations, the increments ΔW_n allow to compute W at the next iteration: $W_n^{q+1} = W_n^q + \Delta W_n^{l_{max}}$. For every block-Jacobi step, a linear system has to be solved. This system could be solved with any direct or iterative method. The classic SSOR technique is actually used as it allows minimum efforts to be adapted from the LU-SSOR method.

Block-Jacobi-SSOR (BJ-SSOR) Strategy

Each equation of the block-Jacobi system Eq. 8.10 could be solved with an iterative SSOR technique that is decomposed in a forward sweep

$$(\mathcal{L}_n + \mathcal{D}_n)X^{s+1/2} = -\left(R_{HBM}(W_n^q) + VD_t\left(\Delta W_n^l\right)\right) - \mathcal{U}_n X^s, \tag{8.11}$$

followed by a backward sweep

$$(\mathcal{D}_n + \mathcal{U}_n)X^{s+1} = -\left(R_{HBM}(W_n^q) + VD_t\left(\Delta W_n^l\right)\right) - \mathcal{L}_n X^{s+1/2}, \tag{8.12}$$

for $s \geq 0$ with $X^0 = \Delta W_n^l$. At the end of the SSOR iterations, $X^{s_{max}}$ is updated into the block-Jacobi steps: $\Delta W_n^{l+1} = X^{s_{max}}$, s_{max} being the number of SSOR forward and backward sweeps inside a block-Jacobi step. The block-Jacobi method imposes the implicit coupling term $D_t\left(\Delta W_n^l\right)$ to be updated at each step l. In other words, the implicit coupling term is computed every $2s_{max}$ sweeps and frozen over the following $2s_{max} - 1$ sweeps. As $\Delta W_n^0 = 0$, it remains null during all the sweeps in the first block-Jacobi step and consequently at least two steps are needed to ensure the coupling of the increments of all instants, $l_{max} \geq 2$. If $l_{max} = 1$, no implicit coupling occurs and Eq. 8.7 is recovered. To reinforce the influence of the implicit coupling, the next method is proposed.

Block-Jacobi-SOR (BJ-SOR) Strategy

The system Eq. 8.10 could also be solved in a special way with alternate SOR techniques. A single loop is needed and the imposed constraint is to have an even number l_{max} of block-Jacobi steps to balance forward and backward sweeps. Indeed, when l is even, the system is solved with only one forward SOR sweep Eq. 8.11 and when l is odd, the system is solved with only one backward SOR sweep Eq. 8.12.

The implicit coupling term $VD_t(\Delta W_n)$ is computed before every sweep (but the first one as $\Delta W_n^0 = 0$) and thus this strategy ensures the strongest coupling. If $s_{max} = 2$ in the BJ-SSOR method for instance, the implicit coupling term is computed before the fifth (forward) sweep and frozen over the three following sweeps. Table 8.1 compares the two methods in terms of SOR sweeps.

HBM Number	BJ-SSOR $s_{max} = 2$			BJ-SOR	
of sweeps	l	s	update	l	update
1	0	0	no	0	no
2	0	0	no	1	yes
3	0	1	no	2	yes
4	0	1	no	3	yes
5	1	0	yes	4	yes
6	1	0	no	5	yes
7	1	1	no	6	yes
8	1	1	no	7	yes
			⋮		

Table 8.1: *Implicit coupling term update. Values of the loop indexes l and s before each sweep, and if the implicit coupling term is updated.*

8.2.4 Numerical assessment of the implicit formulation

We consider in this section the 3D transonic LANN wing [149] in a forced harmonic pitching movement at frequency $f = 24$ Hz. The angle of attack α oscillates as $\alpha(t) = \alpha_0 + \alpha_m \sin(2\pi f t)$ with $\alpha_0 = 0.6^o$ and $\alpha_m = 0.25^o$. The flow conditions are $Ma = 0.822$ and $Re = 5.43 \times 10^6$. Experimental data are available for the time-averaged and the first harmonic of the wall pressure distribution at different cross sections. The mesh is composed of 1 122 816 cells and it is based on a C topology.

First, a numerical study of the different parameters is conducted. The convergence curves for the initial implicit approach is given in Fig. 8.1(a). The solution residual is defined as the root mean square of the residual operator $R(W)$ on all the mesh cells, averaged by the number of instants. Density residuals are normalised by the residual at first iteration to enable comparison. It is observed that the CFL needs to be decreased in order to converge high harmonic computations. For $N = 4$, the CFL must be decreased to approximately 20 (dotted line) as with $CFL = 30$, the computation does not converge (dashed line). The five-harmonic computation needs a few thousand iterations at CFL = 5 to decrease residuals by five orders of magnitude: the convergence rate is very slow. The first block-Jacobi strategy used is the BJ-SOR as it should ensure the best coupling. The results with $l_{\max} = 4$ are presented in Fig. 8.1(b). The benefits of the full implicitation are clear as all the computations are now performed at CFL = 100. Furthermore almost no differences are found between the normalised convergence curves. Even if not all test cases show such a good matching, it is generally observed that the convergence rate is nearly the same for any number of harmonics.

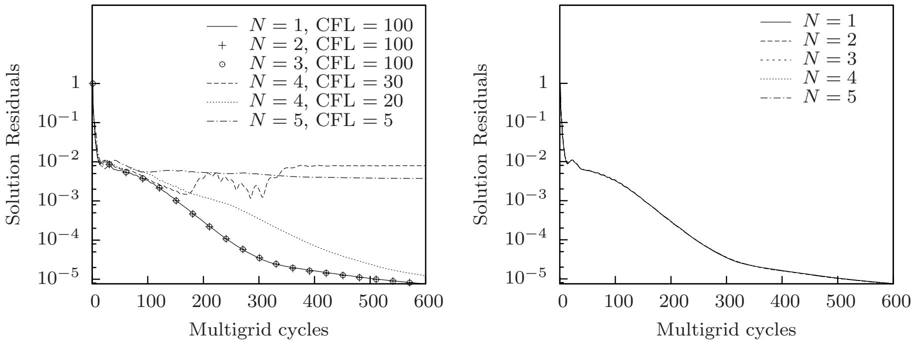

(a) Standard LU-SSOR

(b) BJ-SOR (all CFL = 100)

Figure 8.1: *Convergence of the computations.*

Up to now, results were obtained with the BJ-SOR algorithm with 4 sweeps, leading finally to the first forward sweep without implicit coupling ($\Delta W = 0$ initially) and the three other sweeps with implicit coupling. The influence of the derived strategies is shown in figure 8.2 for the most difficult case $N = 5$. It is observed that the BJ-SOR strategy with $l_{\max} = 2$ (with only the backward sweep ensuring the implicit coupling) is sufficient to obtain convergence at CFL = 100.

Results from the block-Jacobi-SSOR algorithm are represented by marks in Fig. 8.2. As $\Delta W_n = 0$ for the first block-Jacobi step, at least two steps are needed to ensure the coupling of increments. As shown previously with the BJ-SOR method, six sweeps are already expensive. To ensure an implicit coupling as often as possible with this few numbers of sweeps, s_{max} is set to one for the BJ-SSOR algorithm. Even though the coupling occurs less often, the convergence rate is almost the same for the BJ-SOR method with $l_{\max} = 4$ as for the BJ-SSOR method with $l_{\max} = 2$, and slightly slowed down with two additional sweeps for each method (resp. $l_{\max} = 6$ and $l_{\max} = 3$) with respect to the number of multigrid cycles. As the term $D_t(\Delta W_n)$ is only computed every two sweeps, the CPU time required by the BJ-SSOR method is notably reduced compared to the BJ-SOR approach with the same number of sweeps.

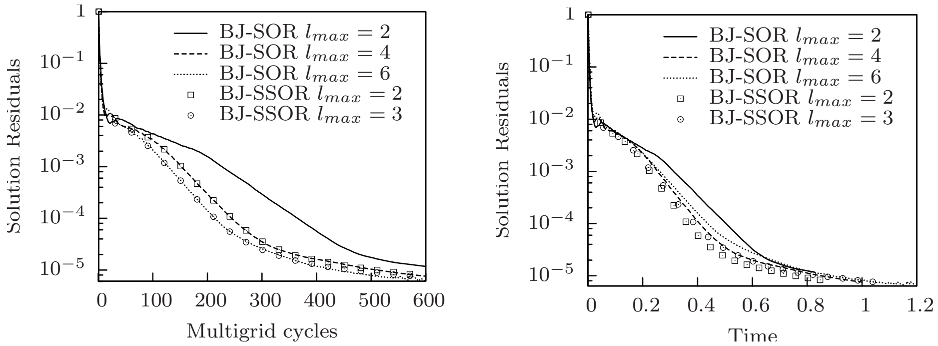

(a) Convergence curves with respect to the number of the number of sweeps

(b) Convergence curves with respect to a dimensionless CPU time

Figure 8.2: *Convergence of the computations.*

8.2.5 Accuracy of the HBM solutions

The computation of pitching airfoil can be done with two different formulations: in a relative or an absolute reference frame. For the relative frame, the mesh remains rigid around the wing and the change of incidence is induced by varying far-field boundary conditions. In this case, the inertial force has to be taken into account through a source term of the Navier-Stokes equations. For the absolute frame of reference, the incidence variation is performed by a change in incidence of the wing itself. This approach needs a mesh deformation technique. In this section, only the absolute reference frame is considered in order to avoid the coupling of HBM with the Arbitrary Lagrangian Eulerian formulation.

Without entering into all details from [131], it is found that a one-harmonic HBM computation is sufficient to match the U-RANS computation almost everywhere but at the shock location, where the solution slightly fluctuates. With higher harmonics ($N = 3$ and $N = 5$), HBM solutions match well the reference U-RANS simulation. Both kinds of simulation give solutions that match the experimental data quite well, although the shock on the upper surface is predicted downstream the experimental location. Overall, it can be concluded that a three-harmonic HBM computation is sufficient to match the U-RANS computation with engineering accuracy. In this case, the HBM is about 2.5 times faster than the reference U-RANS computation.

8.2.6 Conclusions

We introduced four ways to linearise the HBM equations and effectively implemented and tested three techniques. Due to the lack of coupling, the classic LU-SSOR approach is the less efficient. The full implicit treatment was not implemented since it induces a strong coupling of the implicit treatment between separated blocks and therefore, it leads to a high CPU overhead compared to a pure LU-SSOR approach. We mean that in a parallel computation, the full implicit matrix must be built and all flow solutions must be exchanged at each iteration in order to build the off-diagonal terms. Finally, we proposed and compared the BJ-SOR and the BJ-SSOR techniques. In [131], we showed that the block-Jacobi-SSOR scheme enables a fast convergence rate of the computations at a cost of about one fifth more CPU time and 10 % more memory requirements compared to the LU-SSOR method. Nevertheless, the time steps allowed are much larger and the HBM is far less sensitive to either high frequencies or an important number of harmonics than with explicit schemes. It can thus be concluded that the extra numerical cost of the implicit formulation is greatly counterbalanced by the larger time step enabled.

8.3 Comparison of the HBM with linearised and unsteady approaches

The HBM introduced in Sec. 8.2.1 can be seen as an approximation of the time integration procedure for periodic problems. Indeed, the accuracy depends on the number of harmonics taken into account. It is of great interest to compare the current HBM with the linearised equations approach and with the classic URANS technique on oscillating-flap simulations.

In this section, after introducing all discretisation techniques, we perform a comparison of the 3 approaches. This work was published in 2010 [39].

8.3.1 URANS equations for pitching airfoil and mesh deformation

In Cartesian coordinates, the Arbitrary Lagrangian Eulerian (ALE) formulation of the Navier-Stokes equations can be written in semi-discrete form as

$$\frac{\partial(VW)}{\partial t} + R(W, s) = 0. \tag{8.13}$$

V is the volume of a cell (which can vary in time), W is the vector of the conservative variables $W = (\rho, \rho\vec{u}, \rho E)^\top$ complemented with an arbitrary number of turbulent variables as within the RANS framework. The velocity of the mesh s is composed of two contributions $s = s^E + s^D$ where s^E is the entrainment velocity and s^D the deformation velocity. Mesh deformation is performed by a trans-finite interpolation algorithm [33]. $R(W, s)$ is the residual vector resulting from the spatial discretisation of the convective f_{ci} and viscous f_{vi} fluxes.

To obtain a time-accurate numerical solution of Eq. 8.13, a second order Dual Time Stepping (DTS) method can be applied for the time integration [71]. This approach is what we refer to as the “Non-linear method”, since all the nonlinearities of the flow can potentially be captured. The pseudo-time marching for the inner loop is performed by using an efficient implicit time-integration scheme, based on the backward-Euler scheme. The resulting linear system is solved with a scalar Lower-Upper Symmetric Successive Over-Relaxation (LU-SSOR) method [146]. Convergence acceleration in the inner loop is ensured by a two-level V-cycle multigrid algorithm and the use of local time stepping. Mesh deformation is performed at each global-time step.

From a practical point of view, the accuracy of the solution depends on:

- the convergence of the inner-loop iterations, monitored by the reduction of the L2-norm of the residuals;
- the time step, usually expressed as a fraction of the period;
- the physical-time span of the simulation, usually expressed as a number of computed periods.

8.3.2 Linearised method (LUR)

An alternative to URANS simulations is the resolution of the Linearised Unsteady Reynolds-averaged Navier-Stokes equations (LUR). This method was first developed for turbomachinery flows [61, 26] and extended to aircraft applications [109, 89]. It consists in the linearisation of the Navier-Stokes equations with respect to a small perturbation superimposed over a steady flow. The resulting equation is then written in the frequency domain to compute the response to a harmonic motion of the wall surfaces, assuming the flow variables being harmonic of the first order. This yields a complex linear system that can be solved using classic steady CFD pseudo-time marching algorithms. This method allows thus to take into account steady states (with shocks at right locations), but is not able to capture nor model unsteady non-linear phenomena like buffet, limit-cycle oscillations, or massive flow separations.

The linearisation of the Navier-Stokes equations consists, in a first step, in splitting the flow variables into a steady part and a perturbation component ($W = W_s + \delta\mathcal{W}$), and in a second step, in rewriting the fluid equations Eq. 8.13 by retaining only the first-order terms in the perturbation variables $\delta\mathcal{W}$. The subscript “$_s$” stands in this part for the steady variables, and the prefix “δ” for the perturbation ones.

$$V_s \frac{\partial(\delta\mathcal{W})}{\partial t} + W_s \frac{\partial(\delta\mathcal{V})}{\partial t} = -\delta R = -\frac{\partial(\delta\mathcal{F}_i)}{\partial x_i} \tag{8.14}$$

Since the flow perturbation variables and the wall motion ($\delta\mathcal{M}$) are assumed to be harmonic at a frequency ω, the linearised equations Eq. 8.14 can be written in the frequency domain as:

$$\begin{cases} \delta\mathcal{W} &= \delta W.e^{i\omega t} \qquad \text{with } i^2 = -1 \\ \delta\mathcal{M} &= \delta M.e^{i\omega t} \\ \delta\mathcal{F}_i &= \delta f_i.e^{i\omega t} \\ s &= i\omega.\delta M \end{cases}$$

$$i\omega V_s \delta W + i\omega W_s \delta V + \frac{\partial(\delta f_i)}{\partial x_i} = 0 \tag{8.15}$$

where

$$\delta W = \begin{pmatrix} \delta\rho \\ \delta(\rho u_1) \\ \delta(\rho u_2) \\ \delta(\rho u_3) \\ \delta(\rho E) \end{pmatrix}, \quad \delta f_i = \begin{pmatrix} \delta(\rho u_i) - \rho_s s_i \\ u_{1,s}\delta(\rho u_i) + (\rho u_i)_s(\delta u_1 - s_1) + \delta p.\delta_{i1} \\ u_{2,s}\delta(\rho u_i) + (\rho u_i)_s(\delta u_2 - s_2) + \delta p.\delta_{i2} \\ u_{3,s}\delta(\rho u_i) + (\rho u_i)_s(\delta u_3 - s_3) + \delta p.\delta_{i3} \\ u_{i,s}(\delta(\rho E) + \delta p) + (\rho E + p)_s \delta u_i \end{pmatrix} + \begin{pmatrix} 0 \\ \delta\tau_{i1} \\ \delta\tau_{i2} \\ \delta\tau_{i3} \\ \delta u \cdot \tau_{i,s} + u_s \cdot \delta\tau_i - \delta q_i \end{pmatrix}$$

and

$$\begin{aligned} \delta u_i &= \frac{1}{\rho_s}\left(\delta(\rho u_i) - u_{i,s}\delta\rho\right) \\ \delta p &= (\gamma - 1)\Big[\delta(\rho E) + \frac{u_s \cdot u_s}{2}\delta\rho - u_s \cdot \delta(\rho u)\Big] \\ \delta\tau_{ii} &= \frac{2}{3}\mu_s\Big[3\frac{\partial\delta u_i}{\partial x_i} - \frac{\partial\delta u_1}{\partial x_1} - \frac{\partial\delta u_2}{\partial x_2} - \frac{\partial\delta u_3}{\partial x_3}\Big] \\ \delta\tau_{ij} &= \mu_s\Big[\frac{\partial\delta u_i}{\partial x_j} + \frac{\partial\delta u_j}{\partial x_i}\Big] \\ \delta q_i &= -\kappa_s\frac{\partial T}{\partial x_i} \\ \delta T &= \frac{1}{c_v}\left[\frac{1}{\rho_s}\Big(\delta(\rho E) - (\rho E)_s\frac{\delta\rho}{\rho_s}\Big) - u_s \cdot \delta u\right] \end{aligned}$$

The last linearised fluid equation Eq. 8.15 is obtained considering the laminar and turbulent viscosity coefficients frozen to their steady state. It yields a complex linear system in the complex variable $\delta\mathcal{W}$, which is solved using a pseudo-time implicit method (backward Euler LU-SSOR) associated with local time-stepping and multigrid algorithms. The steady solution is computed separately, and used as an input for the resolution of the complex system.

8.3.3 HBM key points for mesh movement

The first step in the HBM is to perform a Fourier decomposition of the flow variables and residuals. The series are then injected in the semi-discrete form of the RANS equations Eq. 8.13 to obtain a set of coupled equations in the frequency domain. An Inverse Discrete Fourier Transform (IDFT) is then used to cast back the system in the time domain. Compared with the approaches introduced in Eq. 8.4 for a fixed grid, the main difference appears in the definition of the source term that involves now the volume of each mesh cell:

$$R(W_n, s_n) + D_t[(VW)_n] = 0, \qquad 0 \leq n < 2N + 1, \tag{8.16}$$

where the subscript n denotes a snapshot of a quantity at the instant $t_n = nT/(2N + 1)$. As before, these steady equations correspond to $2N + 1$ instants equally spaced within the period and the time operator D_t keeps the same form:

$$D_t[\phi] = \sum_{m=-N}^{N} d_m \phi_{n+m}, \tag{8.17}$$

but it is applied now to $\phi = VW$ in Eq. 8.16. The coefficients of the source term remain unchanged.

As before, a pseudo-time derivative τ_n is added to Eq. 8.16 in order to time march the equations to the “steady-state” solutions of all the instants:

$$\frac{\partial (VW)_n}{\partial \tau_n} + R(W_n, s_n) + D_t[(VW)_n] = 0, \qquad 0 \leq n < 2N + 1. \tag{8.18}$$

It can be noted that the HBM can be viewed as the superimposition of a complex perturbation over a time-averaged solution, whereas in the LUR method, the base state is the steady solution.

To solve Eq. 8.18, an issue specific to the ALE approach is the computation of the mesh velocity s_n for each instant. While s_n^E can still be obtained using analytical equations for the rigid-body movement considered, the mesh-deformation velocity needs a special treatment. In a classic unsteady simulation, a simple finite difference operator is usually used:

$$s_n^D = \frac{M_n - M_{n-1}}{\Delta t}, \quad \text{for each mesh point } M.$$

As for any finite difference operator, its accuracy depends on the ratio of the time step Δt to the period of the problem. In a typical URANS calculation, at least 40 instants discretise the period, which gives an accurate evaluation of s^D. In a HBM calculation, the number of instants in the period (typically 3 to 11) cannot provide a good estimate of s^D using this standard finite difference scheme.

An efficient approach to evaluate s_n is to use again the spectral operator of the HBM. Indeed, since for a periodic movement of the body the mesh deformation is harmonic, the HBM operator Eq. 8.17 can be used to evaluate the mesh-deformation speed from the coordinates of the mesh at the $2N + 1$ instants:

$$s_n^D = D_t[M_n] = \frac{2\pi}{T} \sum_{m=-N}^{N} d_m M_{n+m}\,, \tag{8.19}$$

The accuracy of this evaluation depends on the order N of the method, as does the accuracy of the whole HBM. The kind of problem that can occur with the finite difference approach can be illustrated considering a simple pitching airfoil. The mesh velocity on the skin of the airfoil is geometrically linked to the instantaneous rotation speed:

$$\alpha_t = \sin(\omega t) \text{ and } \Omega(t) = \frac{d\alpha}{dt} = \omega\cos(\omega t).$$

Fig. 8.3 compares the exact solution for the rotation speed with a 40-point finite difference solution, a 3-point finite difference solution and the HBM operator with $N = 1$. The 3-point finite difference solution is not only far from the solution in terms of amplitude, but it has the wrong sign for the second instant of the period. At this instant, the airfoil leading edge would appear to be going up, whereas it is actually going down. The HBM solution with $N = 1$ is very accurate.

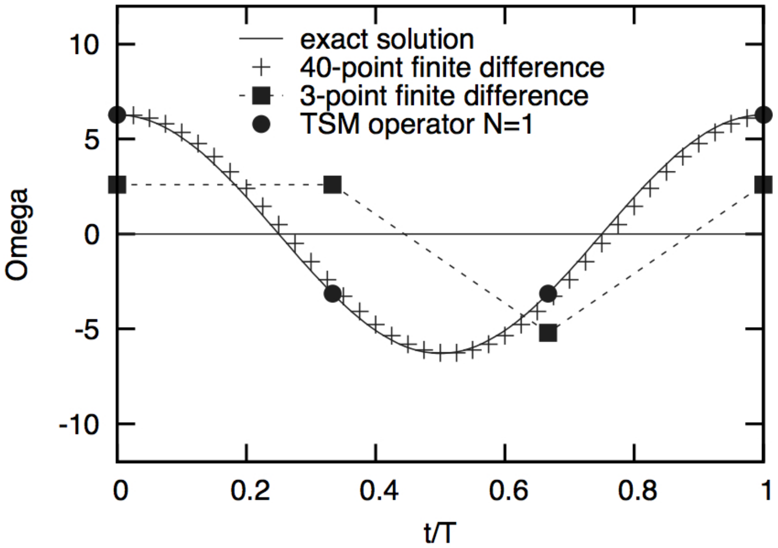

Figure 8.3: *Comparison of the finite difference and HBM to compute the derivative of a sinus.*

8.3.4 Numerical comparison and conclusions

The test case considered here is a two-dimensional NACA 64A006 airfoil with a flap mounted at 75% of the chord, as proposed by AGARD [2]. Several flow configurations are available in the AGARD data set for this geometry, depending on the incoming flow Mach number Ma and angle of attack α_∞, the oscillation frequency f, and the maximum deflection angle δ_0. The two cases retained for the present study are denoted as CT1 and CT6. Another case was considered, for which experimental data are not available. In order to provide a test case in the transonic regime with separation, the angle of attack of the CT6 case was increased so that a detached flow is observed on the upper side of the flap. This case will be referred to as CT6-DF (for Detached Flow). All the test cases are summarised in Tab. 8.2.

All the necessary information regarding the mesh is introduced in [39]. The spatial convective fluxes are discretised with the second-order centred scheme with Jameson-type artificial dissipation [72]. Diffusive terms are computed with a centred second-order scheme. The turbulent viscosity is computed by the Spalart-Allmaras model [133]. The boundary conditions

	α_∞ (°)	Ma (-)	f (Hz)	δ_0 (°)
CT1	0.0	0.794	30.0	1.09
CT6	0.0	0.853	30.0	1.10
CT6-DF	4.0	0.853	30.0	1.10

Table 8.2: *Description of the NACA64A006 test cases.*

are: (i) a non-reflecting far-field conditions on the boundary of the domain and (ii) a no-slip adiabatic wall condition on the airfoil.

In all cases, iterative convergence for the LUR and HBM and time-accuracy for the URANS approach were monitored. For URANS, the choice was to analyse convergence on the basis of the unsteady pressure distribution. That is to say, a computation was considered converged when the first harmonic of the pressure distribution did not significantly change any further with the iterative process. For the URANS case, since harmonic analysis is performed at the end of each simulated period, it was necessary to compute three periods to verify that the unsteady pressure distribution obtained during the second period is converged. The numerical parameters used for the different test-cases are summarised in table 8.3.

		CT1	CT6	CT6-DF
URANS				
	time step	$T/48$	$T/64$	$T/64$
	number of simulated periods	3	3	3
	number of dual iterations	25	50	80
	CFL number	50	50	50
HBM				
	number of iterations	300	500	1000
	CFL number	50	50	5
LUR				
	number of iterations	300	500	–
	CFL number	50	50	–

Table 8.3: *Numerical parameters for all the test cases.*

We do not recall all results presented in [39] but we simply give the main results regarding CT6 and CT6-DF. For CT6, the choice of the technique has a strong impact on the quality of the solution. Even if the LUR solution is obtained 4 times faster, its accuracy is poor near shocks ; the HBM ($N = 3$) solution is as accurate as the URANS, but with a speedup of only 2. For the transonic case with separation over the flap CT6-DF, the LUR does not converge, and the HBM ($N = 2$) is fairly accurate, with a speedup of 6.

To conclude, one important result is that the one-harmonic HBM solution is able to capture unsteady nonlinearities that the LUR solution fails to predict. We contend that the theoretical basis for this behaviour are the following:
(i) the nonlinearities of the Navier-Stokes are preserved in the HBM formulation, whereas the LUR solves a linearised set of equations;
(ii) the one-harmonic HBM takes into account three different meshes in the period, whereas the LUR computes the solution on the initial mesh only and
(iii) the base state on which the one-harmonic perturbation is superimposed is the time-

averaged state for the HBT, whereas it is the steady-state solution for the LUR, which may differ when significant unsteady effects occur.

Finally, it appears that the LUR and HBM methods are valuable alternatives to the URANS method, in terms of accuracy and CPU performance, with different optimal ranges of application. Furthermore, it must be reminded that both methods have a lower computational cost than URANS computations.

8.4 Extension of the HBM approach to handle several frequencies inside the flow

The standard industrial design of multistage turbo machines is usually based on steady analysis, for which the most advanced tools are the RANS steady computations. With the ever growing need to improve performance, aggressive design choices foster unsteady phenomena such as blade interactions in compact turbo-engines, separated / reattached flows at or close to the limit stable operating point, aeroelasticity.... In this context, engineers need to account for these effects early in the development cycle. Thus, unsteady computations are entering industrial practice with the large growth of computational power and efficient and accurate unsteady approaches are receiving a lot of attention.

We already showed that the Harmonic Balance Method can be seen as a reduced model for unsteady simulations containing a given frequency and a few of its harmonics. However, the relative motion of fixed and rotating blades of a turbomachine gives rise to deterministic unsteady interactions associated with the Blade Passing Frequencies (BPF in the following). In a multistage turbomachine, a row sandwiched between two other rows is submitted to (at least) two BPFs, following Tyler and Sofrin theory [136]. It is therefore of great interest to extend the HBM to handle several frequencies [58, 41, 42]. All the variations of the HBM proposed in the literature rely on a uniform time sampling of the longest period of interest (though the number of samples can differ). Ekici and Hall [41] mention the use of non-uniform sampling but do not develop it. However, when the fundamental frequencies involved are significantly different, uniform sampling leads to an unnecessary high number of time samples: given that the shortest period has to be discretised by at least three instants (Shannon [129] requires at least two instants per period to capture a frequency, but an odd number of samples is required for stability issues [137]), uniform sampling of the longest period requires a total number of samples that grows with the largest to the shortest period ratio. This can compromise the efficiency of the method, as too many time samples are computed.

This section is issued from [60]. After introducing the extension of the HBM to multiple frequencies, a new way to find the time samples is introduced and compared with another technique published in the literature. Finally, the validation status presented in [60] is summarised.

8.4.1 Multiple frequencies HBM equations

If the flow variables are composed of non-harmonically related frequencies (which means that the flow spectrum has high-energy discrete-frequency modes), the flow regime can be termed as almost-periodic [11]. Instead of a regular Fourier series, the U-RANS equations are projected on a set of complex exponentials with arbitrary angular frequencies ω_k. The conservative variables and the residuals are then approximated by

$$W(t) \approx \sum_{k=-N}^{N} \widehat{W}_k e^{i\omega_k t}, \quad R(t) \approx \sum_{k=-N}^{N} \widehat{R}_k e^{i\omega_k t}, \tag{8.20}$$

where $\widehat{W}_k$ and $\widehat{R}_k$ are the coefficients of the almost-periodic Fourier series for the frequency $f_k = \omega_k/2\pi$. Injecting this decomposition in Eq. 8.1 yields

$$\sum_{k=-N}^{N} \left(i\omega_k V \widehat{W}_k + \widehat{R}_k\right) e^{i\omega_k t} = 0. \tag{8.21}$$

Sampling in time onto a set of $2N+1$ time levels to solve Eq. 8.21, the following matrix formulation is obtained:

$$A^{-1} \cdot \left(iVP\widehat{W}^{\star} + \widehat{R}^{\star}\right) = 0, \tag{8.22}$$

where the almost-periodic inverse discrete Fourier transform (IDFT) matrix reads:

$$A^{-1} = \begin{bmatrix} exp(i\omega_{-N}t_0) & \cdots & exp(i\omega_0 t_0) & \cdots & exp(i\omega_N t_0) \\ \vdots & & \vdots & & \vdots \\ exp(i\omega_{-N}t_k) & \cdots & exp(i\omega_0 t_k) & \cdots & exp(i\omega_N t_k) \\ \vdots & & \vdots & & \vdots \\ exp(i\omega_{-N}t_{2N}) & \cdots & exp(i\omega_0 t_{2N}) & \cdots & exp(i\omega_N t_{2N}) \end{bmatrix}, \tag{8.23}$$

with $\omega_0 = 0$, $t_0 = 0$, $\omega_{-N} = -\omega_N$ and

$$\begin{aligned} P &= diag\left(-\omega_N, \dots, \omega_0, \dots, \omega_N\right), \\ \widehat{W}^{\star} &= \left[\widehat{W}_{-N}, \dots, \widehat{W}_0, \dots, \widehat{W}_N\right]^{\top}, \\ \widehat{R}^{\star} &= \left[\widehat{R}_{-N}, \dots, \widehat{R}_0, \dots, \widehat{R}_N\right]^{\top}. \end{aligned} \tag{8.24}$$

As opposed to the case of periodic flow, the arbitrary complex exponentials family does not form, *a priori*, an orthogonal basis.

Knowing a time sampling that allows A^{-1} to be invertible, the almost-periodic Fourier coefficients can be approximated thanks to

$$\begin{cases} \widehat{W}^{\star} = AW^{\star}, & \text{with } W^{\star} = \left[W\left(t_0\right), \dots, W\left(t_i\right), \dots, W\left(t_{2N}\right)\right]^{\top}, \\ \widehat{R}^{\star} = AR^{\star}, & \text{with } R^{\star} = \left[R\left(t_0\right), \dots, R\left(t_i\right), \dots, R\left(t_{2N}\right)\right]^{\top}. \end{cases} \tag{8.25}$$

Equation 8.22 thus becomes

$$iVA^{-1}PA + R^{\star} = VD_t[W^{\star}] + R^{\star} = 0, \tag{8.26}$$

where the multiple-frequency HBM time-derivative operator $D_t[.] = iA^{-1}PA$, the HBM source term, cannot be easily derived analytically, and has to be numerically computed. This must be a real matrix, however the authors were not able to prove it mathematically. Nonetheless, numerical experiments tends to confirm this assertion. Indeed, the magnitude of the ratio of the real part over the imaginary part is around 10^{15}. The remaining value of the imaginary numbers may then be attributed to rounding errors.

At this step of the derivation of the method, the time sampling $[t_0, \ldots, t_{2N}]$ remains to be specified. Kundert *et al.* [79] show that the condition number of A, and thus A^{-1}, has a salient role in the convergence of Harmonic Balance computations. The condition number of the almost-periodic DFT matrix A is defined as

$$\kappa(A) = \kappa(A^{-1}) = \|A\| \cdot \|A^{-1}\|, \quad \kappa(A) \geq 1, \tag{8.27}$$

where $\| \cdot \|$ denotes a matrix norm. Considering the resolution of $Ax = b$, if A is invertible and if δA, δx and δb are the numerical errors associated with the computation of A, x and b, respectively, then

$$(A + \delta A)(x + \delta x) = b + \delta b. \tag{8.28}$$

Therefore, the condition number sets an upper bound for the error made on x:

$$\frac{\|\delta x\|}{\|x\|} \leq \kappa(A) \left[\frac{\|\delta A\|}{\|A\|} + \frac{\|\delta b\|}{\|b\|} \right]. \tag{8.29}$$

The error on the iterative resolution of the U-RANS equations can therefore be amplified by the HBM source term. This amplification is led by the condition number of the almost-periodic DFT matrix. This also means that if the errors are small but the condition number is high, and vice-versa, the computation can diverge too. However, the errors cannot be *a priori* controlled, thus the need to minimise the condition number.

In the case of periodic-flows, the DFT matrix is well-conditioned: the uniform sampling for harmonically related frequencies leads to a condition number equal to 1, which is the theoretical lower bound for the condition number. This is linked to the orthogonality of the complex exponential family. On the other hand, when the frequencies are arbitrary, it is usually impossible to choose a uniform set of time instants over which the almost-periodic DFT matrix A is well conditioned. In fact, it is common for uniformly-sampled sinusoids at two or more frequencies to be nearly linearly dependent, which causes them not to be orthogonal, leading to the ill-conditioning encountered in practice. As the frequency set is chosen by the user, the only degrees of freedom left to get a well-conditioned matrix are the time levels.

8.4.2 APFT approach

Based on the work of Kundert *et al.* [79] in electronics, the APFT algorithm was implemented. The aim of the APFT algorithm is to maximise the orthogonality of the almost-periodic DFT matrix in order to minimise its condition number. It is based on the Gram-Schmidt orthogonalization procedure. First, the greatest period $1/\min_k(f_k)$ is oversampled with M equally-spaced time levels, $M \gg 2N + 1$ being specified by the user and N the number of frequencies. Considering these time levels, a rectangular almost-periodic IDFT matrix is built. Noting that every row of this matrix is a vector, a set of M vectors is obtained, numbered from 0 to $M - 1$, and of length $2N + 1$. The first vector V_0 (corresponding to $t = 0$) is arbitrarily chosen as the first time level and any component in the direction of V_0 is removed from the following vectors using the Gram-Schmidt formula:

$$V_s = V_s - \frac{V_0^\top \cdot V_s}{V_0^\top \cdot V_0} V_0, \quad s = 1, \cdots, M - 1. \tag{8.30}$$

The remaining vectors are now orthogonal to V_0. Since the vectors initially have the same Euclidean norm, the vector having the largest norm is the most orthogonal to V_0. It is assigned to V_1. The previous operations are then performed on the $M-2$ remaining vectors using V_1 as V_0. This process is repeated until the required $2N+1$ vectors are defined. As a time instant corresponds to a vector of the Gram-Schmidt decomposition, $2N+1$ time levels are obtained, which enables the construction of the almost-periodic DFT matrix.

As it will be highlighted, the APFT algorithm will improve the results but it cannot be applied to any choice of frequencies and a new algorithm was proposed. It is the mathematical key point in using a multi frequency HBM.

8.4.3 A new way to define time instants (OPT approach)

A more direct approach is to seek directly a set of time levels that minimise the condition number of the associated almost-periodic DFT matrix, instead of using orthogonality properties. This minimisation problem can be solved numerically by an optimisation algorithm. The limited memory optimisation method of Broyden-Fletcher-Goldfarb-Shannon (L-BFGS-B [16]) is used to look for a minimum of the condition number of the almost-periodic IDFT matrix $\kappa\left(A\left[\mathbb{T}\right]\right)$ as function of the time levels vector $\mathbb{T}$. This quasi-Newton algorithm approximates the inverse Hessian matrix $H(\kappa\left(A\left[\mathbb{T}\right]\right))^{-1}$ with the BFGS formula in order to decrease the objective $\kappa\left(A\left[\mathbb{T}\right]\right)$ in the direction $-H(\kappa\left(A\left[\mathbb{T}\right]\right))^{-1}\nabla\kappa\left(A\left[\mathbb{T}\right]\right)$. This descent direction is associated with the search for a zero of the gradient, which is a necessary condition for an extremum, in a second order Taylor series. Finally, a line search on α is performed to minimise $\kappa\left(A\left[\mathbb{T}-\alpha H(\kappa\left(A\left[\mathbb{T}\right]\right))^{-1}\nabla\kappa\left(A\left[\mathbb{T}\right]\right)\right]\right)$. In the present case, the derivative $\nabla\kappa\left(A\left[\mathbb{T}\right]\right)$ of the objective with respect to the time levels is approximated by first-order finite differences. An open-source implementation of this reference broadly-used algorithm is employed [148].

Gradient descent methods being local, the L-BFGS-B method converges to a local minimum of the condition number. This minimum is unsatisfying if the starting point $\mathbb{T}$ is not well chosen, therefore a strategy to find an appropriate one is required. As shown in the following study, APFT or uniform-sampling time levels do not always guarantee acceptable condition numbers, and so cannot be used to provide a starting point for L-BFGS-B. To this aim, the smallest frequency is uniformly sampled:

$$\Omega = [\frac{1}{M}\omega_{min}, \ldots, \frac{m+1}{M}\omega_{min}, \ldots, \omega_{min}], \tag{8.31}$$

where M denotes the desired number of initial guesses. This gives a set of periods. Each of them are evenly sampled to obtain a set of time levels.

$$\mathbb{T}_m = \left[0, \frac{2\pi M}{(2N+1)(m+1)\omega_{min}}, \ldots, \frac{2N\pi M}{(2N+1)(m+1)\omega_{min}}\right] \tag{8.32}$$

These time levels sets are then used as initial guesses for the L-BFGS-B algorithm. The almost-periodic IDFT matrix is built for each of these time levels and the corresponding condition numbers are computed. A large number M, typically thousands, of fractions of the greatest period gives a large set of potential time levels vectors. This is acceptable given the very low cost of the computation of the condition number on such small matrices of size $(2N+1) \times (2N+1)$. From this set, the time levels vector associated with the almost-periodic IDFT matrix having the smallest condition number is taken as a starting point. The optimisation algorithm actually achieves a local adjustment of the time levels.

In this way, the exploitation capability of the gradient-based optimiser is well combined with the exploration capacity of the sampling. This finally gives solutions that are always close to the ideal value of 1.

8.4.4 Comparison of several methods

Let us consider the case of two frequencies, f_1 and f. Without loss of generality it can be assumed that $f \leq f_1$. The dimensionless frequency δ_f^* is defined as:

$$\delta_f^* : \begin{cases} [0 : f_1] & \longmapsto [0 : 2] \\ f & \longmapsto 2 \cdot \dfrac{f_1 - f}{f_1 + f} \end{cases} \tag{8.33}$$

By taking f_1 constant, and having δ_f^* sampled between 0 and 2, the whole range of $f \leq f_1$ is explored. Moreover, as δ_f^* is anti-symmetric ($\delta_f^*(-f) = -\delta_f^*(f)$), and as the almost-periodic IDFT matrix is symmetric $A[-f] = A[f]$, the following relation is obtained for the condition number:

$$\kappa\left(A\left[\delta_f^*(-f)\right]\right) = \kappa\left(A\left[-\delta_f^*(f)\right]\right) = \kappa\left(A\left[\delta_f^*(f)\right]\right), \tag{8.34}$$

meaning that the case $f \geq f_1$ can be deduced in a straightforward way.

For each value of δ_f^*, the condition number of the almost-periodic IDFT matrix $\kappa(A)$ is computed, highlighting the ability of the different algorithms to choose the time levels that minimise the condition number, for any input frequencies. This assessment is only valid for two frequencies, but the tendency is similar when increasing the number of frequencies. Two frequencies are involved thus five time levels are required. The results of three algorithms are depicted Fig. 8.4: (i) APFT: the Almost Periodic Fourier Transform algorithm, (ii) OPT: the gradient-based optimisation algorithm and (iii) EQUI: evenly spaced time levels oversampling the largest period as done in Gopinath *et al.* [58] using $2N+1$ time levels and in Ekici and Hall [41, 42] using $3N+1$ time levels.

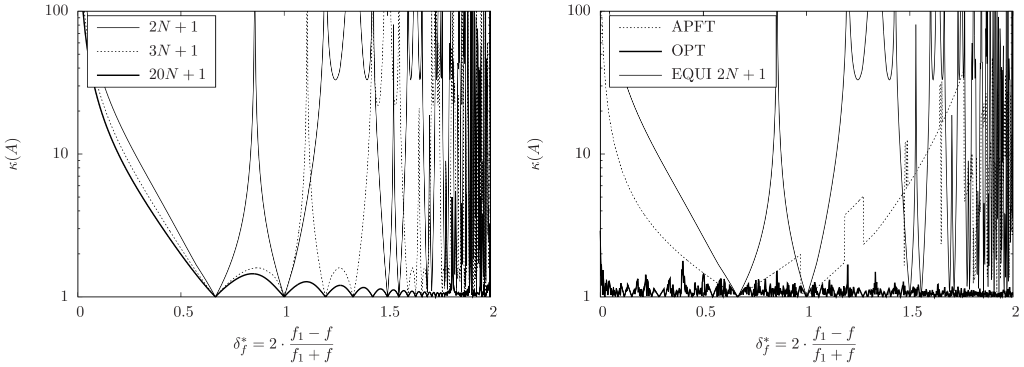

(a) Evenly-spaced time levels algorithms (b) Proposed algorithms

Figure 8.4: *Comparison of the presented algorithms.*

The EQUI algorithms give fair results ($\kappa(A) \leq 2$) only at discrete points, corresponding to the particular cases where f is a multiple of f_1, which are thus similar to the single-frequency case. Oversampling improves the results. In fact, the mean condition number obtained with $20N+1$ time levels indicates that the higher the number of time levels the better the condition number. However the almost-periodic DFT matrix becomes rectangular and the memory cost of such a computation increases drastically, preventing the use of such an approach on industrial cases. The APFT algorithm improves the results, as it gives results with $\kappa(A)$ close to unity for $0.3 \leq \delta_f^* \leq 1.2$. However, when δ_f^* tends to the boundaries (0 and 2), the condition number seems to go to infinity. This corresponds to special values of f:

$$\begin{aligned} &\delta_f^* = 0 \iff f = f_1, \\ &\delta_f^* = 2 \iff f = 0. \end{aligned} \tag{8.35}$$

This means that the APFT algorithm fails to work when the frequencies are too close to one another, and when they are significantly different. This limits the method for a range of frequencies where the HBM could give a salient gain in CPU time. Finally, the OPT algorithm gives a condition number close to unity for any value of δ_f^*. The OPT algorithm thus ensures that the convergence of the HBM is not sensitive to the specified set of frequencies. Table 8.4 summarises the results obtained with each algorithm.

	EQUI			APFT	OPT
# instants	$2N+1$	$3N+1$	$20N+1$	$2N+1$	$2N+1$
min $(\kappa\,[A])$	1.002	1.0	1.0	1.001	1.000
max $(\kappa\,[A])$	$3.024 \cdot 10^{14}$	$1.871 \cdot 10^{11}$	2732.6	823.8	2.905
mean $(\kappa\,[A])$	$3.081 \cdot 10^{11}$	$1.871 \cdot 10^{8}$	10.92	7.742	1.097

Table 8.4: *Global results for the presented algorithms.*

Thus the proposed non-uniform time sampling combined with the OPT algorithm allows to tackle problems with large frequency separation. In such cases, the gain of the HBM compared to classic time-marching methods is expected to be significant: with a time-marching scheme, the time-step has to be small enough to discretise the shortest period, while the number of time steps of the simulation has to be large enough to reach the (almost-)periodic state (*i.e.* the simulation time is equal to several times the longest period). Conversely, the cost of the HBM only depends on the number of frequencies to capture, regardless of their relative values.

8.4.5 Numerical assessments

It is shown in [60] that the OPT algorithm is the only way to be able to perform a simulation using the HBM in an industrial context because it is the method that provides a low condition number for any set of frequencies. This point is first demonstrated on an academic test case on a channel configuration of $L_X = 100m$, with an injection condition at inflow and a fluctuating pressure imposed at the outlet:

$$P_{outlet}(t) = P_m\{1 + A_1 \sin(2\pi f_1 t) + A_2 \sin(2\pi f_2 t)\},$$

where P_m is the temporal average static pressure and A_n represents the amplitude of the $n-th$ mode at its frequency f_n. This configuration is fully turbulent and $Re \simeq 1 \times 10^9$. As a consequence, URANS equations are analysed.

Then, the OPT algorithm is applied to a true turbomachinery application issued from the three first rows of the axial compressor CREATE [59]. The mid-span slice of the inlet guide vane and the first stage of the compressor is considered. Numerical simulations show the great importance of the choice of BPFs to account for during the computation. A focus is also put on the necessary achievement of several frequency harmonics to make the wake go across the interface between rows.

Finally, after the physical flow analysis, the last point of importance concerns the CPU ratio between a classic time marching procedure and the HBM. It is shown that a gain between 2 and 5 is attained on the considered configuration. Such a gain proves the potential of such a technique and improves the results previously published in the literature.

8.5 Conclusions

This chapter is dedicated to the adaptation of the time integration to periodic and almost-periodic simulations by the introduction of the Harmonic Balance Method.

When unsteadiness is driven by one frequency and its harmonics, the Harmonic Balance Method is a reduced model of the full URANS equations that only takes into account the first harmonics of the mean unsteadiness. The principle of HBM is to look for a solution projected on a reduced set of harmonically-related frequencies. In the past, all computations using HBM were performed using an explicit time integration procedure, with many constraints on the time step due to the number of hamonics N to account for, or to a large mean frequency (through the term in $\omega = 2\pi f$).

Our work consisted in proposing and validating a new way to handle implicit computations in order to overcome the high sensitivity to the time step. Among the proposed techniques, we considered two approaches that improve convergence but also avoid many of the numerical drawbacks associated with a full implicit formulation. Our work is the key point for future industrial applications and an interesting CPU gain was demonstrated.

The Harmonic Balance Method with several independent frequencies is the last improvement. Even if the theoretical basics of the method were already published, our work consisted in defining and validating a new algorithm to define the time sampling. We showed that this choice drove the computation (convergence or not), even for very simple test-cases. Combined with an adaptation of our implicit treatment, the efficiency of the HBM on a configuration representative of industrial demands was underlined. The approach is currently available in *elsA* and it will be delivered soon to industries. The results obtained in this chapter show the different steps encountered to transform a new method defined in academy into a predictive tool of interest for industry.

Chapter 9

New diffusion schemes for unstructured grids composed of several element shapes

9.1 Introduction

Unstructured tetrahedral meshes have become widespread in use for low and medium Reynolds number flow computations as complex geometries can be meshed with little effort. Industrial computations however involve high Reynolds number flows with strong shear layers which are best captured on regular and aligned meshes. These meshes contain hexahedral or prismatic elements in the boundary layer in order to increase accuracy in the presence of strong gradients normal to the wall. Hence a versatile CFD discretisation needs to be able to perform well on meshes composed of triangles and quadrilaterals in two dimensions, and tetrahedra, pyramids, prisms and hexahedra in three dimensions.

While irregular meshes can be avoided by switching away from tetrahedra, a discretisation should be able to cope with skewed but regular meshes as often encountered, e.g. along curved boundaries or in turbomachinery simulations. Hence accuracy should be maintained on parallelograms. High Reynolds number flows involve thin boundary layers which may require element aspect ratios in excess of 1000 for an efficient resolution and a discretisation has to be able to cope with that. The emerging unstructured quadrilateral and hexahedral mesh generation algorithms often produce meshes with irregular cells when coping with a complex geometry. Hence a desirable aspect of the discretisation is to maintain accuracy on irregular quadrilaterals and hexahedra. In this context, there are two ways to analyse the problem and to treat it, depending on the mathematical formulation. In the following, the extension is analysed following a cell-vertex approach with data stored at mesh nodes, or a cell-centred formulation with data stored at cell centre.

In the first part of this chapter, we consider a cell vertex finite volume discretisation. In this case, the treatment of convection flux on hybrid grids is straightforward [10] but the discretisation of the diffusive fluxes is more difficult. We recall that the classic approach follows the $\mathcal{P}^1$ finite element discretisation, with a constant gradient on triangles or tetrahedra. Such a finite element approach cannot be directly extended to handle other element shapes. In [115], we analysed diffusion schemes, proposed new schemes and we showed the superior efficiency of our approach.

In the second part of this chapter, we introduce a new diffusion scheme with a compact support for use in a cell-centred finite volume context. We perform a quick review of classic diffusion schemes for unstructured grids composed of several element shapes in the context of finite volume approach and justify our new scheme. This work has never been published in the past and we are currently writing a paper.

9.2 A new diffusion scheme in the cell-vertex formalism

Let $\{\tau_i,\ i = 1, N_\tau\}$ denote the N_τ elements of the mesh. These elements are triangles and quadrilaterals in two dimensions or tetrahedra, prisms, pyramids and hexahedra in three dimensions. From now on, this mesh will be called the "primal" mesh and its elements will be denoted as the "primitive" elements. In the vertex-centred finite-volume approach considered here, the flux balance is evaluated on a dual mesh composed of cells C_i around mesh nodes i.

9.2.1 Definition of dual cells for a hybrid mesh

The well-known extension of the definition of the median dual volume from simplex to primitive elements introduced by Dervieux [35] for the Euler equations and by Rostand and Stoufflet [123] for the Navier-Stokes equations is adopted here (Fig. 9.1). Hence, in two dimensions, the volume C_i around mesh node i is limited by "facets" linking the midpoints of the edges in the primal mesh to the barycentres of the elements obtained by arithmetic averaging of the nodal coordinates. In three dimensions, the dual volume C_i is delimited by triangular facets between the edge midpoints, the face barycentres and the element barycentres.

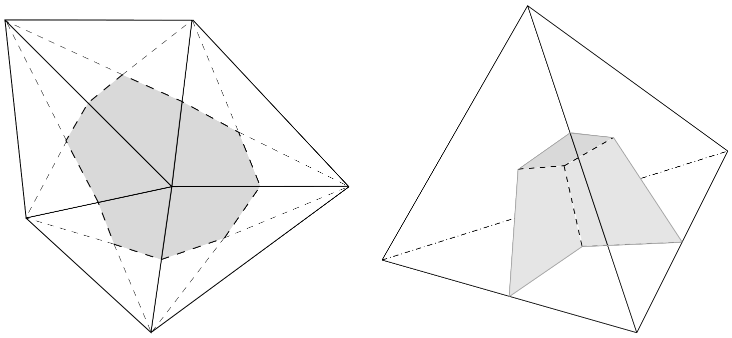

Figure 9.1: *Definition of the dual volume on a triangular mesh (left) and boundary of the dual volume inside a tetrahedron (right).*

On triangular and tetrahedral meshes, the standard $\mathcal{P}^1$ finite-element discretisation induces a constant gradient over the element and a conservative scheme is built with a "good" choice for diffusion coefficients. On the set of primitive mesh elements $E(i)$ containing node i, the diffusive term of $D(W, \nabla W)$ can be written as

$$\int_{\partial C_i} D(W, \nabla W) \cdot \vec{n} ds = \sum_{T \in E(i)} \int_{\partial C_i \cap T} D(W, \nabla W) \cdot \vec{n} ds\,, \tag{9.1}$$

where T is a triangle based on node i. The total flux integral is therefore decomposed into the sum of integrals defined on a simplex element. In this case, the $\mathcal{P}^1$ finite element approach leads to a constant gradient on any simplex mesh element and for a diffusion term D which depends linearly of ∇W, the gradient can be factored out of the integral over $\partial C_i \cap T$. Billey *et al.*

[14] demonstrated the equivalence of piecewise-constant finite-volume and $\mathcal{P}^1$-Galerkin finite-element discretisation on a simplex mesh composed of triangles. Barth [10] gave a simple edge-based expression for the right hand side of Eq. 9.1. However, the equivalence of these finite-volume and finite-element discretisations does not extend to non-simplex primitive elements. There is a range of possible discretisations for the viscous operator on hybrid grids with very distinct properties.

9.2.2 Two new schemes based on a Finite-element reconstruction approach

Many schemes published in the literature were implemented and analysed in [115]. For the sake of clarity, after introducing two classic approaches, our new diffusion schemes based on Finite Element are introduced.

The Edge-Based (EB) approach needs to define a gradient at vertex i by a Green-Gauss formula applied on the dual cell C_i [50]. The mid-edge value is defined as an average of both edge node quantities, assuming a linear variation along the edge. Then, the interface gradient is defined as the mean value of the gradients at its nodes and Crumpton's correction [31] improves the stability. It leads to:

$$\nabla T_{ij}^{corr} = \nabla T_{ij} - \left(\nabla T_{ij} \cdot \vec{\delta}_{ij} - \frac{T_j - T_i}{\|x_j - x_i\|} \right) \vec{\delta}_{ij} \,, \tag{9.2}$$

where x_i and x_j are coordinates of node i and j, $\vec{\delta}_{ij}$ is the unit vector in the direction from node i to node j and $\nabla T_{ij} = 0.5 \left(\nabla T_i + \nabla T_j \right)$ is the averaged interface gradient.

A cell-vertex (CV) approach was proposed by Crumpton *et al.* [30]. It consists in applying the Green-Gauss theorem to define a constant gradient for each primal mesh element. This formulation is easy to implement and it is interesting because the cell gradient is also required for the computation of convective terms in cell-vertex methods [128], resulting in computational savings. Truncation error analysis shows that the numerical scheme is second-order accurate and consistent on meshes composed of parallelograms [5]. On meshes composed of other types of elements, consistence was not demonstrated. However, the stability analysis reveals that the discretisation is not monotone and oscillatory solutions can develop. To avoid these spurious chequer-board modes, a correction similar to the one for the edge-based method (Eq. 9.2) is added to the gradient expression:

$$\nabla T_i^{\tau} = \nabla T^{\tau} - \delta_c \left(\nabla T^{\tau} \cdot \vec{\delta s}_i - \frac{(T^{\tau} - T_i)}{\|x^{\tau} - x_i\|} \right) . \vec{\delta s}_i . \tag{9.3}$$

∇T^{τ} is the gradient following the cell-vertex approach, δ_c is a modelling parameter, T^{τ} is the mean value of T on τ, x^{τ} the centroid coordinates and $\vec{\delta s}_i$ is defined by:

$$\vec{\delta s}_i = \frac{x^{\tau} - x_i}{\|x^{\tau} - x_i\|} . \tag{9.4}$$

This correction introduces a modification of the gradient in the direction of the "diagonal" of the element and this correction makes the formulation non-conservative. A theoretical analysis that takes into account this correction (Eq. 9.3) shows that the scheme is consistent on regular rectangular meshes only and that the discretisation is monotonic if the value for δ_c is chosen in an interval which depends on the mesh geometry [5].

Finally, the last class of approach follows a Finite-Element reconstruction. The $\mathcal{P}^1$ finite-element method can be extended to primitive elements: the idea is to reconstruct the gradient using the finite-element basis functions of the specific element class. One of the advantages of this approach is that the method reverts to the $\mathcal{P}^1$ formulation on simplex elements, which is widely used. The gradient at any point (x, y) of an element τ can be evaluated with the finite-element approach:

$$\nabla T(x, y) = \sum_{k \in S^\tau} T_k \nabla N_k^\tau(x, y), \tag{9.5}$$

where (x, y) are the coordinates of a point which belongs to element τ of the primal mesh. N_k^τ denotes the shape function of element τ associated with node k and S^τ is the set of nodes of τ. The gradient computation is therefore transferred to the evaluation of the shape function gradients. The computation of the shape function gradient is based on the transformation to iso-parametric coordinates. All details are in [115]. This discretisation is consistent on meshes composed of regular parallelograms [5]. The truncation error remains of order $O(h^2)$ on all other kinds of elements. On regular parallelograms, the scheme is monotonic if the elements are not too sheared and have a low aspect-ratio: the ratio between the element length and width must be lower than $\sqrt{3}$ and the minimum angle in the parallelogram ζ must satisfy $0 \leq \cos(\zeta) \leq 0.5$. This point is clearly a drawback for using this finite-element discretisation for high Reynolds number boundary layers where the element aspect ratio can exceed 10^4. Moreover, for a hexahedron the computation of the diffusive flux on $\partial C_A \cap \tau$ requires the inversion of seven 3×3 Jacobian matrices. The numerical cost is therefore too large for practical applications. This approach is called EXFE ("EXact Finite-Element") approach in the following.

Keeping in mind that it is the local and accurate evaluation of the gradient at the interface which bestows the good numerical properties to the EXFE method, we proposed an alternative. Let us propose to evaluate nodal gradients in each element on a "third element" formed from the edges joined at that node (Fig. 9.2). In the case of simplex elements this recovers the $\mathcal{P}^1$ gradients of the EXFE formulation. In the case of primitive elements except one case, this

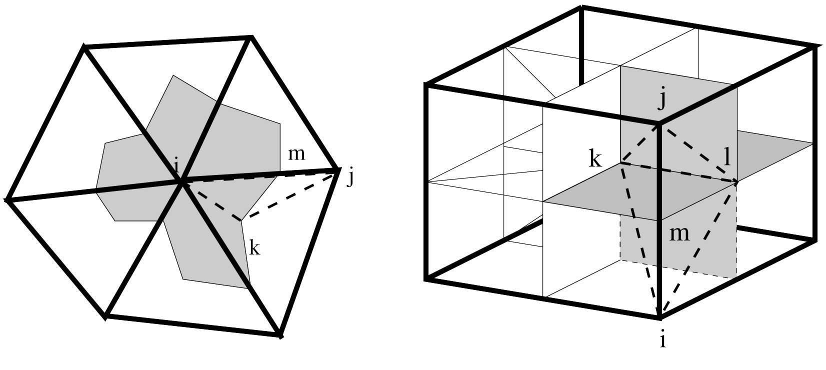

Figure 9.2: *Left hand side: triangle ijk is used for the computation of the flux on dual cell facet mk. Right hand side: tetrahedron ijkl is needed for the computation of the gradient for flux balance on facet klm.*

results in the third element being a simplex of all edges joining at that node. The exception case is the apex node of a pyramid where four edges join: in this case Green-Gauss integration over the pyramid seems appropriate. This method is called “APproximated Finite-Element” method (APFE). As an example, the gradient computation for node A for the two-dimensional quadrilateral in Fig. 9.3 would be based on the triangle ABD and equivalently for the other nodes.

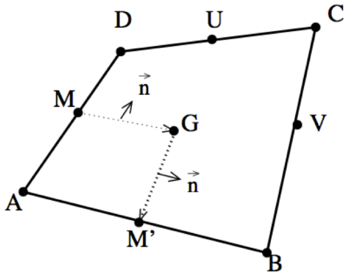

Figure 9.3: *Quadrangle $ABCD$ and notations for the diffusion flux computation.*

For node A, the diffusion flux I is then computed on facet MG (respectively GM') using the mean of gradients in A and D (in A and B respectively). A Taylor analysis shows that this scheme is conservative, and consistent on meshes composed of regular parallelograms. The truncation error remains of order $O(h^2)$ on all other kinds of elements, as for the EXFE method. On the other hand, the discretisation is monotonic on rectangles whatever their aspect-ratio.

9.2.3 Validation and conclusions

All details regarding order of accuracy and schemes capability in recovering linear solution are not recalled here, they are all defined in [115].

For the linear heat equation, it was found that the cell-vertex approach is second order accurate on smooth meshes composed of quadrilaterals and the lack of conservation is the main drawback of the method. The Edge-Based method is very sensitive to grid irregularity. This may be a disadvantage on meshes from unstructured quadrilateral/hexahedral mesh generators with irregular elements and meshes produced with prismatic layers at the boundary extruded from surface triangulations. The method will perform well on regular structured grids which are aligned with the shear layers. The best methods for the heat equation are the finite element-based EXFE and APFE methods. The APFE method appears most suitable as it is only moderately less accurate on distorted quadrilaterals than EXFE method, but maintains full accuracy on high aspect-ratio elements. Both the EXFE and APFE methods are linear preserving on perturbed meshes where the EB method incurs a loss of accuracy.

For the solution of Navier-Stokes equations (laminar or RANS form of equations), it was shown that both APFE and EB schemes perform equivalently well on meshes for which shear layer and grids are strongly aligned. But EB method cannot be expected to work similarly well for detached shear layers which are oblique to the grid.

9.3 A new diffusion scheme for unstructured multi element shape grids

9.3.1 Introduction

In the last section, new schemes based on a $\mathcal{P}^1$ Finite Element approach were proposed, analysed and validated against schemes published in the literature. The goal was to start from the $\mathcal{P}^1$ Finite Element on simplex elements and to extend this approach to meshes composed of classic element shapes (prisms, pyramids and hexahedra). The extension had therefore to be able to deal with directional properties of both grid and solution, especially in the boundary layer.

In this section, the point of view follows another direction. We begin with a cell-centred structured solver like *elsA* and we want to increase its capability in order to cope with unstructured grids. In fact, even if an advanced numerical technique such as chimera grid is implemented and validated, this approach presents some drawbacks. First, chimera grids need data exchange between grid overlapping regions and an interpolation is considered. By nature, chimera grid technique is not conservative. This is a bottleneck in turbomachinery applications for which conservation is a key point. Moreover, chimera grid keeps a large time devoted to mesh generation, in particular for complex geometries: even if the goal is to split the whole geometry in many specific (and small) subparts meshed easily, the time devoted to the meshing process of all parts can be quite long and we have to take care of overlapping regions to exchange information between grids. Unstructured grids composed of tetrahedra, prisms, pyramids and hexahedra are meshed easily on complex geometries, even with regular computers. But the price to pay lies on numerical efficiency. Unstructured grids need unstructured algorithms and the time spent in the use of connectivity tables makes this solution less efficient than with structured grids. So, there is a need to couple structured and unstructured capability inside a mesh. Structured grids give the possibility 1. to align flow physics and mesh lines in regions where the mesh generation is simple and 2. to keep numerical efficiency while unstructured capability enables to mesh complex geometries easily. At the present time, no mesh generation software is able to handle structured and unstructured blocks at the same time and we propose to couple both approaches following a “block interface with mismatched nodes” paradigm. The goal is to introduce new surfaces to separate structured and unstructured discretisations and to authorise two different interface discretisations, one on each side of the interface. In this case, data exchange at the interface is conservative if the interface is planar.

In this context, we started an analysis of diffusion schemes on multi element shape elements, considering first the techniques published in the literature. We found that the best approach needs dedicated data exchange that can be not efficient on massively parallel computations as for Large Eddy Simulations. This section is divided into three parts. First, we begin by introducing the cell-centred Finite Volume paradigm. Then, several classic diffusion schemes are introduced and compared. Finally, before concluding, our new scheme is presented.

We assume in this section that the mesh is composed of N elements denoted $(C_i)_{1\leq i\leq N}$ and ∂C_i denotes the boundary of C_i. The principle of the cell-centred Finite Volume approach is to integrate all equations on any control volume C_i. Using the Green relation, integrals involving a divergence are transformed into a surface integral. As before (Eq. 9.1), the flux balance leads to the following integral:

$$\int_{\partial C_i} D(W, \nabla W) \cdot \vec{n} ds. \tag{9.6}$$

Compared with the cell-vertex approach, the main differences occur first on the surface chosen for integration and then on the term itself to integrate. In the cell-vertex approach with $\mathcal{P}^1$ Finite Element approach, gradients are generally based on nodal quantities while averaged quantities are now considered. The key point is therefore the definition of W and ∇W on the cell boundary using mean quantities over control volumes.

9.3.2 Classic approaches

For the sake of clarity, we recall classic diffusion schemes, explaining their advantages and drawbacks. A good overview of gradient reconstruction can be found in [70].

The "5p" scheme

This is the simplest diffusion scheme to implement. Its name follows *elsA* terminology, issued from a structured grid: the gradient in a quadrangle depends on the cell itself and on its four direct neighbours. This scheme is also called Green-Gauss scheme in the literature. The principle is to define first a cell-centred gradient using Green theorem:

$$\int_{C_i} \nabla W dv = \int_{\partial C_i} W \vec{n} ds,$$

where $\vec{n}$ is the unit vector normal to the boundary and directed outwards. Introducing the mean gradient $\overline{\nabla W}_{C_i}$, the discrete version is:

$$\|C_i\| \overline{\nabla W}_{C_i} = \sum_{f \in faces} W_f \vec{n} S_f,$$

where $\|C_i\|$ is the volume of C_i, f refers to a face of ∂C_i, W_f is the interface value of W and S_f is the surface area. Since geometrical quantities are easily computed, the remaining unknown is the value of W at each interface. Here, a pure centred paradigm leads to an interface value obtained as the mean of left and right quantities.

Once the cell-centred gradient is known, a new gradient on the mesh faces has to be built to close surface integrals. Here, a pure centred formalism is chosen and if Σ is a mesh face between volumes L and R, we have:

$$\nabla W_\Sigma = \frac{\overline{\nabla W}_L + \overline{\nabla W}_R}{2}. \tag{9.7}$$

The 5p scheme is very easy to implement but it can be seen as the use of two centred differences. It is easy to show that the 5p scheme leads to a decoupling. For a cell C_i, the averaged diffusion flux does not depend on the direct neighbouring cells of C_i, but on the cells sharing a face with the direct neighbouring cells of C_i. As any centred scheme, high frequency of the discretisation are not damped and it can be shown that such a discretisation induces oscillations.

Edge-based scheme

A way to circumvent 5p scheme oscillations is to reintroduce the coupling between a cell and its direct neighbours. The easiest way to do so is to introduce a new interface gradient using an edge-based approach. The new interface gradient is a corrected version of the 5p interface gradient (Eq. 9.7) :

$$\overline{\nabla W_\Sigma} = \nabla W_\Sigma - \Big(\nabla W_\Sigma \cdot \overrightarrow{C_L C_R} - (W_R - W_L)\Big) \frac{\overrightarrow{C_L C_R}}{\|\overrightarrow{C_L C_R}\|^2}, \tag{9.8}$$

where C_L (respectively C_R) is the left (resp. right) cell centre coordinates. The goal is therefore to remove the gradient in the direction of the cell centres and to replace this contribution by a pure centred approach (as for finite differences). This scheme is considered in FloXX [92].

Least-Square method

The last class of classic diffusion schemes follows the gradient computation based on Least-Square (LS) approximation. These LS gradients are also encountered for the MUSCL extrapolation (second order accurate convection scheme). We only summarise here the main steps to define the diffusion scheme.

The first step consists in assuming a polynomial reconstruction of data in a region around the cell C_i:

$$\begin{aligned} W_i^R(x - x_i, y - y_i, z - z_i) \;&=\; \overline{W}_i + \left.\frac{\partial W}{\partial x}\right|_i (x - x_i) + \left.\frac{\partial W}{\partial y}\right|_i (y - y_i) + \left.\frac{\partial W}{\partial z}\right|_i (z - z_i) + \\ & \left.\frac{\partial^2 W}{\partial x^2}\right|_i \frac{(x - x_i)^2}{2} + \left.\frac{\partial^2 W}{\partial x \partial y}\right|_i (x - x_i)(y - y_i) + \cdots \end{aligned} \tag{9.9}$$

where (x_i, y_i, z_i) represents the cell centroid coordinates, $\overline{W}_i$ is the mean of W inside C_i (in the sense of the finite volume approach) and the upper script R means “reconstructed”. Now, let $\|C_j\|$ denote the volume of cell C_j, it is clear, using Eq. 9.9 that:

$$\begin{aligned} \textstyle\int_{C_j} W_i^R dv \;&=\; \|C_j\|\overline{W}_i + \left.\frac{\partial W}{\partial x}\right|_i \int_{C_j} (x - x_i) dv + \\ & \left.\frac{\partial W}{\partial y}\right|_i \int_{C_j} (y - y_i) dv + \left.\frac{\partial W}{\partial z}\right|_i \int_{C_j} (z - z_i) dv + \\ & \left.\frac{\partial^2 W}{\partial x^2}\right|_i \int_{C_j} \frac{(x - x_i)^2}{2} dv + \left.\frac{\partial^2 W}{\partial x \partial y}\right|_i \int_{C_j} (x - x_i)(y - y_i) dv + \cdots \end{aligned} \tag{9.10}$$

If we only consider a second order approximation (terms in second order derivative are dropped away), Eq. 9.10 can be cast into a linear system of equations and the unknowns are the gradient values. For any kind of cell with more than 3 faces, there are more equations than unknowns and the system is solved in the least-square paradigm.

Remark 9.3.1 *The LS approach needs the computation of integrals in a pre-processing step. These integrals are kept constant if the mesh is fixed.*

Diamond-cell approach

The principle of Diamond-Cell (DC) techniques is to define a dedicated volume around a mesh interface and to compute a gradient inside this volume. This gradient is then assumed to be the interface gradient. The dual volume is always based on face nodes and the left and right cell centres. A reconstruction of the fields is mandatory at the mesh nodes. Several techniques can be considered, from a least-square reconstruction to simple averaging procedure, using the cell centres nearest to the considered node. Even if formally these approaches are interesting, the bad point concerns the definition of the field at the mesh nodes. In practice, this definition can be difficult, especially in a parallel environment for which dedicated extra communications are needed in a finite volume solver that follows a face-based formalism.

Our new unstructured interface gradient computation

The goal of our Unstructured Interface Gradient (UIG) technique is to define an interface gradient using only information available in a cell centred finite volume discretisation and in a face-based approximation. Our idea is to blend the efficiency and the simplicity of the 5p computation and the principle of a dual volume around a face. For the sake of clarity, all explanations are given in two dimensions.

As suggested in Fig. 9.4, we define the dual volume using cell centroid and face centres in two dimensions. In three dimensions, the dual volume is limited by cell centres, face centres and edge mid points. In many aspects, this kind of dual volume is inspired by the dual volume of the finite element approach discussed in Sec. 9.2.

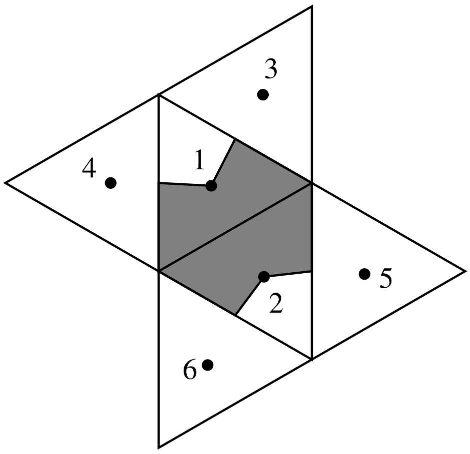

Figure 9.4: Definition of the dual volume around a face

In the following, we assume that the gradient on the interface is equal to the mean gradient on the dual volume C^*.

$$\nabla W_{face} \approx \nabla W_{C^*} = \frac{1}{\|C^*\|} \int_{C^*} \nabla W dv \,, \tag{9.11}$$

with $\|C^*\|$ volume of the dual cell C^*. The gradient is calculated by circulation around the dual cell:

$$\frac{1}{\|C^*\|}\int_{C^*}\nabla W dv = \frac{1}{\|C^*\|}\sum_{\text{facets of } C^*}\int_{facet} W.\vec{n}ds\,, \tag{9.12}$$

where $\vec{n}$ stands for the outward local normal on the facet of the dual cell C^*.

The last question concerns the definition of the interface quantity. We follow here the 5p approach: for a facet issued from a real mesh face, the interface quantity is the average of left and right mean quantities and for the other facets, the values at the cell centres are considered. Let us take an example; for the two dimension dual volume in Fig. 9.4, the interface gradient is:

$$\begin{aligned}\nabla W_{\partial C} = & W_1.S_1\vec{n_1} + W_2.S_2\vec{n_2} + \\ & \frac{(W_1+W_3)}{2}\frac{S_{13}}{2}\vec{n_{13}} + \frac{(W_1+W_4)}{2}\frac{S_{14}}{2}\vec{n_{14}} + \\ & \frac{(W_2+W_5)}{2}\frac{S_{25}}{2}\vec{n_{25}} + \frac{(W_2+W_6)}{2}\frac{S_{26}}{2}\vec{n_{26}}.\end{aligned} \tag{9.13}$$

$S_1\vec{n_1}$ and $S_2\vec{n_2}$ represent the integral of the normal vector on all facets in volumes 1 and 2 respectively. S_{ij} is the surface area of the dual volume between cells i and j, with n_{ij} the corresponding unit outward vector (from cell i to cell j).

Conclusions

An accuracy analysis shows that the UIG scheme is second order accurate in 1D and it is stable in 1D and 2D. Moreover, numerical results for the linear heat equation showed that:

1. The 5p scheme has the poorest properties. It is generally first order accurate only.
2. The Edge-Based scheme has similar properties as the 5p scheme but results are more accurate on meshes composed of squared elements. This is due to the correction that performs well if the gradient is aligned with the mesh.
3. Diamond Cell approaches are accurate on regular meshes but the definition of quantities at mesh nodes is a drawback, especially for High performance Computing needed for LES.
4. Least-Square technique enables to attain nearly a second order of accuracy on irregular meshes but their accuracy is quite limited on regular meshes. This is certainly due to the high difficulty in choosing a directional approach on regular squares or equilateral triangles.
5. The new UIG scheme has better properties than 5p and Edge-Based schemes. It presents the same accuracy as the LS technique on regular meshes but it is less accurate on irregular meshes. Of course, irregular meshes are not considered in LES computations and to our point of view, the UIG scheme is a really good candidate.

All methods have been implemented and tested for the linear heat equation and the Navier-Stokes equations. As an example, consider the laminar flat plate test case. A $Ma = 0.8$ flow at $Re/L = 30000m^{-1}$ is computed over a one-meter adiabatic flat plate. The goal is to compare the friction coefficient obtained with the LS, 5p and UIG schemes. The evolution of the friction coefficient along the flat plate is shown in Fig. 9.5 and the curved named “Blasius” refers to the theoretical law of the friction coefficient on a laminar flat plate [29]:

$$C_f \simeq \frac{0.664}{\sqrt{Re_x}},$$

where Re_x stands for the local Reynolds along the flat plate.

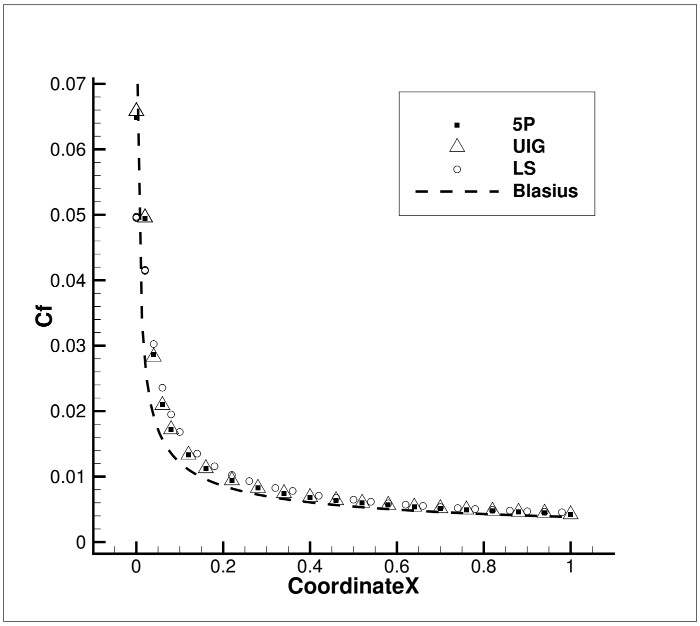

Figure 9.5: *Friction coefficient along a laminar flat plate for the LS, 5p and UIG schemes. Comparison with the theoretical law of the friction coefficient.*

Remark 9.3.2 *We are currently improving a paper on UIG scheme and we plan to submit it soon to a refereed journal: P. Cayot and G. Puigt, Analysis of a new finite volume scheme for diffusion flux on unstructured grids.*

9.4 Conclusions

Diffusion phenomena have regularising effects on the flow and people generally assume that defining an accurate operator is not a very difficult task. Our experience shows that even if defining a diffusion scheme is quite easy, some properties remain difficult to guarantee.

Two new schemes were proposed in the context of cell-vertex discretisation and finite element paradigm. The simplest version of the diffusion scheme attains the best numerical properties. It was therefore chosen for implementation in the industrial CFD code N3S-Natur.

Regarding the cell-centred finite volume approach, the classic diffusion schemes are not well adapted for modelling diffusion phenomena accurately or for an efficient parallel implementation. We introduced a new scheme based on a dual cell approach that was cheap to implement and attained second order of accuracy on the elements of interest for Large Eddy Simulation.

Chapter 10

Numerical effects of block interface with mismatched nodes on unsteady simulations

10.1 Introduction

Industrial flows are defined at large Reynolds number, where turbulence must be accounted for. In order to capture accurately turbulence effects, the tendency was to consider structured meshes in order to align mesh lines with the flow anisotropy, especially in the boundary layer. With such an approach, numerical computations showed that the numerical error was minimal and the global solution accuracy was high. After thousands of computations, industry was able to propose best practices in order to attain the best accuracy possible but at a moderate computational cost. In other words, the solvers were very accurate once the mesh followed some rules. The key point regarding computations was therefore the definition of the mesh. Structured solvers are numerically very efficient since data are easily accessed. However, the structured mesh generation is still a bottleneck. A structured mesh is built by dividing the domain of interest in several hexahedral blocks (this is called a topology) in which cells are referred by a triplet (i, j, k), following the three directions defining the hexahedral block. One of the most famous mesh tool is called ICEM-CFD and it is nowadays distributed by Ansys. Initially, even if the mesh decomposition may need several days or weeks, the fact that the geometry was more or less the same (cruise version of an aircraft...) helped industries to define best practices for a topology and then to discretise the domain from this topology. For parametric studies, the global cost was acceptable as the time spent for the computations is some order of magnitude larger than the time needed to generate the mesh.

Nowadays, cruise condition computations are efficiently managed by industry, and the tendency is to go further in the aggressive design. For an aircraft, it means that the geometrical complexity is so large that industry is not able to afford the expense and several works began in order to simplify the mesh generation process.

Among the methods, the Chimera technique consists in splitting the global geometry in several basic parts and for any basic part, it is obvious to define a basic topology. Finally, all basic parts are meshed independently and the key point is to group these meshes inside a single computational domain. At this level, the principle is to define overlapping regions between all basic meshes. Another point of importance concerns the cell blanking: some cells for a given part may be located inside the true geometry and must not be computed. Data exchange between zones is performed by a simple interpolation based on geometrical rules. Of course, it is not easy to keep conservation during interpolation, even if this is a key point. A toy mesh example is proposed in Fig. 10.1: it consists in the two-dimensional mesh around two cylinders. Both cylinders are meshed independently and then glued. Finally, a background mesh is necessary to account for the true dimensions of the desired computational domain.

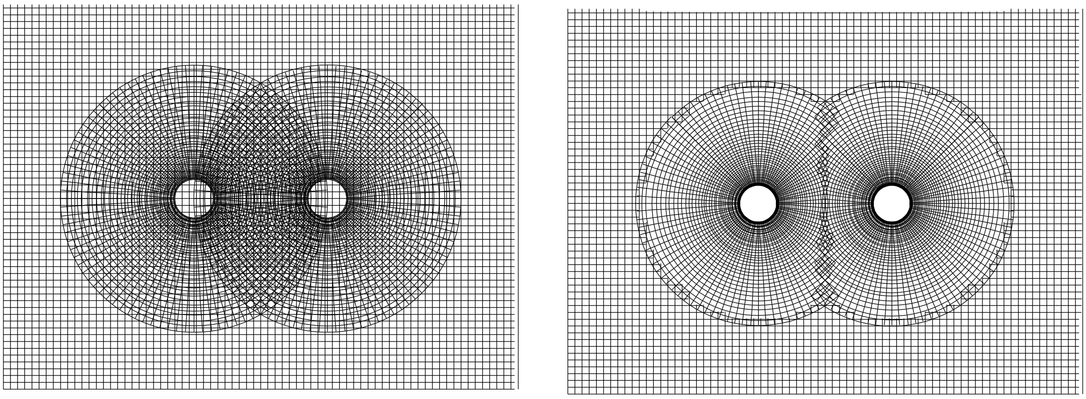

Figure 10.1: *Example of Chimera grid. On the left, the grids before blanking. On the right, the Chimera grid after blanking. This pre-processing step is called grid assembly. The computation in the blanked cells is disabled.*

There exists another way to proceed: it is based on the introduction of the Block Interface with Mismatched Nodes (BIMN) in the computational domain. The idea is simple: the computational domain is divided in certain large parts (wing, HTP, VTP, fuselage...) separated by predefined surfaces added to the CAD. Using these surfaces, the initial domain is split into several subdomains and any subdomain is meshed "independently". The principle of block interface with mismatched nodes (BIMN) is to authorise two different discretisations on both sides of the surface. Hence, the zones limits are topologically identical but in practice, their discrete representations may differ. Of course, the challenge concerns data exchange at the dedicated interface. Our approach consists in defining intersection facets and to treat these facets as with a classic finite volume approach. The key point is therefore transferred to the facets definition. A geometric algorithm is considered for the definition of the facets. In our approach, the treatment is conservative once the intersection surfaces are planar. For the sake of clarity, an example of BIMN for the case of two cylinders is represented in Fig. 10.2. The difference in cell sizes is increased in order to focus attention on the fact that the block interface discretization is not of kind "1 to n segments"[1]: BIMN is can be applied on discretisations with hanging nodes except for the two end points.

A lot of studies about theoretical foundations of BIMN can be found in the literature. The BIMN approach was firstly introduced by Rai [104, 105, 106]. These block interface treatments were used by Biedron *et al.* [13] to compute the F-18 forebody with actuated control strake. Rumsey [125] used BIMN to compute acoustic waves through sliding-zone interfaces. Epstein *et al.* [43] used them to compute a generic 3D wing. Stability of BIMN for the steady compressible Euler equations was studied by Lerat *et al.* [86].

With this very short review, it is clear that the BIMN process is more efficient than the

---

[1] 1 to n segments means that for any given segment on the less refined side, the same number of segments (here n) is recovered on the refined side. There are $n-1$ hanging nodes between two nodes shared by the discretisation.

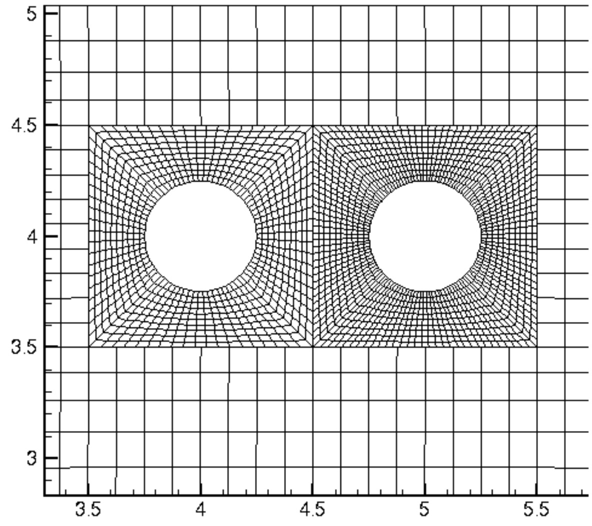

Figure 10.2: *Example of the BIMN technique for the example of two cylinders. The different discretization of a single geometric surface is clearly seen.*

chimera technique. Even if the mesh generation is more or less the same (split the initial computational domain into several parts), the chimera technique needs complex 3D algorithms to glue the domains while the BIMN approach simply needs a surface reconstruction. One can hope that the pre-treatment will be shorter with the BIMN approach since it is local, while the treatment is global for chimera grids. Finally, following classic (directional) high order finite volume techniques, it is easier to define high order extrapolated quantities for all facets, to use an approximated Riemann solver than using high order volume interpolation techniques. For all these technical reasons, we focus attention on the use of BIMN.

BIMN approach was introduced (historically) as a way to glue two domains that share a CAD surface. By essence, it was necessary to discretise both sides with comparable discretisation parameters. But industry also found in non-matching interface a good way to decrease the computational time of Unsteady Reynolds Average Navier-Stokes simulations (URANS). It is shown in Fig. 10.3 that the BIMN after the C- grid around the wing allows to decrease the number of degrees of freedom. Nowadays, this kind of mesh is considered for steady polar computations and the industrial tendency is to extend this technique to unsteady flows. As an example, this kind of mesh can be used to compute the gust response, which is clearly an unsteady phenomenon. For unsteady simulations, BIMN are a good way to introduce larger cells and to decrease the computational cost. This is important for industry when several hundreds of unsteady computations are performed each month. BIMN is also a solution to perform unsteady simulations, as for turbomachinery or Counter-Rotating Open Rotor (CROR). For any row, the mesh is globally a cylinder and two moving cylinders share a single surface: this is a sliding interface.

When the flow is only driven by turbulence effects, the use of RANS or URANS approach can lead to poor results. To overcome this limitation, industry investigates the use of Large

Eddy Simulation (LES). LES consists in computing the largest turbulence scales and in modelling the lowest scales. The largest scales depend on the geometry, while the smallest ones are linked with dissipation by viscous effects. The largest scale effects are a new interesting information to add to the industrial process. Among the phenomenon of potential interest, one can consider the flow at landing or take-off conditions, thermal protection system design... Our goal is to blend structured and unstructured areas for LES in a near future: BIMN is a way to introduce mesh flexibility.

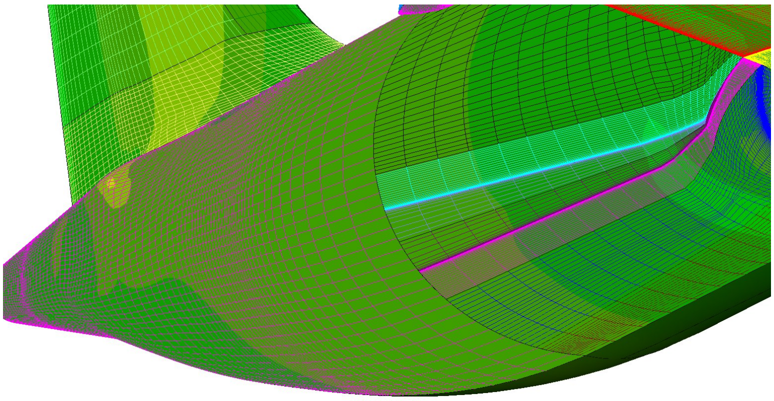

Figure 10.3: *BIMN after the C-grid around the wing. It allows to decrease the number of degrees of freedom.*

The main default of BIMN is that they were developed for steady simulations and simply extended to unsteady simulations without analysing their effect on unsteady phenomena. This is surprising: many efforts concern the measure of temporal / spatial accuracy of numerical schemes. But the scientific community generally forgets to analyse boundary condition treatment. The aim of the present work is to study the BIMN and its stability when used in unsteady simulations (Unsteady Reynolds Averaged Navier-Stokes, LES with low-order schemes) on multi-domain and multi-scale meshes. Given the success of this numerical method, it was already implemented inside the *elsA* software [107] without knowing the limits of the method in unsteady simulations (URANS / LES) on multi-domain and multi-scale meshes.

This chapter is organised as follows. After this introduction, theoretical results regarding BIMN are summarised. Then, numerical results regarding the special test case of the convection of a vortex are introduced. When the coarsening ratio is large, we show spurious reflection due to the numerical treatment of the interface. Finally, we explain in the last section our point of view to reduce these spurious modes.

10.2 Theoretical analysis

10.2.1 Computational domain

Let us consider a toy mesh Fig. 10.4. It is made of two blocks, the left one and the right one, which are separated by a block interface. This block interface can be with matching nodes (coincident) or with mismatched nodes (non-coincident). It depends on the value of h and Δz.

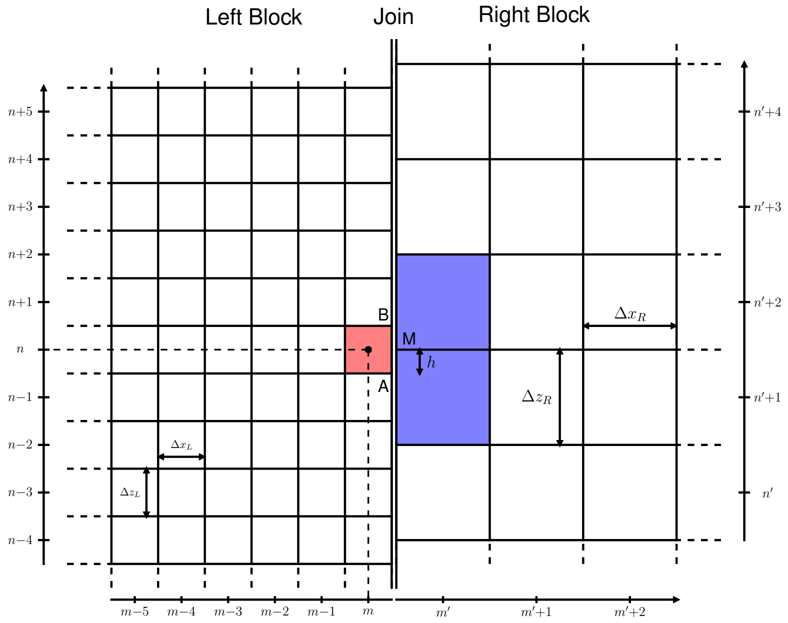

Figure 10.4: *Toy mesh composed of two blocks: the left one ($\Delta x_L, \Delta z_L$) and the right one ($\Delta x_R, \Delta z_R$). The right block can be translated by h along the vertical axis. Following* elsA *terminology, a join is an interface defined to glue two blocks.*

Our aim is to perform a local analysis in the presence of BIMN and a local Fourier analysis is conducted. All results presented in this section are fully described in [140]. Following a simple advection problem, the key point is the frequency analysis of the computed derivative with respect to the exact derivative. As a consequence, we introduce a harmonic function f (Eq. 10.1) where $\vec{k}$ is the wave vector, $k_x = \|\vec{k}\| \cdot \cos(\alpha)$ the projection of $\vec{k}$ on the x-axis, $k_z = \|\vec{k}\| \cdot \sin(\alpha)$ the projection of $\vec{k}$ on the z-axis and α the angle between $\vec{k}$ and the x-axis:

$$f = \exp\left[j\left(k_x \cdot x + k_z \cdot z\right)\right]. \tag{10.1}$$

10.2.2 Discretisation of the partial derivative on x

Following classic finite volume rules for the discretisation, the numerical computation of the derivative of Eq. 10.1 for the left block becomes:

$$\begin{aligned} f_{mn} &= \exp\left[j\left(k_x \cdot m\Delta x_L + k_z \cdot n\Delta z_L\right)\right], \\ \frac{\partial f_{mn}}{\partial x} &= \frac{f_{m+1/2,n} - f_{m-1/2,n}}{\Delta x_L}, \end{aligned} \tag{10.2}$$

and we can choose a centred scheme to define interface fields:

$$f_{m-1/2,n} = \frac{f_{m,n} + f_{m-1,n}}{2}.$$

Interface $(m+1/2, n)$ is on the BIMN and the value of f at this position is not exactly the mean of left and right contributions. Continuing the analysis introduced in Eq. 10.2 and denoting the interface contribution by $f^*_{m+1/2,n}$ (because it is not the mean of left and right contributions), one obtains:

$$\frac{\partial f_{mn}}{\partial x} = \frac{2f^*_{m+1/2,n} - f_{m,n} - f_{m-1,n}}{2\Delta x_L}. \tag{10.3}$$

The principle of the BIMN is to consider intersection facets and to compute the flux on each facets. Then, once the flux is computed on all facets, the facets are grouped in order to define true faces on left and right sides. Using Fig. 10.4, the flux on the left volume is defined as the sum of facets AM and MB. The interface flux for cell $(m', n'+1)$ on the right hand side involves a contribution of cells $(m, n-2)$, $(m, n-1)$ and (m, n). By linearity of the integral, the approach is conservative if the unit vector normal to the interface is kept constant and can be pulled out of the integrals. Using notations defined in Fig. 10.4, one can find an expression for the interface flux on the BIMN denoted $f^*_{m+1/2,n}$:

$$f^*_{m+1/2,n} = f^*_{AM} + f^*_{MB} = \frac{AM}{AB} \cdot \frac{f_{m,n} + f_{m',n'+1}}{2} + \frac{MB}{AB} \cdot \frac{f_{m,n} + f_{m',n'+2}}{2}. \tag{10.4}$$

In Eq. 10.4, the interface value is defined as the mean of left and right contributions, considering a simple average of left and right contributions. In fact, using a centred scheme, it is clear that the BIMN can be seen as two centred contributions relative respectively to AM and MB.

Of course, the same approach can be considered to define the partial derivative in the direction z tangential to the BIMN. Finally, theoretical study can be finalised by an analysis of the numerical scheme on the BIMN for an advection equation. In particular, following the local Fourier analysis, the introduction of a harmonic solution will lead to a numerical derivative. The error between the numerical derivative and the exact derivative gives the dispersion error (phase modification) and the potential amplification factor (wave dissipation or energy increase).

10.2.3 Conclusions

All details are in [140] and only the main results are summarised:

- If each block is uniformly discretised with similar cell sizes on both sides of BIMN, the BIMN can be used without any problem to compute aerodynamic fields:
    - The translation h has no effects on the spectral behaviour if the wave is normal to the BIMN.
    - The translation h has only a small dispersion effect (without dissipation) if the wave is at 45^o of the BIMN.
- If each block is uniformly discretised with different sizes on both sides of the BIMN, one has to take care of Shannon theorem and therefore on the frequency to capture.
    - A pure mesh coarsening along the $x-$axis for the right block causes dispersion and amplification and the computation can become unstable. This situation occurs also for a block interface with non coincident nodes ($h = 0.5$ for instance) or with coincident nodes.

- A pure mesh coarsening along the $z-$axis for the right block has no influence on dissipation nor dispersion if the wave is normal to the BIMN.
- A pure mesh coarsening along the $z-$axis for the right block has a significant effect on dispersion and dissipation if the wave is not normal to the BIMN. Increasing h to $h = 0.5$ has a stabilising effect.

10.3 Numerical analysis

The theoretical analysis presented in Sec. 10.2 gives the mathematical results on a simple configuration. However, a numerical complement is mandatory. It is of great interest to be able to compare analytically the numerical errors introduced by the discretisation and by the BIMN. The "COnvection of a VOrtex" (CO-VO) test case is of great interest since it is solution of the compressible Euler equations. In the following, simulations are performed using the *elsA* code.

10.3.1 Test case: 2D CO-VO

There are several possibilities to define a vortex transported by the flow but the approach considered in this thesis is to analyse the transport (advection at constant velocity) of an isentropic vortex solution of the Euler equations. This test case is inspired by the test case of the High Order Workshop [142] and the goal is to superimpose a vortex to a constant mean flow. The constant mean flow in the (x, z) plane is defined by $p = 101325Pa$, $T = 300K$, $Ma = 0.1$. The vortex is characterised by its radius R_C and its intensity β. Here, $R_C = 0.1m$ and β is computed to obtain the desired velocity fluctuation u_{max} due to the vortex: $\beta = u_{max}\sqrt{\mathrm{e}}/U_0$ with $u_{max} = 1.5m/s$. The vortex is initialised around the point of coordinates $(x_C = 0.5m, z_C = 0.5m)$. Finally, the flow is initialised with:

$$\left\{\begin{array}{lcl} u & = & U_0 - \beta U_0 \cdot (z - z_C)/R_C \cdot \exp\left(-r^2/2\right), \\ w & = & \beta U_0 \cdot (x - x_C)/R_C \cdot \exp\left(-r^2/2\right), \\ T & = & T_0 - 1/2 \cdot \left(\beta U_0\right)^2 \cdot \exp\left(-r^2/2\right)/C_p, \end{array}\right. \tag{10.5}$$

where $C_p = \frac{\gamma R}{\gamma - 1}$ and $r^2 = \frac{(x-x_C)^2+(z-z_C)^2}{R_C^2}$. Since the vortex is isentropic, density is computed using:

$$\rho = \rho_0 \cdot \left(\frac{T}{T_0}\right)^{\frac{1}{\gamma-1}} \tag{10.6}$$

The ratio of specific heats γ is equal to 1.4 and the air gas constant R is equal to $287J\,Kg^{-1}\,K^{-1}$.

The expected solution is simply the initial vortex convected without deformation. A reference test case was computed first and it consists in convecting a vortex over one meter between two blocks which can be separated by the block interface with coincident or non-coincident nodes. The mesh is composed of two blocks of 200 × 500 nodes and it measures $2m$ in both directions. We consider inflow and outflow conditions on the left and right boundaries while periodicity is imposed on the upper and lower faces. The vortex is therefore in the middle of the first block at the beginning and will be in the middle of the second block when the computation is stopped. Convection effects are computed using a pure centred scheme (without dissipation) and an explicit 4th order Runge-Kutta algorithm performs time increment. Time steps were monitored in order to have a numerical error as low as possible.

The domain being bounded, we perform an analysis on the L^∞ norm of the solution error rather than on the L^2 norm. Both norms are equivalent on this domain and the measure of the L^∞ error is easier.

10.3.2 Synthesis of numerical results

The first point to mention is that theoretical results summarised in Sec. 10.2.3 were all recovered by the computations. The effect of waves not normal to the block interface was also analysed, leading to the same conclusions as the theoretical study.

Moreover, following Airbus practice in the wake of C-grid, we were also able to perform an analysis on the huge coarsening. We now consider a CO-VO running in the diagonal direction and the left block size is 200 × 400 while the right block one is 7 × 13. The coarsening level is approximately equal to 32. We expect that the vortex will be dissipated and dispersed due to the large coarsening. But, as it can be seen from Fig 10.5, high-frequency waves seem to be reflected by the interface and energy is spatially reorganised. This numerical reflection cannot be accepted and moreover, the spurious modes are as large as the vortex core intensity on the coarser mesh. In an industrial flow, the reflected waves can interact with the flow in a region of interest, leading to a lack of accuracy or to false results.

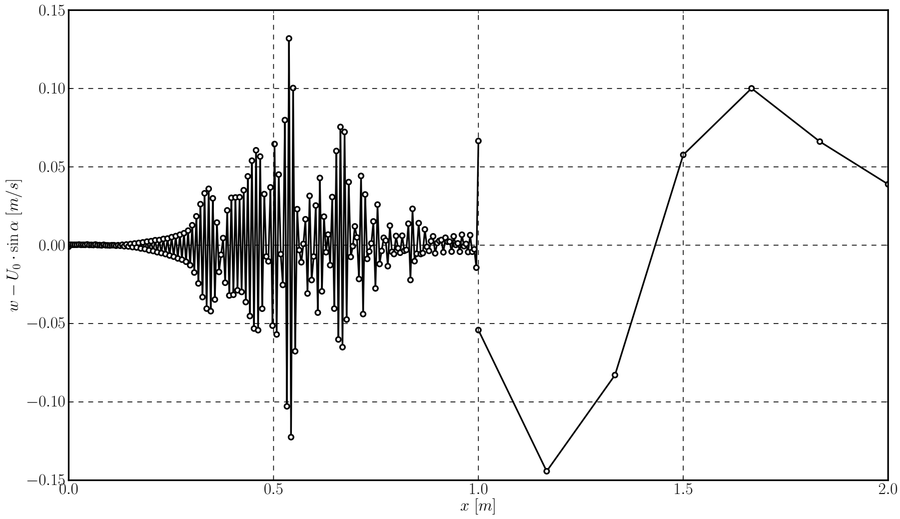

Figure 10.5: *Reflection of high-frequency waves. z-component of the velocity fluctuation. Cut at* $z = 1.5$ $[m]$.

10.3.3 Correction of reflection waves

Let us assume that the spurious modes are created by the coupling between the BIMN and the numerical scheme. Of course, one cannot have any action on the coarsening and the goal is to let the mesh generation as free of constraints as possible. The only parameter is the numerical definition of the scheme at the BIMN.

Following basics of the finite volume approach, the key point to avoid spurious modes is to use a Riemann solver that will take in considerations all waves on both sides. However, a first order Riemann solver makes accuracy decrease and in order to find a solution of interest in any situation, we analysed a high order extrapolation coupled with Roe's approximated Riemann solver [122].

For a pure advection problem, it is well-known that a third order scheme on a uniform mesh is built from a third-order accurate interpolation of the conservative variables at the interface. The interpolation is given by:

$$W^L_{i+1/2} = \frac{5}{6}W_i + \frac{1}{3}W_{i+1} - \frac{1}{6}W_{i-1},\ W^R_{i+1/2} = \frac{5}{6}W_{i+1} + \frac{1}{3}W_i - \frac{1}{6}W_{i+2},$$

and since right and left extrapolations are not generally equal, an approximated Riemann solver (the Roe's scheme) must be introduced.

We adapted the extrapolation technique using the same stencil in order to cope with a large change in local metric but for the sake of clarity, we focus only on constant discretisation lengths on both sides of the interface, as introduced in Fig. 10.6. In this case, the classic analysis using Taylor series expansions is introduced to link W_{i-2}, W_{i-1} and W_{i+1} with W_i and a new second order accurate extrapolation for the left state is given by:

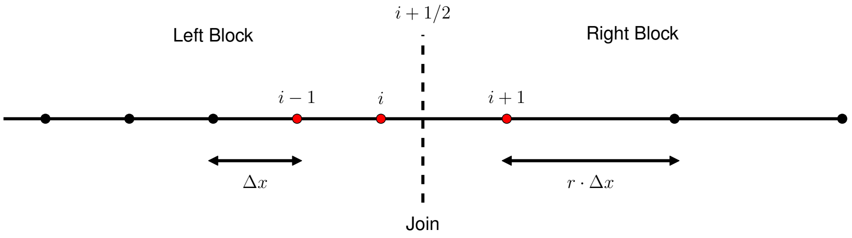

Figure 10.6: *Stencil for the second-order accurate interpolation of left state. The grid is non-uniform. The left block and the right block are separated by a block interface.*

$$W^L_{i+1/2} = \frac{9r+1}{6\,(r+1)} \cdot W_i + \frac{8}{3\,(r+1)\,(r+3)} \cdot W_{i+1} - \frac{3r+1}{6\,(r+3)} \cdot W_{i-1}.$$

The same approach for the right hand side extrapolation leads to:

$$W^R_{i+1/2} = \frac{7r^2-3r+6}{6r\,(r+1)} \cdot W_{i+1} + \frac{4r\,(3-r)}{3\,(1+r)\,(3r+1)} \cdot W_i + \frac{5r^2-3r-6}{6r\,(3r+1)} \cdot W_{i+2}.$$

Fig. 10.7 shows the effects of introducing the Roe's approximated Riemann solver and accounting for local metric. We recall that for all other faces, the classical centred scheme is kept. High-frequency waves are removed and the expected behaviour is recovered. Even if there remains some oscillations of low amplitude in the left block, the computation shows the improvement of the method.

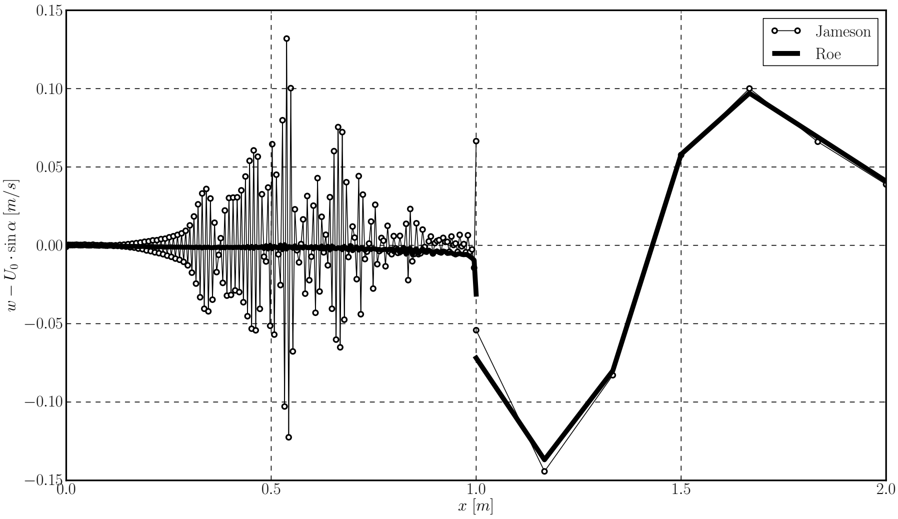

Figure 10.7: *The centred scheme is used everywhere except on the BIMN where Roe's scheme with extrapolated quantities using local metric is considered. The vortex is perfectly convected and spurious reflection disappeared.*

We assume that these oscillations are a consequence of our technique to extrapolate data on the BIMN. The current interpolation is based on three points in the direction normal to the BIMN and the interpolation should take into account the discontinuities of spatial discretisation in the three dimensions. At the present time, the BIMN data structure in *elsA* cannot allow a multidimensional interpolation and we have not been able to prove directly our hypothesis. However, it is of great interest to separate effects and at the present time, we perform a test on a mesh with a coarsening along x-axis to verify that these residual oscillations are caused by the interpolation which does not take into account the three dimensions but only the one orthogonal to the BIMN. We consider $\Delta x_R = 40 \cdot \Delta x_L$, $\Delta y_R = \Delta y_L$ and $\alpha = 0°$: the direction of propagation is orthogonal to the BIMN. Consequently, the block interface involves only matching nodes and there is only a discontinuity of spatial discretisation along $x-$axis. As shown in Fig. 10.8, if the interpolation does not take into account the local metric at the interface, high-frequency waves are reflected. Nonetheless, if the interpolation is dependent on metric, high-frequency waves are totally cut. The residual oscillations observed in Fig. 10.7 totally disappeared, and hence it was absolutely necessary to take into account the local metric for the interpolation of left and right states at the interface.

10.4 Conclusions

Block Interface with Mismatched Nodes entered industry some years ago and they made possible many kinds of simulation. For turbomachinery, they are a key point in the computation of unsteady effects propagation through the sliding mesh version of BIMN. For aircraft simulations, they are located in C-grid wakes in order to decrease the mesh size. Even if BIMN showed good capabilities for steady flows even with high coarsening, the question was still open

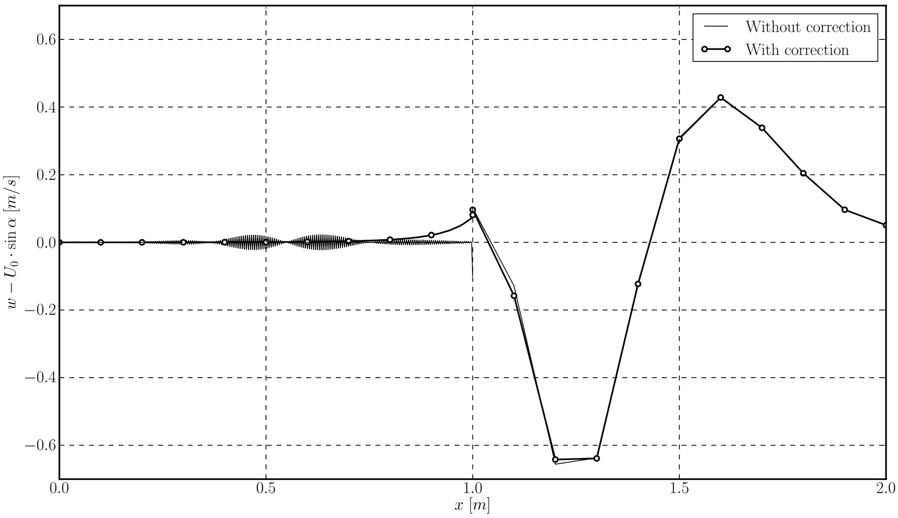

Figure 10.8: *Effect of interpolation of left and right states dependent on metric which is required for the Riemann solver at the interface. Coarsening along x-axis.*

for unsteady flows and our work is a partial answer.

First, we analysed theoretically and numerically the BIMN effect on the flow accuracy. We showed that the BIMN properties are good if the mesh sizes are almost the same. This is particularly a point of importance to guarantee numerical results in turbomachinery where the angular distance between mesh lines is more or less the same between two adjacent rows. However, for aircraft computations, a large coarsening (of value in agreement with the one chosen for steady flows) can lead to spurious reflections. Our analysis showed that two problems must be corrected. First, it is of great importance to account locally for waves propagation and to do so, we proposed to consider a Riemann solver to define the flux on the BIMN. The second key point concerns the extrapolation of quantities on the BIMN for the approximated Riemann solver. When mesh sizes are really different on both sides of the BIMN, it is necessary to account for the local metric in the extrapolation process. Finally, we assume that the best way to proceed is to implement a three-dimensional local interpolation and we are currently extending the process to account for a 3D interpolation using a $k-$exact approach. This 3D interpolation is a prerequisite for the treatment of hybrid BIMN, with a structured block on one side and an unstructured one on the other side.

Part IV

Conclusion and Perspectives

Chapter 11

Conclusion

The work presented in this thesis follows three directions. The first one concerns physical modelling, the second one makes a link between mathematics and physical modelling and numerical schemes is the key point of the last part.

Physical modelling

For turbulent reentry flows, two topics must be accounted for. First, wall roughness has appeared due to ablation of the thermal protection system and wall roughness has a strong influence on wall heat flux. We recall that the wall heat flux is the major parameter for reentry. It is of course very expensive to handle rough elements in a mesh over the true geometry. Moreover, even if it can be performed for sand-grain rough element, the shape of the rough elements is not known for the typical material considered during reentry. As a consequence, we took the decision to introduce a model in the RANS equations. We first developed a formulation of wall functions valid for turbulent compressible flows at high Mach number. The wall functions reproduce the compressible boundary layer over both adiabatic and isothermal walls. The last point of importance is the numerical implementation in the CFD code and our procedure follows an integral formulation issued from the technique to integrate RANS equations in the solver (cell-vertex and cell-centred techniques).

The last topic concerns thermal turbulence and we analysed the compressible versions of coupled dynamic / thermal turbulence models based on 4 partial differential equations. We showed that thermal turbulence had effects in the boundary layer and thermal and dynamic turbulence scales were almost the same for $y^+ > 300$. This is an important point for the development of a two-layer thermal turbulence model: near the wall, thermal turbulence effects are accounted for and they are neglected far from the wall. Regarding wall functions, the results indicated that thermal corrections might be accounted for in the formulation and we proposed new wall functions. This activity was in strong relation with the PhD thesis of S. Galera.

Link between physical modelling and mathematical properties

RANS turbulence models are built from physical properties of the flow. Turbulence models are known to have poor mathematical properties and especially, many of them can violate physical assumptions (bounded and positive variables) during the computational loop, leading to severe stability constraints. Our point of view was to define new turbulence models that were issued from classic ones, but that contained by nature good mathematical properties. In this part, the goal was to make a bridge between the community of physicists and the one of mathematicians. At the present time, the link between these sciences is not fully achieved and there remains some work to perform. In particular, we showed that the procedure for incompressible flow might be upgraded for compressible flows and we are not sure to have found at the present time the good change of variables.

Numerical schemes

This is the most recent activity and three aspects were presented.

Harmonic Balance Method was analysed. HBM is a reduced model to account for periodic flows in the sense that only the first harmonics are explicitly accounted for. For periodic flows, two points were addressed. First, the development of an implicit treatment to monitor convergence of the HBM was performed. Without the implicit treatment, most of the results could not obtained and some conclusions regarding CPU time would be false: the implicit time integration is one of the key points to show the power of HBM. HBM was then compared with other exact and approximated techniques and the superior behaviour of HBM was proved for applications in which non linearity dominates the flow. The last point concerned the multifrequency extension. This extension was mandatory to be able to deal with multistage turbomachinery where different frequencies (not harmonically related) were encountered.

The second activity is in strong relation with the modelling of diffusion phenomena on unstructured grids composed of several (basic) element shapes. In a cell-vertex framework, two new diffusion schemes based on a Finite Element paradigm were proposed and one had properties in agreement with computation prerequisites. In the context of cell-centred finite volume discretisation, classic (published) schemes have quite poor properties or they are not easily made efficient in a parallel environment. Our new scheme consisted in defining a dual cell around each mesh interface, to compute an averaged gradient on the dual cell, and to consider this gradients for the diffusion flux on the boundary. The scheme worked fine on meshes composed of regular cells and kept a compact stencil in agreement with HPC requirements for LES.

Finally, the most recent activity concerns the bridge between structured code and unstructured code. It is clear that structured codes give the best accuracy as mesh lines are chosen aligned with direction of variations for physical quantities. But on complex geometry, switching to an unstructured framework has a sense. Of course, the key point is the coupling between both kind of zones inside a single grid. At the present time, the generation of structured and unstructured blocks is performed by dedicated tools and introducing flexibility in the mesh generation is a key point. To do so, we propose to extend our Block Interface with Mismatched Nodes approach to handle hybrid structured / unstructured block connections. BIMN were never studied for unsteady simulations and before studying these hybrid block interfaces, we focused our attention on unsteady simulations on structured grids using industrial best practices. We showed that the BIMN worked fine for turbomachinery if the sizes of elements were almost the same on the two sides of the interface. This situation does not occur in the wake of C-grid for aircraft computation in industry and an analysis of mesh coarsening effects was performed. It lead us to increase BIMN accuracy by introducing an approximated Riemann solver at the interface and a multidimensional interpolation taking into account local metric.

Chapter 12

Perspectives

Some of my current activities are not introduced in this thesis. This choice is motivated by the fact that these activities are very recent and have not lead to accepted publications at the present time.

The new activities are all related to problems that are not solved currently using industrial RANS and URANS approaches. For off-design, it is clear that unsteadiness is strongly related to turbulence fluctuations and these fluctuations cannot be captured using an averaged formulation. RANS and URANS are too dissipative approaches and they must not be considered for applications regarding transport of information on large distances. It is therefore mandatory to switch to a method that asks for less modelling. Of course, Direct Numerical Simulations and Large Eddy Simulations are the two candidates and for industrial flows, only LES is of interest. All the perspectives presented below concern LES.

Hybrid solver for LES

We already discussed the interest of a hybrid structured / unstructured paradigm to cope with complex geometry while maintaining a large efficiency in regions in which the mesh was easily built. I am involved in the extension of the *elsA* code to handle structured and unstructured grids since 2008. In particular, my work was focused on the data structure definition and on implementing many features, including CGNS-based I/O, convection scheme (Roe with a simple MUSCL), two diffusion schemes, the computation of the distance to the wall and two turbulence models (one version of $k-\omega$ and Spalart-Allmaras turbulence models for unstructured grids). All these developments were performed in a parallel framework based on MPI library. An AIAA Paper is associated with this work [117].

Nowadays, my involvement in the project hybrid *elsA* consists in advising the PhD thesis of P. Cayot founded by Snecma. The goal of this PhD is to define new schemes in the cell-centred formalism to cope with massively parallel LES computations. Classic (published) approaches use a large stencil to define locally a high order (polynomial) representation of quantities and these approaches are not usable for massively parallel computations: the stencil is large and the number of fields to exchange is too high. We first analysed the diffusion scheme presented briefly in Sec. 9.3. Then, we built a new family of convection schemes based on a high order directional extrapolation using a combination of mean values and gradients. The same gradients were considered for the diffusion scheme. Such an approach enables to reduce the total CPU cost by computing data used for both convection and diffusion. The theoretical analysis is finished and the schemes have an order between 3 and 6, depending on parameters and stencil. We also analysed their spectral behaviour using a Von Neumann analysis: they presented a large improvement with respect to classic second order schemes. During the last year of the PhD thesis of P. Cayot, our work will be focused on the validation of this family of schemes.

To conclude, this first activity concerns the extension of an industrial solver to handle LES on hybrid grids. From the numerical point of view, it could be more efficient to change the paradigm and to analyse new techniques. Indeed, industrial solvers can perform several kinds of application and the prize to pay concerns efficiency. It is clear that a dedicated CFD code has better HPC properties. In the next section, our involvement in the development of new kind of unstructured solvers based on a discontinuous spectral paradigm is explained.

Spectral difference approach

A way to overcome large stencils on unstructured grids relies on increasing the number of degrees of freedom inside the element. It is convenient to define a high order representation of quantities inside any mesh element following a polynomial approximation. The high order polynomial approximation being local, it is not assumed to recover continuous data at mesh element interfaces. Among the methods proposed in the literature, we identified three techniques:

The **Discontinuous Galerkin** -DG- technique is based on the Finite Element framework. The principle is to look for a polynomial representation of the solution that satisfies a variational form of the governing system within each element. Even if the technique is quite old (Reed and Hill [118] in 1973), its extension to the full Navier-Stokes equations is recent and many papers were published during the last 10 years.

The **Spectral Volume** -SV- technique is based on the Finite Volume framework and it follows the pioneering work of Z.J. Wang in 2002 [141]. It consists in defining element subdivisions on which a classic Finite Volume technique is considered. The mean quantity over each volume is necessary to build the high order representation of data inside the element.

The **Spectral Difference** -SD- technique follows the Finite Difference approach. Kopriva and Kolias published it in 1998 [78] for structured grids and Liu, Vinokur and Wang [90] published a more general presentation of the technique in 2006, usable for unstructured grids. The idea was to define a high order polynomial approximation of the quantities inside each mesh cell and to solve equations in their strong differential form. Of course, fields are generally discontinuous at the cell interface and a Riemann solver is considered to solve the discontinuity.

All techniques define high-order continuous solutions inside each mesh element. But they differ by the local treatment on each mesh cell: finite element reconstruction, finite volume on sub-cells or resolution of the strong form of equations. Of course, the polynomial reconstruction leads to two different quantities at mesh interface and a Riemann solver is necessary to compute the flux to exchange between cells. The interest of all methods comes also from the possibility to manage both the space refinement parameter h and the degree of the polynomial p. When one compares classic Finite Volume technique with these high-order ones, the main difference lies in the non-universal relation between the mesh element and the number of degrees of freedom (1 mesh element is not associated with 1 degree of freedom as in Finite Volume). This point has a (very) strong impact on the definition of in-memory structure for data.

At Cerfacs, we chose to focus our attention on the Spectral Difference technique. This choice was motivated by the fact that the SD method was built in order to correct some drawbacks of DG and SV. First, it seemed more efficient in term of CPU usage (less computations per degree of freedom) than DG technique. It was also shown that the CFL criterium for stability was less restrictive that for DG method. Moreover, SV suffered a high sensitivity with respect to element decomposition and this drawback was avoided with SD method. Another point of importance concerned the definition of a gradient for the diffusion flux. This activity on SD method began with a Master thesis [80] under my supervision, followed by the post-doc position of N. Villedieu, an engineer training [20] dedicated to the analysis of performance on CPU and GPGPU and another Master thesis [91]. All this work was integrated in *JAGUAR* (proJect of an Aerodynamic solver using General Unstructured grids And high ordeR schemes), a new CFD code designed to perform LES simulations on unstructured grids composed on hexahedra, potentially with hanging nodes. New results were obtained recently during the fixed-term contract of J. Vanharen (before his PhD). At the present time, we are preparing two new papers on the SD method. Our current work concerns extending the SD approach to handle shocks (training period of M. Lemesle). We are currently proposing and analysing new methods to handle shocks and we are currently preparing an article on this topic.

These high order methods are assumed to be expensive. In fact, there are much more local operations than with a classic low-order method. In addition, these approaches are known to have strong CFL constraints. Our experience shows that our implementation of SD and dedicated integration schemes can be as efficient as or more efficient than our current LES solvers (AVBP and *elsA*). Moreover, our optimisation of the implementation lead us to confirm that the CPU cost per degree of freedom is quite constant, even when the polynomial degree increases (up to a $6-th$ order polynomial, and therefore a $7-th$ order approach). The same kind of results was presented during ANADE European project: G. Gassner, C.-D. Munz *et al.* indicated that the sixth-order Discontinuous Galerkin method could be more efficient that the equivalent compact sixth-order classical finite difference approach[1].

An overview of *JAGUAR* status is available on my personal webpages[2]. But some points must be mentioned:

- The Spectral Difference method is designed for compressible flows.
- The fundamental principle is quite simple to understand.
- We obtained a strong scaling from 1 to 2048 cores and from the $4-th$ order scheme to the $7-th$ order one (Fig. 12.1 on Airain[3]).
- On GPGPU, the strong scaling analysis (Fig. 12.2) showed the same efficiency as encountered in the literature (47.0 / 64 in 3D and 49.9 / 64 in 2D).
- In terms of physical efficiency, our results on the CO-VO test case (Fig. 12.3) with severe conditions ($M = 0.05$ and $\max(p_0 - p) = 0.07Pa$ over $101\,000Pa$) proved the capability of the method to transport efficiently small perturbations over large distances.

We are currently involved in a FP7 proposal in order to improve our solver for LES by considering a *hp* mesh adaptation.

---

[1] `http://nrg.iag.uni-stuttgart.de/wp-content/uploads/2014/01/2013_10_24_ANADE_Workshop_HFrank.pdf`

[2] `http://www.cerfacs.fr/~puigt/jaguar.html`

[3] `http://www-ccrt.cea.fr/fr/moyen_de_calcul/airain.htm`

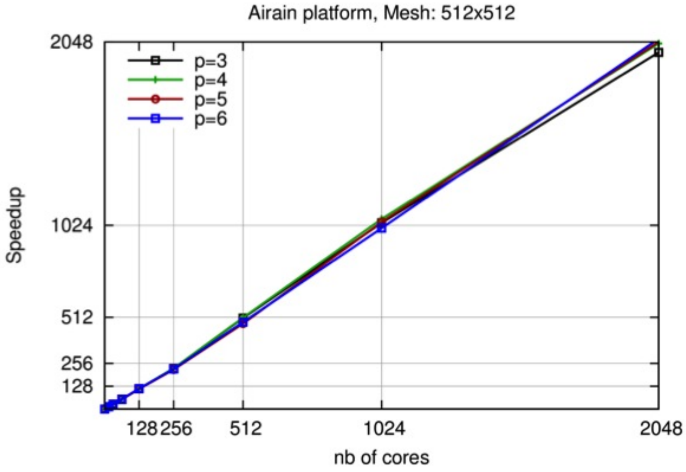

Figure 12.1: *Strong scalability on Airain depending on polynomial degree*

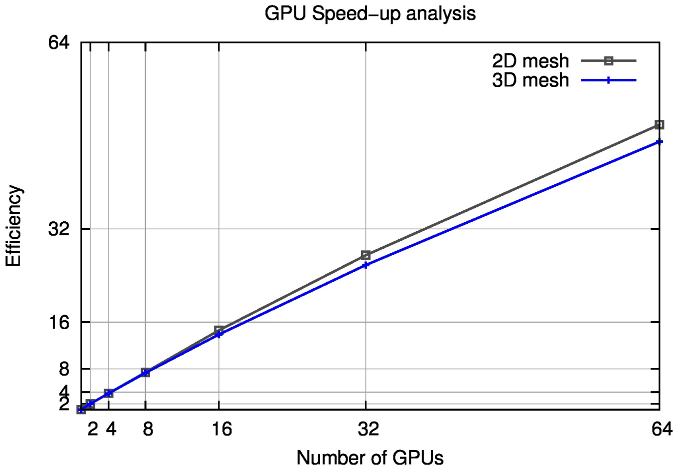

Figure 12.2: *Strong scalability on a cluster of NVidia Tesla M2090 cards, each composed of 512 GPU cores*

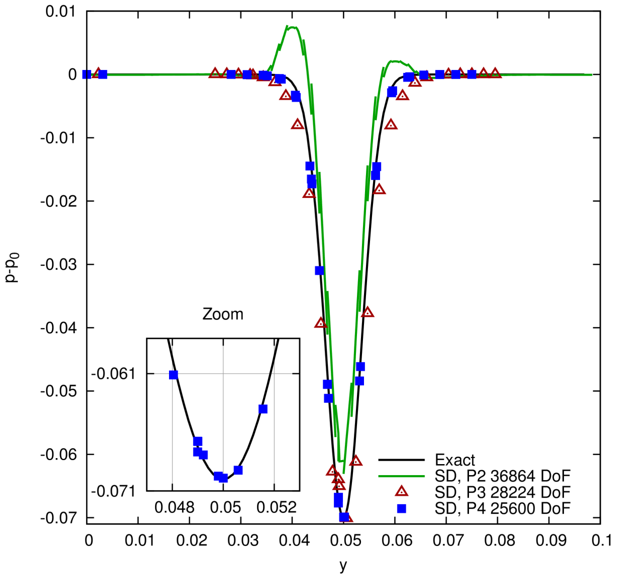

Figure 12.3: *Comparison of numerical and exact solutions for the CO-VO after 50 rotations for different degrees of accuracy. The third order solution ($p = 2$) exhibits discontinuity.*

Lattice-Boltzmann Method (LBM)

Finally, the last technique I would like to focus on is the Lattice Boltzmann approach. Nowadays, the time spent for the mesh generation is still large, even for unstructured grids. Any technique with a reduced mesh generation cost has an interest for CFD. Among the possible techniques, the Lattice Boltzmann codes solve the discrete Boltzmann equation with a collision model such as Bathnagar-Gross-Krook. The principle is to project the resolution on several space directions and to account for collisions between particles. A cartesian grid with an octree approach is considered in order to define refinement areas.

LBM consists in a collision term and then a streaming term where the transport with streaming is non-diffusive. Nowadays, LBM approach has entered industry for low-speed applications and its high accuracy and low dissipation makes it a good candidate for many LES applications [74]. In Fig. 12.4, a LES computation performed with PowerFlow, a LBM code developed and distributed by EXA[4], is considered to compute the unsteady and massively separated flow around the LAGOON landing gear system.

In my opinion, LBM and SD approaches are complementary: SDM will need time for the mesh generation but it can account easily for compressibility effects. On the other side, LBM is easy to pre-process but at the present time, the method is intrinsically limited to low compressibility effects.

---

[4] `www.exa.com`

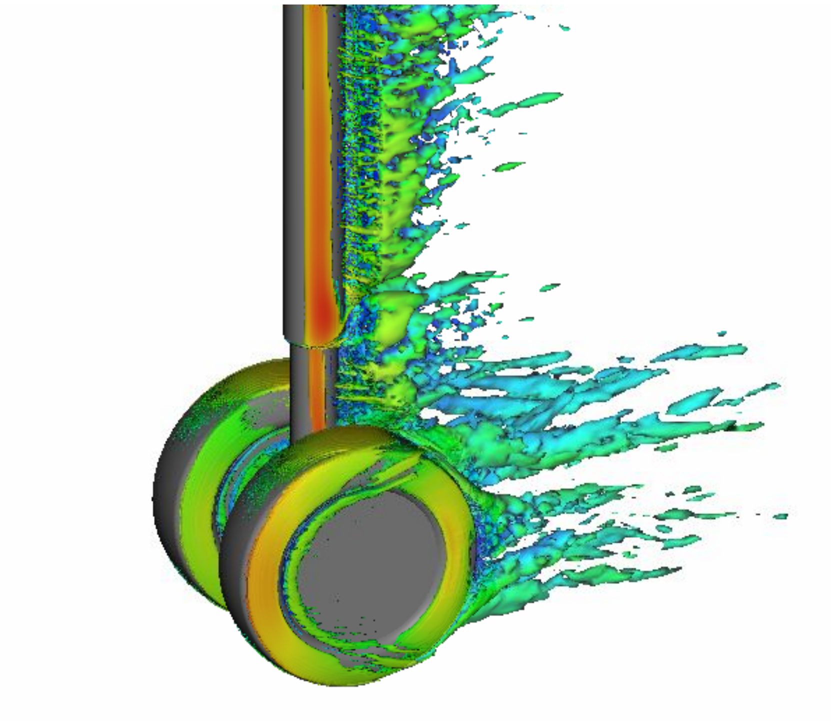

Figure 12.4: *Snapshot of the unsteady computation around the LAGOON test case using a LBM solver.*

Appendix

A Curriculum Vitae

Guillaume Puigt

CERFACS-CFD
42, avenue G. Coriolis
31057 Toulouse Cedex, France

38 years
French
Married, two children

guillaume.puigt@cerfacs.fr
`www.cerfacs.fr/~puigt/index.html`

Senior Researcher specialised in CFD

⟹ Research objectives

- Turbulence modelling including averaged and large-scale approaches
- Decrease of computation restitution time using:
  - Reduced models for the turbulent boundary layer
  - Harmonic approach for periodic and almost-periodic flows
  - Hybrid grids composed of structured and unstructured zones
- Schemes for the resolution of the Navier-Stokes equations on hybrid grids
- High order discretisation techniques based on spectral discontinuous approaches

⟹ Working experience

Since 2005 Senior Researcher at CERFACS. Applied research work on CFD, including modelling, numerical schemes, implementation and validation of new discretisation techniques. Write scientific proposals, implement the proposal, drive the project and execute contractual activities for aircraft industry (Airbus, ONERA, SNECMA / Turbomeca). Provide support for user and developer.

2003 - 2005 Research engineer at Commissariat à l'Énergie Atomique / Centre d'Études Scientifiques et Techniques d'Aquitaine in the group in charge of reentry, studies and conception. Research work on reentry CFD codes Ares, Galadriel and Thot (turbulence modelling, wall roughness, CFD simulation coupled with radiation). Work on reentry for CNES and ESA (for Mars)

2001 - 2003 Post-doctoral fellow at CERFACS. I worked on several activities and among them: wake vortex simulations (European project C-WAKE PCRD GDR1-1999-10332), wall functions for turbulent boundary layer and hypersonic laminar flow in chemical equilibrium in the CFD code called **NSMB**.

$\Longrightarrow$ Education

2001 PhD thesis in Applied Mathematics from University of Montpellier II, under the direction of Prof. B. Mohammadi. Thesis performed in the context of a scientific contract between CEA/CESTA and University of Montpellier II. Thesis defended on September 27th, 2001.

1998 Diplôme d'Etudes Approfondies in Mathematics (Convex Analysis option) with honours, University of Montpellier II.

1993 Math and Science Baccalaureate with honours.

$\Longrightarrow$ Main collaborations

- **ONERA** (France): implementation of methods in the flow solver *elsA*.
- **SAFRAN** (France): research projects on harmonic balance technique and on numerical schemes for LES on hybrid structured / unstructured grids.
- **AIRBUS** (France): applied research for RANS computations on hybrid structured / unstructured grids.
- **ISAE-SupAero**, Département Aérodynamique, Énergétique et Propulsion (France): high order methods based on spectral discontinuous approaches.
- **CORIA** (France): Spectral Difference Method.
- **CENAERO** (Belgium): Spectral discontinuous methods, high order mesh and visualisation
- **NVIDIA** (France and USA): Efficiency of CFD codes on GPGPU using CUDA.
- **University of Kansas** (USA): Discussions with Prof. Z.J. Wang, one of the Spectral Difference Method fathers.

$\Longrightarrow$ Working tools

- Operating systems: Unix, Linux, MacOS, Windows
- Software: LaTeX, OpenOffice, Microsoft-Office, Icem-CFD, Tecplot, *elsA*, *DEPICT*, *JAGUAR*
- Programming languages: Fortran90, C++, MPI / OpenMP, beginner in Python and HTML.
- Library: CGNS (CFD General Notation System)

B Teaching

I introduce in the following sections my involvement in teaching. My involvement in the lessons is explained through the number of hours per year and the presence of course material.

B.1 Training at Cerfacs

Cerfacs organises training sessions since 2011 and I participate in these lectures:
– In 2011 and 2012, Hugues Deniau and I taught two lessons (3h each lecture):

- Basics of CFD and link between mesh, discretisation, degrees of freedom. Course material of 50 pages. Full involvement in this lecture
- Numerical schemes for convection, from Godunov to MUSCL and non-MUSCL techniques. Involvement in 50% for the course material but lessons given by H. Deniau. Applications with a simple 2D Euler solver based on a cartesian grid.

– In 2012 and 2013, training session named *Fundamentals to understand and analyse high fidelity compressible Large Eddy Simulations.* I focus my presentations on 2 topics (3h each topic). First, I introduce the basics of CFD to understand all the courses. Then, I introduce schemes for LES. This training session is performed twice each year. In May 2013 and May 2014, I was replaced by colleagues who took my slides. I am the corresponding person for this training session since summer 2013.

Note that I also performed a training at CEA/CESTA on turbulence during reentry.

B.2 Teaching outside Cerfacs

I am a temporary worker at ISAE-SupAero and I teach for second and third year students since 2009. The course deals with Fluid Dynamics, their computation, and mathematical properties:
– During three years (2006-2009), I taught CFD for second year students who won't do CFD in the future. The goal was therefore to give and explain the key words and the main difficulties. I wrote a course material of 80 pages. 2h45 each year.
– Since 2010, I have taught one lesson on Euler and Navier-Stokes equations in the continuous regime and another one on mesh generation. Lessons for third year students specialised in CFD. 5h each year. I wrote the general course material of 127 pages that addressed the important aspects of CFD (generalities, schemes, etc.).
– Since 2010, I have proposed with Jean-François Boussuge CFD applications with *elsA* for third year students specialised in CFD. They performed steady and unsteady computations with explicit and implicit time integrations, play with the CFL number, etc. 2h30 each year.
– Since 2012, I am involved in CFD in-depth studies (third year students) and I generally work on software development with one or two groups of students. The list of studies is given in Sec. B.2. 20h per year.
– Since 2012, I am participating in the general course on mathematics for second year students. The goal is to teach the main principles of hyperbolic systems and the way to solve them following characteristics and Rankine Hugoniot jumps and then the mathematical analysis of elliptic systems with Lax-Milgram theorem. These courses are finished with numerical

applications. 23h45 of lessons and 5 to 10h of applications.
– Since 2013, I am participating in in-depth studies for third year students specialised in Simulations for Complex Systems (20h). For the sake of clarity, the work performed is introduced in Sec. B.2.

I was also invited to make two presentations on the interaction between math and CFD:
– *On some interactions between mathematics and CFD*, G. Puigt, invited conference, Seminar for students, Université de Nantes - Département de Mathématiques, January, 20th, 2012.
– *On some interactions between applied mathematics and computational fluid dynamics for industrial applications*, G. Puigt, invited conference, Seminar for students, Institut Supérieur de l'Aéronautique et de l'Espace ISAE, campus SupAero, February, 20th 2013.

CFD in-depth studies

– V. Tissot and P. Penet, implementation of Spalart-Allmaras turbulence model in a cell centred finite volume CFD code prototype, SupAero, Aero, 2014.
– P. Gueye and G. Wissocq, implementation of the NSCBC outflow condition in a Spectral Difference Navier-Stokes prototype and application to simple aeroacoustic test-cases, SupAero, Aero, 2014.
– J. Bonnici and C. Sommariva, implementation of classical conditions in a Spectral Difference Navier-Stokes prototype, SupAero, Aero, 2014.
– J. Vanharen, numerical analysis of diffusion schemes based on least-square reconstruction in a Navier-Stokes CFD prototype, SupAero, Aero, 2013.
– H. Montanelli, implementation of a matrix-free GMRES solver in a Euler CFD prototype based on a Finite Volume approach, SupAero, Aero, 2013.
– P. Cantin and E. Toomey, implementation of Jameson Schmidt Turkel convection scheme in a Euler CFD prototype based on a Finite Volume approach, SupAero, Aero, 2013.
– A. Massi and A. Fiumara, Polar computation with *elsA*, SupAero, Aero, 2012.
– M. Kuzmin, Implementation of an edge-based diffusion scheme in a Navier-Stokes CFD prototype, SupAero, Aero, 2012.
– I. Cardenas-Sanchez, implementation of a diffusion scheme based on a diamond path in a Navier-Stokes prototype, SupAero, 2012.

Complex systems in-depth studies

– N.A.K. Doan, C. Ortega-Absil and N. Abderrahaman, numerical analysis and implementation of a heat equation solver based on spectral difference, SupAero, Complex Systems, 2014.

C Supervision of students

I am currently co-advisor of four PhD thesis (J. Vanharen, C. Pérez-Arroyo, P. Cayot, S. Le Bras) and I also directly supervise one (or more) trainee each year. Here is a brief overview of their subjects.

C.1 PhD Thesis

PhD Thesis for which I am co-advisor:
– J. Vanharen (2014-2017) Coupling different algorithms inside a single computation, application to the CFD simulation involving high order schemes for structured and unstructured zones in *elsA*, PhD thesis founded by Airbus, advised by J-C. Jouhaud and myself up to my HDR and then only by myself.
– C. Pérez-Arroyo (2013-2016), Aeroacoustic computations of dual stream jets including shocks with *elsA*, Aerotranet-2 Marie-Curie fellow, PhD thesis advised by Prof. Christophe Airiau et co-advised by myself.
–S. Le Bras (2012-2015) Development, implementation and validation of advanced numerical techniques dedicated to aeroacoustics within *elsA*, thesis founded by Cerfacs within a contract with Airbus. PhD advised by Prof. Christophe Bogey and co-advised by myself.
– P. Cayot (2012-2015) Convection and diffusion schemes for LES on unstructured and hybrid grids inside *elsA*, PhD thesis founded by Snecma and CIRT, advised by J-C. Jouhaud and I. Involvement of Prof. P. Sagaut.

PhD Thesis in which I participated and for which my involvement is justified by an article:
– PhD Thesis of S. Galera defended in 2005.
– PhD Thesis of V. Auffray defended in 2007
– PhD Thesis of F. Sicot defended in 2009.
– PhD Thesis of F. Guédeney defended in 2012.

C.2 Training students

2014	– Marie Lemesle. *Analysis and implementation of a shock capturing scheme compatible with the spectral difference method.* Master 2 training. Co-advised with Nadège Villedieu. – Nicolas Dewidehem. *Can Spectral Difference Method be considered for aeroacoustic simulations?* Master 1 training. Co-advised with Nadège Villedieu.
2013	– Isabelle Marter. *Handling different h and p refinements in the framework of spectral difference method.* Master 2 training. Co-advised with Nadège Villedieu. – Adrien Cassagne. *Implémentation multi GPU de la méthode spectral difference pour un code de CFD.* Master 2 training. Co-advised with Nadège Villedieu and Jean-François Boussuge. – Aurélien Genot. *Analyse de l'efficacité du code Spectral Difference JAGUAR sur machine parallèle.* Master 1 training. Co-advised with Nadège Villedieu and Jean-François Boussuge. – Julien Vanharen. *Theoretical and numerical analysis of block interfaces with mismatched nodes. Emphasis on unsteady flows.* Last training for SupAero school.
2012	Maxim Kuzmin. *Spectral difference method for the Euler equations on unstructured grids.* Last training for SupAero school. Advised at 80% and co-advised by Hugues Deniau and Pierre Cayot.

2011	Pierre Cayot. *Towards LES on hybrid grids with* elsA. Last training for INSA Toulouse.
2009	W. Mahmoudi. *Analysis of clocking effects in turbomachinery with the harmonic balance technique in* elsA.
2008	– M. Devilliers. *Towards a hybrid structured / unstructured block interface treatment* – P. Rauschenberger. *Implementation in* elsA *and validation of the harmonic balance technique with several frequencies.* – M. Boger. *Implementation of a gas-kinetic BGK solver in the* elsA *code.* Advised by H. Deniau (70%) and co-advised (30%) by myself.
2007	– A. Fosso-Pouangué. *Implementation of a hybrid mesh technique in* elsA. *Study of diffusion schemes.* – E. Germaine. *Implementation of wall functions for LES in* elsA. Co-advised with J-C. Jouhaud
2005	– V. Arrecgros (DEA). *Implementation and validation of an alternative turbulence model with good mathematical properties.* – V. Arrecgros (DESS). *Validation of the implementation of the* $k-\omega$ *turbulence model in THOT-2D solver.*
2004	O. Frayssinet au CESTA. *A new database for rough wall elements including real gas effects.*
2002	D. Lizarazu au CERFACS. *Implementation and validation of wall functions for steady and unsteady flows in* elsA.

D List of communications

D.1 Refereed papers

1. J. Vanharen, G. Puigt and M. Montagnac, Theoretical and numerical analysis of nonconforming grid interface for unsteady flows, submitted to *Journal of Computational Physics* in August 2014.

2. T. Guédeney, A. Gomar, F. Gallard, F. Sicot, G. Dufour and G. Puigt, Non-uniform time sampling for multiple-frequency harmonic balance computations, *Journal of Computational Physics*, 236(1):317-345, 2013.

3. G. Dufour, F. Sicot, G. Puigt, C. Liauzun, A. Dugeai, Contrasting the Harmonic Balance and Linearized Methods for Oscillating-Flap Simulations, *American Institute of Aeronautics and Astronautics Journal*, 48(4):788-797, 2010.

4. G. Puigt, J.-D. Müeller and V. Auffray, Discretisation of diffusive fluxes on hybrid grids, *Journal of Computational Physics*, 229(5):1425-1447, 2010.

5. F. Sicot, G. Puigt and M. Montagnac, Block-Jacobi Implicit Algorithms for the Time Spectral Method, *American Institute of Aeronautics and Astronautics Journal*, 46(12):3080-3089, 2008.

6. B. Mohammadi and G. Puigt, Wall Functions in Computational Fluid Dynamics, *Computers and Fluids*, 35(10):1108-1115, 2006.

7. S. Galera, B. Mohammadi and G. Puigt, Turbulence Modeling for Hypersonic Flows Over Isothermal Walls, *International Journal of Computational Fluid Dynamics*, 20(8):549-561, september 2006.

8. B. Mohammadi and G. Puigt, Generalized Wall functions for Rough Walls Based on Data Assimilation, *International Journal of Computational Fluid Dynamics*, 17(6):453-465, 2003.

9. B. Mohammadi and G. Puigt, Mathematical and Numerical Analysis of an Alternative Well-Posed Two-Layer Turbulence Model, *ESAIM: Mathematical Modelling and Numerical Analysis - Modélisation Mathématique et Analyse Numérique*, 35(6):1111-1136, 2001.

10. B. Mohammadi and G. Puigt, Generalized Wall Functions for High Speed Flows over Adiabatic and Isothermal Walls, *International Journal of Computational Fluid Dynamics*, 14(3):183-200, 2001.

D.2 Conference papers

A. N. Villedieu, G. Puigt and J-F. Boussuge, High Order Workshop: computations performed with JAGUAR, an in-house CFD code based on a spectral difference formalism. In *2nd International Workshop on High-Order CFD Methods*, May 27-28, Cologne, 2013.

B. G. Puigt, M. Gazaix, M. Montagnac, M.-C. Le Pape, M. de La Llave Plata, C. Marmignon, J.-F. Boussuge and V. Couaillier, Development of a new hybrid compressible solver inside the CFD *elsA* software, *20th Computational Fluid Dynamics Conference*, 27-30 June, Honolulu (HI), USA, AIAA Paper 2011-3379, 2011.

C. F. Dezitter, K. Zeggai, K. Britchford, H. Bezard, G. Joubert and G. Puigt, Installation Effects Characterization of VHBR Engines: 3. CFD Assessment for Jet Mixing, in *15th AIAA/CEAS Aeroacoustics Conference (30th AIAA Aeroacoustics Conference)*, Miami, Florida, May 11-13, AIAA Paper 2009-3370, 2009.

D. O. Frayssinet, G. Puigt, J. Couzi, P. Tran, Radiative Transfer in PRE-X Flowfield, in *5th European Workshop on Thermal Protection Systems and Hot Structures*, 17-19 May, ESA, Noordwijk, The Netherlands, 2006.

E. S. Galera, L. Hallo, B. Mohammadi, G. Puigt, Wall-Laws for Heat Transfer Predictions in Thermal Turbulent Flows, in *38th AIAA Thermophysics Conference*, Toronto, Ontario, June 6-9, AIAA Paper 2005-5200, 2005.

F. S. Galera, G. Puigt, L. Hallo and B. Mohammadi, Wall-Laws Including Thermal Model ling for Hypersonic Turbulent Flows, in *4th International Symposium on Atmospheric Reentry Vehicles and Systems*, organised by AAAF and EADS Space, 21-23 Mars, Arcachon (France), 2005.

G. G. Puigt and B. Mohammadi, Les lois de paroi en mécanique des fluides supersoniques, in *Conférence de la Société de Mathématiques Appliquées et Industrielles (SMAI)*, 28 mai - 1 juin, Pompadour, France (in French), 2001.

H. G. Puigt and B. Mohammadi, Generalized Wall Functions for Adiabatic and Isothermal Walls, in *European Congress on COmputational Methods for Applied Sciences - ECCOMAS*, 11 - 14 september, Barcelona (Spain), 2000.

I. B. Koobus, B.Mohammadi, G. Puigt, Distributed 3D Shape Optimization with Incomplete Sensitivities and CAD-Free Framework for High- Speed Inviscid and Viscous Turbulent Regimes, in *18th Applied Aerodynamics Conference*, Denver, Colorado, USA, AIAA Paper 2000-4526, 2000.

J. G. Puigt and B. Mohammadi, Generalized Wall Functions for High-Speed Flows over Adiabatic and Isothermal Walls, in *Fluids With Interactions Conference*, organised by CNRS (GDR 1135) and INRIA, 11 - 14 october, Sophia Antipolis (France), 1999.

D.3 Research report available on the web

(a) B. Mohammadi and G. Puigt, Wall-Laws for High Speed Flows over Adiabatic and Isothermal Walls, INRIA research report, RR-3948, 2000.

E Contract reports

Contract reports represent the transfer of knowledge between research and industry. I am involved in many contract reports, essentially for Cerfacs' shareholders. I tried to group reports by thematics.

E.1 Wake vortex

- G. Puigt, *Numerical study of wake vortices of the F11 aircraft model : Effects of differential flap setting on wake vortices.* Cerfacs Contract report CR/CFD/03/6, 2003.

E.2 Wall functions

- G. Puigt, *Optimization of computational costs - Implementation and validation of wall-functions for moving / deformable meshes.* Cerfacs Contract Report CR/CFD/08/156, 2008.

E.3 Harmonic Balance Method

- G. Puigt, N. Gourdain and J-F. Boussuge, *Premier rapport d' avancement du projet AITEC fiche A5, Phase 1 : Time harmonic balance T0+3mois.* Cerfacs Contract Report CR/CFD/06/14, 2006.
- G. Puigt, *Première note de conception de la THB projet AITEC fiche a5, phase 1 : Génération des scripts python - T0+6 mois.* Cerfacs Contract Report CR/CFD/06/39, 2006.
- G. Puigt, *Second rapport d'avancement du projet AITEC fiche A5, phase 1 : Time harmonic balance t0+6 mois.* Cerfacs Contract Report CR/CFD/06/40, 2006.

- G. Puigt, N. Gourdain and J-F. Boussuge, *Second rapport d'avancement du projet AITEC fiche a5, phase 1 : Time harmonic balance T0+9 mois.* Cerfacs Contract Report CR/CFD/06/66, 2006.
- G. Puigt, F. Sicot, N. Gourdain and J-F. Boussuge, *Troisième rapport d'avancement du projet AITEC fiche A5, phase 1 : Time harmonic balance t0+15 mois.* Cerfacs Contract Report CR/CFD/07/29, 2007.
- G. Puigt, F. Sicot, N. Gourdain and J-F. Boussuge, *Dernier rapport contractuel du projet AITEC fiche a5, phase 1 : Time harmonic balance - t0+18 mois.* Cerfacs Contract Report CR/CFD/07/57, 2007.
- G. Dufour, G. Puigt, F. Sicot, N. Gourdain and J-F. Boussuge, *Projet MACAO.* Cerfacs Contract report CR/CFD/07/106, 2007.
- G. Dufour, G. Puigt, F. Sicot, N. Gourdain and J-F. Boussuge, *Projet MACAO : application d'une méthode harmonique non-linéaire au cas du flottement d'un rotor isolé - WP2 (t0 + 8 mois) : Pré-traitement des calculs.* Cerfacs Contract Report CR/CFD/08/17, 2008.
- G. Dufour, G. Puigt, F. Sicot, N. Gourdain and J-F. Boussuge, *Projet MACAO : application d'une méthode harmonique non-linéaire au cas du flottement d'un rotor isolé - WP3 (t0 + 10 mois) : Implémentation et validation 2D.* CerfacsContract Report CR/CFD/08/49, 2008.
- G. Dufour, G. Puigt, F. Sicot, N. Gourdain and J-F. Boussuge, *Projet MACAO : application d'une méthode harmonique non-linéaire au cas du flottement d'un rotor isolé - WP4 (t0 + 12 mois) : Implémentation et validation 3D.* Cerfacs Contrat Report CR/CFD/08/66, 2008.
- F. Sicot, G. Puigt and J-F. Boussuge, *Premier rapport d'avancement du projet AITEC fiche a5, phase 2.* Cerfacs Contract report CR/CFD/08/91, 2008.
- G. Dufour, G. Puigt and J-F. Boussuge, *Projet ANANAS II :activités CERFACS - Etude de l'approche d'équilibrage harmonique pour écoulements à incidence périodique sur configuration industrielle - premier rapport d'avancement.* Cerfacs Contract Report CR/CFD/08/95, 2008.
- G. Dufour, F. Sicot, G. Puigt and J-F. Boussuge, *Contrat ANANAS2 : Calculs périodiques de type pitching airfoil avec approche TSM dans le logiciel* elsA *. rapport d'avancement à T0+6M.* Cerfacs Contrat Report CR/CFD/08/130, 2008.
- G. Dufour, F. Sicot, G. Puigt, N. Gourdain and J-F. Boussuge, *Projet MACAO: Application d'une méthode harmonique non-linéaire au cas du flottement d'un rotor isolé - WP5: Mise en oeuvre et validation des conditions aux limites.* Cerfacs Contract Report CR/CFD/09/2, 2009.
- F. Sicot, G. Puigt and J-F. Boussuge, *Second rapport du projet AITEC fiche a5, phase 2 : Time spectral method T1+6m.* Cerfacs Contract Report CR/CFD/09/3, 2009.

- F. Sicot, G. Dufour, G. Puigt and J-F. Boussuge, *Projet AITEC fiche A5, phase 2 : time spectral method T1 + 9 mois.* Cerfacs, Contract report CR/CFD/09/26, 2009.

- J-F. Boussuge, G. Puigt, N. Gourdain, F. Sicot and G. Dufour, *Développement de la méthode HBT bi-fréquences dans le logiciel elsA : Lot 1 (t0 + 6 mois) - synthèse bibliographique.* Cerfacs Contract Report CR/CFD/09/30, 2009.

- G. Dufour, G. Puigt, F. Sicot and J-F. Boussuge, *Contrat PHYV-ANANAS II - calculs périodiques de type pitching airfoil avec TSM dans le logiciel elsA - rapport contractuel final de la phase 1.* Cerfacs Contract Report CR/CFD/09/63, 2009.

- F. Sicot, F. Dufour, G. Puigt and J-F. Boussuge, *Projet AITEC, fiche a5, phase 2 : Time spectral method - T1+15 mois.* Cerfacs, Contract Report CR/CFD/09/79, 2009.

- G. Dufour, T. Guedeney, F. Sicot, G. Puigt, N. Gourdain and J-F. Boussuge, *Développement de la méthode HBT bi-fréquences dans le logiciel: Lots 2 et 3.1 (t0+12 mois): D:éveloppement, implantation et première validation.* Cerfacs Contract Report CR/CFD/09/113, 2009.

- N. Gourdain, F. Sicot, G. Dufour, G. Puigt and J-F. Boussuge, *Rapport final AITEC phase 2. Simulation numérique des écoulements instationnaires à l'aide de la méthode TSM : applications aux calculs aéroacoustiques dans les turbomachines.* Cerfacs Contract Report CR/CFD/11/6, 2011.

- T. Guédeney, A. Gomar, F. Gallard, F. Sicot, G. Dufour and G. Puigt, *Non-uniform time sampling for multiple frequency harmonic balance computations.* Cerfacs Contract Report TR/CFD/12/42, 2012.

E.4 Aeroacoustics

- G. Puigt, J-F. Boussuge and H. Deniau, *Projet JECOP - Aéroacoustique des jets supersoniques - rapport final - commande airbus 2882986.* Cerfacs Contract Report CR/CFD/12/71, 2012.

- G. Puigt, J-F. Boussuge and H. Deniau, *Projet JECOP2 - Aéroacoustique des jets supersoniques - rapport intermédiaire.* Cerfacs Contract Report CR/CFD/12/117, 2012.

- G. Daviller, G. Puigt and J-F. Boussuge, *Rapport de synthèse projet REBECCA : Réduction du bruit de jet.* Cerfacs Contract Report CR/CFD/13/36, 2013.

- G. Daviller, G. Puigt, J-F. Boussuge and J. Delville, *Rapport commun Pprime CERFACS de synthèse au projet REBECCA.* Cerfacs Contract report CR/CFD/13/38, 2013.

- G. Puigt, J-F. Boussuge and H. Deniau, *Projet JECOP2 - aéroacoustique des jets supersoniques - rapport final.* Cerfacs Contract report CR/CFD/13/44, 2013.

- G. Daviller, G. Puigt and J-F. Boussuge, *Validation of meshing technique and two-steps procedure jet noise simulation RANS/LES.* Cerfacs Contract Report CR/CFD/13/108, 2013.

E.5 Unstructured and hybrid capability in *elsA*

- G. Puigt, M. Montagnac and M. Gazaix. *Avancement du projet elsA hybride au 30 avril 2009.* Cerfacs Technical Report TR/CFD/09/31, 2009.

F Software development

Due to my position at Cerfacs, just between academic research and industry, my work cannot be only analysed regarding communications. A large part of my activity concern software development. I added many functionalities inside the *elsA* code of ONERA, but I want to introduce in this section my involvement in *DEPICT* and *JAGUAR*.

F.1 *JAGUAR*

JAGUAR is a CFD code based on unstructured mesh composed of hexahedra only and it solves the Navier-Stokes equations following a Spectral Difference paradigm. *JAGUAR* was introduced in Chapter. 12 and the main results won't be recalled here. Just to mention that *JAGUAR* is written in fortran 90, it is based on a hybrid OpenMP / MPI formalism and can be run on GPGPU. The code contains about 20 000 lines for CPU architecture and 5 000 lines for GPGPU.

F.2 *DEPICT*

Nowadays, the size of the *elsA* code is too large to be handled easily by students. It means that students can perform simulations but they need many hours of training and a large knowledge of the CFD code before being able to perform modifications in the kernel. The situation is worse for adding new functionalities.

elsA is based on a cell-centred formalism and new efforts concern its unstructured part. It is therefore of great interest to be able to propose a CFD code in which development is made easy by an efficient and readable data structure. *DEPICT* was designed with this objective. *DEPICT* means DEvelopment Platform for hIgh order schemes on unstruCTured grids. It is written in fortran 90 and can perform simulations in sequential or in parallel following a MPI approach. I/O are performed using CGNS library and tecplot files. *DEPICT* contains 2 convection schemes and 5 diffusion schemes. Time integration is performed with a Runge-Kutta procedure but an implicit matrix-free GMRES was developed and validated for Euler flows and it will be reintroduced in the kernel soon. It is the platform used to develop new schemes dedicated to LES on unstructured grids. The kernel is not really optimised: it is written with the goal to be easily readable. Source files are under the source code management system git.

DEPICT was used during many in-depth studies at SupAero.

Bibliography

[1] *elsA* web site. `http://elsa.onera.fr`.

[2] AGARD. Compendium of unsteady aerodynamic measurements. Technical Report 702, Advisory Group for Aerospace Research and Development, North Atlantic Treaty Organization, 1982.

[3] S.R. Allmaras, F.T. Johnson, and P.R. Spallart. Modifications and clarifications for the implementation of the Spalart-Allmaras turbulence model. In *Seventh International Conference on Computational Fluid Dynamics (ICCFD7), Big Island, Hawaii, 9-13 July, Paper ICCFD7-1902*, 2012.

[4] R.A. Antonia and J. Kim. Turbulent Prandtl number in the near-wall region of a turbulent channel flow. *International Journal of Heat and Mass Transfer*, 34:1905–1908, 1991.

[5] V. Auffray. *Étude comparative de schémas numériques pour la modélisation de phénomènes diffusifs sur maillages hybrides.* PhD thesis, Institut National Polytechnique de Toulouse, 2007.

[6] B. Aupoix. Introduction to turbulence modelling for compressible flows. In *VKI Lecture Series 2000-04, Introduction to the modeling of turbulence III.* Von Kármán Institute, 2000.

[7] B. Aupoix. A general strategy to extend turbulence models to rough surfaces: Application to Smith's $k-l$ model. *Journal of Fluids Engineering*, 129(10):1245–1254, 2007.

[8] N. Bagheri, C.J. Strataridakis, and B.R. White. Measurements of turbulent boundary layer Prandtl numbers and space-time temperatures correlations. *AIAA Journal*, 30:35–42, 1992.

[9] B.S. Baldwin and H. Lomax. Thin layer approximation and algebraic model for separated turbulent flows. In *AIAA 16th Aerospace Sciences Meeting, January 16-18, Huntsville, Alabama*, 1978. AIAA Paper 78-257.

[10] T.J. Barth. Aspects of unstructured grids and finite-volume solvers for the Euler and Navier-Stokes equations. In *VKI Lecture Series 1994-05.* Von Kármán Institute, Rhode-St.-Genèse, Belgium, 1995.

[11] A.S. Besicovitch. *Almost Periodic Functions.* Cambridge University Press, 1932.

[12] P.L. Bhatnagar, E.P. Gross, and M. Krook. A model for collisional processes in gases i: small amplitude processes in charged and in neutral one-component systems. *Physical Review*, 94:511–525, 1954.

[13] R.T. Biedron and J.L. Thomas. A generalized patched-grid algorithm with application to the F-18 forebody with actuated control strake. *Computing Systems in Engineering*, 1:563–576, 1990.

[14] V. Billey, J. Periaux, B. Stoufflet, A. Dervieux, L. Fezoui, and V. Selmin. Recent improvements in Galerkin and upwind Euler solvers and application to 3-D transonic flow in aircraft design. *Computer Methods in Applied Mechanics and Engineering*, 75(1-3):409–414, 1989.

[15] J. Boussinesq. *Théorie de l'écoulement tourbillonant et tumultueux des liquides dans les lits rectilignes à grande section*, volume I,II. Gauthier Villars, Paris, 1897.

[16] R.H. Byrd, P. Lu, J. Nocedal, and C. Zhu. A limited memory algorithm for bound constrained optimization. *SIAM Journal on Scientific Computing*, 16:1190–1208, 1994.

[17] L. Cambier, S. Heib, and S. Plot. The Onera *elsA* CFD software: input from research and feedback from industry. *Mechanics and Industry*, 14(3):159–174, 2013.

[18] C. Canuto, M.Y. Hussaini, A. Quarteroni, and V.V. Rusanov T.A. Orszag. *Spectral Methods in Fluid Dynamics.* Springer-Verlag, 1987.

[19] B. Cardot, B. Mohammadi, and O. Pironneau. A few tools for turbulence models in Navier-Stokes equations. In *Incompressible computational fluid dynamics. Trends and Advances*, pages 1–16. Cambridge University Press, 1993.

[20] A. Cassagne. Implémentation multi-GPU de la méthode spectral differences pour un code de CFD. Technical report, Cerfacs, Technical Report WN/CFD/14/5 (inFrench), 2014.

[21] S. Catris and B. Aupoix. Density corrections for turbulence models. *Aerospace Science and Technology*, 4(1):1–11, 2000.

[22] P. Chassaing. *Mécanique des fluides.* Editions Cepadues, 1995.

[23] H.C. Chen and V.C. Patel. Near-wall turbulence models for complex flows including separation. *AIAA Journal*, 26(6):641–648, 1988.

[24] J.H. Chen. Petascale direct numerical simulation of turbulent combustion - fundamental insights towards perdictive models. *Proceedings of the Combustion Institute*, 33:99–123, 2011.

[25] K-Y. Chien. Predictions of channel and boundary-layer flows with a low-Reynolds-number turbulence model. *AIAA Journal*, 20(1):33–38, 1982.

[26] W.S. Clark and K.C. Hall. A time-linearized Navier-Stokes analysis of stall flutter. *Journal of Turbomachinery*, 122(3):467–476, July 2000.

[27] Y. Colin. *Simulation numérique de la distortion générée par une entrée d'air de moteur civil par vent de travers.* PhD thesis, École Nationale Supérieure de l'Aéronautique et de l'Espace, 2007.

[28] S. Corsin. Heat transfer in isotropic turbulence. *Journal of Applied Physics*, 23:113–118, 1952.

[29] J. Cousteix. *Turbulence et couche limite.* Cepadues, 1990.

[30] P.I. Crumpton, J.A. Mackenzie, and K.W. Morton. Cell vertex algorithms for the compressible Navier-Stokes equations. *Journal of Computational Physics*, 109(1):1–15, 1993.

[31] P.I. Crumpton, P. Moinier, and M.B. Giles. An unstructured algorithm for high Reynolds number flows on highly stretched grids. In C. Taylor and J. T. Cross, editors, *Numerical Methods in Laminar and Turbulent Flow*, pages 561–572. Pineridge Press, 1997.

[32] D.B. DeGraff and J.K. Eaton. Reynolds-number scaling of the flat plate boundary layer. *Journal of Fluid Mechanics*, 422:319–346, 2000.

[33] J. Delbove. *Full Navier-Stokes Unsteady Simulations: Application to Flutter Prediction – Contribution aux Outils de Simulation Aéroélastique des Aéronefs : Prédiction du Flottement et Déformation Statique des Voilures.* PhD thesis, École Nationale Supérieure de l'Aéronautique et de l'Espace, 2005.

[34] J. Delery and M.C. Coet. Experiments on shock-wave/boundary-layer interactions produced by two-dimensional ramps and three-dimensional obstacles. In *Proceeding of Workshop on Hypersonic Flows for Reentry Problem, Antibes, France*, 1990.

[35] A. Dervieux. Steady Euler simulations using unstructured meshes. In *16th VKI Lecture Series on Computational Fluid Dynamics 1985-04.* Von Kármán Institute, 1985.

[36] P. Dreyfus. Results for a turbulent system with unbounded viscosities: weak formulations, existence of solutions, boundedness, smoothness. *Nonlinear Analysis: Thoery, Methods and Applications*, 68(6):1462–1478, 2008.

[37] P. Dreyfus. Analysis of a singular convection diffusion system arising in turbulence modelling. *International Journal of Partial Differential Equations*, Article ID 940924, 16 pages, 2013.

[38] G. Duffa. *Ablation.* CESTA, Edition 1 du 28 novembre 1996 (in French), 1996.

[39] G. Dufour, F. Sicot, G. Puigt, C. Liauzun, and A. Dugeai. Contrasting the harmonic balance and linearized methods for oscillating-flap simulations. *AIAA Journal*, 48(4):788–797, 2010.

[40] P.A. Durbin, G. Medic, J.M. Seo, J.K. Eaton, and S. Song. Rough wall modification of two-layer $k - \varepsilon$. *ASME Journal of Fluids Engineering*, 123:16–21, 2001.

[41] K. Ekici and K.C. Hall. Nonlinear analysis of unsteady flows in multistage turbomachines using harmonic balance. *AIAA Journal*, 45(5):1047–1057, 2007.

[42] K. Ekici and K.C. Hall. Nonlinear frequency-domain analysis of unsteady flows in turbomachinery with multiple excitation frequencies. *AIAA Journal*, 46(8):1912–1920, 2008.

[43] B. Epstein and S. Peigin. Treatment of nonmatched grids for high-accuracy Navier-Stokes solutions. *AIAA Journal*, 48:1542–1553, 2010.

[44] A. Favre, L.S.G. Kovasnay, R. Dumas, J. Gaviglio, and M. Coantic. *La turbulence en mécanique des fluides*. Gauthier Villars ED., 1976.

[45] Advisory Council for Aviation Research and Innovation in Europe (ACARE). *Strategic Research and Innovation Agenda, Vol 1.* September 2012.

[46] O. Frayssinet. Lois de paroi pour écoulements hypersoniques sur parois rugueuses. Master's thesis, Ecole des Mines de Nancy, reference DAM/CESTA/DIA/SCDA/GREC DO 582 du 11/08/2004, 2004.

[47] S. Galera. *Modélisation thermique de la turbulence en régime hypersonique. Application au développement de lois de paroi pour paroi lisse et rugueuse.* PhD thesis, Université de Montpellier II, France (in French), 2005.

[48] S. Galera, B. Mohammadi, and G. Puigt. Turbulence modeling for hypersonic flows over isothermal walls. *International Journal of Computational Fluid Dynamics*, 20(8):549–561, 2006.

[49] S. Galera, G. Puigt, L. Hallo, and B. Mohammadi. Wall-laws including thermal modelling for hypersonic turbulent flows. In *4th International Symposium on Atmospheric Reentry Vehicles and Systems, organized by AAAF and EADS Space, 21-23 Mars, Arcachon (France)*, 2005.

[50] M. Galle. Unstructured viscous flow solution using adaptive hybrid grids. ICASE/LaRC workshop on adaptive grid methods, NASA Langley Research Center, 1995.

[51] T. Gallouët, J. Lederer, R. Lewandowski, F. Murat, and L. Tartar. On a turbulent system with unbounded eddy viscosities. *Nonlinear Analysis: Theory, Methods and Applications*, 52(4):1051–1068, 2003.

[52] M. Gómez Mármol and F. Ortegón Gallego. Coupling the Stokes and Navier-Stokes equations with two scalar nonlinear parabolic equations. *Mathematical Modelling and Numerical Analysis*, 33(1):157–167, 1999.

[53] M. Gómez Mármol and F. Ortegón Gallego. Existence of solution to non-linear elliptic systems arising in turbulence modelling. *Mathematical Models and Methods in Applied Sciences*, 10(2):247–260, 2000.

[54] E. Goncalves. *Implantation et validation de lois de paroi dans un code Navier-Stokes.* PhD thesis, Ecole Nationale Supérieure de l'Aéronautique et de l'Espace, 2001.

[55] E. Goncalves and R. Houdeville. Reassessment of the wall functions approach for RANS computations. *Aerospace Science and Technology*, 15(1):1–14, 2001.

[56] A. Gopinath and A. Jameson. Time spectral method for periodic unsteady computations over two- and three- dimensional bodies. In *43rd Aerospace Sciences Meeting and Exhibit, Reno, Nevada. AIAA Paper 2005-1220*, 2005.

[57] A. Gopinath and A. Jameson. Application of the time spectral method to periodic unsteady vortex shedding. In *44th AIAA Aerospace Sciences Meeting and Exhibit, Reno, Nevada. AIAA Paper 2006-0449*, 2006.

[58] A. Gopinath, E. van der Weide, J.J. Alonso, A. Jameson, K. Ekici, and K.C. Hall. Three-dimensional unsteady multi-stage turbomachinery simulations using the harmonic balance technique. In *45th AIAA Fluid Dynamics Conference and Exhibit, Reno. AIAA Paper 2007-0892*, 2007.

[59] N. Gourdain, X. Ottavy, and A. Vouillarmet. Experimental and numerical investigation of unsteady flows in a high speed three stage compressor. In *8-th European Turbomachinery Conference*, Graz (Austria), 2009.

[60] T. Guédeney, A. Gomar, F. Gallard, F. Sicot, G. Dufour, and G. Puigt. Non-uniform time sampling for multiple-frequency harmonic balance computations. *Jorunal of Computational Physics*, 236(1):317–345, 2013.

[61] K.C. Hall. A linearized Euler analysis of unsteady flows in turbomachinery. Technical report, MIT Gas Turbine Laboratory, Report GTL-190, 1987.

[62] K.C. Hall, J.P. Thomas, and W.S. Clark. Computation of unsteady nonlinear flows in cascades using a harmonic balance technique. *AIAA Journal*, 40:879–886, 2002.

[63] K.C. Hall, J.P. Thomas, K. Ekici, and D.M. Voytovich. Frequency domain techniques for complex and nonlinear flows in turbomachinery. In *33rd AIAA Fluid Dynamics Conference and Exhibit, Orlando, Florida. AIAA Paper 2003-3998*, 2003.

[64] H. Hattori, Y. Nagano, and M. Tagawa. Analysis of turbulent heat transfer under various thermal conditions with two-equation models. In *Engineering turbulence Modelling and Experiments 2, Elsevier*, pages 43–52, 1993.

[65] M. El Hayek. *Transfert de chaleur par convection en régime turbulent : Aspects physiques et numériques*. PhD thesis, Faculté Polytechnique de Mons, 1996.

[66] K. Horiuti. Assessment of two-equation models of turbulent passive-scalar diffusion in channel flow. *Journal of Fluid Mechanics*, 283:405–433, 1992.

[67] C.B. Hwang and C.A. Lin. A low Reynolds number two-equation $k_\theta - \tilde{\varepsilon_\theta}$ model to predict thermal fiels. *International Journal of Heat and Mass Transfer*, 42(17):3217–3230, 1999.

[68] Y. Iritani, N. Kasagi, and M. Hirata. Heat transfer mechanism and associated turbulence structure in the near-wall region of a turbulent boundary layer. In *Symposium on Turbulent Shear Flows, 4th, Karlsruhe, West Germany*, pages 17.31–17.36, 1983.

[69] C.A.K. Irwin and P.R. Guyett. The subcritical response and flutter of a swept wing model. Technical Report 3497, Aeronautical Research Council Reports and Memoranda, August 1965.

[70] A. Jalali and C. Ollivier-Gooch. Accuracy assessment of finite volume discretizations of diffusive fluxes on unstructured meshes. In *50th AIAA Aerospace Sciences Meetinf including the New Horizons Forum and Aerospace Exposition, 09-12 January, Nashville, Tennessee, AIAA Paper 2012-0608*, 2012.

[71] A. Jameson. Time dependent calculations using multigrid, with applications to unsteady flows past airfoils and wings. In *AIAA 10th Computational Fluid Dynamics Conference, June 24-26, Honolulu, HI. AIAA Paper 1991-1596*, 1991.

[72] A. Jameson, W. Schmidt, and E. Turkel. Numerical solution of the Euler equations by finite volume methods using Runge-Kutta time-stepping schemes. In *AIAA 14th Fluid and Plasma Dynamic Conference, June 23-25, Palo Alto, California, AIAA paper 1981-1259*, 1981.

[73] M. Jisha and H.B. Rieke. About the prediction of turbulent Prandtl and Schmidt numbers from modeled transport equations. *International Journal of Heat and Mass Transfer*, 22:1547–1555, 1979.

[74] J-C. Jouhaud. Evaluation of the Lattice-Boltzmann method on aircraft applications. Technical report, Cerfacs, 2014.

[75] G. Kalitzin, G. Medic, G. Iaccarino, and P. Durbin. Near-wall behavior of RANS turbulence models and implications for wall functions. *Journal of Computational Physics*, 204:265–291, 2005.

[76] W.M. Kays. Turbulent Prandtl numbers - where are we ? *Transactions of the ASME, Journal of Heat Transfer*, 116:284–295, 1947.

[77] J. Kim and P. Moin. Transport of passive scalars in a turbulent channel flow. In *Symposium on Turbulent Shear Flows, 6th, AIAA 16th Aerospace Sciences Meeting, January 16-18, Huntsville, Alabama*, pages 85–96, 1987.

[78] D.A. Kopriva. A staggered-grid multidomain spectral method for the compressible Navier-Stokes equations. *Journal of Computational Physics*, 143:125–158, 1998.

[79] K. Kundert, G. Sorkin, and A. Sangiovanni-Vincentelli. Applying harmonic balance to almost-periodic circuits. *IEEE Transactions on microwaves Theory and Techniques*, 36:366–378, 1988.

[80] M. Kuzmin. Spectral difference method for the Euler equations on unstructured grids. Master's thesis, ISAE - SupAero, 2012.

[81] L. Landau and E. Lifchitz. *Physique théorique.* Mir Ed., second edition, 1989.

[82] R.H. Landon. NACA0012 oscillatory and transient pitching. Technical report, AGARD Report 702, Dataset 3, Compendium of Unsteady Aerodynamic Measurements, August 1982.

[83] P. Larrieu. Private communications.

[84] B.E. Launder. *Turbulence : Heat and Mass Transport.* P. Bradshaw ed., Springer Verlag, 1976.

[85] M.k. Lee, N. Malaya, and R.D. Moser. Petascale direct numerical simulation of turbulent channel flow on up to 786k cores. In *SC '13 Proceedings of SC13: International Conference for High Performance Computing, Networking, Storage and Analysis, Denver, CO*, 2013.

[86] A. Lerat and Z. N. Wu. Stable conservative multidomain treatments for implicit Euler solvers. *Journal of Computational Physics*, 123:45–64, 1996.

[87] A.J. Lew, G.C. Buscaglia, and P.M. Carrica. A note on the numerical treatment of the $k-\varepsilon$ turbulence model. *International Journal of Computational Fluid Dynamics*, 14(3):201–209, 2001.

[88] R. Lewandowski and B. Mohammadi. Existence and positivity results for the $\phi-\theta$ and a modified $k-\varepsilon$ two-equations turbulence models. *Mathematical Models and Methods in Applied Sciences*, 3(2):195–215, 1993.

[89] C. Liauzun, E. Canonne, and G. D. Mortchéléwicz. Flutter numerical computations using the linearized Navier-Stokes equations. In *RTO-MP-AVT-154 - Advanced Methods in Aeroelasticity, papers presented at the RTO Applied Vehicle Technology Panel (AVT) Specialists' Meeting held in Loen, Norway, 5-8 May*, 2008.

[90] Y. Liu, M. Vinokur, and Z.J. Wang. Spectral difference method for unstructured grids I: Basic formulation. *Journal of Computational Physics*, 216:780–801, 2006.

[91] I. Marter. Handling different h and p in the framework of spectral difference method. Master's thesis, Université de Pau et Pays de l'Adour, 2013.

[92] G. May and A. Jameson. Unstructured algorithms for inviscid and viscous flows embedded in a unifier solver architecture floxx. In *43rd AIAA Aerospace Sciences Meeting and Exchibit, Reno, January 10-13. AIAA Paper 2005-318*, 2005.

[93] M. McMullen, A. Jameson, and J. Alonso. Acceleration of convergence to a periodic steady state in turbomachinery flows. In *39th Aerospace Sciences Meeting, Reno, Nevada. AIAA Paper 2001-0152*, 2001.

[94] F.R. Menter. Two-equation eddy-viscosity turbulence models for engineering applications. *AIAA Journal*, 32(8):1598–1605, August 1994.

[95] B. Mohammadi. A stable algorithm for the $k-\varepsilon$ model for compressible flows. Technical report, INRIA, RR-1355, December 1990.

[96] B. Mohammadi. Complex turbulent flows computations with a two-layer approach. *International Journal for Numerical Methods in Fluids*, 15:747–771, 1992.

[97] B. Mohammadi. Fluid dynamics computation with NCS2KE: an user-guide. Technical report, INRIA, RT-0164, May 1994.

[98] B. Mohammadi and O. Pironneau. Compressibility corrections and two-layer $k-\varepsilon$ models for hypersonic turbulent flows on unstructured grid. *International Journal of Computational Fluid Dynamics*, 4(3-4):285–306, 1995.

[99] B. Mohammadi and G. Puigt. Generalized wall functions for high speed flows over adiabatic and isothermal walls. *International Journal of Computational Fluid Dynamics*, 14(3):183–200, 2001.

[100] B. Mohammadi and G. Puigt. Mathematical and numerical analysis of an alternatice well-posed two-layer turbulence model. *Mathematical Modelling and Numerical Analysis*, 35(6):1111–1136, 2001.

[101] B. Mohammadi and G. Puigt. Generalized wall functions for rough walls based on data assimilation. *International Journal of Computational Fluid Dynamics*, 17(6):453–465, 2003.

[102] B. Mohammadi and G. Puigt. Wall functions in computational fluid dynamics. *Computers & Fluids*, 35(10):1108–1115, 2006.

[103] B. Mohammadi and J.H. Saiac. Turbulent compressible axisymmetric flows computations with the $k-\varepsilon$ model. *International Journal of Computational Fluid Dynamics*, 2(1):115–133, 1993.

[104] M. Mohan Rai. A conservative treatment of zonal boundaries for Euler equation calulations. *Journal of Computational Physics*, 62:472–503, 1986.

[105] M. Mohan Rai. An implicit, conservative, zonal-boundary scheme for Euler equation calculations. *Computers & Fluids*, 14:295–319, 1986.

[106] M. Mohan Rai. A relaxation approach to patched-grid calculations with the Euler equations. *Journal of Computational Physics*, 66:99–131, 1986.

[107] M. Montagnac. Non coincident conservative adjacent join boundary condition. Technical report, CERFACS.

[108] Y. Morchoisne. Résolution des équations de Navier-Stokes par une méthode pseudospectrale en espace-temps. *La Recherche Aérospatiale*, 5:293–306, 1979.

[109] G. D. Mortchéléwicz. Aircraft aeroelasticity computed with linearized RANS equations. In *Book of abstracts of the 43rd Israel Annual Conference on Aerospace Sciences*, 2003.

[110] Y. Nagano. Modelling heat transfer in near-wall flows. In *Proceedings of the conference entitled Closure Strategies For Modelling Turbulent And Transitional Flows, Cambridge, Uniter Kingdom*, pages 1–52, 1999.

[111] Y. Nagano and C. Kim. A two-equation model for heat transport in wall turbulent shear flows. *Journal of Heat Transfer (Transaction of the ASME)*, 110:583–589, 1988.

[112] Y. Nagano, M. Tagawa, and T. Tsuji. An improved heat transfer model for wall turbulent shear flows. In *Proceedings of the 3rd ASME/JMSE Thermal Engineering Joint Conference 3*, pages 233–240, 1991.

[113] G. Puigt. *Modélisation, étude mathématique et validation de lois de paroi pour les écoulements hypersoniques pour parois lisses et rugueuses*. PhD thesis, Université Montpellier II, 2001.

[114] G. Puigt. Optimization of computational costs - implementation and validation of wall-functions for moving / deformable meshes. Technical report, CERFACS, CR-CFD-08-156, 2008.

[115] G. Puigt, V. Auffray, and J.D. Müller. Discretisation of diffusive fluxes on hybrid grids. *Journal of Computational Physics*, 229(5):1425–1447, 2010.

[116] G. Puigt and H. Deniau. Mesh and discretization release 1.1 - CFD e-Learning. Technical Report US/CFD/11/54, CERFACS, January 2011.

[117] G. Puigt, M. Gazaix, M. Montagnac, M.-C. Le Pape, M. de La Llave Plata, C. Marmignon, J.-F. Boussuge, and V. Couaillier. Development of a new hybrid compressible solver inside the CFD *elsA* software. In *20th Computational Fluid Dynamics Conference, 27-30 June 2011, Honolulu (HI), USA, 2011. AIAA Paper 2011-3379*, 2011.

[118] W.H. Reed and T.R. Hill. Triangular mesh methods for the neutron transport equation. Technical report, Los Alamos National Laboratory, New Mexico, USA, Tech. Report LU-UR-73-279, 1973.

[119] A.J. Reynolds. *Turbulent Flows in Engineering.* John Wiley & Sons, London (UK), 1974.

[120] A.J. Reynolds. The prediction of turbulent Prandtl and Schmidt numbers. *International Journal of Heat and Mass Transfer*, 18:1055–1069, 1975.

[121] O. Reynolds. On the dynamical theory of incompressible viscous fluids and the determination of the criterion. *Papers on Mechanical and Physical Subjects II*, pages 535–477, 1901.

[122] P.L. Roe. Approximate Riemann solvers, parameter vectors and difference schemes. *Journal of Computational Physics*, 135(2):250–258, 1981.

[123] P. Rostand and B. Stoufflet. Finite volume Galerkin methods for viscous gas dynamics. Technical report, INRIA, RR-863, 1988.

[124] C. J. Roy and F. G. Blottner. Review and assessment of turbulence models for hypersonic flows. *Progress in Aerospace Sciences*, 42(7):469–530, 2006.

[125] C. L. Rumsey. Computation of acoustic wave through sliding-zone interfaces using an Euler/Navier-Stokes code. In *2nd AIAA/CEAS Aeroacoutics Conference State College, PA. AIAA Paper AIAA 96-1752*, 1996.

[126] Y. Saad. *Iterative Methods for Sparse Linear Systems.* SIAM, 2nd edition, 2003.

[127] H. Schlichting. *Boundary Layer Theory.* McGraw-Hill, 1968.

[128] T. Schönfeld and M. Rudgyard. Steady and unsteady flows simulations using the hybrid flow solver AVBP. *AIAA Journal*, 37(11):1378–1385, 1999.

[129] C.E. Shannon. Communication in the presence of noise. *Proceeding of the IRE*, 37(1):10–21, January 1949.

[130] E.V. Shishov, P.S. Roganov, S.I. Grabarnik, and V.P. Zabolotsky. Heat transfer in the recirculating region formed by a backward-facing step. *International Journal of Heat and Mass Transfer*, 31:1557–1562, 1988.

[131] F. Sicot, G. Puigt, and M. Montagnac. Block-Jacobi implicit algorithms for the time spectral method. *AIAA Journal*, 46(12):3080–3089, 2008.

[132] B.R. Smith. The $k - kl$ turbulence model and wall layer model for compressible flows. In *AIAA 21st Fluid and Plasma Dynamics Conference, Seattle, Washington*, 1990. AIAA Paper 90-1483.

[133] P.R. Spalart and S.R. Allmaras. A one-equation turbulence transport model for aerodynamic flows. In *30th AIAA Aerospace Sciences Meeting and Exhibit, Reno, Nevada. AIAA Paper 92-0439*, 1992.

[134] M.A. Spiker, J.P. Thomas, R.E. Kielb, K.C. Hall, and E.H. Dowell. Modeling cylinder flow vortex shedding with enforced motion using a harmonic balance approach. In *47th AIAA/ASME/ASCE/AHS/ASC Structures, Structural Dynamics and Materials (SDM) Conference, Newport, RI. AIAA Paper 2006-1965*, 2006.

[135] J.P. Thomas, E.H. Dowell, and K.C. Hall. Nonlinear inviscid aerodynamic effects on transonic divergence, flutter, and limit-cycle oscillations. *AIAA Journal*, 40(4):638–646, April 2002.

[136] J.M. Tyler and T.G. Sofrin. Axial flow compressor noise studies. *Transactions of the Society of Automotive Engineers*, 70:309–332, 1962.

[137] E. van der Weide, A. Gopinath., and A. Jameson. Turbomachinery applications with the time spectral method. In *35th AIAA Fluid Dynamics Conference and Exhibit, Toronto, Ontario, Canada, AIAA Paper 2005-4905*, 2005.

[138] E.R. Van Driest. Turbulent boundary layers in compressible fluids. *Journal of Aeronautics Science*, 18(3):145–160, 1951.

[139] D. Vandromme. *Contribution à la modélisation et à la prédiction d'écoulements turbulents à masse volumique variable.* PhD thesis, Université of Lille, 1983.

[140] J. Vanharen. Theoretical and numerical analysis of block interfaces with mismatched nodes. emphasis on unsteady flows. Master's thesis, SupAero, 2013.

[141] Z.J. Wang. Spectral (finite) volume method for conservation laws on unstructured grids: Basic formulation. *Journal of Computational Physics*, 178:210–251, 2002.

[142] Z.J. Wang, K. Fidkowski, R. Abgrall, F. Bassi, D. Caraeni, A. Cary, H. Deconinck, R. Hartmann, K. Hillewaert, H.T. Huynh, N. Kroll, G. May, P-O. Persson, B. van Leer, and M. Visbal. Review article - high-order CFD methods: Current status and perspective. *International Journal for Numerical Methods in Fluids*, 72:811–845, 2013.

[143] Z. Warhaft and J.L. Lumley. An experimental study of the decay of temperature fluctuations in grid-generated turbulence. *Journal of Fluid Mechanics*, 88(4):659–684, 1978.

[144] D.C. Wilcox. *Turbulence Modeling for CFD.* DCW Industries, La Cañada, California, second edition, 1998.

[145] M. Wolfshtein. The velocity and temperature distribution in one-dimensional flow with turbulence augmentation and pressure gradient. *International Journal of Mass and Heat Transfer*, 12:301–318, 1969.

[146] S. Yoon and A. Jameson. An LU-SSOR scheme for the Euler and Navier-Stokes equations. In *AIAA 25th Aerospace Sciences Meeting, AIAA Paper 1987-0600*, 1987.

[147] M.S. Youssef, Y. Nagano, and M. Tagawa. A two-equation heat transfer model for predicting turbulent thermal fields under arbitrary wall thermal conditions. *International Journal of Heat and Mass Transfer*, 35(11):3095–3104, 1992.

[148] C. Zhu, R.H. Byrd, P. Lu, and J. Nocedal. Algorithm 778: L-BFGS-B: Fortran subroutines for large-scale bound-constrained optimization. *ACM Transactions on Mathematical Software*, 23(4):550–560, 1997.

[149] R.J. Zwaan. LANN wing. Pitching oscillation. Compendium of unsteady aerodynamic measurements. Addendum No. 1. Technical Report 702, AGARD, 1982. Data Set 9.

Part V

Appendix - List of most important papers

The five most important papers are:

– B. Mohammadi and G. Puigt, Wall functions in computational fluid mechanics, *Computers and Fluids*, 35:1108–1115, 2006.

– F. Sicot, G. Puigt and M. Montagnac, Block-Jacobi implicit algorithms for the time spectral method, *AIAA Journal*, 46(12):3080–3089, 2008.

– G. Dufour, F. Sicot, G. Puigt, C. Liauzun and A. Dugeai, Contrasting the harmonic balance and linearized methods for oscillating-flap simulations, *AIAA Journal*, 48(4):788–797, 2010.

– T. Guédeney, A. Gomar, B. François, F. Gallard, F. Sicot, G. Dufour and G. Puigt, Non-uniform time sampling for multiple-frequency harmonic balance computations, *Journal of Computational Physics*, 236:317–345, 2013.

– G. Puigt, V. Auffray and J.-D. Müller, Discretisation of diffusive fluxes on hybrid grids, *Journal of Computational Physics*, 229:1425–1447, 2010.

Available online at www.sciencedirect.com
ScienceDirect
Computers & Fluids 35 (2006) 1108–1115
computers & fluids
www.elsevier.com/locate/compfluid

Wall functions in computational fluid mechanics

B. Mohammadi [a,*], G. Puigt [b]

[a] *Institut de Mathématiques et Modélisation de Montpellier, 34095 Montpellier, France*
[b] *CEA/CESTA, B.P. 2, 33114 Le Barp, France*

Received 15 September 2004; accepted 15 February 2005
Available online 27 December 2005

Abstract

Wall functions are a powerful tool in complex flows calculations. Unfortunately, often blind and inappropriate use of them have given the impression that they should be avoided. Our aim though this paper is, without being exhaustive, to correct some of these prejudges and to point some advantages of wall functions, not only from the complexity point of view but also from their greater modeling capacity.

1. Introduction

By wall functions we mean space and time dimension reduction in a given model following a domain decomposition procedure in order to couple the obtained low-complexity and the original models. There is therefore no chemistry or mysterious procedures in the development and implementation of these boundary conditions.

Originally, the aim in using wall functions was to remove the stiff part from boundary layers, replacing the classical no-slip boundary condition by a more sophisticated relation between the variables and their derivatives. But wall function modeling can be used in other situations where direct simulation is out of reach.

One important aspect is the implementation of wall functions for general separated and unsteady compressible or incompressible flows. Following the historical development of our research, we made the choice of weak formulation on unstructured meshes to solve the flow. This choice was not easy to defend 25 years ago as most of the CFD community were defending computations, especially for viscous flows, on structured type meshes. It is therefore of great satisfaction to see that this is not anymore the case and industrial softwares have made the choice of running on unstructured meshes made mainly of tetrahedra. Another reason for unstructured meshes in their natural ability to integrate mesh adaptation capabilities. A close integration of computation, adaptation and optimization is for sure the next necessary evolution for commercial softwares.

We would like to show some situations where complex flows need explicit time integration, sometimes even if we are interested in mean quantities. Indeed, to capture the flow feature in large eddy simulation (LES) or unsteady Reynolds averaged Navier–Stokes (RANS) type simulations, the Courant–Fredriech–Levy (CFL) number during the calculation has to remain small. It is nice to notice that the global time step given by the classical stability criteria for Navier–Stokes on meshes needed for simulations with wall functions is of the right order for this purpose.

2. Mathematical context

The system of Navier–Stokes equations and a generic two-equation turbulence model (to fix the idea consider the $k-\varepsilon$ model [1]) in conservation form can be cast into the following formulation:

$$\frac{\partial W}{\partial t}+\nabla\cdot(F(W)-N(W))=S(W) \tag{1}$$

---

[*] Corresponding author.
E-mail address: mohamadi@math.univ-montp2.fr (B. Mohammadi).

0045-7930/$ - see front matter © 2005 Elsevier Ltd. All rights reserved.
doi:10.1016/j.compfluid.2005.02.009

where $W = (\rho, \rho\vec{u}, \rho E, \rho k, \rho\varepsilon)^{\mathrm{T}}$ is the vector of conservation variables, F and N are the convective and diffusive operators and $S = (0, \ldots, 0, S_k, S_\varepsilon)$ contains the source terms of the turbulence model. The presentation below holds for other turbulence modeling including large eddy simulation approaches. We would like to show where wall functions modeling is needed without going into the details of the numerical method to the solution of (1) but we are interested in the solution of these equations in weak form.

Once the weak formulation chosen (finite volume or finite element), integration by part introduces the following integrals on boundaries:

$$\int_\Gamma W(\vec{u}\cdot\vec{n})\,\mathrm{d}\sigma \tag{2}$$

$$\int_\Gamma p\vec{n}\,\mathrm{d}\sigma \tag{3}$$

$$\int_\Gamma p(\vec{u}\cdot\vec{n})\,\mathrm{d}\sigma \tag{4}$$

$$\int_\Gamma (\mathbf{S}\cdot\vec{n})\,\mathrm{d}\sigma \tag{5}$$

$$\int_\Gamma (\vec{u}\mathbf{S})\vec{n}\,\mathrm{d}\sigma \tag{6}$$

$$\int_\Gamma (\chi+\chi_t)\frac{\partial T}{\partial n}\mathrm{d}\sigma \tag{7}$$

$$\int_\Gamma (\mu+\mu_t)\frac{\partial k}{\partial n}\mathrm{d}\sigma \quad \text{and} \quad \int_\Gamma (\mu+c_\varepsilon\mu_t)\frac{\partial \varepsilon}{\partial n}\mathrm{d}\sigma \tag{8}$$

where p denotes the pressure given by the state equation, S the Newtonian stress tensor, μ_t the eddy viscosity, χ_t the eddy conductivity and $(\vec{t}, \vec{t}', \vec{n})$ a local orthonormal basis on the boundary; n being the unit normal to the boundary and $(\vec{t}, \vec{t}')$ a local basis for the tangent plane to the boundary.

On solid walls, we make the particular choice of $\vec{t}\|\vec{u}$ and $\vec{t}\perp\vec{t}'$ together with the condition $\vec{u}\cdot\vec{n} = g$. $g = 0$ represents the non-penetration boundary condition but injection-suction or transpiration conditions can also be introduced considering non-homogeneous g. For sake of simplicity, in what follows we consider the case of $g = 0$.

With the non-penetration boundary condition, we are left with (5)–(8) for the momentum, energy and turbulent variables equations in weak form.

3. Dimension reduction

In presence of anisotropy, it is mathematically consistent to take advantage of the difference of magnitude in the phenomena, following the different spatial directions to reduce the complexity of the model to be solved. This is the starting point in the development of wall functions. We assume that near the wall the variables variations are mainly in the direction normal to the wall. Despite this assumption is questionable near separation and attachment areas, we will see that it gives satisfactory results even for these situations. This can therefore be seen as an a posteriori validation of this hypothesis. To express (5), we split $\mathbf{S}\cdot\vec{n}$ over $(\vec{t}, \vec{t}', \vec{n})$:

$$\mathbf{S}\cdot\vec{n} = (\mathbf{S}\cdot\vec{n}\cdot\vec{n})\vec{n} + (\mathbf{S}\cdot\vec{n}\cdot\vec{t})\cdot\vec{t} + (\mathbf{S}\cdot\vec{n}\cdot\vec{t}')\cdot\vec{t}' \tag{9}$$

With the particular choice of the local basis mentioned above, we make a first approximation (modeling) neglecting the first and the last terms (S_{nn} and $S_{nt'}$) in the expression above $\mathbf{S}\cdot\vec{n} \sim (\mathbf{S}\cdot\vec{n}\cdot\vec{t})\cdot\vec{t} = S_{nt}\vec{t}$.

Let us introduce u_τ, a scalar quantity having the dimension of a velocity and called friction velocity, defined as $\rho_w u_\tau |u_\tau| = S_{nt}$ with ρ_w the density at the wall and let us denote by y the normal coordinate to the wall and by x the tangential coordinate in the direction of the flow.

To specify $\int_\Gamma (\chi+\chi_t)\partial T/\partial y$, consider the viscous part of the time-independent energy equation written in the boundary layer (i.e. suppose $\partial/\partial x << \partial/\partial y$)

$$\frac{\partial}{\partial y}\left((\vec{u}\cdot\vec{t})(\mu+\mu_t)\frac{\partial(\vec{u}\cdot\vec{t})}{\partial y}\right) + \frac{\partial}{\partial y}\left((\chi+\chi_t)\frac{\partial T}{\partial y}\right) = 0$$

When we integrate this equation between $y = 0$ and $y = \delta$, as $(\vec{u}.\vec{t})|_0 = 0$ we obtain

$$(\chi+\chi_t)\frac{\partial T}{\partial y}\bigg|_\delta + (\vec{u}\cdot\vec{t})(\mu+\mu_t)\frac{\partial(\vec{u}\cdot\vec{t})}{\partial y}\bigg|_\delta = \chi\frac{\partial T}{\partial y}\bigg|_0 \tag{10}$$

As a consequence, in wall function calculations, to evaluate the heat transfer at isothermal walls, we have to use the following formula:

$$C_h \sim \frac{\chi\partial_y T|_0}{\rho_\infty u_\infty^3} = \frac{(\chi+\chi_t)\partial_y T|_\delta + (\vec{u}\cdot\vec{t})_\delta \rho_w u_\tau^2}{\rho_\infty u_\infty^3}$$

This is important as industrial solvers usually do the post-processing in a separate level than computation and the fluxes are not communicated between the two modules. In other words, with these codes, when using wall functions as well as with low-Reynolds models, only the first term is present in a heat flux evaluation above. This might also explain some of the reported weakness of wall functions for heat transfer.

For adiabatic walls, the boundary integral for the energy equation vanishes (since $\partial T/\mathrm{r}y|_0 = 0$), while for the isothermal wall case, it reduces to

$$\int_\Gamma \chi\frac{\partial T}{\partial y}\bigg|_0 \mathrm{d}\sigma$$

In the same way, turbulent variables equations can be integrated in the direction normal to the wall:

$$\frac{\partial}{\partial y}\left((\mu+\mu_t)\frac{\partial k}{\partial y}\right) = P_k(y) - \rho\varepsilon, \quad \varepsilon = \frac{k^{3/2}}{l_\epsilon} \tag{11}$$

where l_ε is a given algebraic mixing length and P_k the production term in the turbulence model which can be expressed as $P_k = (\rho_w u_\tau^2)^2/(\mu+\mu_t)$ with μ_t a given mixing length eddy viscosity of the form [2,23]:

$$\mu_t^+ = \mu_t/\mu = Ay^+(1-\exp(-By^+))^2 \quad A, B > 0 \tag{12}$$

chosen compatible with the original turbulence model. For ε, we can either use a Dirichlet boundary condition as in (11) or express its boundary integral linearizing expression (11) in y.

Above, δ is an a priori length chosen in order for the hypothesis above to be valid.

To close the expressions above we need to specify ρ_w, u_τ and $\chi\frac{\partial T}{\partial y}|_0$ for isothermal walls.

If anisotropy is assumed and if time variations are supposed to be smaller that spatial variations normal to the wall,[1] shear is constant in the normal direction (we denote $u = \vec{u}\cdot\vec{t}$)

$$\rho_w u_\tau |u_\tau| = (\mu + \mu_t)\frac{\partial u}{\partial y}\bigg|_{y=\delta} = \mu\frac{\partial u}{\partial y}\bigg|_{y=0} \tag{13}$$

Using u_τ we introduce a local Reynolds number:

$$y^+ = \frac{\rho_w y u_\tau}{\mu_w} \tag{14}$$

Now if $\mu_t(y^+)$ is a known function of y^+ (such as (12)), expression (13) can be integrated for $0 \leqslant y \leqslant \delta$

$$\rho_w u_\tau |u_\tau| = \frac{u_\delta}{\int_0^\delta \frac{\mathrm{d}y}{\mu+\mu_t}} \tag{15}$$

To specify the thermal contribution in case of isothermal walls, integration in the normal direction leads to the following relation:

$$\chi\frac{\partial T}{\partial y}\bigg|_0 = \frac{T_\delta - T_w}{\int_0^\delta \frac{\mathrm{d}y}{\chi+\chi_t}} + u_\delta \rho_w u_\tau |u_\tau| \tag{16}$$

In separation and recirculation areas $u = \vec{u}\cdot\vec{t}$ is small and this leads to an underestimation of the heat flux. In these area, by dimension argument, we choose the local velocity scale to be $u = c_\mu^{-3/4}\sqrt{k}$.

4. Analytical wall functions

The approach above is mathematically consistent and should be adopted if the underlying turbulence model is valid for the targeted flow. On the other hand, we observe that if the flow is not in the validity domain of the model this dimension reduction approach does not always lead to satisfactory results [5,7]. This is mainly the case when we need to include thermal or compressibility effects into turbulence as most turbulence models have been developed for flows in the incompressible range and were directly generalized to simulate compressible effects. In these cases, we notice that direct accounting for physics in wall functions is more suitable. In fact, for these flows we get better results with a wall function approach rather than with an up-to-the-wall simulation of the flow with a pseudo-extension to low-Reynolds calculation of an unsuitable turbulence model [5,7].

To avoid the difficulty above one possibility is to push the integration presented above further and to express the behavior of $u^+ = u/u_\tau$ in term of y^+ (and also $T^+ = T/T_w$ in term of y^+ for isothermal walls) injecting physical information during this integration [5,4,3,2]. Once the derivation is achieved, linearization permits to recover the boundary integral specified above.

To be suitable for the capture of separated and unsteady flows, our experience shows that we should follow some principles. It is important for the wall function to be global, valid up to the wall (i.e. $\forall y^+ \geqslant 0$). The parameter δ in wall functions needs also to remain small. This means that the computational domain should not be too far from the wall. One important weakness of implementations and calculations with wall functions is the use of inappropriate meshes usually too coarse in the boundary layer regions. Mesh independent results should be aimed as in the computations with low-Reynolds type turbulence models. Indeed, we notice that users associate the idea of wall functions to the use of 'too' coarse meshes. Mesh adaptation by metric control is a natural way to perform this task [14,15,19].

However, as the development of analytical wall function is based on physical considerations during the integration, it is clear that there is not a unique way to introduce these informations and this makes that there is no uniqueness for the wall functions we can obtain. Example of analytical wall functions development is given in [5,4,3].

5. Wall functions and data assimilation

Data assimilation is a powerful engineering tool to treat some applications where full modeling is out of reach and where data distribution is such that statistical approaches are suitable because some correlations are observed in the data. For instance, to account for wall roughness in compressible flows, engineering empirical relations such as PAssive Nosetip Technology (PANT) [20] are usually used for a posteriori correction to heat transfer computed on smooth walls. But these corrections are mostly available for sand grain type roughness. On the other hand, theoretical works usually use homogenization techniques which consist in solving a cell problem for a roughness with periodic boundary conditions on lateral boundaries. The cell problem enables to link variables and fluxes on the upper cell boundary [21]. However, there are limitations on the level of the physical complexity which can be treated. In addition, in cases where the roughness geometry changes in time and space, as during ablation, the cell problem needs to be solved together with the global flow problem making the approach unrealistic.

If the impact of roughness is local, to study roughness effects on the flow, an alternative approach is to introduce an a priori model for the correction to the wall functions derived for smooth walls. For instance, consider the following local relation between the friction along a smooth and rough wall under the same flow conditions

---

[1] These can also be considered as locally constant leading to slightly modified wall functions [4].

$$P_{C_f} = \frac{C_{f_{\text{rough}}}}{C_{f_{\text{smooth}}}} = P_2(F, R)$$

where F denotes the variables defining the flow condition and R a set of parameters describing the shape of the roughness. In sand grain modeling R is the height of the grain, but for complex roughness it has to be seen as an ensemble of geometrical CAD-based parameters. P_2 is a polynomial of degree 2 on all variables (order 2 was observed to be suitable for the friction and order 3 for heat transfer [7]).

To close this model, we need to identify the coefficients of the polynomial. After sampling of the parameter space (e.g. Mach number, Reynolds number, inflow and wall temperatures, roughness description), a data base is generated by distributed direct simulation of simple configurations on each point of the sampling. The parameters in the polynomial are identified solving a least-square problem minimizing the distance of the polynomial to this data basis.

In least-squares analysis, the results are not accurate if the matrix is ill-conditioned. This is often due to large deviations among the various values to be assimilated by the model. To improve the condition of the system and also to avoid the difficulty of manipulating quantities with different physical dimension we normalize all variables as

$$\overline{X_i} = \frac{X_i - X_M}{X_\sigma} \tag{17}$$

where X_M is the averaged quantity and X_σ is the standard deviation defined as

$$X_M = \frac{1}{N}\sum_{i=1}^{N} X_i \quad \text{and} \quad X_\sigma = \sqrt{\frac{1}{N}\sum_{i=1}^{N}(X_i - X_M)^2}$$

To illustrate this development, we consider an isothermal 35 degree compression ramp presented in [16]. The inflow Mach and Reynolds numbers are, respectively, 8.2 and 8.10^6. The corner is at 0.163 m from the leading edge. The inflow temperature is $T_\infty = 1280$ K and the wall temperature $T_{\text{wall}} = 288$ K. Experimental data for the heat transfer coefficient are available for a smooth and a rough cases.[2] The same mesh has been used for both the smooth and rough cases. It has about 10,000 nodes and the first node in the normal direction is at a distance of 10^{-5} m from the wall. The same smooth geometry has been considered for both simulations. Fig. 1 show calculations with wall functions for smooth and rough walls with two different turbulence models ($v^2 - f$ turbulence model [18] and the classical $k - \varepsilon$ [1]). The wall function for rough walls has been developed using the present statistical approach. This again shows that some reported weakness in calculations can have other origins than the use of wall functions.

6. Wall functions and sensitivity analysis

In shape design and optimization problems the sensitivity of a functional is often aimed. Consider the following relation linking a set of control parameter c, geometrical quantities q and state variables W (here the flow solution through the flow equations) to a functional J

$$J : c \rightarrow q(c) \rightarrow W(q(c)) \rightarrow J(c, q(c), W(q(c)))$$

The sensitivity of J with respect to control parameters has different contributions

$$\frac{\mathrm{d}J}{\mathrm{d}c} = \frac{\partial J}{\partial c} + \frac{\partial J}{\partial q}\frac{\partial q}{\partial c} + \frac{\partial J}{\partial W}\frac{\partial W}{\partial c} \tag{18}$$

and it is well known that most of the computational effort is spent in $\partial W/\partial c$ [4]. In incomplete sensitivity concept we try to reduce this complexity approximating this former sensitivity linearizing an approximate state equation $\widetilde{W}(q(c))$ which leads to the following incomplete definition for the sensitivity:

$$\frac{\mathrm{d}J}{\mathrm{d}c} \approx \frac{\partial J(W)}{\partial c} + \frac{\partial J(W)}{\partial q}\frac{\partial q}{\partial c} + \frac{\partial J(W)}{\partial W}\frac{\partial \widetilde{W}}{\partial c}\frac{W(c)}{\widetilde{W}(c)} \tag{19}$$

$\widetilde{W}$ is used here only to simplify the computation of $\partial\widetilde{W}/\partial c$. It is important to notice that the reduced model needs to be valid only over the support of the control parameters. Wall functions are natural $\widetilde{W} = \widetilde{W}(y^+)$ candidates and in [13,9] we show how they can impact positively the computational time in sensitivity calculations if the parameterization is shape deformation in the normal direction y. Another advantage of this formulation is that it is only based on the shape with no volume information needed in shape sensitivity evaluation. This is important when using a commercial software where it is easy to build user-defined procedures for boundaries.

7. Wall function as control parameter

Beyond complexity reduction for sensitivity evaluation in optimization problems pointed above, wall functions can also be considered as control parameter in some simulations and design problems.

Large eddy simulation (LES) at high Reynolds number for external flows implies the capture of anisotropy in boundary layers requiring too fine meshes normal to the wall making LES calculations extremely complex [10,11]. On the other hand, it seems to be really difficult to find general wall functions for LES calculations [8]. One way to consider this problem is to see wall functions as control parameters at the wall to be defined from the solution of a control problem requiring the averaged LES solution to tend into a Reynolds averaged type solution (Rans). For example, for a channel flow we require the LES calculation to recover in average the log-law profile for the axial velocity and having in average the other velocity components vanishing [10]. This can be done minimizing the following functional:

---

[2] The rough case is based on a sand grain type roughness with a roughness parameter $h = 310^{-4}$ m [17].

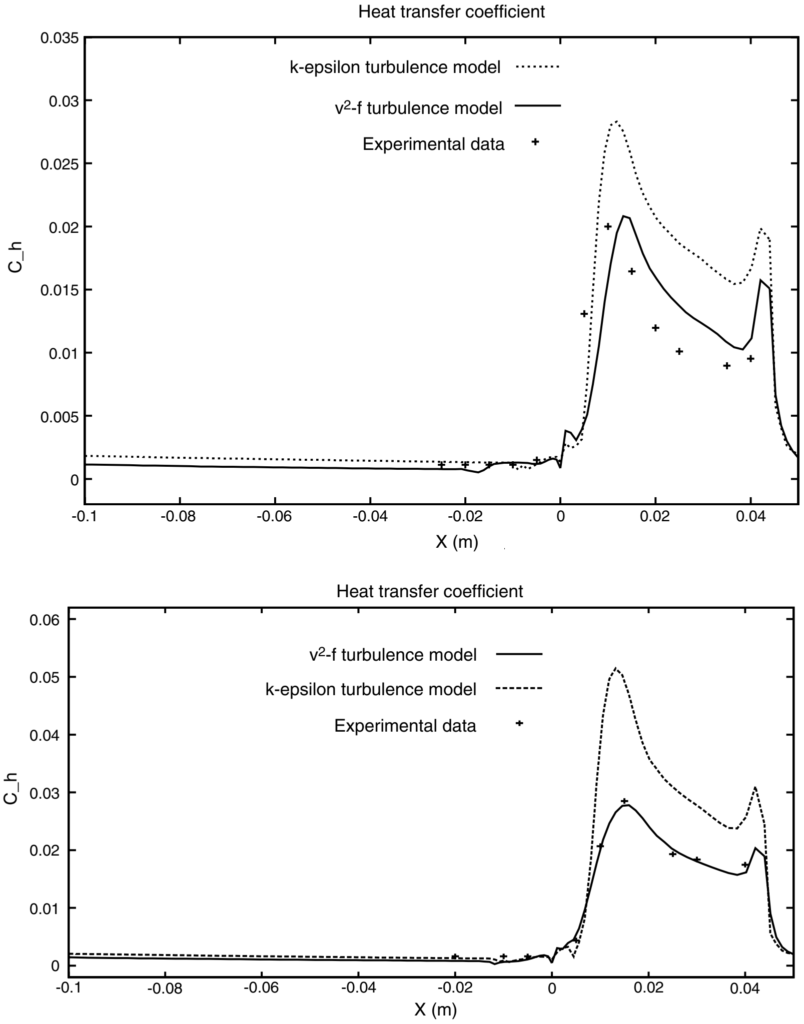

Fig. 1. Smooth isothermal compression ramp ($M_\infty = 8.2$, $Re_\infty = 8.10^6$, $T_{\text{wall}} = 288$ K and $T_\infty = 1280$ K). Heat transfer with $k - \varepsilon$ and $v^2 - f$ models and same wall functions (upper: smooth, lower: rough).

$$J = \int_{\text{channel}} \mathrm{d}x\,\mathrm{d}y\,\mathrm{d}z\Big((\overline{u_1} - u_1^{\text{target}})^2 + (\overline{u_2})^2 + (\overline{u_3})^2\Big)$$

where $\overline{u}(x,y,z) = 1/T\int_0^T u(t,x,y,z)\,\mathrm{d}t$ denotes a Reynolds averaged quantity. Unfortunately, this approach has two drawbacks: it requires the knowledge of the targeted Rans solution and this is unknown in general configurations, and it requires the solution of an expensive adjoint problem [10]. Often also an unsteady Rans solution should be targeted and not a necessary steady solution making the calculation of the adjoint variable even more delicate. A more recent progress consists in considering only the coefficients in the Rans wall functions mentioned above as control variables to be simply set for the eddy quantities (eddy viscosity and conductivity) in the Rans and LES models to match. This is called dynamic wall function and leads to promising results [11]. For external flows again, in case Detached Eddy Simulation (DES) [12] is aimed the situation is even more favorable as we can take advantage of both the ability of Rans models to handle meshes with high aspect ratios near the wall and the time scale compatibility of wall functions with Rans models.

Another example of wall functions as control parameters is roughness optimization. Indeed, we saw above that roughness can be modeled adding corrections to wall functions for smooth walls. The correction being statistically built in some situations. Adaptive statistical modeling permits inverse roughness design to recover a target flow.

8. Impacts of wall functions on numerics

Wall functions are interesting as they remove from the computational domain the regions where the gradients are the sharpest and therefore permit coarser meshes to be used with larger time steps and therefore explicit time integration schemes. Indeed, even if low-Reynolds number corrections may appear physically more meaningful, they lead to much stiffer numerical problems.

For instance, with the compression ramp example shown below at Mach number of 5 and Reynolds number of 10^7, a low-Reynolds approach needs meshes with a first node placed at a distance of 10^{-7} m from the wall in the normal direction and between 10^{-4} m and 10^{-2} m in the tangential direction along the wall. This means aspect ration of 10^5. With wall functions, this simulation can be performed with the first node at 10^{-4} m in the normal direction. If we use the standard stability criteria for local time stepping, at $\mathrm{CFL} = 1$, this implies at least three orders of magnitude in the size of the time step.[3] This means that if we intended to use the same time step, we would need an implicit scheme and $\mathrm{CFL} = 10^3$. In addition, the linear system obtained on such meshes is highly ill-conditioned. Furthermore the generation of unstructured meshes with so high aspect ratio is difficult in 3D, not to speak of the problem of adaptivity [6].

When the variables are located at the nodes, the implementation of wall functions can be done using the fictitious boundary approach. The parameter δ denotes then the distance from the wall to the boundary of the calculation domain. In practice, we do not make the difference between this boundary and the physical wall because compared to the length scale L of the shape δ is usually negligible. Implicitly, This is as doing the computation not for the original Reynolds number $Re = \rho U \quad L/\mu$ but for $\widetilde{Re} = \rho U(L + \delta)/\mu \sim Re$. On the other hand, when variables are not defined on nodes (for instance in cell centered or staggered approaches), we can take advantage of this to introduce directly the no-slip boundary condition at the wall defining δ as being the distance from the node to the wall. Care should be given therefore to the fact that if this distance is locally varying or fluctuating (as in a fully unstructured mesh), the computed quantities exhibit these fluctuations.

From implementation point of view, there is another important difference between the two presentations above of wall functions. In the original dimension reduction approach there is usually no non-linear equation to solve. Friction and heat transfer are obtained after numerical integration in (15) and (16). On the other hand, in the analytical approach we have to solve a non-linear equation which needs to satisfy an admissibility condition in the definition of δ for the solution method (e.g. Newton method) to converge [7]. This condition on δ recovers our requirement for the fictitious and physical walls to remain close.

9. Numerical examples

This section is to show some results obtained with the ingredients presented above for turbulent flows. We are interested in using unstructured mesh adaptation in these computations and show that unstructured meshes are also suitable for boundary layer calculations.

Unsteady separated flows are pretended usually difficult to capture with wall functions. We particularly show here that complex flows can be captured with this approach but accurate time integration must be used. Indeed, we think that unfortunately the use of inadequate meshes and over-diffusive numerical schemes often hide the true performance of wall functions.

9.1. Stall prediction at low speed

This case is interesting as it shows that it is sometimes important to use accurate time integration and small time steps for a correct stall prediction, especially when stall is due to the apparition of unsteadiness in the wake at some incidence (Figs. 2 and 3). Simulations are presented for a 2D profile called ONERA-A (kindly made available to us by Onera-Cert [22]) at incidence of 7, 13, and 15 degrees using the same accuracy for time and space integrations for all three cases and mesh adaptation is used for both three cases. Stall is expected for the former incidence. Steady state calculations of the flow with similar turbulence modeling did not permit for stall prediction [22].

9.2. Flow over an isothermal compression ramp

We consider an isothermal 35 degrees compression ramp [24] (Fig. 4). The inflow Mach and Reynolds numbers are respectively 5 and 4×10^7. The inflow temperature is $T_\infty = 83$ K and the wall temperature $T_{\mathrm{wall}} = 288$ K. The corner being at 0.25 m from the leading edge. The mesh used has about 8000 nodes and mesh independence is achieved with a mesh having its first point at 10^{-4} m from the wall, to be compared to values of less than 10^{-7} m observed with low-Reynolds calculations up to the wall. Heat transfer agrees in a reasonable way with experimental data, comparable to the best results obtained with low-Reynolds up-to-the-wall calculations [5]. As we said, there is not a unique way to introduce physical informations in the development of analytical wall functions and wee see the effect of this on the results (Fig. 4).

10. Concluding remarks

Wall functions can be a powerful tool to complex flows analysis reducing the complexity of the calculations. This complexity reduction is very important and makes the simulation tool realistic to use in the context of industrial

---

[3] In time-dependent applications, it is even worse as the stability condition implies the use of the smallest time step to advance the flow.

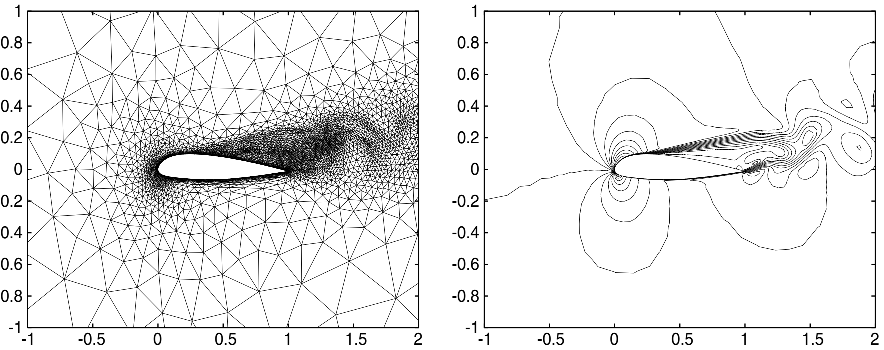

Fig. 2. Stall prediction for a Onera A profile. Intermediate adapted mesh and iso-Mach contours at 15° incidence.

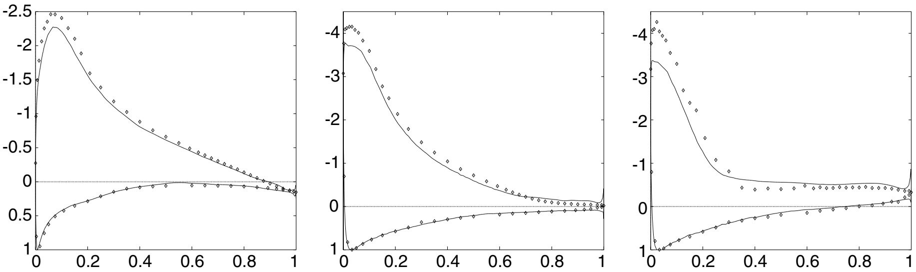

Fig. 3. Stall prediction for a Onera A profile. Mean pressure distribution for 7 (left) and 13 (middle) and 15 (right) degrees incidence vs. experience (dots). Stall is predicted at the right incidence but the pressure level is too low around the leading edge.

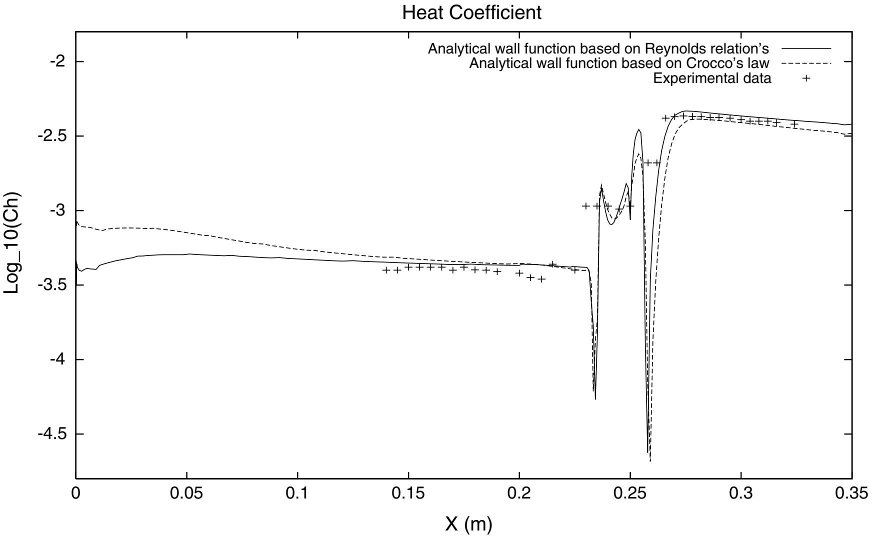

Fig. 4. Isothermal compression ramp ($M_\infty = 5$, $Re_\infty = 4 \times 10^7$). Heat transfer obtained with two alternative analytical wall functions [5].

simulations where complex geometries, mesh generation and adaptation issues and the need for the integration of the simulation tool into an optimization platform need to be handled.

References

[1] Launder BE, Spalding DB. Mathematical models of turbulence. Academic Press; 1972.

[2] Cousteix J. Turbulence et couche limite. Cepadues publisher; 1990.

[3] Mohammadi B, Pironneau O. Analysis of the *k*-epsilon turbulence model. Wiley; 1994.

[4] Mohammadi B, Pironneau O. Applied shape optimization for fluids. Oxford University Press; 2001.

[5] Mohammadi B, Puigt G. Generalized wall functions for high-speed flows over adiabatic and isothermal walls. IJCFD 2000;14:20–41.

[6] Alauzet F, George PL, Frey P, Mohammadi B. Transient fixed point based unstructured mesh adaptation. Int J Numer Methods Fluids 2003;43(6–7):729–45.

[7] Mohammadi B, Puigt G. Generalized wall functions for rough walls based on data assimilation. IJCFD 2002;17(6):453–76.

[8] Cabot W, Moin P. Approximate wall boundary conditions in the large Eddy simulation of high Reynolds number flow. Flow Turb Combust 2000;63:269–91.

[9] Mohammadi B, Pironneau O. Shape optimization in fluid mechanics. Ann Rev Fluid Mech 2004;36:255–79.

[10] Nicoud F, Baggett JS, Moin P, Cabot W. LES wall modeling based on suboptimal control theory. Phys Fluids 2000;13(10).

[11] Wang M. Dynamic wall modeling for LES of complex turbulent flows. Center Turbulent Res Briefs 2000:241–50.

[12] Spalart PR, Jou WH, Strelets M, Allmaras SR. Comments on the feasibility of LES for wings, and on a hybrid RANS/LES approach. In: First AFOSR International Conference On DNS/LES, August 4–8, 1997, Ruston, Louisiana.

[13] Mohammadi B, Moreau S, Stanciu M. Low complexity models to improve incomplete sensitivities for shape optimization. IJCFD 2002;11(2):245–66.

[14] Castro-Diaz M, Hecht F, Mohammadi B. Anisotropic grid adaptation for inviscid and viscous flows simulations. Int J Numer Methods Fluid 1995;25:475–91.

[15] Borouchaki H, George PL, Mohammadi B. Delaunay mesh generation governed by metric specifications. Part II: applications, finite element in analysis and design. Special issue on mesh adaptation; 1996.

[16] Prince SA, Vannahme M, Stollery JL. 1999. Experiments on the hypersonic turbulent shock-wave/boundary-layer interaction and the effects of surface roughness. AIAA Paper 99-0147. In: 37th aerospace science meeting, Reno NzV. January 11–14; 1999.

[17] Richardson G, Quin N. Effects of compressibility and roughness for turbulence modelling of hypersonic ramp flow. AIAA Paper 99-1019. In: 37th aerospace science meeting, Reno NzV. January 11–14; 1999.

[18] Durbin P. Separated flow computation with the $k-\varepsilon-\overline{v^2}$ model. AIAA J 1995;33:659–64.

[19] Hecht F, Mohammadi B. Mesh adaptation by metric control for multi-scale phenomena and turbulence. Amer Inst Aeronautics Astronautics. 97-0859; 1997.

[20] Duffa G. Ablation. CESTA edition 1 du 28 novembre 1996.

[21] Valentin F. Nouvelles conditions aux limites équivalentes pour des interfaces rugueuses en mécanique des fluides: développement, analyse et mise en oeuvre numérique, PhD Thesis, University Pierre et Marie Curie, Paris VI; 1998.

[22] Goncalves E. Implantation et validation de lois de paroi dans un code Navier–Stokes, PhD Thesis; 2001.

[23] Van Driest ER. Turbulent boundary layers in compressible fluids. J Aeronautics Sci 1951:18–145.

[24] Delery J, Coet MC. Experiments on shock-wave/boundary-layer interactions produced by two-dimensional ramps and three-dimensional obstacles. In: Proc. Workshop on Hypersonic Flows for Reentry Problems, Antibes; 1990.

AIAA JOURNAL
Vol. 46, No. 12, December 2008

Block-Jacobi Implicit Algorithms for the Time Spectral Method

Frédéric Sicot,* Guillaume Puigt,† and Marc Montagnac‡
*European Center for Research and Advanced Training in Scientific Computation,
F-31057 Toulouse Cedex 01, France*

DOI: 10.2514/1.36792

Many industrial applications involve flows periodic in time. Such flows are not simulated with enough efficiency when using classical unsteady techniques, as a transient regime must be bypassed. New techniques, dedicated to time-periodic flows and based on Fourier analysis, have been developed recently. Among these, the time spectral method casts a time-periodic flow computation in several coupled steady computations, corresponding to a uniform sampling of the period. Up until now, the steady states were reached using an explicit pseudotime algorithm. Thus, very small time steps were needed and the convergence rate slowed down when increasing the number of harmonics. In this paper, a block-Jacobi approach is presented to solve the stationary problems with an implicit algorithm. Numerical simulations show, on one hand, the good quality of the results and, on the other hand, the interest of the proposed method to reduce the sensitivity of computations to a large number of harmonics.

I. Introduction

EVEN if three-dimensional steady turbulent flow simulations begin to be handled routinely in the aircraft industry, three-dimensional unsteady turbulent flow simulations still require large amounts of computing time, and a substantial acceleration of the calculations is needed to reduce design cycles. Depending on the spatial and time scales to be resolved, numerous nonlinear time-marching methods are available. Direct numerical simulations and even large eddy simulations are still too expensive with respect to the best computing resources available today to satisfy industrial requirements. So far, unsteady Reynolds-averaged Navier–Stokes (U-RANS) techniques have proven to be the most efficient to meet industrial needs. Efficiency is not an absolute notion because it results from a tradeoff between the quality of the physics and the time needed to complete the simulation. In industry, U-RANS techniques are generally predictive enough and require relatively short time simulations.

To build an efficient method for unsteady flows, it is interesting to take into consideration all the flow characteristics. As an example, a large range of applications leads to time-periodic flows: turbomachinery, pitching wings, helicopter blades, wind turbines, etc. Several dedicated methods have been developed during the last years. They consider flow variables either in the time domain or in the frequency domain. The frequency-domain techniques are extensively reviewed in [1,2]. Linearized methods [3] form an important group among these methods. They superimpose perturbations over a steady flow and do not really rely on a time-marching procedure. Consequently, they are very inexpensive to compute. However, when the flow presents strong shock discontinuities, for instance, the linearity assumption is no longer true. Ning and He [4] extend these techniques to take account of the nonlinearities, yielding the nonlinear harmonic method. This one is limited to only one harmonic of the flow and requires a specific treatment for the time stepping.

In recent years, a more efficient time-domain method dedicated to time-periodic flows has been developed. Hall et al. introduced a harmonic balance (HB) method [5] for blade cascades computations. Then Gopinath and Jameson presented the time spectral method (TSM) [6] for external aerodynamic applications. Both methods are essentially the same and allow one to capture the fundamental frequency of the flow and a given number of its harmonics. They cast the unsteady governing equations in a set of coupled steady equations corresponding to a uniform sampling of the flow within the time period. These steady equations can then be solved using standard steady RANS methods with convergence acceleration techniques such as local time stepping and multigrid. The convergence of a steady computation is better mastered than the transient needed by an unsteady computation to reach the periodic state. This method proved to be efficient in periodic problem computations such as vortex shedding [7,8], flutter [9], and turbomachinery applications [1,10]. Later, the HB method was extended for multistage turbomachinery [11] where several frequencies appear, not necessarily integer multiples of each other. For sake of clarity, the notation TSM is retained in this paper to refer to computations with a single fundamental frequency.

In [5–11], explicit algorithms such as Runge–Kutta methods are used to advance the calculations in pseudotime. This makes the pseudotime steps relatively small and therefore requires a large number of iterations to reach the steady state of all the instants. Furthermore, it has been observed that the convergence rate decays as the number of harmonics is increased [5]. To circumvent this, van der Weide et al. [10] use a spectral interpolation of computations with a low number of harmonics to produce good initial conditions for higher harmonics computations. This requires one to make several computations and to interpolate between each. An implicit time integration scheme, such as backward-Euler, could enable much larger time steps and make the TSM even more efficient. For this reason, the goal of the present paper is to derive and implement an implicit version of the TSM.

The following section recalls the formulation of the time spectral method and its stability criteria. Then, the new implicit treatment is described and two solving processes are derived. A numerical study is then carried out, followed by an application of a pitching wing in forced harmonic oscillations.

II. Time Spectral Method

A. Governing Equations

The Navier–Stokes equations in Cartesian coordinates are written in semidiscrete form as

---

Received 23 January 2008; revision received 9 July 2008; accepted for publication 3 September 2008.

*Doctoral Candidate, Computational Fluid Dynamics/Advanced Aerodynamics and Multiphysics, 42 Avenue Coriolis.

†Senior Researcher, Computational Fluid Dynamics/Aérodynamique et Applications Multiphysiques, 42 Avenue Coriolis.

‡Research Engineer, Computational Fluid Dynamics/Aérodynamique et Applications Multiphysiques, 42 Avenue Coriolis.

$$V\frac{\partial W}{\partial t} + R(W) = 0 \tag{1}$$

where V is the volume of a cell, and W is the vector of conservative variables

$$W = (\rho, \rho u_1, \rho u_2, \rho u_3, \rho E)^T$$

complemented with an arbitrary number of turbulent variables as within the RANS framework. $R(W)$ is the residual vector resulting from spatial discretization of the convective f_{ci} and viscous f_{vi} fluxes

$$R(W) = \frac{\partial}{\partial x_i} f_i(W)$$

with $f_i = f_{\mathrm{ci}} - f_{\mathrm{vi}}$ and

$$f_{\mathrm{ci}} = \begin{pmatrix} \rho u_i \\ \rho u_i u_1 + p\delta_{i1} \\ \rho u_i u_2 + p\delta_{i2} \\ \rho u_i u_3 + p\delta_{i3} \\ \rho u_i E + p u_i \end{pmatrix}, \qquad f_{\mathrm{vi}} = \begin{pmatrix} 0 \\ \tau_{i1} \\ \tau_{i2} \\ \tau_{i3} \\ u \cdot \tau_i - q_i \end{pmatrix} \tag{2}$$

Here, δ denotes the Kronecker symbol. The components of the stress tensor are

$$\tau_{11} = \frac{2}{3}\mu\left(2\frac{\partial u_1}{\partial x_1} - \frac{\partial u_2}{\partial x_2} - \frac{\partial u_3}{\partial x_3}\right)$$

$$\tau_{12} = \tau_{21} = \mu\left(\frac{\partial u_2}{\partial x_1} + \frac{\partial u_1}{\partial x_2}\right)$$

$$\tau_{22} = \frac{2}{3}\mu\left(-\frac{\partial u_2}{\partial x_2} + 2\frac{\partial u_2}{\partial x_2} - \frac{\partial u_3}{\partial x_3}\right)$$

$$\tau_{13} = \tau_{31} = \mu\left(\frac{\partial u_3}{\partial x_1} + \frac{\partial u_1}{\partial x_3}\right)$$

$$\tau_{33} = \frac{2}{3}\mu\left(-\frac{\partial u_3}{\partial x_3} - \frac{\partial u_2}{\partial x_2} + 2\frac{\partial u_3}{\partial x_3}\right)$$

$$\tau_{23} = \tau_{32} = \mu\left(\frac{\partial u_2}{\partial x_3} + \frac{\partial u_3}{\partial x_2}\right)$$

The heat flux vector q components are $q_i = -\kappa \partial T/\partial x_i$, where T is the temperature and

$$\kappa = C_p\left(\frac{\mu_{\mathrm{lam}}}{Pr_{\mathrm{lam}}} + \frac{\mu_{\mathrm{turb}}}{Pr_{\mathrm{turb}}}\right)$$

The total viscosity μ is the sum of the laminar μ_{lam} and turbulent μ_{turb} viscosities. Pr_{lam} and Pr_{turb} are the associated Prandtl number. For an ideal gas, the closure is provided by the equation of state

$$p = (\gamma - 1)\rho\left(E - \frac{u_i u_j}{2}\right)$$

B. Fourier-Based Time Discretization

If W is periodic with period $T = 2\pi/\omega$, then so is $R(W)$, and the Fourier series of Eq. (1) is

$$\sum_{k=-\infty}^{\infty} (ik\omega V\hat{W}_k + \hat{R}_k)e^{ik\omega t} = 0 \tag{3}$$

where $\hat{W}_k$ and $\hat{R}_k$ are the Fourier coefficients of W and R corresponding to mode k. Because the set of complex exponential functions forms an orthogonal basis, the only way for Eq. (3) to be true is that the weight of every mode k is zero. An infinite number of steady equations in the frequency domain is obtained as expressed by

$$ik\omega V\hat{W}_k + \hat{R}_k = 0, \quad \forall\ k \in \mathbb{Z} \tag{4}$$

McMullen et al. [12] solve a subset of these equations up to mode N, $-N \leq k \leq N$, yielding the nonlinear frequency-domain method.

The time spectral method [6] uses a discrete inverse Fourier transform (DIFT) to cast back in the time domain this subset of $2N + 1$ equations from Eq. (4). The DIFT induces linear relations between Fourier's coefficients $\hat{W}_k$ and a uniform sampling of W within the period

$$W_n = \sum_{k=-N}^{N} \hat{W}_k \exp(i\omega n\Delta t), \qquad 0 \leq n < 2N + 1$$

with $W_n \equiv W(n\Delta t)$ and $\Delta t = T/(2N + 1)$. This leads to a time discretization with a new time operator D_t as follows:

$$R(W_n) + VD_t(W_n) = 0, \qquad 0 \leq n < 2N + 1 \tag{5}$$

These steady equations correspond to $2N + 1$ instants equally spaced within the period. The new time operator connects all time levels and can be expressed analytically by

$$D_t(W_n) = \sum_{m=-N}^{N} d_m W_{n+m}$$

with

$$d_m = \begin{cases} \frac{\pi}{T}(-1)^{m+1}\csc(\frac{\pi m}{2N+1}), & m \neq 0 \\ 0, & m = 0 \end{cases}$$

A similar derivation can be made for an even number of instants, but it is proven in [10] that it can lead to an odd–even decoupling and, as a consequence, the method can become unstable. Time-dependent boundary conditions could also benefit from such a derivation, but this is not an issue for external aerodynamic applications and has not been done yet.

A pseudotime derivative τ_n is added to Eq. (5) to time march the equations to the steady-state solutions of all instants:

$$V\frac{\partial W_n}{\partial \tau_n} + R(W_n) + VD_t(W_n) = 0, \qquad 0 \leq n < 2N + 1 \tag{6}$$

The term $VD_t(W_n)$ appears as a source term that represents a high-order formulation of the initial time derivative in Eq. (1). For stability reasons, the computation of the local time step is modified [10] to take into account this additional source term:

$$\Delta\tau = \mathrm{CFL}\frac{V}{\parallel \lambda \parallel + \omega NV} \tag{7}$$

where CFL denotes the Courant–Friedrichs–Lewy number. An extra term ωNV is added to the spectral radius $\parallel \lambda \parallel$ to restrict the time step. Equation (7) implies that a high frequency and/or a high number N of harmonics can considerably constrain the time step. Actually, it has been observed [5] that the convergence of the method slows down for increasing N. Explicit schemes are used in [5–11], such as Runge–Kutta, to carry out the pseudotime integration. Their limited stability criteria on CFL numbers is very sensitive to such a restriction. Conversely, implicit schemes are more stable and allow larger CFL numbers, reducing this sensitivity. Such schemes would have the same behavior when the frequency of the unsteadiness increases. The following section describes the backward-Euler algorithm for the TSM.

III. Implicit Time Integration

Let us recall the backward-Euler algorithm for the Navier–Stokes equations and the standard solving lower upper-symmetric successive overrelaxation [13] (LU-SSOR) method.

A. Algorithm for Steady Navier–Stokes Equations

The time derivative in Eq. (1) is discretized by a first-order scheme

$$V\frac{\Delta W}{\Delta t} = -R(W) \tag{8}$$

where $\Delta W = W^{q+1} - W^q$ is the increment of the conservative variables between the iterations q and $q+1$. By considering $R(W)$ at iteration $q+1$, the implicit backward-Euler scheme is derived. As $R(W^{q+1})$ is unknown, it is linearized. Let J be the Jacobian matrix of the residual vector $J = \partial R(W)/\partial W$. The linearization of $R(W^{q+1})$ is then

$$R(W^{q+1}) = R(W^q) + J\Delta W + \mathcal{O}(\Delta W^2) \tag{9}$$

Equations (8) and (9) lead to the following linear system:

$$\left(\frac{V}{\Delta t}I + J\right)\Delta W = -R(W^q)$$

The LU-SSOR method is used to approximate the solution of this system. Formally, the matrix A of the linear system is split into three matrices:

$$A\Delta W = (\mathcal{L} + \mathcal{D} + \mathcal{U})\Delta W = -R(W^q) \tag{10}$$

with $\mathcal{L}$ a lower triangular matrix, $\mathcal{D}$ a diagonal matrix, and $\mathcal{U}$ an upper triangular matrix. One LU-SSOR step is composed of the forward and backward sweeps of the iterative symmetric successive overrelaxation (SSOR) method [Eq. (11)], performed one after the other for $s \geq 0$,

$$\begin{cases} (\mathcal{L} + \mathcal{D})\Delta W^{s+1/2} = -R(W^q) - \mathcal{U}\Delta W^s, \\ (\mathcal{U} + \mathcal{D})\Delta W^{s+1} = -R(W^q) - \mathcal{L}\Delta W^{s+1/2} \end{cases} \tag{11}$$

with $\Delta W^0 = 0$. These two sweeps are repeated several times and $W^{q+1} = W^q + \Delta W^{s_{\max}}$, $s_{\max}$ corresponding to the maximum number of LU-SSOR steps.

Convective fluxes are written with a first-order Steger and Warming [14] flux vector splitting for the residual linearization to end up with a diagonally dominant implicit matrix, which ensures that the method is convergent. Viscous terms are also linearized and preserve this diagonal dominance. Artificial dissipation is added for stability issues. The boundary conditions could be linearized in a same manner as the residual operator. As the scalar LU-SSOR is used in this paper, this point is not required to get convergence. The relaxation parameter is set to unity as it gives the best performances. This is equivalent to removing overrelaxation and using lower upper-symmetric Gauss–Seidel. Nevertheless, in the following sections, we keep the LU-SSOR designation but, for the sake of simplicity, the derived equations do not mention the relaxation parameter. This method has proven its efficiency in an industrial context for several years.

B. Extension for the Time Spectral Method

To introduce an implicit algorithm in the TSM, the first approach is to linearize only the residual $R(W_n)$ of Eq. (6), but not the source term $VD_t(W_n)$. This leads to the augmented system

$$\begin{pmatrix} \frac{V}{\Delta\tau_0}I + J_0 & 0 & \dots & 0 \\ 0 & \frac{V}{\Delta\tau_1}I + J_1 & \ddots & \vdots \\ \vdots & \ddots & \ddots & 0 \\ 0 & \dots & 0 & \frac{V}{\Delta\tau_{2N}}I + J_{2N} \end{pmatrix} \begin{pmatrix} \Delta W_0 \\ \Delta W_1 \\ \vdots \\ \Delta W_{2N} \end{pmatrix} = -\begin{pmatrix} R_{\mathrm{TSM}}(W_0^q) \\ R_{\mathrm{TSM}}(W_1^q) \\ \vdots \\ R_{\mathrm{TSM}}(W_{2N}^q) \end{pmatrix} \tag{12}$$

with $R_{\mathrm{TSM}}(W_n^q) = R(W_n^q) + VD_t(W_n^q)$ on the right-hand side of the TSM equations, and J_n the Jacobian of the standard residual operator at instant n, $J_n = \partial R(W_n)/\partial W_n$. The augmented matrix is block diagonal and an LU-SSOR algorithm can be applied independently on each instant n. In other words, $2N+1$ steady flows are computed, and they are only coupled through the explicit residuals. This is clearly an advantage because this approach has no impact on message passing and does not need any new development on the implicit side. However, it will be shown in Sec. IV that convergence is not achieved easily with this technique, and the present paper proposes another alternative.

C. Full Implicitation Method for the Time Spectral Method

To improve the performances, the source term of the TSM needs to be taken into account. The TSM equations with W considered at iteration $q+1$ read

$$V\frac{\Delta W_n}{\Delta\tau_n} = -\left[R\left(W_n^{q+1}\right) + VD_t\left(W_n^{q+1}\right)\right], \qquad 0 \leq n < 2N+1 \tag{13}$$

As the operator D_t is linear, applying it on W_n at iteration $q+1$ gives

$$D_t\left(W_n^{q+1}\right) = D_t\left(W_n^q\right) + D_t(\Delta W_n) \tag{14}$$

In the same manner as the TSM new time operator D_t couples together the conservative variables at all instants, Eq. (14) leads to a coupling of the increments ΔW at all instants. Equation (13) turns into

$$\left(\frac{V}{\Delta\tau_n}I + J_n\right)\Delta W_n + VD_t(\Delta W_n) = -R_{\mathrm{TSM}}\left(W_n^q\right), \qquad 0 \leq n < 2N+1$$

As $d_0 = 0$, the diagonal terms are identical to the diagonal terms of Eq. (12). The matrix of the system becomes

$$A^* = \begin{pmatrix} \frac{V}{\Delta\tau_0}I + J_0 & Vd_1I & \dots & Vd_NI & Vd_{-N}I & \dots & Vd_{-1}I \\ Vd_{-1}I & \ddots & \ddots & \vdots & \ddots & \ddots & \vdots \\ \vdots & \ddots & \ddots & Vd_1I & \ddots & \ddots & \vdots \\ Vd_{-N}I & \dots & Vd_{-1}I & \frac{V}{\Delta\tau_N}I + J_N & Vd_1I & \dots & Vd_NI \\ \vdots & \ddots & \ddots & Vd_{-1}I & \ddots & \ddots & \vdots \\ \vdots & \ddots & \ddots & \vdots & \ddots & \ddots & Vd_1I \\ Vd_1I & \dots & Vd_NI & Vd_{-N}I & \dots & Vd_{-1}I & \frac{V}{\Delta\tau_{2N}}I + J_{2N} \end{pmatrix}$$

The new matrix A^* is not block sparse anymore and couples all the increments ΔW_n of all the instants n. This probably explains why the adapted LU-SSOR scheme of Sec. III.B fails to converge for a high number of harmonics, as shown in Sec. IV: the linearization error grows as the number of harmonics increases, and so the convergence rate decays.

A^* could be decomposed as a sum of three matrices $A^* = \mathcal{L}^* + \mathcal{D}^* + \mathcal{U}^*$, with $\mathcal{L}^*$ a lower block triangular matrix, $\mathcal{D}^*$ a block diagonal matrix, and $\mathcal{U}^*$ an upper block triangular matrix. Then, a classical SSOR algorithm could be applied on the whole system, but it would necessitate one to go all over the blocks and thus would break down code efficiency in terms of CPU requirement. To remove this drawback, two solving algorithms based on the block-Jacobi method are now presented.

D. Block-Jacobi Strategies for Full Implicit Time Spectral Method

Applied to the TSM, the iterative block-Jacobi method [15] allows one to move the implicit coupling term $VD_t(\Delta W_n)$ to the right-hand side and yields $2N + 1$ independent linear systems. A Jacobi step l reads

$$\left(\frac{V}{\Delta\tau_n} I + J_n\right)\Delta W_n^{l+1} = -R_{\mathrm{TSM}}\left(W_n^q\right) - VD_t\left(\Delta W_n^l\right), \qquad 0 \le n < 2N+1 \tag{15}$$

with $l \ge 0$, $\Delta W_n^0 = 0$, and at the end of the $l_{\max}$ block-Jacobi iterations, the increments ΔW_n allow one to compute W at the next iteration: $W_n^{q+1} = W_n^q + \Delta W_n^{l_{\max}}$. For every block-Jacobi step, a linear system has to be solved. This system could be solved with any direct or iterative method. The classical SSOR technique is actually used, as it allows minimum efforts to be adapted from the LU-SSOR method.

1. *Block-Jacobi Symmetric Successive Overrelaxation Strategy*

Each equation of the block-Jacobi system, Eq. (15), could be solved with an iterative SSOR technique, classically decomposed in a forward sweep

$$(\mathcal{L}_n + \mathcal{D}_n)X^{s+1/2} = -\left[R_{\mathrm{TSM}}\left(W_n^q\right) + VD_t\left(\Delta W_n^l\right)\right] - \mathcal{U}_n X^s \tag{16}$$

followed by a backward sweep

$$(\mathcal{D}_n + \mathcal{U}_n)X^{s+1} = -\left[R_{\mathrm{TSM}}\left(W_n^q\right) + VD_t\left(\Delta W_n^l\right)\right] - \mathcal{L}_n X^{s+1/2} \tag{17}$$

for $s \ge 0$ with $X^0 = \Delta W_n^l$. At the end of the SSOR iterations, $X^{s_{\max}}$ is updated into the block-Jacobi steps: $\Delta W_n^{l+1} = X^{s_{\max}}$, $s_{\max}$ being the number of SSOR forward and backward sweeps inside a block-Jacobi step. It should be noticed that $\mathcal{L}_n$, $\mathcal{D}_n$, and $\mathcal{U}_n$ refer to Eq. (10), where the splitting of the implicit matrix was obtained for one instant n. The block-Jacobi method imposes the implicit coupling term $D_t(\Delta W_n^l)$ to be updated at each step l. In other words, the implicit coupling term is computed every $2s_{\max}$ sweeps and frozen over the following $2s_{\max} - 1$ sweeps. As $\Delta W_n^0 = 0$, it remains null during all the sweeps in the first block-Jacobi step and, consequently, at least two steps are needed to ensure the coupling of the increments of all instants $l_{\max} \ge 2$. If $l_{\max} = 1$, no implicit coupling occurs and Eq. (12) is recovered. The solving algorithm uses two nested loops as described by Algorithm 1.

To reinforce the influence of the implicit coupling, the next method is proposed.

2. *Block-Jacobi Successive Overrelaxation Strategy*

The system Eq. (15) could also be solved in a special way with alternate successive overrelaxation (SOR) techniques. Only a loop is needed and the imposed constraint is to have an even number $l_{\max}$ of block-Jacobi steps to balance forward and backward sweeps. Indeed, when l is even, the system is solved with only one forward SOR sweep [Eq. (16)], and when l is odd, the system is solved with only one backward SOR sweep [Eq. (17)]. Algorithm 2 describes this strategy.

Algorithm 1 Block-Jacobi-SSOR algorithm for the time spectral method

```
Require: $W_n^q$, $l_{\max} \ge 2$, $s_{\max} \ge 1$
  $\Delta W_n^0 = 0$
  for $l = 0$ to $l_{\max} - 1$ do
    compute $D_t(\Delta W_n^l)$
    $X^0 = \Delta W_n^l$
    for $s = 0$ to $s_{\max} - 1$ do
      solve Eq. (16) {Forward sweep}
      solve Eq. (17) {Backward sweep}
    end for
    $\Delta W_n^{l+1} = X^{s_{\max}}$
  end for
Ensure: $W_n^{q+1} = W_n^q + \Delta W_n^{l_{\max}}$
```

Algorithm 2 Block-Jacobi-SOR algorithm for the time spectral method

```
Require: $W_n^q$, $l_{\max}$ even
  $\Delta W_n^0 = 0$
  for $l = 0$ to $l_{\max} - 1$ do
    compute $D_t(\Delta W_n^l)$
    if $l$ is even then {Forward sweep}
      $X^s = \Delta W_n^l$, solve Eq. (16), $\Delta W_n^{l+1} = X^{s+1/2}$
    else {$l$ is odd, Backward sweep}
      $X^{s+1/2} = \Delta W_n^l$, solve Eq. (17), $\Delta W_n^{l+1} = X^{s+1}$
    end if
  end for
Ensure: $W_n^{q+1} = W_n^q + \Delta W_n^{l_{\max}}$
```

The implicit coupling term $VD_t(\Delta W_n)$ is computed before every sweep (but the first one as $\Delta W_n^0 = 0$), and thus this strategy ensures the strongest coupling. If $s_{\max} = 2$ in the block-Jacobi symmetric successive overrelaxation (BJ-SSOR) method, for instance, the implicit coupling term is computed before the fifth (forward) sweep and frozen over the three following sweeps. Table 1 enables the comparison between the two methods in terms of SOR sweeps.

The LU-SSOR and the new block-Jacobi methods are now compared. The influence of the number of block-Jacobi iterations on convergence rate is also studied.

IV. Validation of the Implicit Time Spectral Method

The TSM technique has been implemented in the parallel structured multiblock solver elsA [16]. The code capability is wide, as it can simulate steady and unsteady, internal and external flows, in a relative or fixed motion. The solver uses a conservative cell-centered finite volume approach for the spatial discretization. Several spatial and time integration schemes are available. In this paper, the second-order Jameson–Schmidt–Turkel centered scheme [17] is used for convective terms and a central second-order scheme is used for diffusive terms. In combination with local time stepping, a

Table 1 Example of implicit coupling term update up to eight sweeps (values of the loop indexes l and s before sweep, and if the implicit coupling term is updated)

Number of sweeps	BJ-SSOR $s_{\max} = 2$			BJ-SOR	
	l	s	Update	l	Update
1	0	0	No	0	No
2	0	0	No	1	Yes
3	0	1	No	2	Yes
4	0	1	No	3	Yes
5	1	0	Yes	4	Yes
6	1	0	No	5	Yes
7	1	1	No	6	Yes
8	1	1	No	7	Yes

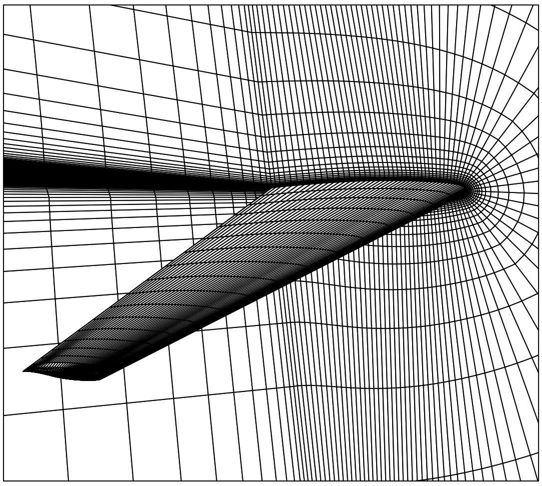

Fig. 1 Navier–Stokes mesh of the LANN wing (for a better readability, the mesh is coarsened twice in every direction).

V-cycle multigrid technique with two levels of coarse grids is used to accelerate the convergence of the steady computations. The Spalart–Allmaras [18] turbulence model is used in all the simulations.

The new implicit algorithm has been validated with the flow simulation around a transonic wing in a forced pitching movement. This wing has been designed by Lockheed Georgia, Air Force Flight Dynamic Laboratory, NASA Langley, and National Aerospace Laboratory (The Netherlands), yielding the name of LANN wing. Experimental data [19] are provided for the frequency $f = 24$ Hz. The angle of attack α oscillates as $\alpha(t) = \alpha_0 + \alpha_m \sin(2\pi f t)$ with $\alpha_0 = 0.6\,\mathrm{deg}$ and $\alpha_m = 0.25\,\mathrm{deg}$. The flow conditions are $M_\infty = 0.822$ and $Re = 5.43 \times 10^6$. Experimental data are available for the time-averaged and the first harmonic values of the wall pressure coefficient C_p at different wing cross sections.

The numerical simulations are conducted on a mesh composed of 1,122,816 cells as shown in Fig. 1. The grid extent is shown Fig. 2 where B denotes the wingspan.

A. Numerical Study

First, a numerical study of the different parameters is conducted. The convergence curves for the first approach described in Sec. III.B are given in Fig. 3a. The solution residual is defined as the root mean square of the residual operator $R(W)$ on all the mesh cells, averaged by the number of instants. The curves indicate the residual on the density residual ρ and are normalized by the residual at first iteration to enable comparison. It is observed that the CFL needs to be decreased to converge high-harmonic computations. For $N = 4$, the CFL must be decreased to 20 (dotted line) because, with 30, the computation does not converge (dashed line). The five-harmonic computation needs a few thousand iterations at CFL = 5 to lose 5 orders of magnitude: the convergence rate is very slow. The first block-Jacobi strategy used is the BJ-SOR, Sec. III.D.2, as it should ensure the best coupling. The results with $l_{\max} = 4$ are presented in Fig. 3b. The benefits of the full implicitation are clear as all the computations are now performed at CFL = 100. Furthermore, almost no differences are found between the normalized convergence curves. Not all test cases show such a good matching, but it is observed that the convergence rate is nearly the same for any number of harmonics.

Up until now, results have been obtained using four SOR sweeps, leading finally to the first forward sweep without implicit coupling ($\Delta W = 0$ initially) and the three other sweeps with implicit coupling (cf. Table 1). The influence of the derived strategies is shown in Fig. 4 for the most difficult case $N = 5$. It is observed that the BJ-SOR

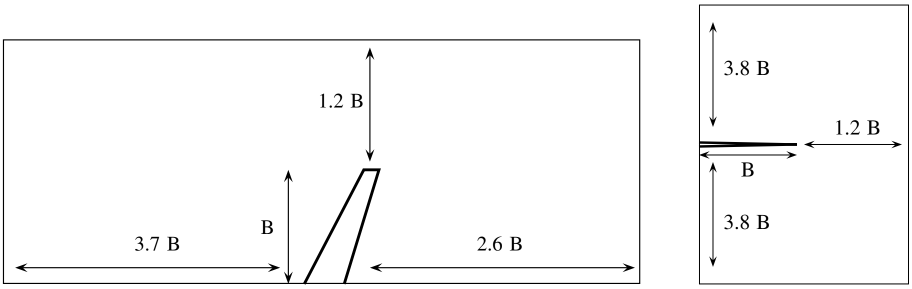

a) Top view: upstream, downstream, and spanwise grid boundaries

b) Front view: upper, lower, and spanwise grid boundaries

Fig. 2 Grid extent (not to scale).

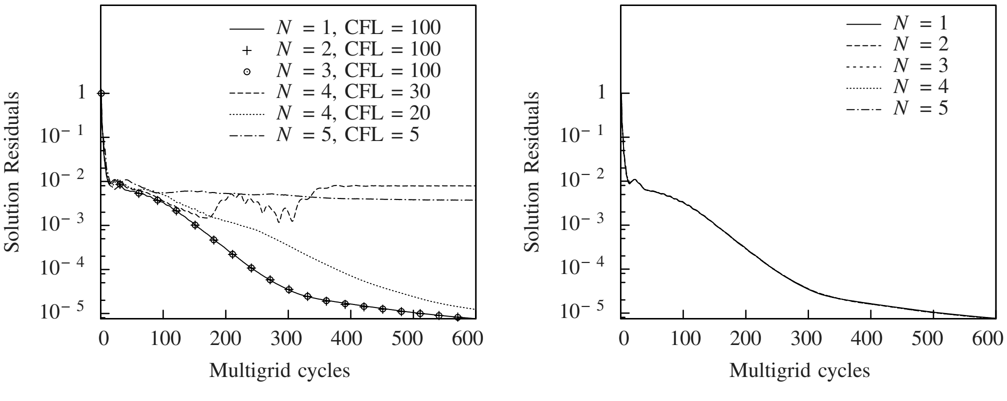

a) Standard LU-SSOR

b) BJ-SOR (all CFL = 100)

Fig. 3 Convergence of the computations.

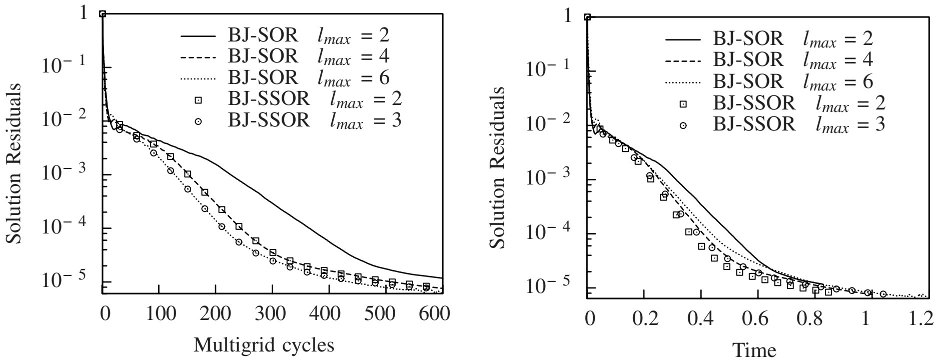

a) Convergence curves with respect to the number of multigrid cycles

b) Convergence curves with respect to a nondimensional CPU time

Fig. 4 Effect of the number of modified LU-SSOR steps on convergence (all CFL = 100).

strategy with $l_{\max} = 2$ (with only the backward sweep ensuring the implicit coupling) is sufficient to obtain convergence at CFL = 100. Thanks to the three coupling sweeps, the BJ-SOR method with $l_{\max} = 4$ substantially speeds up the convergence with respect to the number of multigrid cycles (Fig. 4a). The nondimensional time of computation (Fig. 4b) remains mostly in favor of the BJ-SOR method. The best convergence rate in terms of multigrid cycles is obtained with the BJ-SOR strategy with $l_{\max} = 6$, but this advantage is lost when considering the time spent. The extra CPU cost induced by the two supplementary sweeps is not worth the gain in convergence rate.

Results from the BJ-SSOR algorithm described in Sec. III.D.1 are represented by marks in Fig. 4. As $\Delta W_n = 0$ for the first block-Jacobi step, at least two steps are needed to ensure the coupling of increments (see Table 1). As shown previously with the BJ-SOR method, six sweeps are already expensive. To ensure an implicit coupling as often as possible with this few numbers of sweeps, $s_{\max}$ is set to one for the BJ-SSOR algorithm. Even though the coupling occurs less often, the convergence rate is almost the same for the BJ-SOR method with $l_{\max} = 4$ as for the BJ-SSOR method with $l_{\max} = 2$, and slightly slowed down with two additional sweeps for each method (respectively, $l_{\max} = 6$ and $l_{\max} = 3$) with respect to the number of multigrid cycles. As the term $D_t(\Delta W_n)$ is only computed every two sweeps, the CPU time required by the BJ-SSOR method is notably reduced compared with the BJ-SOR approach with the same number of sweeps.

The CPU and memory costs of the implicitation are not negligible, as shown in Fig. 5. The lines show the trend and do not necessarily pass exactly through the data points. All the computations are performed on a parallel computer, which shows a variation of up to 5% in CPU time, so that this statistic is averaged over four runs of simulation. They are all performed with four sweeps, either $l_{\max} = 4$ for the BJ-SOR method or $l_{\max} = 2$ for the BJ-SSOR method. All the curves are normalized by the cost of three uncoupled steady

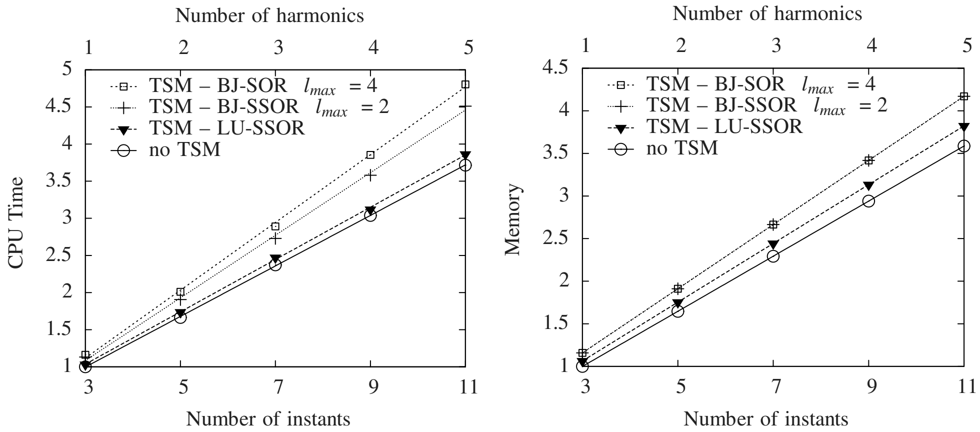

a) CPU cost

b) Memory cost

Fig. 5 Costs of the different implicitation strategies.

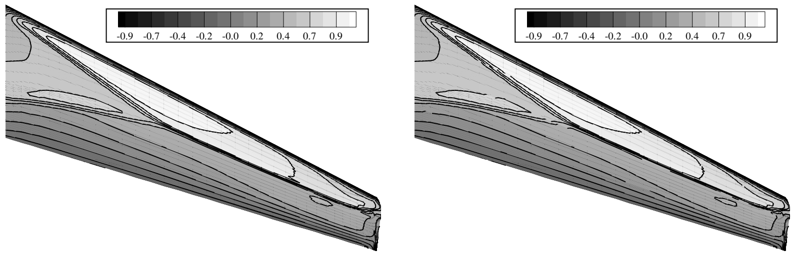

a) U-RANS

b) TSM

Fig. 6 LANN wing upper surface. Instantaneous pressure coefficient at $\alpha = 0.6$ deg for increasing α.

computations. The circles indicate the CPU time and memory consumption required for $2N + 1$ uncoupled steady computations. The inverted triangles denote the TSM with the first approach of Eq. (12) with standard LU-SSOR. The complexity of the computation of D_t is quadratic with respect to the number of instants, but it is only involved in a small part of the global calculations, and the whole time remains linear with respect to the number of instants. Finally, the first approach adds penalties of about 3.5% in CPU time and 6.5% in memory. When considering the BJ-SOR method (squares), D_t is applied several times over the conservative variable increment ΔW_n inside the SOR sweeps. Nevertheless, the CPU time remains linear. The extra cost is significant as the CPU time is increased by 30% and the memory by 10% compared with the LU-SSOR method. With the BJ-SSOR method (plus signs), the implicit coupling term is less often computed so that the extra CPU cost is reduced to 20%. The memory consumption remains identical, as the same information is stored though not computed at the same moment.

Finally, the BJ-SSOR scheme enables a fast convergence rate of the computations at a cost of about one-fifth more CPU time and 10% more memory requirements compared with the LU-SSOR method. Nevertheless, the time steps allowed are much larger and the TSM is far less sensitive to either high frequencies or an important number of harmonics than with explicit schemes. It can thus be concluded that the extra numerical cost of the implicitation is greatly counterbalanced by the larger time step enabled.

B. Pitching Wing

The quality of the presented implicit time spectral method is now studied. The BJ-SSOR method with 300 multigrid cycles and $l_{\max} = 2$ is retained in the following simulations of the LANN wing in forced harmonic oscillations. The time spectral method is compared with a reference U-RANS computation [20] on the same mesh shown in Fig. 1. A dual-time-stepping backward-difference-formula scheme advances the equations in time with 50 inner iterations that take advantage of the same acceleration techniques as for the previous TSM computations. Indeed, an implicit backward-Euler time integration method is used for the inner iterations. The resulting linear system is solved with a scalar LU-SSOR method. Four periods

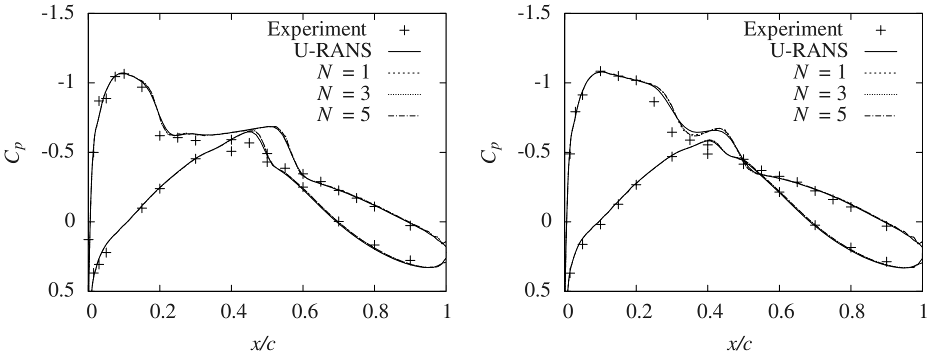

a) 20.0% of wingspan **b) 32.5% of wingspan**

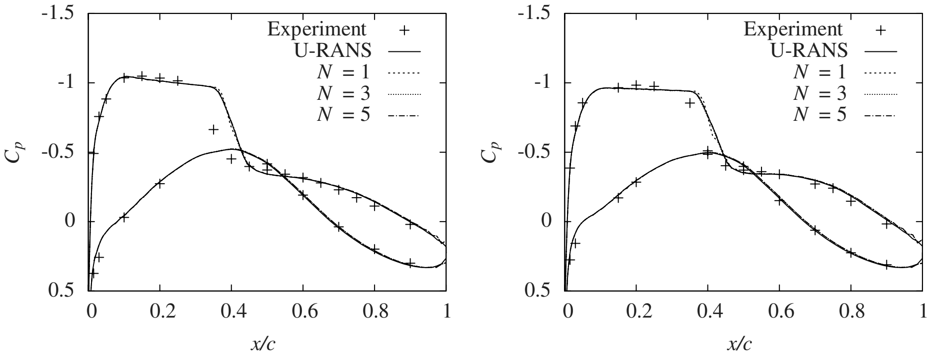

c) 47.5% of wingspan **d) 65.0% of wingspan**

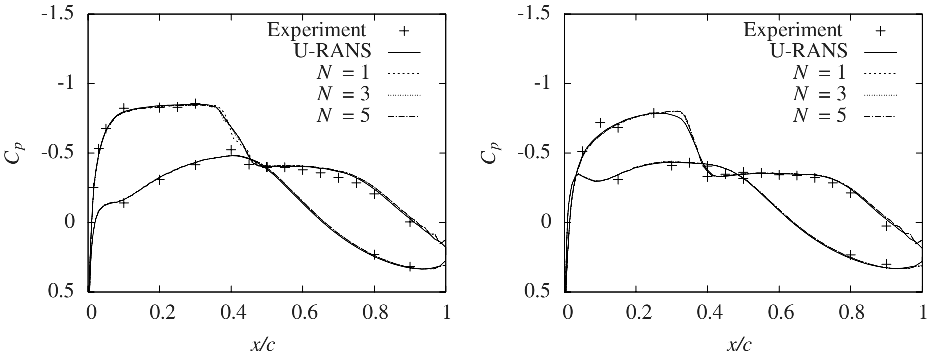

e) 82.5% of wingspan **f) 95.0% of wingspan**

Fig. 7 Time average of the wall wingspan pressure coefficient C_p.

of the flow are discretized by 30 time steps each, leading to 6000 multigrid cycles.

The TSM computations can be carried out in two ways: in a wing-relative or an absolute reference frame. For the first one, the mesh remains rigid around the wing and the variation of incidence is induced by different far-field boundary conditions applied at each instant. In this case, the inertial force has to be taken into account through a source term of the Navier–Stokes equations. In an absolute reference frame, the incidence variation is produced by deforming the mesh around the wing skin while the far-field boundary conditions remain fixed. In an arbitrary Lagrangian–Eulerian formulation, the deformation velocity of the mesh is introduced in the computation of the fluxes, Eq. (2), and as the cell volume V also varies in time, the TSM operator is applied on VW, leading to the following semidiscrete equation:

$$V_n \frac{\partial W_n}{\partial \tau_n} + R(W_n) + D_t(V_n W_n) = 0, \qquad 0 \le n < 2N + 1$$

Both methods lead to very close results and cannot be discriminated.

An instantaneous snapshot of the pressure coefficient C_p is presented for U-RANS and TSM in Fig. 6 at $\alpha = 0.6\,\mathrm{deg}$ for increasing angle of attack. A λ shock is clearly visible near the wing root.

The Fourier analysis is conducted on six sections at 20.0, 32.5, 47.5, 65.0, 82.5, and 95.0% of the wingspan. The time-averaged part is presented in Fig. 7. A one-harmonic TSM computation is sufficient to match the U-RANS computation almost everywhere but at the shock location, where the solution slightly fluctuates. With higher harmonics ($N = 3$ and $N = 5$), TSM solutions match well the reference U-RANS simulation. Both kinds of simulation give solutions that match the experimental data quite well, although the shock on the upper surface is predicted downstream of the experimental location.

The real and imaginary parts of the first harmonic of the pressure coefficient are presented in Figs. 8 and 9. The differences are more pronounced, and it appears that one harmonic is not sufficient to match the U-RANS computation, as it shows a small phase lag and some over- and undershoots around the shock area. These drawbacks are removed with a three-harmonic TSM computation,

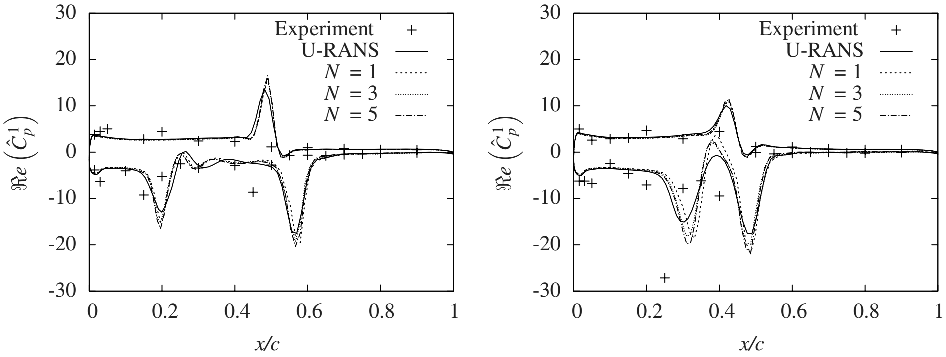

a) 20.0% of wingspan

b) 32.5% of wingspan

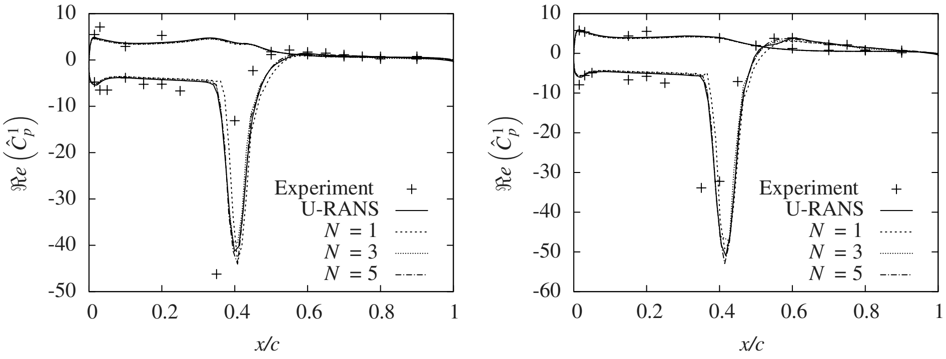

c) 47.5% of wingspan

d) 65.0% of wingspan

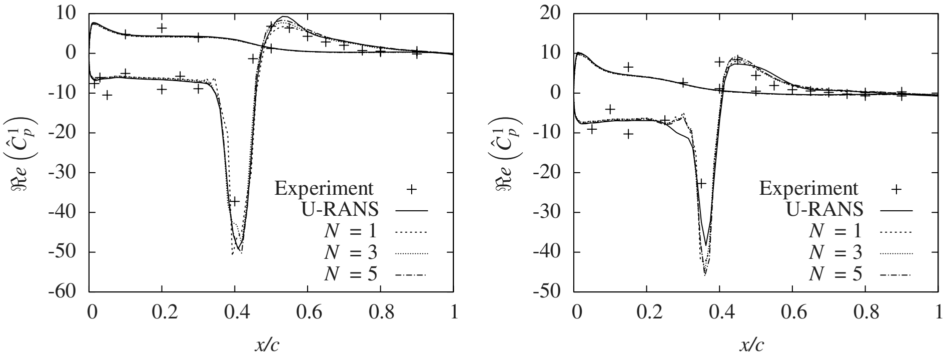

e) 82.5% of wingspan

f) 95.0% of wingspan

Fig. 8 Real part of the first harmonic of C_p.

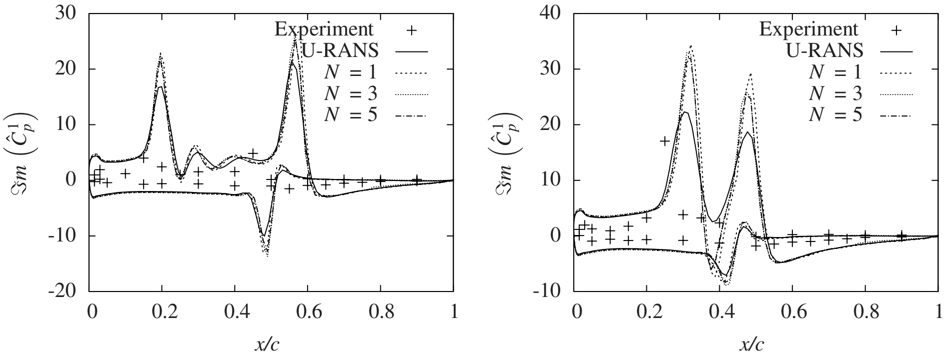

a) 20.0% of wingspan **b) 32.5% of wingspan**

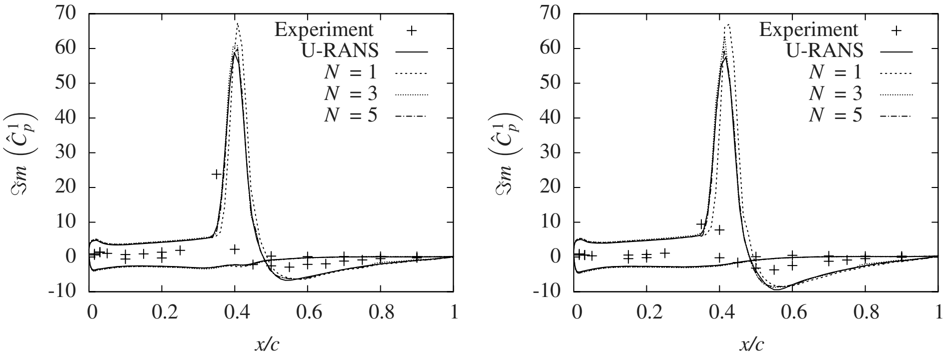

c) 47.5% of wingspan **d) 65.0% of wingspan**

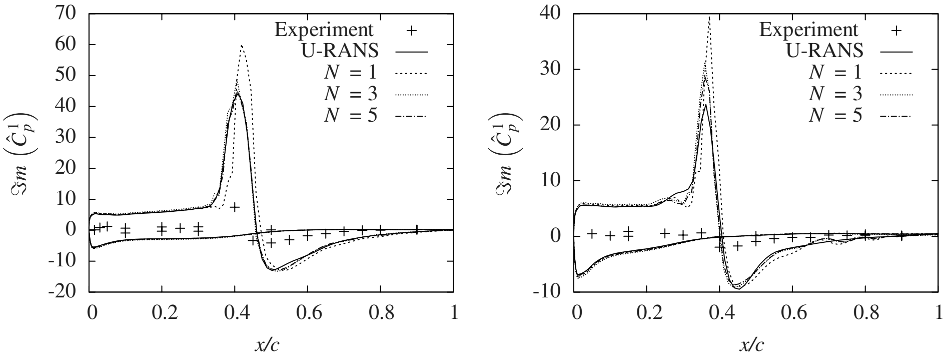

e) 82.5% of wingspan **f) 95.0% of wingspan**

Fig. 9 Imaginary part of the first harmonic of C_p.

although some peaks are still sharp. A five-harmonic computation works better to lessen the irregularities at the peaks.

This point emphasizes the need for an accurate and efficient implicit formulation because all authors using an explicit time-step algorithm mention the difficulty of getting convergence with a higher number of harmonics. Overall, it can be concluded that a three-harmonic TSM computation is sufficient to match the U-RANS computation with engineering accuracy. In this case, the TSM is about 2.5 times faster than the reference U-RANS computation (see Fig. 10).

V. Conclusions

The time spectral method is dedicated to simulate time-periodic flows with a better efficiency than classical time-marching methods, that is, a quality of physics close to good U-RANS computations with a faster convergence rate. Up until now, the coupled steady computations have only been solved with explicit time marching, yielding in small time steps, further decreased by the stability criteria, which restricts the time step for high frequencies and for a large number of harmonics. In an industrial context, it was therefore

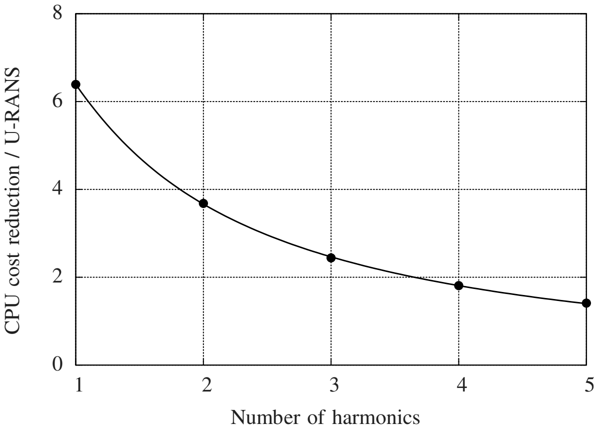

Fig. 10 CPU cost reduction of TSM compared with the reference U-RANS computation.

necessary to propose an alternative to the explicit time marching. Based on the LU-SSOR decomposition, new block-Jacobi implicit approaches have been derived to reduce the sensitivity of the method to high-frequency issues. Several solving processes have been tested to retain the most efficient approach. Finally, the BJ-SSOR approach enables better performances and faster convergence.

Our current effort concerns the extension of the time spectral method to turbomachinery. The frequencies met in these applications are much higher than in pitching wing flows and the present implicit treatments should ensure convergence. Even though the BJ-SSOR approach does not offer the best CPU performances, it will still be considered for turbomachine applications, as it ensures the strongest coupling.

Acknowledgments

This work has benefited from the generous support of the Direction des Programmes Aéronautiques Civils (French Civil Aviation Agency) as part of the Analyse Instationnaire des Turbomachines en aÉrodynamique et aCoustique program. The authors would also like to thank Societe Nationale d'Etude et de Construction de Moteurs d'Aviation for its active sponsoring. And finally, ONERA, the French aerospace laboratory and owner of the elsA solver, is greatly acknowledged for its scientific support.

References

[1] Hall, K. C., Thomas, J. P., Ekici, K., and Voytovich, D. M., "Frequency Domain Techniques for Complex and Nonlinear Flows in Turbomachinery," *33rd AIAA Fluid Dynamics Conference and Exhibit*, AIAA Paper 2003-3998, June 2003.

[2] McMullen, M., and Jameson, A., "The Computational Efficiency of Non-Linear Frequency Domain Methods," *Journal of Computational Physics*, Vol. 212, No. 2, March 2006, pp. 637–661.
doi:10.1016/j.jcp.2005.07.021

[3] Verdon, J. M., and Caspar, J. R., "A Linearized Unsteady Aerodynamic Analysis for Transonic Cascades," *Journal of Fluid Mechanics*, Vol. 149, 1984, pp. 403–429.
doi:10.1017/S002211208400272X

[4] Ning, W., and He, L., "Computation of Unsteady Flows Around Oscillating Blades Using Linear and Nonlinear Harmonic Euler Methods," *Journal of Turbomachinery*, Vol. 120, No. 3, July 1998, pp. 508–514.

[5] Hall, K. C., Thomas, J. P., and Clark, W. S., "Computation of Unsteady Nonlinear Flows in Cascades Using a Harmonic Balance Technique," *AIAA Journal*, Vol. 40, No. 5, May 2002, pp. 879–886.
doi:10.2514/2.1754

[6] Gopinath, A., and Jameson, A., "Time Spectral Method for Periodic Unsteady Computations over Two- and Three- Dimensional Bodies," *43rd Aerospace Sciences Meeting and Exhibit*, AIAA Paper 2005-1220, Jan. 2005.

[7] Gopinath, A., and Jameson, A., "Application of the Time Spectral Method to Periodic Unsteady Vortex Shedding," *44th AIAA Aerospace Sciences Meeting and Exhibit*, AIAA Paper 2006-0449, Jan. 2006.

[8] Spiker, M. A., Thomas, J. P., Kielb, R. E., Hall, K. C., and Dowell, E. H., "Modeling Cylinder Flow Vortex Shedding with Enforced Motion Using a Harmonic Balance Approach," *47th AIAA/ASME/ASCE/AHS/ASC Structures, Structural Dynamics and Materials (SDM) Conference*, AIAA Paper 2006-1965, May 2006.

[9] Thomas, J. P., Dowell, E. H., and Hall, K. C., "Nonlinear Inviscid Aerodynamic Effects on Transonic Divergence, Flutter, and Limit-Cycle Oscillations," *AIAA Journal*, Vol. 40, No. 4, April 2002, pp. 638–646.
doi:10.2514/2.1720

[10] van der Weide, E., Gopinath, A., and Jameson, A., "Turbomachinery Applications with the Time Spectral Method," *35th AIAA Fluid Dynamics Conference and Exhibit*, AIAA Paper 2005-4905, June 2005.

[11] Gopinath, A., van der Weide, E., Alonso, J., Jameson, A., Ekici, K., and Hall, K., "Three-Dimensional Unsteady Multi-Stage Turbomachinery Simulations Using the Harmonic Balance Technique," *45th AIAA Aerospace Sciences Meeting and Exhibit*, AIAA Paper 2007-0892, Jan. 2007.

[12] McMullen, M., Jameson, A., and Alonso, J., "Acceleration of Convergence to a Periodic Steady State in Turbomachinery Flows," *39th Aerospace Sciences Meeting*, AIAA Paper 2001-0152, Jan. 2001.

[13] Yoon, S., and Jameson, A., "An LU-SSOR Scheme for the Euler and Navier-Stokes Equations," *AIAA 25th Aerospace Sciences Meeting*, AIAA Paper 87-0600, Jan. 1987.

[14] Steger, J. L., and Warming, R. F., "Flux Vector Splitting of the Inviscid Gas-Dynamic Equations with Applications to Finite Difference Methods," *Journal of Computational Physics*, Vol. 40, April 1981, pp. 263–293.
doi:10.1016/0021-9991(81)90210-2

[15] Saad, Y., *Iterative Methods for Sparse Linear Systems*, 2nd ed., Society for Industrial and Applied Mathematics, Philadelphia, 2003.

[16] Cambier, L., and Veuillot, J., "Status of the elsA Software for Flow Simulation and Multi-Disciplinary Applications," *46th AIAA Aerospace Sciences Meeting and Exhibit*, AIAA Paper 2008-0664, Jan. 2008.

[17] Jameson, A., Schmidt, W., and Turkel, E., "Numerical Solutions of the Euler Equations by Finite Volume Methods Using Runge–Kutta Time-Stepping Schemes," *AIAA 14th Fluid and Plasma Dynamic Conference*, AIAA Paper 81-1259, June 1981.

[18] Spalart, P. R., and Allmaras, S. R., "A One-Equation Turbulence Transport Model for Aerodynamic Flows," *30th AIAA Aerospace Sciences Meeting and Exhibit*, AIAA Paper 92-0439, Jan. 1992.

[19] Zwaan, R. J., "LANN Wing. Pitching Oscillation. Compendium of Unsteady Aerodynamic Measurements. Addendum No. 1," AGARD TR 702, 1982, Data Set 9.

[20] Delbove, J., "Full Navier–Stokes Unsteady Simulations: Application to Flutter Prediction: Contribution aux outils de Simulation Aéroélastique des Aéronefs: Prédiction du Flottement et Déformation Statique des Voilures," Ph.D. Thesis, École Nationale Supérieure de l'Aéronautique et de l'Espace, Toulouse, France, 2005.

K. Powell
Associate Editor

AIAA JOURNAL
Vol. 48, No. 4, April 2010

Contrasting the Harmonic Balance and Linearized Methods for Oscillating-Flap Simulations

Guillaume Dufour,* Frédéric Sicot,† and Guillaume Puigt*
European Center for Research and Advanced Training in Scientific Computing, 31057 Toulouse Cedex 01, France
and
Cédric Liauzun‡ and Alain Dugeai‡
French Aerospace Laboratory, 92322 Châtillon Cedex, France

DOI: 10.2514/1.43401

In the framework of unsteady aerodynamics, forced-harmonic-motion simulations can be used to compute unsteady loads. In this context, the present paper assesses two alternatives to the unsteady Reynolds-averaged Navier–Stokes approach, the linearized unsteady Reynolds-averaged Navier–Stokes equations method, and the harmonic balance approach. The test case is a NACA 64A006 airfoil with an oscillating flap mounted at 75% of the chord. Emphasis is put on examining the performances of the methods in terms of accuracy and computational cost over a range of physical conditions. It is found that, for a subsonic flow, the linearized unsteady Reynolds-averaged Navier–Stokes method is the most efficient one. In the transonic regime, the linearized unsteady Reynolds-averaged Navier–Stokes method remains the fastest approach, but with limited accuracy around shocks, whereas a one-harmonic harmonic balance solution is in closer agreement with the unsteady Reynolds-averaged Navier–Stokes solution. In the case of separation in the transonic regime, the linearized unsteady Reynolds-averaged Navier–Stokes method fails to converge, whereas the harmonic balance remains robust and accurate.

I. Introduction

UNSTEADY aerodynamics has always been a major concern for aircraft manufacturers, whether it is for flutter assessment, flight dynamics data generation, or gust response evaluation. All these problems may be tackled in the framework of periodic forced-motion response. Recent advances in computational fluid dynamics (CFD) have made possible the numerical prediction of these kinds of nonlinear unsteady flows. A reference approach for such predictions is the resolution of the unsteady Reynolds-averaged Navier–Stokes (URANS) equations for a prescribed harmonic motion. However, this kind of simulation is still too expensive in terms of computational time in an industrial context, in which routine design investigations have to be performed on a daily basis.

An alternative to the URANS approach is the resolution of the linearized unsteady Reynolds-averaged Navier–Stokes (LUR) equations. This method was first developed for turbomachinery flows [1,2] and extended to aircraft applications [3,4]. It consists of the linearization of the URANS equations with respect to a small perturbation superimposed over a base flow. The resulting equation is then written in the frequency domain, assuming the flow variables to be first-order harmonic. This yields a complex linear system, which can be solved using classical steady CFD pseudo-time-marching algorithms. Thus, this approach allows one to take into account reference states (with shocks at definite locations), but is neither able to capture nor model unsteady nonlinear phenomena like buffet, limit-cycle oscillations, or massive flow separations.

Finally, a recently developed technique is the harmonic balance (HB) method, proposed by Hall et al. [5] for time-periodic flows. This method can be viewed as an equivalent in the time domain of the frequency-domain approach proposed by He and Ning [6]. Then, Gopinath and Jameson [7] presented the time spectral (TS) method, which is essentially similar to the HB method: both methods capture the fundamental frequency of the flow and a given number of its harmonics. Later on, the HB and TS methods were merged and extended for multistage turbomachinery computations [8] in which several frequencies appear, not necessarily integer multiples of each others. The method resulting from both teams' work is referred to as the HB method. In the present paper the notation HB is retained, though all the computations presented here consider a single fundamental frequency. This method has proven its efficiency in decreasing the total CPU time of forced-motion simulations, while ensuring a good accuracy (see Sicot et al. [9], among others).

Although He and Ning [6] evaluated their frequency-domain harmonic method against linearized computations, there is no such comparison in the available literature for time-domain harmonic methods. Therefore, the primary objective of the present paper is to contrast the accuracy and efficiency of the LUR and HB methods with the URANS predictions. The published information is scarce (see [4], for instance, for the LUR) regarding detailed and consistent CPU time requirement comparisons of the two methods with URANS (for example, Hall et al. [5] compare their approach to steady computations). As can be expected, it appears to be problem and implementation dependant (compare [9,10], for instance). A second objective of the present paper is thus to make the assessment over a range of significantly different flow conditions, but for the same physical problem and within the same code. Finally, a specific practical issue discussed herein is the actual difference between a linearized solution and a one-harmonic HB solution, which seem similar as a "base state" and only the first harmonic of the flow are evaluated in both cases.

To achieve these objectives, the test case considered is the harmonic oscillation of a flap mounted on a NACA 64A006 airfoil. The flow regimes examined cover a wide range of physical conditions: 1) the subsonic regime, 2) the transonic regime, and 3) the transonic regime with separation over the upper side of the flap. The paper is organized as follows. Section II presents the three methods investigated, and Sec. III presents the analysis of the numerical

---

Received 23 January 2009; revision received 31 July 2009; accepted for publication 30 October 2009.

[*] Senior Researcher, Computational Fluid Dynamics Team, 42 Avenue Coriolis.

[†] Doctoral Candidate, Computational Fluid Dynamics Team, 42 Avenue Coriolis; currently Research Engineer, French Aerospace Laboratory, 92322 Châtillon Cedex, France.

[‡] Research Engineer, Aeroelasticity and Structural Dynamics Department, 29 Avenue de la Division Leclerc, Boîte Postale 72.

results obtained. The last section makes a synthesis of the results and draws the conclusions of the study.

II. Presentation of the Methods

In this section, we first recall the Reynolds-averaged Navier–Stokes equations with the arbitrary Lagrangian Eulerian (ALE) formulation. Then, the three methods used are presented. All the numerical choices presented are related to the elsA code used for the present study [11], which is briefly described at the end of the section.

A. Arbitrary Lagrangian Eulerian Formulation of the Reynolds-Averaged Navier–Stokes Equations

In Cartesian coordinates, the ALE formulation of the RANS equations can be written in semidiscrete form as

$$\frac{\partial(VW)}{\partial t} + R(W, s) = 0 \tag{1}$$

where V is the volume of a cell (which can vary in time) and W is the vector of the conservative variables:

$$W = (\rho, \rho u_1, \rho u_2, \rho u_3, \rho E)^T$$

complemented with an arbitrary number of turbulent variables defined by the turbulence modeling framework. For second-order turbulence modeling, the total energy $E = e + u^2/2 + k$ includes the contribution of the turbulent kinetic energy. The velocity of the mesh is

$$s = s^E + s^D$$

where s^E is the entrainment velocity and s^D the deformation velocity. The residual vector $R(W, s)$ resulting from the spatial discretization of the convective f_{ci} and viscous f_{vi} terms is defined as

$$R(W, s) = \frac{\partial}{\partial x_i} f_i(W, s)$$

with $f_i = f_{ci} - f_{vi}$ and

$$f_{ci} = \begin{pmatrix} \rho(u_i - s_i) \\ \rho u_i(u_1 - s_1) + p\delta_{i1} \\ \rho u_i(u_2 - s_2) + p\delta_{i2} \\ \rho u_i(u_3 - s_3) + p\delta_{i3} \\ \rho u_i E + p u_i \end{pmatrix}, \qquad f_{vi} = \begin{pmatrix} 0 \\ \tau_{i1} \\ \tau_{i2} \\ \tau_{i3} \\ u \cdot \tau_i - q_i \end{pmatrix} \tag{2}$$

where δ_{ij} denotes the Kronecker symbol. For second-order turbulence modeling, a contribution from the turbulent kinetic energy is added to the static pressure term: $p = p_s + \frac{2}{3}\rho k$. The components of the combined stress and Reynolds tensors are

$$\tau_{11} = \frac{2}{3}\mu\left(2\frac{\partial u_1}{\partial x_1} - \frac{\partial u_2}{\partial x_2} - \frac{\partial u_3}{\partial x_3}\right), \qquad \tau_{12} = \tau_{21} = \mu\left(\frac{\partial u_2}{\partial x_1} + \frac{\partial u_1}{\partial x_2}\right)$$

$$\tau_{22} = \frac{2}{3}\mu\left(-\frac{\partial u_1}{\partial x_1} + 2\frac{\partial u_2}{\partial x_2} - \frac{\partial u_3}{\partial x_3}\right), \qquad \tau_{13} = \tau_{31} = \mu\left(\frac{\partial u_3}{\partial x_1} + \frac{\partial u_1}{\partial x_3}\right)$$

$$\tau_{33} = \frac{2}{3}\mu\left(-\frac{\partial u_1}{\partial x_1} - \frac{\partial u_2}{\partial x_2} + 2\frac{\partial u_3}{\partial x_3}\right), \qquad \tau_{23} = \tau_{32} = \mu\left(\frac{\partial u_2}{\partial x_3} + \frac{\partial u_3}{\partial x_2}\right)$$

where the total viscosity μ is the sum of the laminar μ_{lam} and turbulent μ_{turb} viscosities. Pr_{lam} and Pr_{turb} are the associated Prandtl numbers. The heat-flux vector q components are $q_i = -\kappa\partial T/\partial x_i$, where T is the temperature and

$$\kappa = C_p\left(\frac{\mu_{\text{lam}}}{Pr_{\text{lam}}} + \frac{\mu_{\text{turb}}}{Pr_{\text{turb}}}\right)$$

is the thermal conductivity. For an ideal gas, the closure is provided by the equation of state

$$p_s = (\gamma - 1)\rho\left(E - \frac{u_i u_i}{2}\right)$$

B. Nonlinear Method (Unsteady Reynolds-Averaged Navier–Stokes)

In the present study, the URANS approach is used as a reference for the comparisons because the other two methods are basically derived from it. To obtain a time-accurate numerical solution of Eqs. (1), the choice is made to use a second-order dual time-stepping method for the time integration [12]. This approach is what we refer to as the nonlinear method, because all the nonlinearities of the mean flow can potentially be captured. For each global time step, a steady problem is resolved using pseudo-time-marching techniques. The inner-loop time integration is performed by an implicit backward-Euler scheme. The resulting linear system is solved with a scalar lower–upper symmetric successive overrelaxation (LU-SSOR) method [13]. Local time stepping and a two-level V-cycle multigrid algorithm are used to accelerate the convergence in pseudotime. The mesh deformation is performed at each global time step, using a transfinite interpolation algorithm [14] for the present study. The associated mesh-deformation velocity is computed using a simple finite difference operator:

$$s_n^D = \frac{M_n - M_{n-1}}{\Delta t} \tag{3}$$

for each mesh point M. From a practical point of view, the accuracy of the solution depends on three aspects: 1) the convergence of the inner-loop iterations, monitored by the reduction of the L^2 norm of the residuals; 2) the time step, usually expressed as a fraction of the period; and 3) the time span of the simulation, usually expressed as a number of periods computed. One has to find a tradeoff between these three parameters.

C. Linearized Method (Linearized Unsteady Reynolds-Averaged Navier–Stokes)

The linearization of the Navier–Stokes equations consists, in a first step, of splitting the flow variables into base and a perturbation components ($W = W_b + \delta\mathcal{W}$), and in a second step, of rewriting the fluid Eqs. (1) by retaining only the first-order terms in the perturbation variables ($\delta\mathcal{W}$). The subscript b stands in this part for the base variables, and the prefix δ for the perturbation ones. Assuming the base state is a steady solution of Eqs. (1), the following equation is obtained:

$$V_b\frac{\partial(\delta\mathcal{W})}{\partial t} + W_b\frac{\partial(\delta\mathcal{V})}{\partial t} = -\delta R = -\frac{\partial(\delta\mathcal{F}_i)}{\partial x_i} \tag{4}$$

Because the flow perturbation variables and the wall motion ($\delta\mathcal{M}$) are assumed to be harmonic at a pulsation ω, the previously linearized Eqs. (4) can be written in the frequency domain as

$$\begin{cases} \delta\mathcal{W} = \delta W.e^{i\omega t}, \quad \text{with } i^2 = -1 \\ \delta\mathcal{M} = \delta M.e^{i\omega t}, \\ \delta\mathcal{F}_i = \delta f_i.e^{i\omega t}, \\ s = i\omega.\delta M \end{cases}$$

$$i\omega V_b\delta W + i\omega W_b\delta V + \frac{\partial(\delta f_i)}{\partial x_i} = 0 \tag{5}$$

where

$$\delta W = \begin{pmatrix} \delta\rho \\ \delta(\rho u_1) \\ \delta(\rho u_2) \\ \delta(\rho u_3) \\ \delta(\rho E) \end{pmatrix}$$

$$\delta f_i = \begin{pmatrix} \delta(\rho u_i) - \rho_b s_i \\ u_{1,b}\delta(\rho u_i) + (\rho u_i)_b(\delta u_1 - s_1) + \delta p.\delta_{i1} \\ u_{2,b}\delta(\rho u_i) + (\rho u_i)_b(\delta u_2 - s_2) + \delta p.\delta_{i2} \\ u_{3,b}\delta(\rho u_i) + (\rho u_i)_b(\delta u_3 - s_3) + \delta p.\delta_{i3} \\ u_{i,b}(\delta(\rho E) + \delta p) + (\rho E + p)_b \delta u_i \end{pmatrix} + \begin{pmatrix} 0 \\ \delta\tau_{i1} \\ \delta\tau_{i2} \\ \delta\tau_{i3} \\ \delta u \cdot \tau_{i,b} + u_b \cdot \delta\tau_i - \delta q_i \end{pmatrix}$$

and

$$\delta u_i = \frac{1}{\rho_b}(\delta(\rho u_i) - u_{ib}\delta\rho)$$

$$\delta p = (\gamma - 1)\left[\delta(\rho E) + \frac{u_b \cdot u_b}{2}\delta\rho - u_b \cdot \delta(\rho u)\right]$$

$$\delta\tau_{ii} = \frac{2}{3}\mu_b\left[3\frac{\partial\delta u_i}{\partial x_i} - \frac{\partial\delta u_1}{\partial x_1} - \frac{\partial\delta u_2}{\partial x_2} - \frac{\partial\delta u_3}{\partial x_3}\right]$$

$$\delta\tau_{ij} = \mu_b\left[\frac{\partial\delta u_i}{\partial x_j} + \frac{\partial\delta u_j}{\partial x_i}\right]$$

$$\delta q_i = -\kappa_b\frac{\partial T}{\partial x_i}$$

$$\delta T = \frac{1}{c_v}\left[\frac{1}{\rho_b}\left(\delta(\rho E) - (\rho E)_b\frac{\delta\rho}{\rho_b}\right) - u_b \cdot \delta u\right]$$

The latter linearized fluid equation (5) has been obtained considering the laminar and turbulent viscosity coefficients frozen to their base state. For a given base state, it yields a complex linear system in the complex variable $\delta\mathcal{W}$, which is solved using a pseudotime-implicit method (backward-Euler LU-SSOR) associated with local time-stepping and multigrid algorithms. The choice is naturally made to use the steady solution as a base state. It is computed separately for the zero-deflection position of the flap, and it is an input for the resolution of the system in the frequency domain.

D. Harmonic Balance Method

1. *Fourier-Based Time Discretization*

For a periodic flow, the first step in the HB method is to perform a Fourier decomposition of the flow variables and residuals [5,7]. The series are then injected in the semidiscrete form of the RANS equations Eqs. (1) to obtain a set of coupled equations in the frequency domain. A subset of these equations is solved up to mode N, the number of harmonics retained in the Fourier series. A discrete inverse Fourier transform is then used to cast back the system in the time domain. A set of mathematically steady equations coupled by a source term is finally obtained:

$$R(W_n, s_n) + D_t[(VW)_n] = 0, \qquad 0 \leq n < 2N + 1 \tag{6}$$

where the subscript n denotes a snapshot of a quantity at the instant $t_n = nT/(2N + 1)$. These "steady" equations thus correspond to $2N + 1$ instants equally spaced within the period. The new time operator D_t connects all the instants and can be expressed analytically as

$$D_t[\phi] = \sum_{m=-N}^{N} d_m \phi_{n+m} \tag{7}$$

where ϕ is a flow variable [$\phi = (VW)$ in Eq. (6)], with

$$d_m = \begin{cases} \frac{\pi}{T}(-1)^{m+1}\csc(\frac{\pi m}{2N+1}), & m \neq 0, \\ 0 & m = 0 \end{cases}$$

The source term $D_t[(VW)_n]$ can be viewed as a high-order spectral formulation of the initial time derivative in Eqs. (1). This spectral operator is applied to all the flow variables, including the turbulent ones.

Following the dual time-stepping approach, a pseudotime derivative t_n^* is added to Eq. (6) to time march the equations to the "steady-state" solution for each instant.

For stability reasons, the computation of the local pseudotime step is modified [15] to take into account the HB source term. Here, the Block–Jacobi symmetric-overrelaxation implicit treatment of the HB source term proposed by Sicot et al. [9] is used.

Interestingly, the HB method could be viewed as the superimposition of a high-order complex perturbation over a time-averaged solution (the zero-order term of the Fourier series), whereas in the LUR method, the base state is the steady solution, and the perturbation is of the first order; hence, there is some similarity between a LUR and a one-harmonic HB solutions.

2. *Grid Deformation Velocity*

An issue specific to the ALE approach is the computation of the mesh velocity s_n for each instant. Although the use of the harmonic approach within the ALE framework has already been presented in the literature [16], no mention is made of the way the mesh velocity is computed. Although s_n^E can still be obtained using analytical equations for the rigid-body movement considered, the mesh-deformation velocity needs special treatment.

Obviously, the accuracy of Eq. (3) depends on the ratio of the time step Δt to the period of the problem. In a typical URANS calculation, at least 40 instants discretize the period, which yields an accurate evaluation of s^D. In an HB calculation, the number of instants in the period (typically 3–11) cannot provide a good estimate of s^D using this standard finite difference scheme, as illustrated later (see Fig. 1). For a transfinite interpolation approach with fixed outer boundaries, there is no analytical derivation of s^D; therefore, an alternative is needed.

An efficient approach to evaluate s^D is to apply the HB spectral operator to the coordinates of the mesh at the $2N + 1$ instants:

$$s_n^D = D_t[M_n] = \sum_{m=-N}^{N} d_m M_{n+m} \tag{8}$$

The accuracy of this evaluation depends on the order N of the method, as does the accuracy of the whole HB approach. The kind of problem that can occur with the finite difference approach can be illustrated considering a simple pitching airfoil. The mesh velocity on the skin of the airfoil is geometrically linked to the instantaneous rotation speed:

$$\alpha(t) = \sin(\omega \cdot t), \quad \text{and} \quad \Omega(t) = \frac{\mathrm{d}\alpha}{\mathrm{d}t} = \omega \cdot \cos(\omega \cdot t)$$

Figure 1 compares the exact solution for the rotation speed with a 40-point finite difference solution, a three-point finite difference solution, and the $N = 1$ HB operator solution. The three-point finite difference solution is not only far from the solution in terms of amplitude, but it has the wrong sign for the second instant of the period. At that instant in the period, the airfoil leading edge would

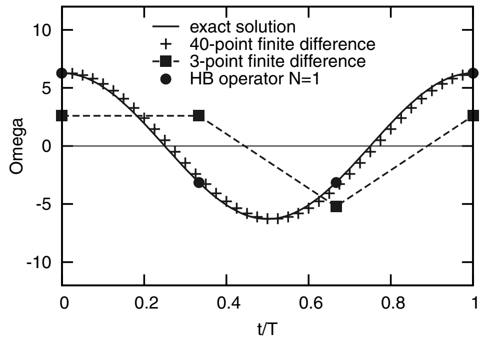

Fig. 1 Comparison of the finite difference and HB operators to compute the derivative of a sinus.

appear to be going up, whereas it is actually going down. In contrast, the HB ($N = 1$) solution is very accurate.

E. Numerical Aspects

All the simulations are performed with the elsA software, a multi-application CFD flow solver that solves the three-dimensional Navier–Stokes equations using a finite volume cell-centered formulation on multiblock structured meshes [11]. Here, the spatial convective fluxes are discretized by the second-order centered scheme with Jameson-type artificial dissipation [17]. Diffusive terms are computed with a second-order scheme. In the present study, two different models are used to compute the turbulent viscosity: the one-equation Spalart–Allmaras model [18], and the shear stress transport (SST) k–ω model of Menter [19] with a Zheng limiter [20].

III. Results and Discussion

A. Test Cases and Setup

1. NACA 64A006 with Oscillating Flap

The test case considered here is a two-dimensional case proposed by AGARD, presented in [21]. It consists of a NACA 64A006 airfoil with a flap mounted at 75% of the chord. Several flow configurations are available in the AGARD data set for this geometry, depending on the incoming flow Mach number M_∞ and angle of attack α_∞, the oscillation frequency f, and the maximum deflection angle δ_0. The two cases retained for the present study are denoted as CT1 and CT6.

Table 1 Description of the NACA 64A006 test cases

	α_∞, deg	M_∞	f, Hz	δ_0, deg
CT1	0.0	0.794	30.0	1.09
CT6	0.0	0.853	30.0	1.10
CT6-DF	4.0	0.853	30.0	1.10

Another case has been considered, for which experimental data are not available. To provide a test case in the transonic regime with separation, the angle of attack of the CT6 case has been increased so that a detached flow is observed on the upper side of the flap. This case will be referred to as CT6-DF (for detached flow). All the test cases are summarized in Table 1.

2. Numerical Setup

The two-dimensional domain extends 30 chords upstream, downstream, below, and above the airfoil. The computational mesh is made of a C-type block around the airfoil and an H-type block for the blunt trailing edge. The C block has 354 nodes on the airfoil and 70 points in the normal direction. Close to the wall, the mesh refinement is such that about 25 points are located in the boundary layer, with a first cell height at $y^+ \sim 1$. Downstream of the airfoil, 9 points are put across the blunt trailing edge, and 41 points discretize the wake in the streamwise direction. The total number of points is therefore about 30,000.

The boundary conditions are a nonreflecting far-field condition on the boundary of the domain and a no-slip adiabatic wall condition on the airfoil. The steady, URANS, and HB simulations are initialized by a uniform flow. Because the Spalart–Allmaras model has proven its efficiency in computing external attached flows, it was retained to run the simulations for the CT1 and CT6 cases. In the detached case, a very slow convergence of the turbulent field was observed, which improved using the SST k–ω model of Menter.

B. Numerical Studies

The choice of the numerical parameters is of paramount importance when the performances of the methods are compared in terms of CPU time. For all the computations, iterative convergence for the LUR and HB calculations was monitored, as well as time accuracy for the URANS solution. The choice was made to monitor convergence on the basis of the unsteady pressure distribution. That is to say, a computation was considered converged when the first harmonic of the pressure distribution did not significantly change any further with the iterative process. It should be emphasized here that integrated forces can be converged faster than pressure distributions. The numerical parameters used for the different test cases are summarized in Table 2.

For the subsonic case (CT1), a smooth convergence was obtained for all the methods, as can be observed in Fig. 2. For the HB case, the fastest convergence was obtained with a linear increase of the Courant–Friedrichs–Lewy (CFL) number from 50 to 100 during the first 100 iterations.

For the transonic case (CT6), the number of time steps was slightly increased for the URANS case. For the LUR case, a low number of iterations still provided a good solution. For the HB case, the strategy of a linear increase of the CFL number was maintained, but the lower value of the CFL was reduced and the number of iterations was increased. The iterative convergence curves of the residuals for the LUR and HB methods are shown in Fig. 2.

Table 2 Numerical parameters for all the test cases

	CT1	CT6	CT6-DF		
URANS					
Time step	$T/48$	$T/64$	$T/64$		
Number of simulated periods	3	3	3		
Max. number of dual iterations	25	50	80		
CFL number	50	50	50		
HB			$N = 1$–3	$N = 4$	$N = 5$
Number of iterations	250	300	800	1200	3000
Min. CFL number	50	5	1	1	1
Max. CFL number	100	100	50	10	5
Linear evolution range	50	50	100	200	500
LUR					
Number of iterations	200	200	——		
CFL number	50	50	——		

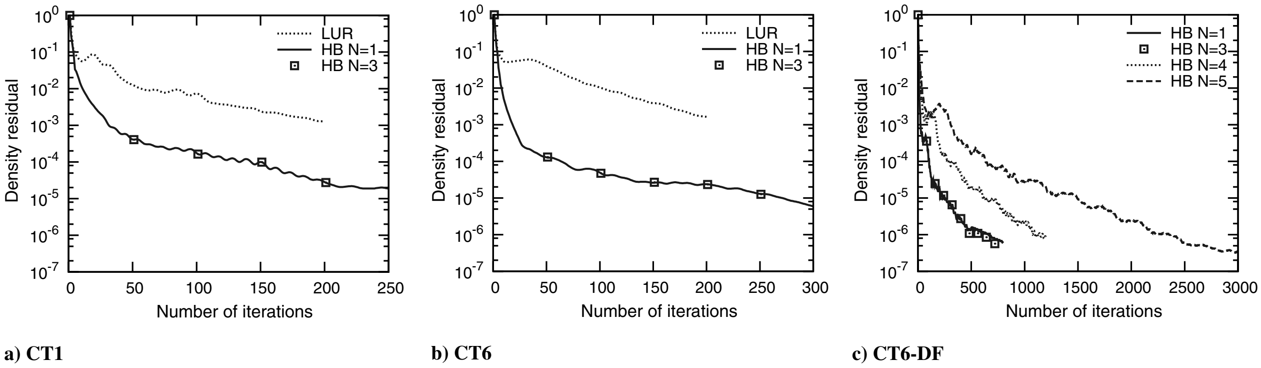

a) CT1 b) CT6 c) CT6-DF

Fig. 2 Convergence of the computations: mean residual of the density, normalized by the value at the first iteration.

In the transonic regime with detached flow (CT6-DF), convergence was somehow harder to obtain. For the URANS, the number of dual iterations had to be increased. In this case, it was not possible to obtain a converged solution with the LUR method. The matrix of the linear system Eq. (5), depending on the Jacobian matrices of the steady fluxes ($\partial f_i/\partial W$), has eigenvalues for which the real part is negative. Because this matrix remains constant during the resolution process, every time-marching algorithm will diverge exponentially in time. However, a solution could be computed using a generalized minimal residual method (GMRES) type of algorithm, or a direct resolution of the linear system, but at a possibly higher cost. Such methods are not yet implemented in the elsA code. For the HB method, the maximum CFL number was reduced to 10 for $N = 4$ harmonics and to 5 for $N = 5$ harmonics. It was therefore necessary to increase the number of iterations above three harmonics. Convergence difficulties when increasing the number of harmonics have already been reported in the literature [15], sometimes leading to divergence [5].

C. Physical Analysis

In this section, the physical accuracy of the results is analyzed. The comparison is focused on the pressure coefficient C_p distribution along the airfoil obtained by the three methods. To analyze the unsteady evolution of the pressure coefficient, the first harmonic C_{p1} is computed. For the HB and URANS results, the mean value C_{p0} is obtained from an arithmetic time average. For the LUR results, the steady solution is used for the comparisons.

It should be stressed here that the purpose of the paper is to assess the capability of the LUR and HB methods to reproduce the URANS results. Of course, comparisons with the experimental results are of interest, but are not the main focus of the study.

1. CT1 Case

In this case, the flow remains subsonic all around the airfoil, as shown by the mean value of the C_p in Fig. 3. The LUR and HB results are perfectly superimposed on the URANS results. The computational results are in good agreement with the experimental data.

The first harmonic of the C_p is shown in Fig. 4. For the real and imaginary parts of the LUR and one-harmonic HB solutions, some slight differences can be observed. Altogether, these differences are negligible. For $N = 2$, the HB solution is superimposed to the URANS results. Overall, the computational results are only in fair agreement with the experimental data. In [21], the authors mention a lack of rigidity of the flap, which could explain some of the discrepancies.

2. CT6 Case

In this case, the flow is transonic, with a shock alternatively forming on both sides of the airfoil, at about midchord. In Fig. 5, the steady solution associated with the LUR method is significantly different from the time-averaged solution, as expected for such a case with large shock motion (as shown later in this section; see Fig. 7). For the HB results, there is a noticeable influence of the number of harmonics: for $N = 1$, there are some discrepancies with the URANS near the shocks; for $N = 2$ these differences are negligible.

Considering the first harmonic of the C_p presented in Fig. 6, the solutions differ around the shocks, but are identical in the rest of the flow. For the LUR, the amplitude of the peaks is overestimated, whereas the width is underpredicted. This point is discussed further later on. The behavior of the linearized method could be explained by the structure of the unsteady flow, as shown in Fig. 7: the URANS simulation shows that the shock moves along the chord, whereas the LUR method is only able to model a shock staying at its steady location. Another point is that the shock disappears and reappears within the period. This phenomenon is an unsteady nonlinearity, which cannot be properly modeled by the LUR method. For the HB solution, $N = 2$ yields fair accuracy, and the solution is superimposed to the URANS reference for $N \geq 3$.

Despite minor discrepancies, Fig. 6 gives an empirical indication that the HB solution is better than the LUR solution in the vicinity of

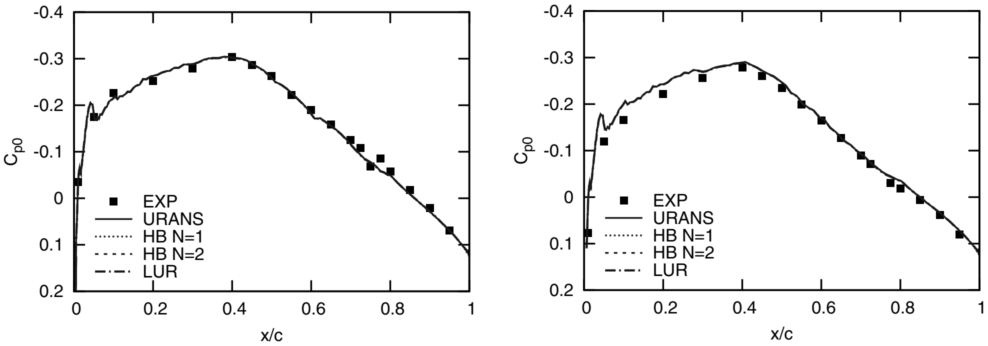

a) Upper side b) Lower side

Fig. 3 CT1 case: mean (URANS and HB) and steady (LUR) distributions of the pressure coefficient.

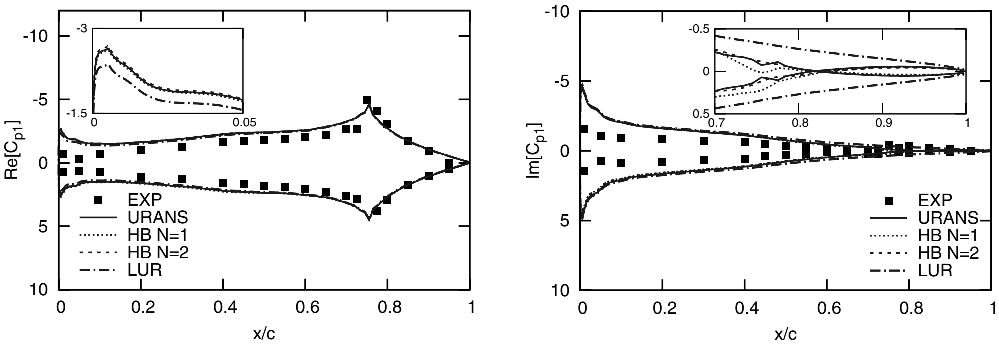

a) Real part

b) Imaginary part

Fig. 4 CT1 case: first harmonic of the pressure coefficient, with a close-up view of the areas of interest.

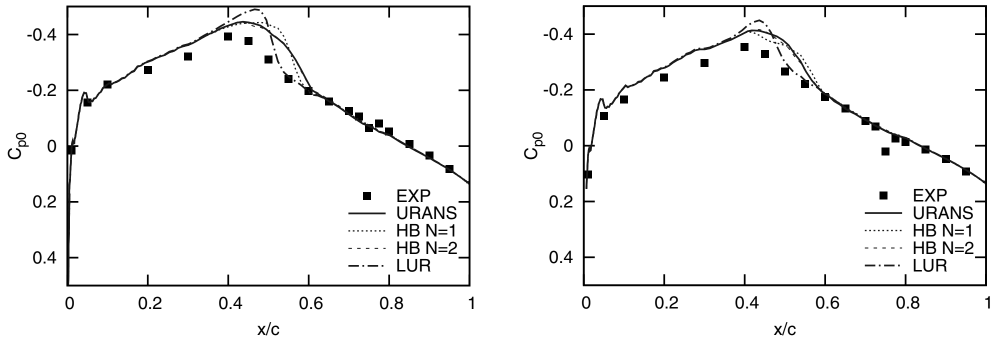

a) Upper side

b) Lower side

Fig. 5 CT6 case: mean (URANS and HB) and steady (LUR) distributions of the pressure coefficient.

shocks. Our theoretical explanations for this behavior are the following:

1) The main difference between the linearized and the one-harmonic methods is the step at which the harmonic truncation is done. In the LUR case, the equations are linearized before the numerical resolution. In the HB case, Eq. (6) retains all the nonlinearities of the spatial operators of the Navier–Stokes equations, and the truncation is done at the level of the resolution, via the number of harmonics retained. Indeed, in the HB technique, the residual R is computed by the same routines as in the nonlinear URANS approach.

2) A second difference is that the one-harmonic HB solution (and, of course, HB solutions of higher order) takes into account the true flap position at several different instants in the period, via the mesh deformation, thus allowing one to model, to some extent, shock motions.

To further contrast the quality of the LUR and HB predictions, the unsteady aerodynamic forces are analyzed. One way to do this is to compute the generalized aerodynamic force (GAF). Harmonic analysis is performed on the unsteady GAF signal (nondimensionalized by the upstream dynamic pressure and the chord), and the modulus and phase of the first harmonic are presented in Table 3. As noticed before, the LUR overestimates the amplitude of the peaks and underpredicts their width: these errors cancel each other out after integration, and the unsteady force is predicted quite well, with about a 5% error. The HB results are within 1% of the URANS ones, whatever the number of harmonics.

Regarding the comparison of the numerical and experimental results, the first harmonic of C_p is fairly well predicted except around the shock, where the peak is predicted downstream of the experimental location, with a significant overestimation of its magnitude.

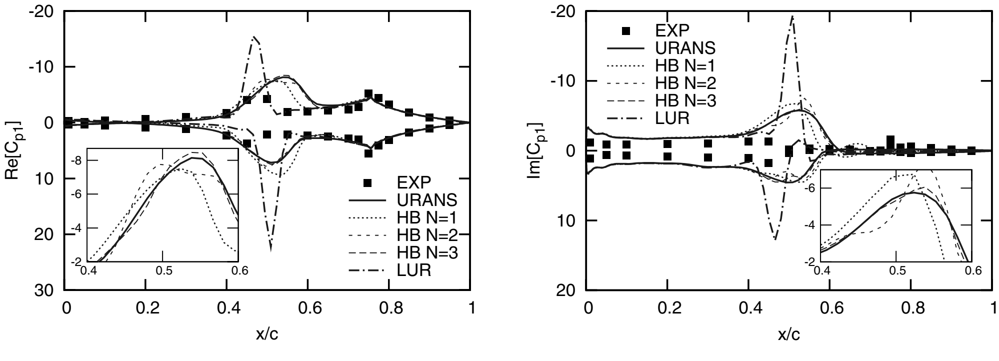

a) Real part

Imaginary part

Fig. 6 CT6 case: first harmonic of the pressure coefficient, with a close-up view of the areas of interest.

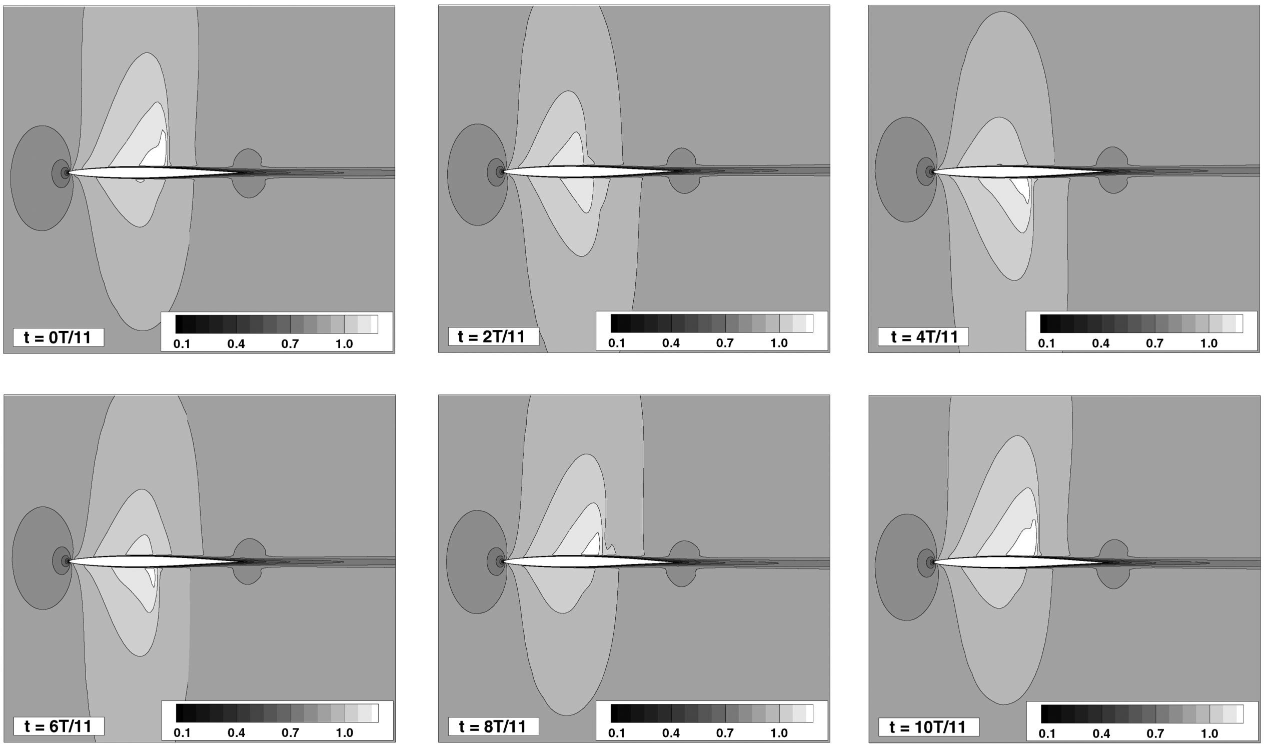

Fig. 7 CT6 case: snapshots of the flow computed by the URANS method.

Besides the remarks made in the preceding section, it can be added that the amplitude of the peaks is hard to measure accurately, because it requires a clustering of pressure taps in the areas where they occur. However, it is likely that some flow features could not be resolved by either the numerical strategies adopted or the mesh resolution used.

3. *CT6-DF Case*

This case is derived from the CT6 case: the flow is transonic and the angle of attack is increased to 4 deg, so that the flow is detached on the upper side of the flap. As mentioned earlier, in this case the LUR computation did not converge.

Figure 8 presents the flow computed by the URANS and the HB ($N = 1$) methods. The two visualizations are snapshots at $t = T/3$ (flap up, going down), with contours of the Mach number and some streamlines. This figure illustrates the size of the separation zone. It also shows the good agreement between the two methods with regard to the qualitative prediction of the flowfield.

The distribution of the mean value of the C_p is presented in Fig. 9 for the HB and URANS solutions. On both sides of the airfoil, all the HB solutions are superimposed to the URANS ones.

In Fig. 10, the real and imaginary part of the C_p are plotted for the URANS and HB methods. An interesting point is that the HB solution does not change when the number of harmonics is increased over $N = 2$. To account for this, the frequency content of the wall pressure at $x/c = 0.5$ is examined (the point is located in the region where the shock moves). For the URANS, Fourier analysis is performed on the unsteady signal over five periods (after the initial convergence stage). The results for the CT6 and CT6-DF cases are given in Fig. 11. Close agreement between the URANS and the HB results is found. It appears that the frequency content of the CT6-DF case is indeed much poorer than that of the CT6 case, hence the faster convergence of the HB in this case with regard to the number of harmonics. Our physical explanation is that the detached-flow area limits the amplitude of the unsteady motion of the shock.

D. Performance Analysis

As a preliminary, we note here that the initial motivation for the development of harmonic and linearized approaches is a reduction in the CPU time. However, little information on this issue is available. Hall et al. [5] compare their approach to steady computations, which is not suited to our case, because the goal is to substitute the HB computation with the URANS ones. Gopinath et al. mention a significant CPU reduction for turbomachinery applications (two orders of magnitude, but partly due to a domain reduction thanks to specific boundary conditions) [8], but they do not provide the equivalent information for external aerodynamics flows [7]. With a slightly different approach for the implicit treatment of the source term, Woodgate and Badcock [10] show a significant gain (about a factor of 10) as compared to URANS for external flows.

The restitution time is used to assess the performances of the methods. The gain is defined as the ratio between the URANS restitution time and the LUR/HB restitution time. For the LUR, the inclusion of the calculation time of the steady solution in the total time is a point of concern. In the present case, because a single

Table 3 CT6 case: Comparison of the nondimensionalized generalized aerodynamic forces; analysis of the first harmonic

		URANS	LUR		HB				
				$N=$	1	2	3	4	5
GAF	Modulus ($\times 10^7$)	1.26	1,20		1.25	1.27	1.27	1.27	1.26
	Phase, rad	2.97	3.11		2.99	2.98	2.98	2.97	2.98
Rel. error	Modulus, %	——	5.3		0.4	−0.5	−0.6	−0.7	−0.8
	Phase, %	——	4.6		0.6	0.5	0.5	0.1	0.4

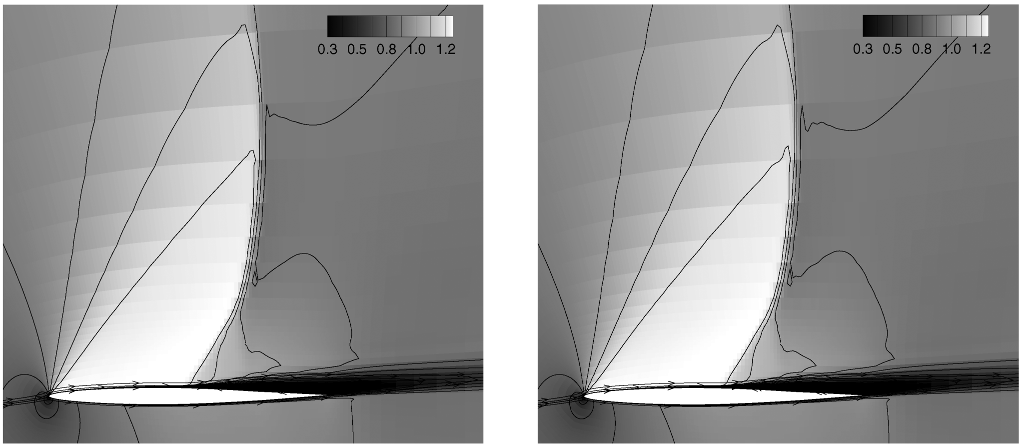

a) URANS **b) HB N=1**

Fig. 8 CT6-DF case: color contours of the Mach number with streamlines.

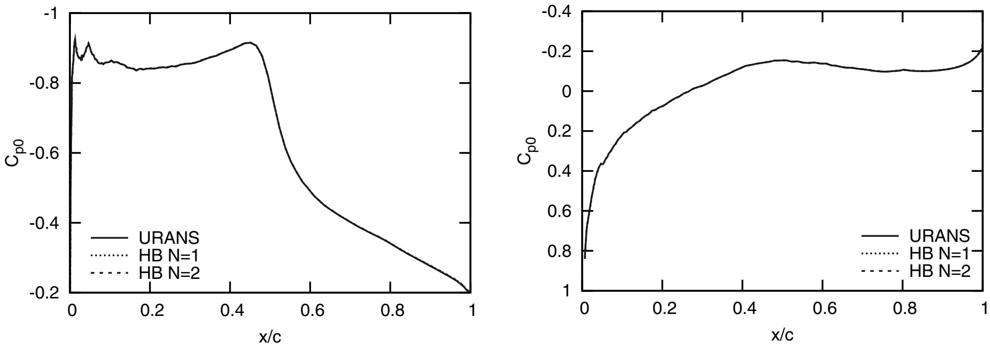

a) Upper side **b) Lower side**

Fig. 9 CT6-DF case: mean value of the pressure coefficient.

operating point is examined and because the URANS and HB computations are initialized by a uniform field, the choice was made to include the calculation time of the steady solution in the total time. Figure 12 presents the gains obtained for all the test cases, plotted as a function of the number of harmonics used for the HB computations. To allow consistent comparisons of the methods, the gain of the LUR solution is plotted as a line on the same graph, although it does not depend on N.

For the subsonic test case CT1, the LUR is over seven times faster than the URANS, whereas the HB computations are up to four times faster than the URANS.

For the transonic test case CT6, the LUR is about eight times faster than the URANS. The fact that the LUR calculation time is not much reduced as compared to the CT1 case, in spite of an increased time for the URANS, is due to a longer steady computation. The $N = 1$ HB is about six times faster than the URANS.

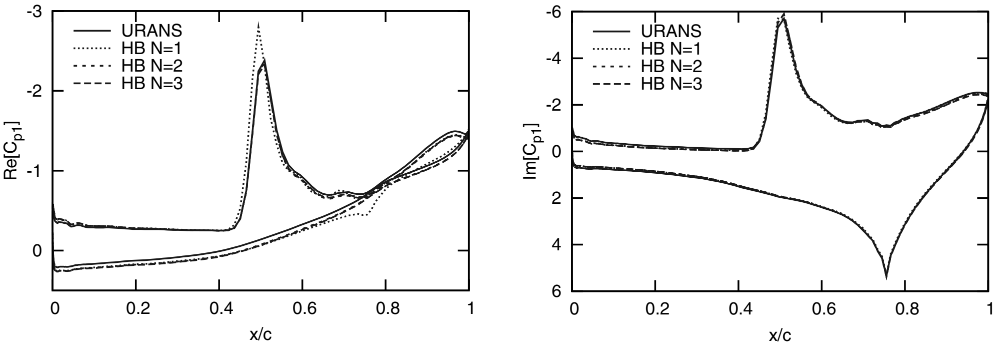

a) Real part **b) Imaginary part**

Fig. 10 CT6-DF case: first harmonic of the pressure coefficient.

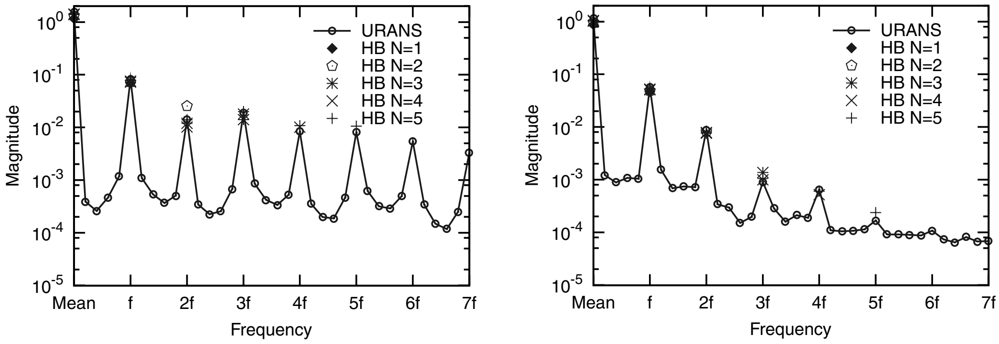

a) CT6 **b) CT6-DF**

Fig. 11 Fourier analysis of the wall unsteady pressure at $x/c = 0.5$. The URANS signal is analyzed over five periods.

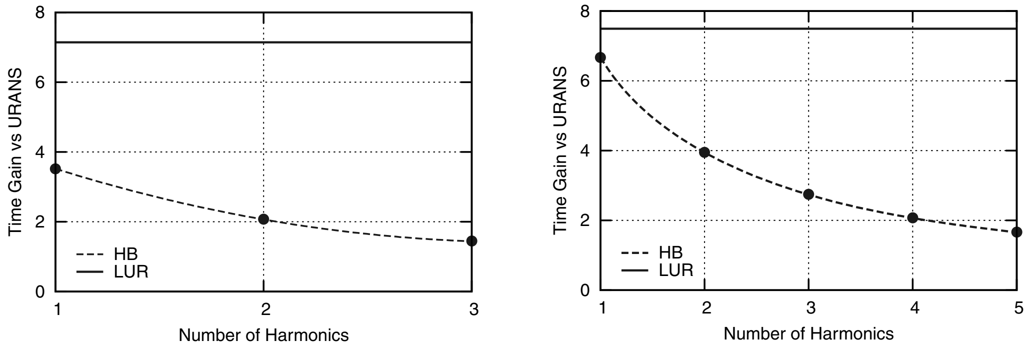

a) CT1 subsonic case **b) CT6 transonic**

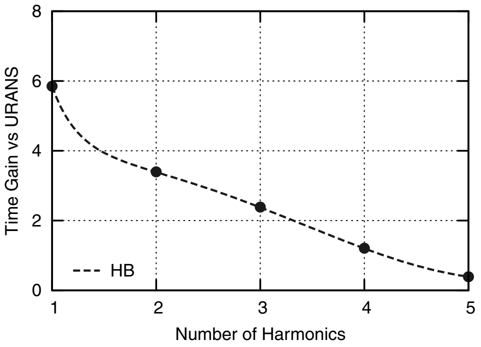

c) CT6-DF transonic detached flow

Fig. 12 CPU time gain for the LUR and HB methods versus URANS for all the test cases.

For the transonic test case with detached flow CT6-DF, the conclusion is that the HB is the only alternative to the URANS. For $N \geq 2$, the HB solution is no longer dependent on the number of harmonics and is about three times faster than the URANS.

It should be emphasized here that the objectivity of the gain evaluation highly depends on the numerical parameters chosen for all the methods. For the subsonic case CT1, the gain is moderate because the URANS converges with a low time resolution and few dual iterations. For the transonic case CT6, the HB method is quite efficient because the robustness of the implicit approach [9] allows for large CFL numbers. For a number of harmonics below three, the HB method remains robust in the transonic test case with detached flow CT6-DF. Generally speaking, it is expected that the gain with the HB approach increases with the length of the URANS transitory phase.

Regarding the memory requirements of the methods, the LUR requires only about 1.6 times the memory of the URANS. For the HB technique, the memory cost for the one-harmonic computation is significant, about a factor of 3 compared to that of the URANS, and it scales linearly as the number of instants (i.e., a $N = 3$ computation requires seven times the URANS memory).

IV. Conclusions

One of the reference approaches to predict unsteady aerodynamic loads is to perform URANS forced-motion simulations. The present study examines two alternatives to that technique, namely, the linearized method and the harmonic balance method. The assessment of these two methods against URANS predictions is carried out for a NACA 64A006 airfoil with a flap mounted at 75% of the chord for three flow regimes. Of particular interest is the fact that the same test case is evaluated over a range of significantly different flow conditions with varying levels of nonlinearities. Particular emphasis is put on the objective evaluation of the performances of the LUR and HB methods in terms of CPU time gain as compared to the URANS. All the simulations are performed within the ALE framework. For the HB technique, a specific approach for the computation of the mesh velocity is proposed, based on the same spectral operator as for the HB source term.

For the subsonic case CT1, it appears that the LUR method is the most appropriate one, because it is as accurate as the URANS method, with a computational time reduced by a factor of 7 as compared to the URANS and by almost a factor of 2 as compared to the HB ($N = 1$). For the transonic case CT6, the choice depends on the level of accuracy required by the intended application: the LUR solution is obtained about eight times faster, but with poor accuracy around shocks, whereas the HB ($N = 1$) solution is slower but more accurate. However, the discrepancies for the local pressure distribution cancel each other out after integration, yielding a fair prediction of the unsteady force. For $N = 2$, the HB is as accurate as the URANS, with a speedup of four. For the transonic case with separation over the flap CT6-DF, the LUR does not converge, and the HB ($N = 2$) is quite accurate, with a speedup of about three. For the LUR method, a possible improvement to get a solution for the detached case would be the use of a GMRES-like algorithm, or a direct resolution of the linear system, which are not implemented in the solver used for the present study. These are topics currently under investigation.

One important result is that the one-harmonic HB solution is able to capture unsteady nonlinearities that the LUR solution fails to predict. We contend that the theoretical basis for this behavior is the following:

1) The nonlinearities of the spatial operators of the Navier–Stokes equations are preserved in the HB formulation, whereas the LUR solves a linearized set of equations.

2) The one-harmonic HB takes into account three different meshes in the period, whereas the LUR computes the solution on the initial mesh only.

3) The "pseudo base state" on which the one-harmonic perturbation is superimposed is the time-averaged state for the HB, whereas it is the steady-state solution for the LUR, which may differ when significant unsteady effects occur.

As far as practical aspects are involved, it should be emphasized that the LUR and HB methods have a lower setup cost than the URANS, because it is easier to monitor iterative convergence than time accuracy.

References

[1] Hall, K. C., "A Linearized Euler Analysis of Unsteady Flows in Turbomachinery," Massachusetts Inst. of Technology Gas Turbine Lab. Rept. 190, 1987.

[2] Clark, W. S., and Hall, K. C., "A Time-Linearized Navier–Stokes Analysis of Stall Flutter," *Journal of Turbomachinery*, Vol. 122, No. 3, July 2000, pp. 467–476.
doi:10.1115/1.1303073

[3] Mortchéléwicz, G. D., "Aircraft Aeroelasticity Computed with Linearized RANS Equations," Technion—Israel Institute of Technology Paper 34, Feb. 2003.

[4] Liauzun, C., Canonne, E., and Mortchéléwicz, G. D., "Flutter Numerical Computations Using the Linearized Navier–Stokes Equations," *Advanced Methods in Aeroelasticity*, NATO Research and Technology Organisation, Rept. RTO/AVT-154, May 2008.

[5] Hall, K. C., Thomas, J. P., and Clark, W. S., "Computation of Unsteady Nonlinear Flows in Cascades Using a Harmonic Balance Technique," *AIAA Journal*, Vol. 40, No. 5, May 2002, pp. 879–886.
doi:10.2514/2.1754

[6] He, L., and Ning, W., "Efficient Approach for Analysis of Unsteady Viscous Flows in Turbomachines," *AIAA Journal*, Vol. 36, No. 11, Nov. 1998, pp. 2005–2012.
doi:10.2514/2.328

[7] Gopinath, A., and Jameson, A., "Time Spectral Method for Periodic Unsteady Computations over Two- and Three-Dimensional Bodies," AIAA Paper 2005-1220, Jan. 2005.

[8] Gopinath, A., Van der Weide, E., Alonso, J., Jameson, A., Ekici, K., and Hall, K., "Three-Dimensional Unsteady Multi-Stage Turbomachinery Simulations Using the Harmonic Balance Technique," AIAA Paper 2007-0892, Jan. 2007.

[9] Sicot, F., Puigt, G., and Montagnac, M., "Block–Jacobi Implicit Algorithms for the Time Spectral Method," *AIAA Journal*, Vol. 46, No. 12, Dec. 2008, pp. 3080–3089.
doi:10.2514/1.36792

[10] Woodgate, M., and Badcock, K. J., "Implicit Harmonic Balance Solver for Transonic Flow with Forced Motions," *AIAA Journal*, Vol. 47, No. 4, April 2009, pp. 893–901.
doi:10.2514/1.36311

[11] Cambier, L., and Veuillot, J., "Status of the elsA Software for Flow Simulation and Multi-Disciplinary Applications," AIAA Paper 2008-0664, Jan. 2008.

[12] Jameson, A., "Time Dependent Calculations Using Multigrid, with Applications to Unsteady Flows Past Airfoils and Wings," AIAA Paper 1991-1596, 1991.

[13] Yoon, S., and Jameson, A., "An LU-SSOR Scheme for the Euler and Navier–Stokes Equations," AIAA Paper 87-0600, Jan. 1987.

[14] Delbove, J., "Unsteady Simulations for Flutter Prediction," *Computational Fluid Dynamics 2004*, Springer, Berlin/Heidelberg, 2006, pp. 205–210.
doi:10.1007/3-540-31801-1_26

[15] Van der Weide, E., Gopinath, A., and Jameson, A., "Turbomachinery Applications with the Time Spectral Method," AIAA Paper 2005-4905, June 2005.

[16] Thomas, J. P., Dowell, E. H., and Hall, K. C., "Nonlinear Inviscid Aerodynamic Effects on Transonic Divergence, Flutter, and Limit-Cycle Oscillations," *AIAA Journal*, Vol. 40, No. 4, April 2002, pp. 638–646.
doi:10.2514/2.1720

[17] Jameson, A., Schmidt, W., and Turkel, E., "Numerical Solutions of the Euler Equations by Finite Volume Methods Using Runge–Kutta Time-Stepping Schemes," AIAA Paper 81-1259, June 1981.

[18] Spalart, P. R., and Allmaras, S. R., "A One-Equation Turbulence Transport Model for Aerodynamic Flows," AIAA Paper 92-0439, Jan. 1992.

[19] Menter, F. R., "Zonal Two Equation (k–ω) Turbulence Models for Aerodynamic Flows," AIAA Paper 93-2906, July 1993.

[20] Zheng, X., Liao, C., Liu, C., Sung, C. H., and Huang, T. T., "Multigrid Computation of Incompressible Flows Using Two-Equation Turbulence Models: Part I—Numerical Method," *Journal of Fluids Engineering*, Vol. 119, 1997, p. 893–899.
doi:10.1115/1.2819513

[21] "Compendium of Unsteady Aerodynamic Measurements," AGARD R-702, 1982.

N. Wereley
Associate Editor

Journal of Computational Physics 236 (2013) 317–345

Contents lists available at SciVerse ScienceDirect

Journal of Computational Physics

journal homepage: www.elsevier.com/locate/jcp

Non-uniform time sampling for multiple-frequency harmonic balance computations

Thomas Guédeney [a,b], Adrien Gomar [b,*], François Gallard [b], Frédéric Sicot [b], Guillaume Dufour [b,c], Guillaume Puigt [b]

[a] Safran Snecma Villaroche, Rond-point René-Ravaud, 77550 Moissy-Cramayel, France
[b] Centre Européen de Recherche et de Formation Avancée au Calcul Scientifique (CERFACS), CFD Team, 42 Avenue Gaspard Coriolis, 31057 Toulouse Cedex 1, France
[c] Université de Toulouse, Institut Supérieur de l'Aéronautique et de l'Espace (ISAE), 10 Avenue Edouard Belin, 31400 Toulouse, France

ARTICLE INFO

Article history:
Received 14 June 2012
Received in revised form 12 November 2012
Accepted 14 November 2012
Available online 29 November 2012

Keywords:
Harmonic balance
Almost-periodic flow
Time sampling
Condition number
Turbomachinery

ABSTRACT

A time-domain harmonic balance method for the analysis of almost-periodic (multi-harmonics) flows is presented. This method relies on Fourier analysis to derive an efficient alternative to classical time marching schemes for such flows. It has recently received significant attention, especially in the turbomachinery field where the flow spectrum is essentially a combination of the blade passing frequencies. Up to now, harmonic balance methods have used a uniform time sampling of the period of interest, but in the case of several frequencies, non-necessarily multiple of each other, harmonic balance methods can face stability issues due to a bad condition number of the Fourier operator. Two algorithms are derived to find a non-uniform time sampling in order to minimize this condition number. Their behavior is studied on a wide range of frequencies, and a model problem of a 1D flow with pulsating outlet pressure, which enables to prove their efficiency. Finally, the flow in a multi-stage axial compressor is analyzed with different frequency sets. It demonstrates the stability and robustness of the present non-uniform harmonic balance method regardless of the frequency set.

1. Introduction

The standard industrial design of multistage turbomachines is usually based on steady analysis, for which the most advanced tools are three-dimensional Reynolds-Averaged Navier–Stokes (RANS) steady computations. With the ever growing need to improve performances, aggressive design choices foster unsteady phenomena, such as: blade interactions in compact turbo-engines, separated flows at/or close to stable operability limits, or aeroelastic phenomenon, to name but a few. In such a context, engineers now need tools to account for these effects as early as possible in the design cycle. With the growth of computational power, unsteady computations are entering industrial practice, but the associated restitution time remains an obstacle for daily basis applications. For this reason, efficient and/or accurate unsteady approaches are receiving a lot of attention. Different ways can be pursued to achieve an appropriate trade-off between efficiency and accuracy.

A first approach is to deal with the model equations: the Unsteady Reynolds-Averaged Navier–Stokes (U-RANS) equations can be simplified using some level of linearization (see Refs. [1–3]) to obtain a fast solution but with some limitations in

---

* Corresponding author.

E-mail addresses: thomas.guedeney@cerfacs.fr (T. Guédeney), adrien.gomar@cerfacs.fr (A. Gomar), francois.gallard@cerfacs.fr (F. Gallard), frederic.sicot@cerfacs.fr (F. Sicot), guillaume.dufour@isae.fr (G. Dufour), guillaume.puigt@cerfacs.fr (G. Puigt).

0021-9991/$ - see front matter
http://dx.doi.org/10.1016/j.jcp.2012.11.010

nonlinear regimes (see Ref. [4] for an example of accuracy issues, and Ref. [3] for some cure of stability problems). Conversely, the Large-Eddy Simulation (LES) approach can be used to increase accuracy [5,6], but at a prohibitive cost.

A second approach, usually based on the U-RANS equations but not necessarily, is to work on the time-integration algorithm to reduce the computational cost as compared to standard time-marching techniques. To achieve this, Fourier-based methods for periodic flows have undergone major developments in the last decade (see He [7] for a recent review, or the special issue of the Int. J. CFD [8]). The basic idea is to decompose time-dependent flow variables into Fourier series, which are then injected into the equations of the problem. The time-domain problem is thus made equivalent to a frequency-domain problem, where the complex Fourier coefficients are the new unknowns. At this point, two strategies coexist to obtain the solution. The first one is to solve directly the Fourier coefficients, using a dedicated frequency-domain solver, as proposed by He and Ning [9,10]. The second strategy is to cast the problem back to the time domain using the inverse Fourier transform, as proposed by Hall [11,12] with the Harmonic Balance (HB) method. The unsteady time-marching problem is thus transformed into a set of steady equations coupled by a source term that is a high-order spectral evaluation of the time-derivative of the initial equations. The main advantage of solving in the time domain is that it can be implemented in an existing classical RANS solver, taking advantage of all classical convergence-accelerating techniques for steady state problems. The HB approach has demonstrated significant reduction of computational time, typically of a factor 2–10.

In turbomachines, the relative motion of fixed and rotating blades gives rise to deterministic unsteady interactions at frequencies termed BPFs (Blade Passing Frequencies). In a multi-stage turbomachine, a row sandwiched between two other rows is submitted to (at least) two BPFs (see Tyler and Sofrin [13] for instance), hence the need for multiple frequency methods. Initially developed for single frequency problems, harmonic methods have been extended to account for multiple frequencies [14–16]. All the variations of the HB technique proposed in the literature rely on a uniform time sampling of the longest period of interest (though the number of samples can differ). Ekici and Hall [15] mention the use of non-uniform sampling but do not develop it. However, when the fundamental frequencies involved are significantly different, uniform sampling leads to an unnecessary high number of time samples: given that the shortest period has to be discretized by at least three instants (Shannon [17] requires at least two instants per period to capture a frequency, but an odd number of samples is required for stability issues [18]), uniform sampling of the longest period requires a total number of samples that grows with the largest to the shortest period ratio. This can compromise the efficiency of the method, as too many time samples are computed. Besides, as demonstrated in the present contribution, uniform time sampling can also raise stability issues. To overcome these computational limitations, a new approach using non-uniform time sampling is proposed in the present contribution.

This paper is organized as follows: First, in Section 2, mono- and multi-frequency HB methods are presented, and the impact of time sampling on numerical stability is discussed. Then, two algorithms for an automatic choice of the time samples are presented and compared in Section 3. The proposed non-uniform sampling is assessed for a model problem in Section 4. Finally, Section 5 is dedicated to the application to a turbomachinery configuration, with emphasis on the choice of frequencies.

2. Time-domain harmonic balance technique

The Unsteady Reynolds-Averaged Navier–Stokes (U-RANS) equations in integral form are given by

$$\int_{\Omega} \frac{\partial W}{\partial t} dV + \oint_{\partial\Omega} \vec{F} \cdot \vec{N} ds = 0, \tag{1}$$

where $\vec{F}$ is the flux across $\partial\Omega$ and W is the vector of the conservative unknowns (conservative variables and turbulent variables). Assuming Ω is a control volume, the semi-discrete finite-volume form of the U-RANS equations is obtained from Eq. (1):

$$\frac{d}{dt}(V\overline{W}) + R(\overline{W}) = 0, \tag{2}$$

with V the volume of the cell Ω, R the residual resulting from the discretization of the fluxes and the source terms (including the turbulent equations), and $\overline{W}$ the mean of the unknowns over the control volume. In the following, the over line symbol $\bar{\cdot}$ is dropped out for clarity. Moreover, the mesh is considered not deformable, which allows to remove the volume V of the time derivative in Eq. (2), and simplifies explanations. However, the treatment remains valid if the mesh is deformable (see Ref. [4] for instance).

2.1. Periodic flows

If the mean flow variables W are periodic in time of period $T = 2\pi/\omega$, so are the residuals $R(W)$ and the Fourier series of Eq. (2) is

$$\sum_{k=-\infty}^{\infty} \left(ik\omega V\widehat{W}_k + \widehat{R}_k \right) e^{ik\omega t} = 0, \tag{3}$$

where $\widehat{W}_k$ and $\widehat{R}_k$ are the Fourier coefficients of W and R corresponding to the mode k:

$$W(t)=\sum_{k=-\infty}^{\infty}\widehat{W}_k e^{ik\omega t},\quad R(t)=\sum_{k=-\infty}^{\infty}\widehat{R}_k e^{ik\omega t}. \tag{4}$$

The complex exponential family forming an orthogonal basis, the only way for Eq. (3) to be true is that the weight of every mode k is zero, which leads to an infinite number of steady equations in the frequency domain:

$$ik\omega V\widehat{W}_k+\widehat{R}_k=0,\quad \forall k\in\mathbb{Z}. \tag{5}$$

McMullen et al. [19–21] solve a subset of these equations up to mode N, $-N\leqslant k\leqslant N$, yielding the Non-Linear Frequency Domain (NLFD) method.

The principle of the time-domain harmonic balance approach, sometimes referred to as Time Spectral Method (TSM) [12,22], is to use an Inverse Discrete Fourier Transform (IDFT) to cast the equations back into the time domain. The IDFT then induces linear relations between Fourier coefficients $\widehat{W}_k$ and a uniform sampling of W at $2N+1$ instants in the period:

$$W_n=\sum_{k=-N}^{N}\widehat{W}_k\exp(i\omega n\Delta t),\quad 0\leqslant n<2N+1, \tag{6}$$

with $W_n\equiv W(n\Delta t)$ and $\Delta t=T/(2N+1)$. This leads to a new system of $2N+1$ mathematically steady equations coupled by a source term:

$$R(W_n)+VD_t(W_n)=0,\quad 0\leqslant n<2N+1. \tag{7}$$

The source term $VD_t(W_n)$ appears as a high-order formulation of the initial time derivative in Eq. (2). This new time operator connects all the time levels and can be expressed analytically as

$$D_t(W_n)=\sum_{m=-N}^{N}d_mW_{n+m}, \tag{8}$$

with

$$d_m=\begin{cases}\frac{\pi}{T}(-1)^{m+1}\csc\left(\frac{\pi m}{2N+1}\right), & m\neq 0,\\ 0, & m=0.\end{cases} \tag{9}$$

This equation clearly states that the source term is real for periodic flows. A similar derivation can be made for an even number of instants, but it is proved in Ref. [18] that it can lead to a numerically unstable odd–even decoupling.

A pseudo-time (τ_n) derivative is added to Eq. (7) to march the equations in pseudo-time to the steady-state solutions of all the instants:

$$V\frac{\partial W_n}{\partial\tau_n}+R(W_n)+VD_t(W_n)=0,\quad 0\leqslant n<2N+1. \tag{10}$$

This time step is defined locally in a given cell and can be different for all the HB instants. For stability reasons, its computation is modified [18] to take into account the additional source term,

$$\Delta\tau_n=\text{CFL}\frac{V}{\|\xi_n\|+\omega NV}. \tag{11}$$

The extra term ωNV is added to the spectral radius $\|\xi_n\|$ to restrict the time step. Eq. (11) implies that a high frequency and/or a high number of harmonics N can considerably restrict the time step, especially for explicit Runge–Kutta time integration scheme, as mentioned in [11]. Several implicit schemes, which are theoretically unconditionally stable and thus allow larger CFL number, have been derived for the HB method: Krylov-space based methods are used in [23,24], and Antheaume et al. [25] propose a point Jacobi algorithm. The present paper uses the block-Jacobi algorithm derived in Ref. [22] to improve robustness and efficiency.

This time-domain harmonic balance method has been implemented in the *elsA* solver [26] developed by ONERA and CERFACS. This code solves the RANS equations using a cell-centered approach on multi-blocks structured meshes. Using the HB method, significant savings in CPU cost have been observed in various applications such as dynamic derivatives computation [27], aeroelasticity [4] and rotor/stator interactions [28]. However, this approach is limited to periodic flows (*i.e.* a single fundamental frequency) and is unfit when the main frequencies of the system are not integers multiple of each other (such as multi-stage turbomachines for instance). The single-frequency HB method is therefore extended to the case where the flow is not periodic in time but is almost periodic.

2.2. Almost-periodic flows

2.2.1. Mapping on a set of arbitrary frequencies

If the flow variables are composed of non-harmonically related frequencies (*i.e.* the flow spectrum has high-energy discrete-frequency modes), the flow regime can be termed as almost-periodic [29]. Instead of a regular Fourier series, the U-RANS equations are projected on a set of complex exponentials with arbitrary angular frequencies ω_k. The conservative variables and the residuals are then approximated by

$$W(t) \approx \sum_{k=-N}^{N} \widehat{W}_k e^{i\omega_k t}, \quad R(t) \approx \sum_{k=-N}^{N} \widehat{R}_k e^{i\omega_k t}, \tag{12}$$

where $\widehat{W}_k$ and $\widehat{R}_k$ are the coefficients of the almost-periodic Fourier series for the frequency $f_k = \omega_k/2\pi$. Injecting this decomposition in Eq. (2) yields

$$\sum_{k=-N}^{N} \left(i\omega_k V \widehat{W}_k + \widehat{R}_k \right) e^{i\omega_k t} = 0. \tag{13}$$

Sampling in time onto a set of $2N+1$ time levels to solve Eq. (13), the following matrix formulation is obtained:

$$A^{-1} \cdot \left(iVP\widehat{W}^\star + \widehat{R}^\star \right) = 0, \tag{14}$$

where the almost-periodic inverse discrete Fourier transform (IDFT) matrix reads:

$$A^{-1} = \begin{bmatrix} exp(i\omega_{-N}t_0) & \cdots & exp(i\omega_0 t_0) & \cdots & exp(i\omega_N t_0) \\ \vdots & & \vdots & & \vdots \\ exp(i\omega_{-N}t_k) & \cdots & exp(i\omega_0 t_k) & \cdots & exp(i\omega_N t_k) \\ \vdots & & \vdots & & \vdots \\ exp(i\omega_{-N}t_{2N}) & \cdots & exp(i\omega_0 t_{2N}) & \cdots & exp(i\omega_N t_{2N}) \end{bmatrix}, \tag{15}$$

with $\omega_0 = 0,\ t_0 = 0,\ \omega_{-N} = -\omega_N$ and

$$\begin{aligned} &P = diag(-\omega_N, \ldots, \omega_0, \ldots, \omega_N), \\ &\widehat{W}^\star = [\widehat{W}_{-N}, \ldots, \widehat{W}_0, \ldots, \widehat{W}_N]^\top, \\ &\widehat{R}^\star = [\widehat{R}_{-N}, \ldots, \widehat{R}_0, \ldots, \widehat{R}_N]^\top. \end{aligned} \tag{16}$$

As opposed to the case of periodic flow, the arbitrary complex exponentials family does not form, *a priori*, an orthogonal basis.

Knowing a time sampling that allows A^{-1} to be invertible, the almost-periodic Fourier coefficients can be approximated thanks to

$$\begin{cases} \widehat{W}^\star = AW^\star, & \text{with } W^\star = [W(t_0), \ldots, W(t_i), \ldots, W(t_{2N})]^\top, \\ \widehat{R}^\star = AR^\star, & \text{with } R^\star = [R(t_0), \ldots, R(t_i), \ldots, R(t_{2N})]^\top. \end{cases} \tag{17}$$

Eq. (14) thus becomes

$$iVA^{-1}PA + R^\star = VD_t[W^\star] + R^\star = 0, \tag{18}$$

where the multiple-frequency HB time-derivative operator $D_t[\cdot] = iA^{-1}PA$, the HB source term, can not be easily derived analytically, and has to be numerically computed. This must be real matrix, however the authors were not able to prove it mathematically. Nonetheless, numerical experiments tends to confirm this assertion. Indeed, the magnitude of the ratio of the real part over the imaginary part is around 10^{15}. The remaining value of the imaginary numbers may then be attributed to rounding errors.

At this step of the derivation of the method, the time sampling $[t_0, \ldots, t_{2N}]$ remains to be specified.

2.2.2. Condition number and convergence

Kundert et al. [30] show that the condition number of A, and thus A^{-1}, has a salient role in the convergence of harmonic balance computations. The condition number of the almost-periodic DFT matrix A is defined as

$$\kappa(A) = \kappa(A^{-1}) = \|A\| \cdot \|A^{-1}\|, \quad \kappa(A) \geqslant 1, \tag{19}$$

where $\|\cdot\|$ denotes a matrix norm. Considering the resolution of $Ax = b$, if A is invertible and if $\delta A,\ \delta x$ and δb are the numerical errors associated with the computation of $A,\ x$ and b, respectively, then

$$(A + \delta A)(x + \delta x) = b + \delta b. \tag{20}$$

Therefore, the condition number sets an upper bound for the error made on x:

$$\frac{\|\delta x\|}{\|x\|} \leqslant \kappa(A)\left[\frac{\|\delta A\|}{\|A\|} + \frac{\|\delta b\|}{\|b\|}\right]. \tag{21}$$

The error on the iterative resolution of the U-RANS equations can therefore be amplified by the HB source term. This amplification is led by the condition number of the almost-periodic DFT matrix. This also means that if the errors are small but the condition number is high, and vice versa, the computation can diverge too. However, the errors can not be *a priori* controlled, thus the need to minimize the condition number.

In the case of periodic-flows, the DFT matrix is well-conditioned: the uniform sampling for harmonically related frequencies leads to a condition number equal to 1, which is the theoretical lower bound for the condition number. This is linked to the orthogonality of the complex exponential family. On the other hand, when the frequencies are arbitrary, it is usually impossible to choose a uniform set of time instants over which the almost-periodic DFT matrix A is well conditioned. In fact, it is common for uniformly-sampled sinusoids at two or more frequencies to be nearly linearly dependent, which causes them not to be orthogonal, leading to the ill-conditioning encountered in practice. As the frequency set is chosen by the user, the only degrees of freedom left to get a well-conditioned matrix are the time levels. The following section describes two algorithms to find a non-uniform time sampling that minimizes the almost-periodic DFT matrix condition number.

3. Non-uniform time sampling algorithms

Two algorithms that automatically choose the time levels in order to minimize the condition number are presented: first, the Almost Periodic Fourier Transform (APFT) algorithm, initially proposed in the literature for electronics problems, is described, then a gradient-based optimization algorithm over the condition number (OPT) is presented.

3.1. The APFT algorithm

Based on the work of Kundert et al. [30] in electronics, the APFT algorithm has been implemented. The aim of the APFT algorithm is to maximize the orthogonality of the almost-periodic DFT matrix in order to minimize its condition number. It is based on the Gram–Schmidt orthogonalization procedure. First, the greatest period $1/\min_k(f_k)$ is oversampled with M equally-spaced time levels, $M \gg 2N+1$ being specified by the user and N the number of frequencies. Considering these time levels, a rectangular almost-periodic IDFT matrix is built. Noting that every row of this matrix is a vector, a set of M vectors is obtained, numbered from 0 to $M-1$, and of length $2N+1$. The first vector V_0 (corresponding to $t=0$) is arbitrarily chosen as the first time level and any component in the direction of V_0 is removed from the following vectors using the Gram–Schmidt formula:

$$V_s = V_s - \frac{V_0^\top \cdot V_s}{V_0^\top \cdot V_0} V_0, \quad s = 1, \ldots, M-1. \tag{22}$$

The remaining vectors are now orthogonal to V_0. Since the vectors initially have the same Euclidean norm, the vector having the largest norm is the most orthogonal to V_0. It is assigned to V_1. The previous operations are then performed on the $M-2$ remaining vectors using V_1 as V_0. This process is repeated until the required $2N+1$ vectors are defined. As a time instant corresponds to a vector, $2N+1$ time levels are obtained, which enables the construction of the almost-periodic DFT matrix. This algorithm is summarized in Algorithm 1.

Algorithm 1. The almost periodic Fourier transform algorithm.

```
$\omega_{min} \leftarrow min(|\omega_k|, 1 \leqslant k \leqslant N)$
for $m \leftarrow 0, \ldots, M-1$ do
    $t_m \leftarrow \frac{2\pi}{\omega_{min}} \frac{m}{M}$
end for
for $n \leftarrow 1, \ldots, 2N$ do
    for $m \leftarrow n+1, \ldots, M$ do
        $V_m \leftarrow V_m - \frac{V_n^\top \cdot V_m}{V_n^\top \cdot V_n} V_n$
    end for
    argmax () returns the index of the largest member of a set
    $k = \mathbf{argmax}(\|V_s^n\|, n+1 \leqslant s \leqslant M)$
    swap$(V_{n+1}, V_k)$
    swap$(t_{n+1}, t_k)$
end for
$\mathbb{T}_{optimized} \leftarrow [t_0, \ldots, t_{2N}]$
```

3.2. Gradient-based optimization algorithm (OPT)

A more direct approach is to seek directly a set of time levels that minimize the condition number of the associated almost-periodic DFT matrix, instead of using orthogonality properties. This minimization problem can be solved numerically by an optimization algorithm.

The limited memory optimization method of Broyden–Fletcher–Goldfarb–Shannon (L-BFGS-B, [31]) is used to look for a minimum of the condition number of the almost-periodic IDFT matrix $\kappa(A[\mathbb{T}])$ as function of the time levels vector $\mathbb{T}$. This quasi-Newton algorithm approximates the inverse Hessian matrix $H(\kappa(A[\mathbb{T}]))^{-1}$ with the BFGS formula in order to decrease the objective $\kappa(A[\mathbb{T}])$ in the direction $-H(\kappa(A[\mathbb{T}]))^{-1}\nabla\kappa(A[\mathbb{T}])$. This descent direction is associated with the search for a zero of the gradient, which is a necessary condition for an extremum, in a second order Taylor series. Finally, a line search on α is performed to minimize $\kappa(A[\mathbb{T} - \alpha H(\kappa(A[\mathbb{T}]))^{-1}\nabla\kappa(A[\mathbb{T}])])$. In the present case, the derivative $\nabla\kappa(A[\mathbb{T}])$ of the objective with respect to the time levels is approximated by first-order finite differences. An open-source implementation of this reference broadly-used algorithm is employed [32].

Gradient descent methods being local, the L-BFGS-B method converges to a local minimum of the condition number. This minimum is unsatisfying if the starting point $\mathbb{T}$ is not well chosen, therefore a strategy to find an appropriate one is required. As shown in the following comparison, APFT or uniform-sampling time levels do not always guarantee acceptable condition numbers, and so cannot be used to provide a starting point for L-BFGS-B. To this aim, the smallest frequency is uniformly sampled:

$$\Omega = \left[\frac{1}{M}\omega_{min}, \ldots, \frac{m+1}{M}\omega_{min}, \ldots, \omega_{min}\right], \tag{23}$$

where M denotes the desired number of initial guesses. This gives a set of periods. Each of them are evenly sampled to obtain a set of time levels.

$$\mathbb{T}_m = \left[0, \frac{2\pi M}{(2N+1)(m+1)\omega_{min}}, \ldots, \frac{2N\pi M}{(2N+1)(m+1)\omega_{min}}\right]. \tag{24}$$

These time levels sets are then used as initial guesses for the L-BFGS-B algorithm.

The almost-periodic IDFT matrix is built for each of these time levels and the corresponding condition numbers are computed. A large number M, typically thousands, of fractions of the greatest period gives a large set of potential time levels vectors. This is acceptable given the very low cost of the computation of the condition number on such small matrices of size $(2N+1) \times (2N+1)$. From this set, the time levels vector associated with the almost-periodic IDFT matrix having the smallest condition number is taken as a starting point. The optimization algorithm actually achieves a local adjustment of the time levels.

In this way, the exploitation capability of the gradient-based optimizer is well combined with the exploration capacity of the sampling. This finally gives solutions that are always close to the ideal value of 1, as shown in Table 1. The OPT method is summarized in Algorithm 2.

Algorithm 2. The gradient-based optimization algorithm (OPT).

```
$\omega_{min} \leftarrow min(|\omega_k|, 1 \leqslant k \leqslant N)$
for $m \leftarrow 0, \ldots, M-1$ do
    $\omega_m \leftarrow \frac{m+1}{M} \cdot \omega_{min}$
    for $i \leftarrow 0, \ldots, 2N$ do
        $t_i \leftarrow \frac{i \cdot 2\pi}{\omega_m \cdot (2N+1)}$
    end for
    $\mathbb{T}_m \leftarrow [t_0, \ldots, t_i, \ldots, t_{2N}]$
    $C_m \leftarrow \kappa(A[\mathbb{T}_m])$
end for
argmin () returns the index of the smallest member of a set
$k \leftarrow$ argmin$(C_m, 0 \leqslant m \leqslant M-1)$
min_l-bfgs-b$(\kappa(A[\mathbb{T}]), \mathbb{T}_{ini})$ returns the optimal time levels vector $\mathbb{T}$ with the condition number $\kappa(A[\mathbb{T}])$ as objective
    function using the L-BFGS-B algorithm and $\mathbb{T}_{ini}$ as starting point.
$\mathbb{T}_{optimized} \leftarrow$ min_l-bfgs-b$(\kappa(A[\mathbb{T}]), \mathbb{T}_{ini} = \mathbb{T}_k)$
```

3.3. Assessment of the algorithms

Let us consider the case of two frequencies, f_1 and f. Without loss of generality it can be assumed that $f \leqslant f_1$. The non-dimensional frequency δ_f^* is defined as:

Table 1
Global results for the presented algorithms.

	EQUI			APFT	OPT
# instants	$2N+1$	$3N+1$	$20N+1$	$2N+1$	$2N+1$
$\min(\kappa[A])$	1.002	1.0	1.0	1.001	1.000
$\max(\kappa[A])$	3.024×10^{14}	1.871×10^{11}	2732.6	823.8	2.905
$\mathrm{mean}(\kappa[A])$	3.081×10^{11}	1.871×10^{8}	10.92	7.742	1.097

$$\delta_f^* : \begin{cases} [0:f_1] & \mapsto [0:2] \\ f & \mapsto 2\cdot\frac{f_1-f}{f_1+f}. \end{cases} \tag{25}$$

By taking f_1 constant, and having δ_f^* sampled between 0 and 2, the whole range of $f \leqslant f_1$ is explored. Moreover, as δ_f^* is anti-symmetric ($\delta_f^*(-f) = -\delta_f^*(f)$), and as the almost-periodic IDFT matrix is symmetric $A[-f] = A[f]$, the following relation is obtained for the condition number:

$$\kappa(A[\delta_f^*(-f)]) = \kappa\Big(A\Big[-\delta_f^*(f)\Big]\Big) = \kappa(A[\delta_f^*(f)]), \tag{26}$$

meaning that the case $f \geqslant f_1$ can be deduced in a straightforward way.

For each value of δ_f^*, the condition number of the almost-periodic IDFT matrix $\kappa(A)$ is computed, highlighting the ability of the different algorithms to choose the time levels that minimize the condition number, for any input frequencies. This assessment is only valid for two frequencies, but the tendency is similar when increasing the number of frequencies. Two frequencies are involved thus five time levels are required. The results of three algorithms are depicted in Fig. 1: (i) APFT: the Almost Periodic Fourier Transform algorithm, (ii) OPT: the gradient-based optimization algorithm and (iii) EQUI: evenly spaced time levels oversampling the largest period as done in Gopinath et al. [14] using $2N+1$ time levels and in Ekici and Hall [15,16] using $3N+1$ time levels.

The EQUI algorithms give fair results ($\kappa(A) \leqslant 2$) only at discrete points, corresponding to the particular cases where f is a multiple of f_1, which are thus similar to the single-frequency case. Oversampling improves the results. In fact, the mean condition number obtained with $20N+1$ time levels indicates that the higher the number of time levels the better the condition number. However the almost-periodic DFT matrix becomes rectangular and the memory cost of such a computation increases drastically, preventing the use of such an approach on industrial cases. The APFT algorithm improves the results, as it gives results with $\kappa(A)$ close to unity for $0.3 \leqslant \delta_f^* \leqslant 1.2$. However, when δ_f^* tends to the boundaries (0 and 2), the condition number seems to go to infinity. This corresponds to special values of f:

$$\begin{aligned} \delta_f^* = 0 &\iff f = f_1, \\ \delta_f^* = 2 &\iff f = 0. \end{aligned} \tag{27}$$

This means that the APFT algorithm fails to work when the frequencies are too close to one another, and when they are significantly different. This limits the method for a range of frequencies where the HB method could give a salient gain in CPU time. Finally, the OPT algorithm gives a condition number close to unity for any value of δ_f^*. The OPT algorithm thus ensures that the convergence of the HB method is not sensitive to the specified set of frequencies. Table 1 summarizes the results obtained with each algorithm.

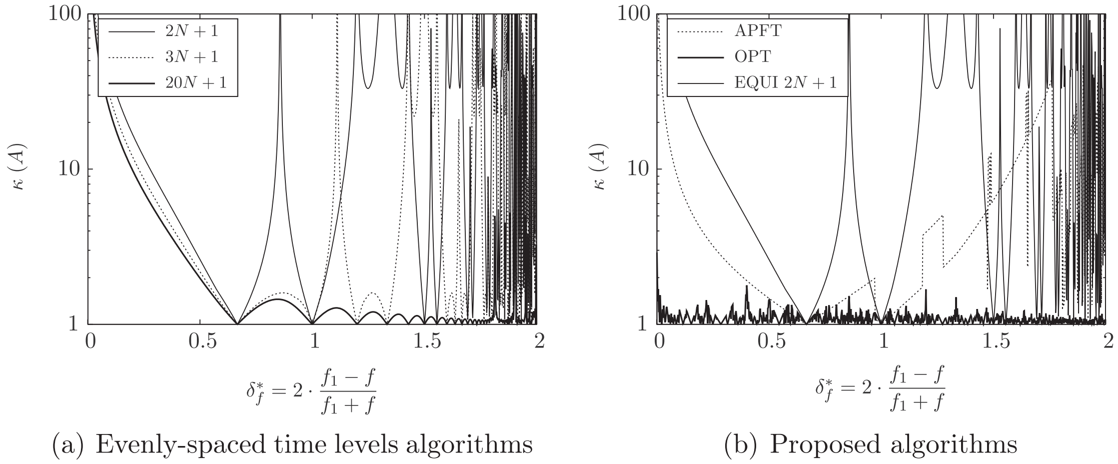

(a) Evenly-spaced time levels algorithms (b) Proposed algorithms

Fig. 1. Comparison of the presented algorithms.

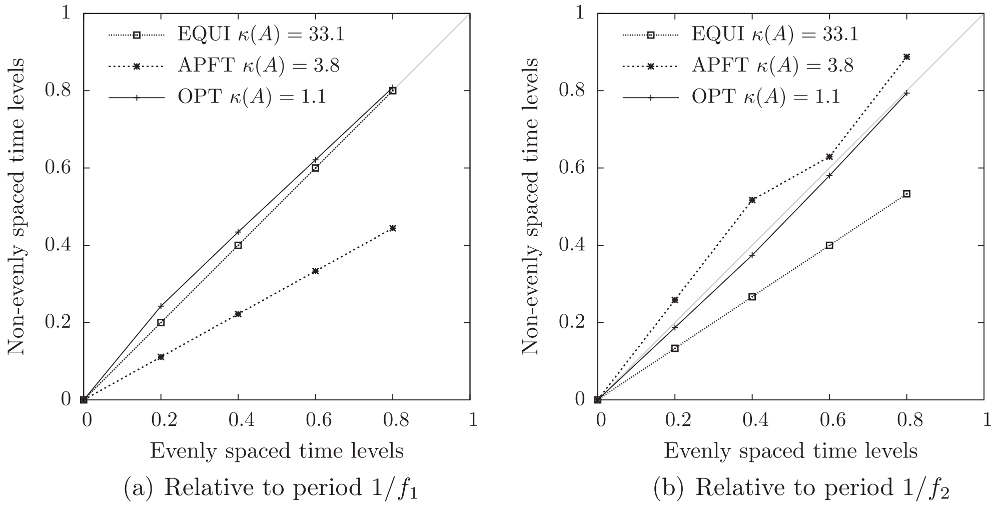

(a) Relative to period $1/f_1$ (b) Relative to period $1/f_2$

Fig. 2. Distribution of the time levels on each frequency periods.

Thus the proposed non-uniform time sampling combined with the OPT algorithm allows to tackle problems with large frequency separation. In such cases, the gain of the HB approach compared to classical time-marching methods is expected to be significant: with a time-marching scheme, the time-step has to be small enough to discretize the shortest period, while the number of time steps of the simulation has to be long enough to reach the (almost-) periodic state (*i.e.* the simulation time is equal to several times the longest period). Conversely, the cost of the HB method only depends on the number of frequencies to capture, regardless of their relative values.

3.4. Distribution of the time levels

For harmonically-related frequencies, the optimal time levels correspond to a uniform set sampling the fundamental frequency period as it gives the theoretical lower bound $\kappa(A) = 1$. Since the frequencies are harmonically related, the distribution of the time levels on the other frequencies is also uniform. Considering the frequency vector $F = [f_1, \dots, f_k = kf_1, \dots, Nf_1]$ and the time levels vector $\mathbb{T}$:

$$\mathbb{T} = \left[0, \frac{1}{f_1 \cdot (2N+1)}, \dots, \frac{2N}{f_1 \cdot (2N+1)}\right], \tag{28}$$

then the product of the *i*th term of $\mathbb{T}$ to its associated frequency is

$$f_1 \cdot \frac{i}{f_1 \cdot (2N+1)} = kf_1 \cdot \frac{i}{kf_1 \cdot (2N+1)} = f_k \cdot \frac{i}{f_k \cdot (2N+1)}. \tag{29}$$

Eq. (29) means that evenly-spaced time levels for the fundamental frequency are still seen as evenly spaced by the *k*th harmonic. This is an explanation why the condition number of the almost-periodic IDFT matrix A^{-1} will be unity as each frequency is sampled by evenly spaced time levels [33].

Now, considering non-harmonically related frequencies, there is mathematically no reason for evenly-spaced time levels over the smallest frequency to be seen as evenly spaced by the other frequencies in general. Therefore, the use of non-evenly spaced time levels, and algorithms to automatically choose them, becomes necessary.

Fig. 2 shows the distribution of the time levels, relative to each frequency period, obtained by the presented algorithms for the frequencies $f_1 = 3$ Hz and $f_2 = 17$ Hz (*i.e.* $\delta_f^* = 1.4$). To do so, the chosen time levels are redistributed on the considered frequency period by applying a modulo to it:

$$\mathbb{T}_j^{[f_k]} = \mathbb{T}_j \,\text{modulo}\, 1/f_k. \tag{30}$$

Then, they are divided by the latter, so that the results are dimensionless. In light gray line is depicted the $y = x$ function representing the evenly-spaced solution on the considered period. Keeping in mind that if each frequency sees evenly-spaced time levels, then the condition number is the smallest, the optimal solution would be to have relative time levels on $y = x$ for each period. Running the EQUI, APFT and OPT algorithms leads to a condition number of 33.1, 3.8 and 1.1, respectively. The EQUI algorithm is perfect for the period $1/f_1$ but is really far from the evenly spaced time levels for period $1/f_2$. The APFT algorithm is far from the evenly spaced solution for both the periods considered, but closer than EQUI regarding period $1/f_2$. Finally, the OPT algorithm is the only one to be close to the evenly spaced solution for each considered period, allowing the proposed HB method to be used for any set of frequencies.

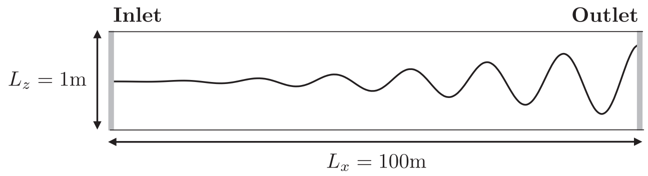

Fig. 3. Schematic diagram of the channel case.

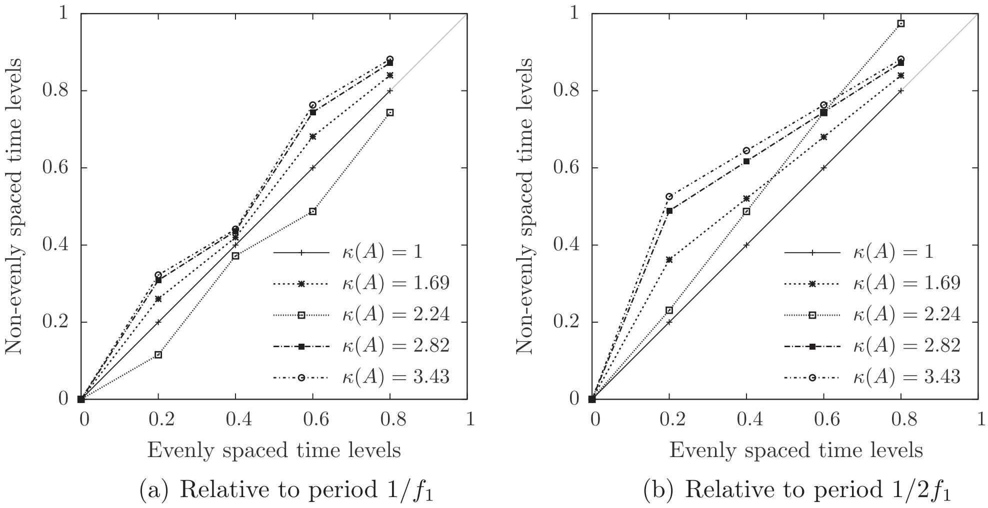

(a) Relative to period $1/f_1$

(b) Relative to period $1/2f_1$

Fig. 4. Distribution of the time levels on each frequency periods.

The source code of the proposed algorithms and the scripts to generate in Figs. 1 and 2 are available over the internet.[1]

The impact of the time sampling on HB computations is now investigated for the simple case of a channel flow with fluctuating pressure outlet.

4. Channel flow

4.1. Test case description

A channel configuration is set up to study the properties of the proposed HB method and the above algorithms for non-uniform time sampling. It is a 2D channel of length $L_x = 100$ m in the axial direction and $L_z = 1$ m in the transverse one. The boundary conditions are: (i) an injection condition for the inlet, (ii) symmetric conditions for the upper and lower bounds as the flow is assumed to be symmetric in the transverse direction, and (iii) a fluctuating pressure imposed at the outlet:

$$P_{outlet}(t) = P_m \cdot [1 + A_1 \cdot \sin(2\pi f_1 t) + A_2 \cdot \sin(2\pi f_2 t)], \tag{31}$$

where P_m is the temporal average static pressure, A_n the amplitude of the nth mode and f_n its frequency. The mean outlet pressure P_m is set to 60% of the inlet total pressure $P_{i0} = 101,325$ Pa.

Pressure waves travel within the flow with the velocity $u + c$ and $u - c$, where u denotes the local flow velocity and c the sound velocity. Since the pressure waves are generated at the outlet, only the $u - c$ waves are visible, resulting in pressure waves propagating upstream of the channel, which are damped by the effect of viscosity. Fig. 3 shows a schematic diagram of the channel case, illustrating the propagation and attenuation of the pressure waves.

The mesh consists of 997 points along the axial direction and 9 in the transverse one, which amounts to almost equal spacings in both directions.

This configuration is turbulent as the Reynolds number based on the inlet flow velocity and the axial length of the channel is about $R_e \approx 2.0 \times 10^9$. Turbulence is modeled using the one-equation model of Spalart and Allmaras [34], and the third-order upwind Roe scheme [35] is used to compute the convective fluxes.

4.2. Convergence sensibility analysis

As mentioned previously, the condition number is of great importance for the convergence of the proposed HB method. To highlight this feature, the presented channel case is computed with a single frequency at the outlet: $f_1 = 3$ Hz with an

---

[1] http://cerfacs.fr/~gomar/PyLeap.html.

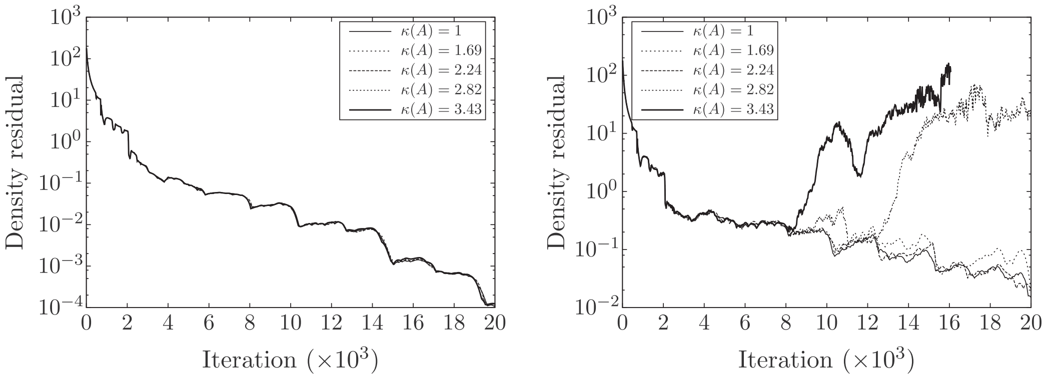

(a) $A_1 = 0.01$ (b) $A_1 = 0.05$

Fig. 5. Relation between the condition number $\kappa(A)$ and the convergence of the solution.

amplitude $A_1 = 0.05$ for the first case and $A_1 = 0.01$ for the second one, the second frequency having a zero amplitude: $A_2 = 0$. Two frequencies are specified for the HB computation: f_1 and its first harmonic $2f_1$. The time levels are chosen to reach varying condition numbers such that $1 \leqslant \kappa(A) \leqslant 3.43$. Since the input frequencies of the HB computation are harmonically related, the minimal conditioning $\kappa(A) = 1$ is obtained with evenly spaced time levels. The OPT algorithm is modified by subtracting the targeted conditioning to the objective function, so that the different condition numbers can be reached. The distribution of the time levels for each condition number is shown in Fig. 4. The time levels deviate from the evenly spaced solution as the condition number grows. The results in Fig. 5 show that for a condition number $\kappa(A) \geqslant 3.43$ and wave input amplitude $A_1 = 0.05$, the computation diverges. However, the computations with the same condition numbers but a smaller input amplitude $A_1 = 0.01$ converge. In fact, the condition number amplifies the errors made during the iterative process. When the input waves have a smaller amplitude, the iterative errors are slighter, hence the convergence as explained in Section 2.2.2.

4.3. Validation of the multi-frequency HB method

To validate the proposed HB method, two non-harmonically related frequencies are chosen as input for the outlet boundary condition: $f_1 = 3$ Hz and $f_2 = 17$ Hz.

A classical time-marching scheme is taken for comparison, namely the Dual Time Stepping scheme (DTS [36]). The DTS method is a 2nd-order implicit time-marching scheme. Convergence in time discretization is obtained after 20 periods using 160 instants per almost-period. Since the frequencies are integers and coprime, the period is $T = 1$ s. Iterative convergence

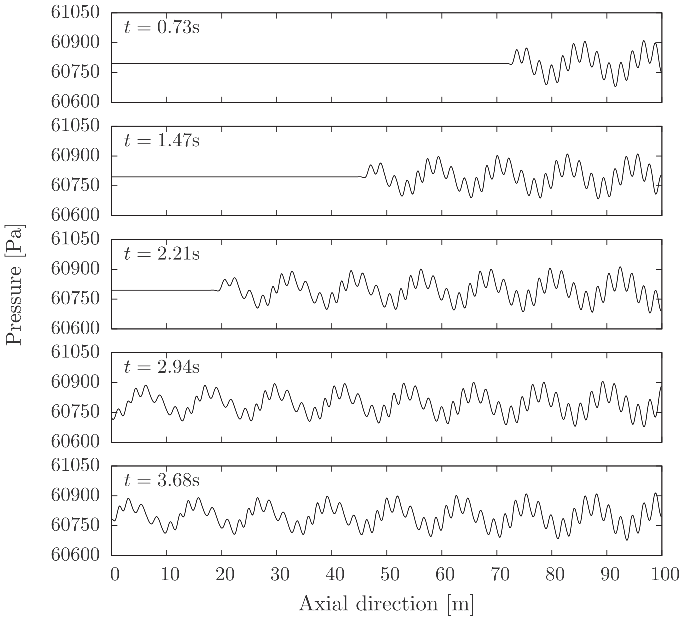

Fig. 6. DTS computation: transient propagation of the pressure waves.

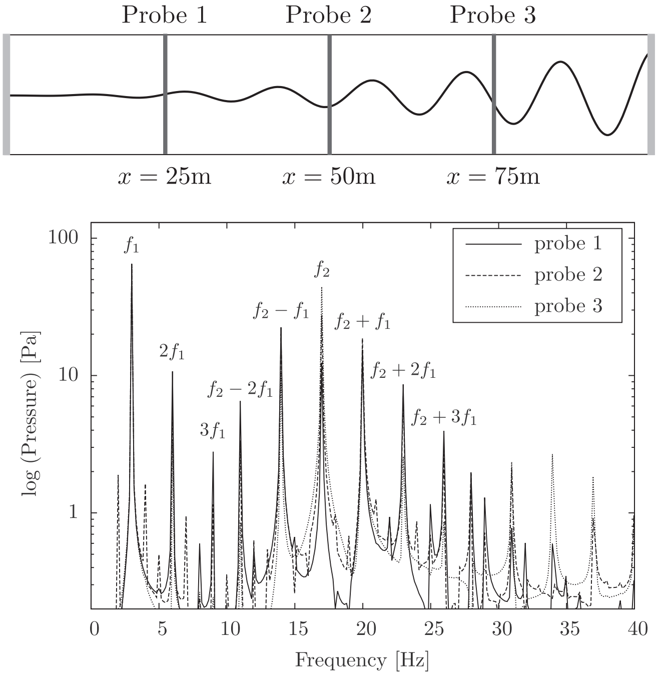

Fig. 7. Spectrum of pressure signals.

for the inner loop is considered achieved when the normalized residuals drop by 10^{-2} within a maximum of 50 subiterations.

The results obtained with the DTS scheme are compared to the HB results for pressure waves amplitudes of $A = A_1 = A_2 = 0.001$. The transient of the DTS computation is shown in Fig. 6, illustrating the wave propagation with a slight attenuation of the high-frequency waves.

The results are analyzed for frequencies $1 < f < 40$ Hz and the dominant frequencies (the one that have the highest amplitudes) are set for the HB computation. To do so, pressure signals are probed upstream, in the middle and downstream of the channel at $x = [25\text{ m},50\text{ m},75\text{ m}]$ and $z = 0.5$ m, respectively. The spectrum of the aforementioned unsteady pressure signals, obtained with a Fourier Transform, are plotted in Fig. 7. The labeled frequencies are the dominant ones, as for each probe, these have a high amplitude. They are thus selected for the HB computation. For such frequencies, the OPT algorithm gives a set of time levels leading to a condition number of 1.4.

A Discrete Fourier Transform is computed at several axis positions, resulting in the spatial evolution of the different harmonics, which is used for the comparison of the HB and DTS approaches, in the middle of the canal ($z = 0.5$ m). In Fig. 8, the results are plotted for the frequencies that have been set for the HB computation. The overall agreement is fair. Some local discrepancies can be observed upstream for frequencies $f_2 + 3f_1, f_2 - f_1$ and $f_2 - 2f_1$. These are caused by aliasing but they are minimal regarding the temporal evolution, as shown in Fig. 9, where the time evolution of pressure signals is extracted at all probes. The difference between the HB and the DTS method is negligible, proving that the proposed HB method is able to reproduce the unsteady almost-periodic phenomena.

The goal of this section was not to show significant CPU savings but rather the capacity of the present HB method to capture an almost-periodic flow on a model problem. It is now applied to a more complex configuration, namely a turbomachinery element, where its computational efficiency is also emphasized.

5. Turbomachinery application

Under the assumption that all unsteady phenomena in a blade row during stable operation are periodic and can be correlated with the rotation rate Ω of the shaft, the dominant frequencies are those created by the passage of the neighboring blades. In a multi-row turbomachine, a blade row sandwiched between the upstream and downstream rows is subjected to wake and potential effects. In practical turbomachines, the blade counts of neighboring rows are generally different and coprime. Consequently, a sandwiched blade row resolves various combinations of the frequencies, which are additions and/or subtractions of multiples of the blade passing frequencies: according to Tyler and Sofrin [13], the kth frequency in the blade row j is given by

$$\omega_k^{rowj} = \sum_{i=1}^{nRows} n_{k,i} B_i (\Omega_i - \Omega_j). \tag{32}$$

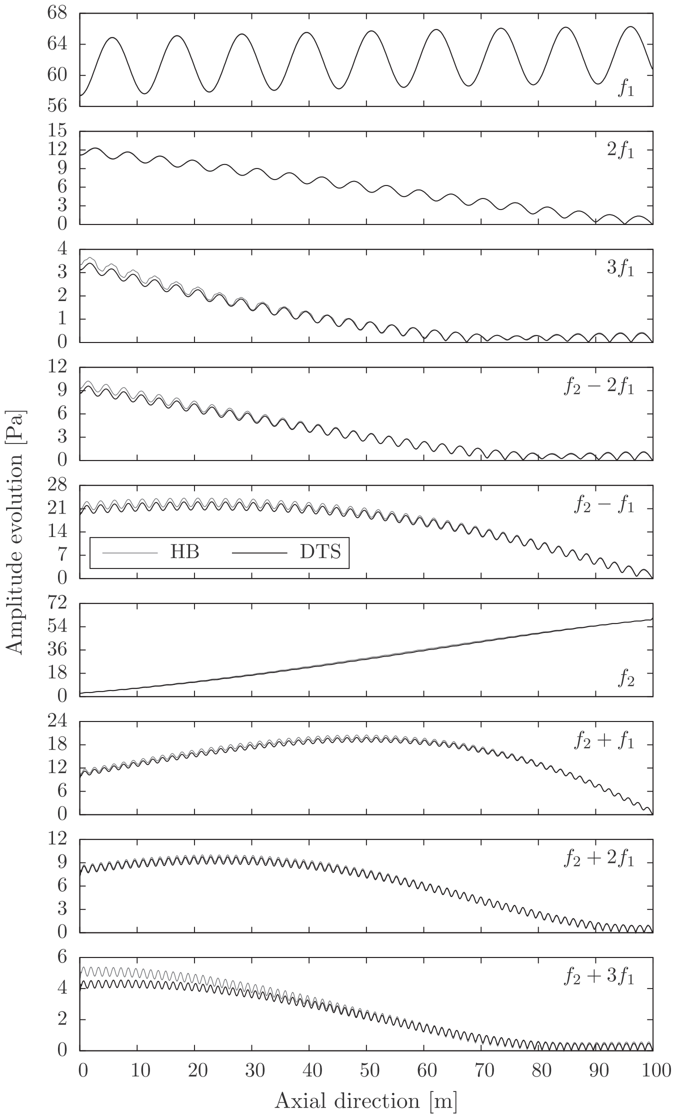

Fig. 8. Spatial evolution of the amplitude of the dominant frequencies in the channel, for $f_1 = 3$ Hz and $f_2 = 17$ Hz.

Here, B_i and Ω_i are respectively the blade count and the rotation rate of the ith blade row, $n_{k,i}$ is the kth set of *nRows* integers driving the frequency combinations. It must be noted that only the blade rows that are mobile relative to the considered j one contribute to its temporal frequencies and that every blade row solves its own set of frequencies and thus its own set of time levels. To set up a HB computation for a multistage configuration, it is of course impossible to use each and every possible $n_{k,i}$, and the user has to choose which frequency combinations will appear in the computation of each row.

In the literature, Gopinath et al. [14] and Ekici and Hall [15] assessed their implementation of the harmonic balance on a 2D multi-stage compressor (namely configuration D). It is composed of a rotor sandwiched by two stators having 32, 40 and 50 blades, respectively. Various combinations of the stators BPFs are considered, but always with evenly-spaced time levels sampling the largest period. While Gopinath et al. use $2N+1$ samples, Ekici and Hall over-sample this period with $3N+1$ time levels. This leads to a rectangular $(2N+1) \times (3N+1)$ almost-periodic Fourier Matrix and requires the computation of its Moore–Penrose pseudo-inverse. The chosen frequencies and the *a posteriori* associated condition numbers of the above references are given in Table 2. For $N = 4$, the $3N+1$ instants oversampling approach of Ekici and Hall efficiently reduces the condition number. But for this case, the use of evenly-spaced time levels is sufficient as the condition number seems to be small enough for the considered magnitude of unsteadiness. However, such an approach fails when dealing with more widely-separated frequencies as illustrated in the present contribution in Section 3. Moreover, using an oversampling increases the CPU cost and the required memory as the number of steady computations to solve simultaneously is higher. These two reasons highlight the need for a non-uniform HB method as proposed in the current paper.

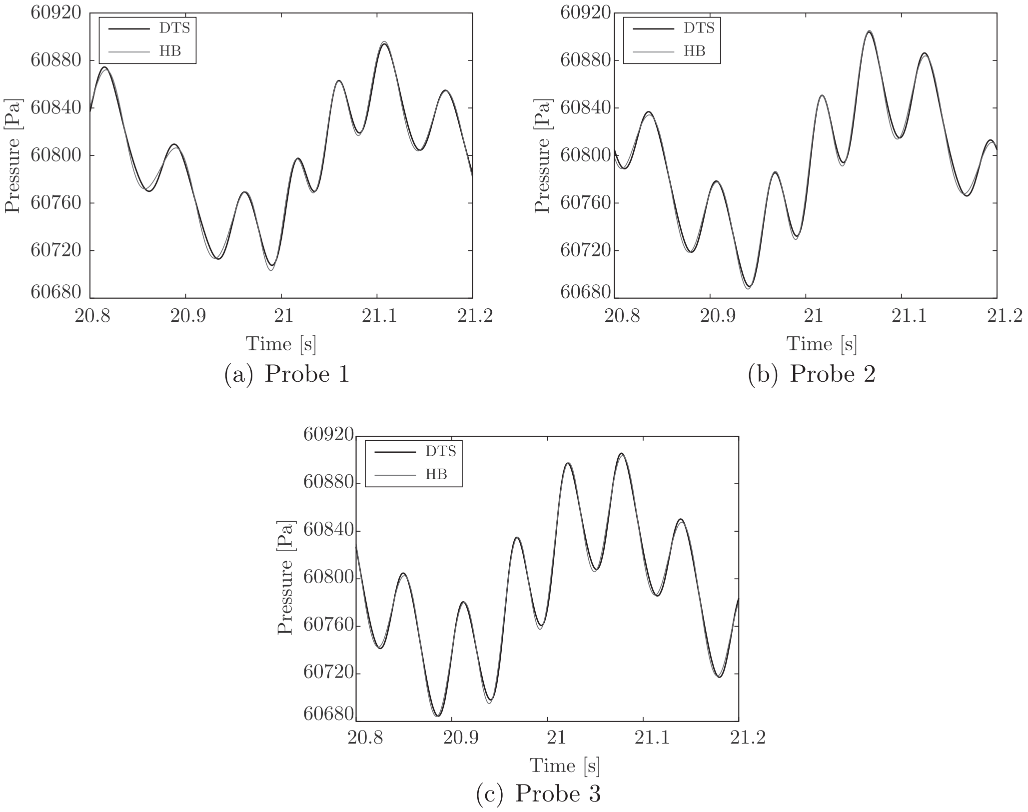

(a) Probe 1 (b) Probe 2 (c) Probe 3

Fig. 9. Unsteady pressure signals at different axial positions.

Table 2
Frequency combinations and associated condition number of computations made in the literature.

	Frequencies		$\kappa(A)$			
	n S1	n S2	EQUI $2N+1$	EQUI $3N+1$	APFT	OPT
$N=2$ Ref. [14]	1 0	0 1	**3.79**	3.00	1.72	1.08
$N=3$ Ref. [15]	1 0 1	0 1 1	5.40	**3.84**	1.71	1.00
$N=4$ Ref. [14]	1 0 1 1	0 1 1 −1	**11.25**	2.07	3.46	1.13
$N=7$ Ref. [14]	1 0 1 1 2 2 2	0 1 1 −1 0 −1 1	**16.66**	14.61	12.95	1.00

5.1. Boundary conditions for sector reduction

Section 3 showed how to contain the problem size by reducing the time span over which the solution is sought. In the following sections, it is explained how to cut down the mesh size by using a grid that spans only one blade passage per row.

5.1.1. Phase-lagged azimuthal boundary conditions

In a single blade passage computation of a multi-row configuration, the phase-lag condition [37] needs to be used to take the space–time periodicity into account. It states that the flow in one blade passage θ is the same as next blade passage $\theta + \Delta\theta$ but at another time $t + \delta t$:

$$W(\theta+\Delta\theta,t)=W(\theta,t+\delta t), \tag{33}$$

where $\Delta\theta$ is the pitch of the considered row. Assuming that every temporal lag is associated with a rotating wave of rotational speed ω_k, the constant time lag can be expressed as

$$\delta t=\frac{\beta_k}{\omega_k},\quad \forall k, \tag{34}$$

where

$$\beta_k=2\pi\operatorname{sign}(\omega_k)\left(1-\frac{1}{B_j}\sum_{i\neq j}n_{k,i}B_i\right), \tag{35}$$

the $n_{k,i}$ being the integers specified for the computation of the frequencies from Eq. (32), B_i the number of blades in row i and subscript j denoting the current row.

The phase-lag condition was adapted to the time-domain HB by Gopinath et al. [12]. The derivation starts with the almost-periodic Fourier transform of Eq. (33):

$$\sum_{k=-N}^{N}\widehat{W}_k(\theta+\Delta\theta,t)e^{i\omega_k t}=\sum_{k=-N}^{N}\widehat{W}_k(\theta,t)e^{i\omega_k\delta t}e^{i\omega_k t}. \tag{36}$$

Thus, the flow spectrum from one blade passage is equal to that of the next blade passage modulated by the inter-blade phase angle β_k:

$$\widehat{W}_k(\theta+\Delta\theta,t)=\widehat{W}_k(\theta,t)e^{i\omega_k\delta t}=\widehat{W}_k(\theta,t)e^{i\beta_k}. \tag{37}$$

Using the same notation as previously, the following matrix formulation is obtained:

$$W^{\star}=A^{-1}MAW^{\star}(\theta), \tag{38}$$

where

$$M=diag(-\beta_N,\ldots,\beta_0,\ldots,\beta_N), \tag{39}$$

and A^{-1} is given by Eq. (15).

5.1.2. Stage coupling

Each blade row has its own frequency set and therefore its own time sampling. Therefore, the nth time level in the jth and $(j+1)$th rows do not necessarily match the same physical time. Consequently, at the interface between adjacent blade rows, the flow field on the donor side needs to be generated for all the time levels of the receiver side using a spectral interpolation. A non-abutting join interface is used to perform the spatial communications between the two rows [38]. In order to account for the pitch difference and relative motion, a duplication of the flow is carried out in the azimuthal direction using the phase-lag periodicity. Moreover, as described in Ref. [28], the time levels at the interface are oversampled and filtered to prevent aliasing.

5.2. Application to a subsonic compressor

In order to validate the non-uniform HB method on a turbomachinery test case, a subsonic compressor case is studied. It is the mid-span slice of the inlet guide vanes (IGV) and the first stage of the axial compressor CREATE [39], located in Lyon

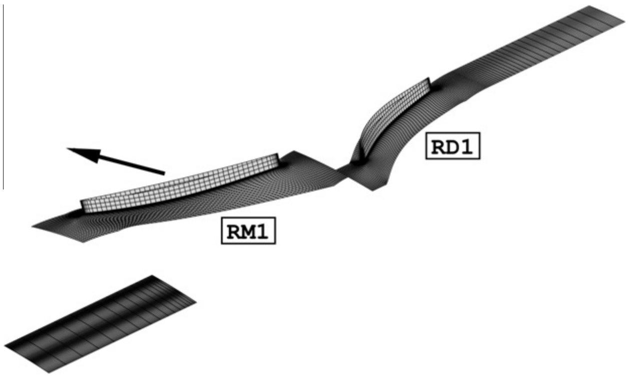

Fig. 10. Geometry of the studied compressor slice.

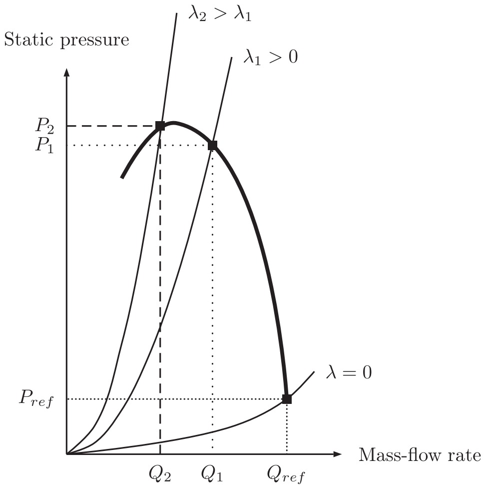

Fig. 11. Valve condition at the outlet.

(France) at the Laboratoire de Mécanique des Fluides et Acoustique (LMFA). This configuration is composed of 32 IGV blades, 64 rotor (RM1) blades and 96 stator (RD1) blades. The full 3D 3.5-stage computation is presented in Ref. [40].

5.2.1. Mesh and numerical parameters

As shown in Fig. 10, the blade passages are meshed with a block-structured topology. It is composed of five grid points in the radial direction, 33 in the azimuthal direction and 100 in the axial direction for both rows. This leads to a total number of approximately 50,000 mesh cells.

The IGV blade is not actually meshed but taken into account through a non-uniform injection boundary condition that represents the wake of the IGV entering the RM1 domain. This injection follows the self-similarity law of Lakshminarayana and Davino [41], which states that the spatial evolution of a wake can be described by a Gaussian function. As $B_{RD1} = 3 \cdot B_{IGV}$, the frequency content remains mono-frequential in the rotor (*i.e.*, the BPF of the downstream rotor is just an harmonic of the

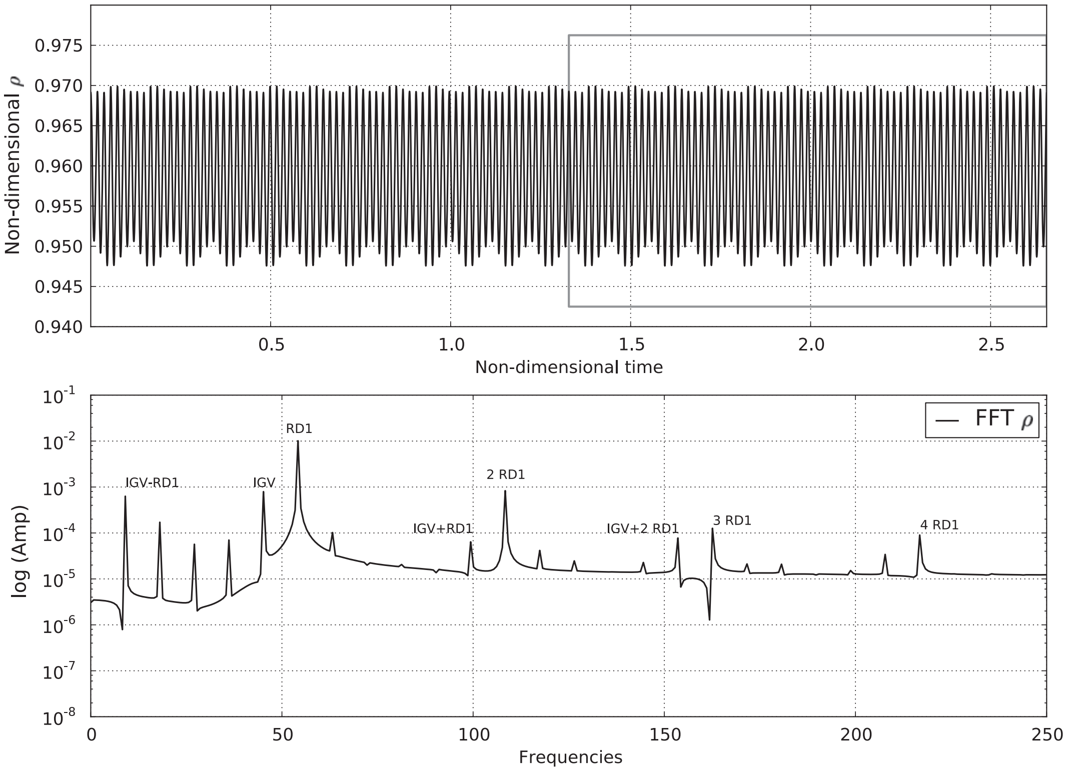

Fig. 12. Time signal and spectrum of non-dimensional ρ at the outlet of the rotor (DTS).

IGV's BPF). Therefore the number of blades composing the IGV has been changed from 32 to 80 so that the configuration still presents a $2\pi/16$ periodicity but the frequency content is now multi-frequential in the rotor.

The outlet duct is modeled by a valve condition coupled with a simplified radial equilibrium equation. The reference outlet static pressure P_s for the radial equilibrium integration is imposed according to the formula $P_s = P_{ref} + \lambda(Q/Q_{ref})^2$, as illustrated in Fig. 11. P_{ref} is a reference static pressure chosen such that when $\lambda = 0$ Pa the compressor is choked, and Q_{ref} is the corresponding mass flow. Q is the current mass flow and $\lambda \geqslant 0$ is a user-defined pressure. Its different values allow to move along the compressor map: when λ increases, the outlet static pressure rises and the mass flow rate decreases and vice versa (Fig. 11). At the blades' surfaces, wall laws [42] are imposed. The lower and upper radial conditions are slip walls.

The convective fluxes are discretized using the second-order Jameson scheme [43] with added artificial viscosity, or a second-order Roe scheme [35,44]. For this study, the turbulent viscosity is computed with the one-equation model proposed by Spalart and Allmaras [34].

The DTS scheme is used to get a numerical reference solution. The periodicity of the different blade passages is such that a $2\pi/16$ periodicity is enough to perform the unsteady computations. To reach an established periodic state, 67 passages (using 400 instants per azimuthal period) of the periodic sector are necessary.

Fig. 12 plots the time evolution of the fluid density ρ and its associated spectrum downstream of the rotor. The spectrum is not only composed of the blade passing frequencies and their harmonics but also of combinations of them as estimated by Tyler and Sofrin [13]. The amplitude of a frequency combination may also be higher than an harmonic of a blade passing frequency. For example, $\text{BPF}_{IGV} - \text{BPF}_{RD1}$ is higher than the third and fourth harmonics of BPF_{RD1}. This highlights the necessity of being able to take into account these frequency combinations in a HB computation.

5.2.2. A posteriori computations: HB computations with frequencies known beforehand

5.2.2.1. Frequency content, time sampling and convergence. The convergence of the harmonic balance computations is done in two steps: first 15,000 iterations with a second order Roe scheme, then 10,000 iterations with the Jameson scheme (with the

Table 3
Frequency combination coefficients.

	n IGV	n RM1	n RD1	Initialization
$N = 3$	1	1	−1	Restart from steady computation
	1	2	0	15,000 it. with Roe second order scheme
	0	3	1	then 10,000 it. with Jameson scheme
$\kappa(A)$ APFT	1.0	2.0	1.0	
$N = 4$ v1	1	1	−1	Restart from steady computation
	1	2	0	15,000 it. with Roe second order scheme
	0	3	1	then 10,000 it. with Jameson scheme
	1	4	1	
$\kappa(A)$ APFT	1.0	1.0	1.0	
$N = 4$ v2	1	1	−1	Restart from steady computation
	1	2	0	15,000 it. with Roe second order scheme
	0	3	1	then 10,000 it. with Jameson scheme
	2	4	0	
$\kappa(A)$ APFT	1.0	1.76	1.0	
$N = 4$ v3	1	1	−1	Restart from steady computation
	1	2	0	15,000 it. with Roe second order scheme
	0	3	1	then 10,000 it. with Jameson scheme
	0	4	2	
$\kappa(A)$ APFT	1.0	2.0	1.0	
$N = 5$	1	1	−1	
	1	2	0	Restart from $N = 4$ v1
	0	3	1	10,000 it. with Jameson scheme $k_4 = 0.064$
	2	4	0	then 10,000 it. with Jameson scheme $k_4 = 0.032$
	0	5	2	
$\kappa(A)$ APFT	1.0	2.34	1.0	
$N = 6$	1	1	−1	
	2	2	−2	Restart from $N = 5$
	1	3	0	5000 it. with Jameson scheme $k_4 = 0.064$
	0	4	1	then 5000 it. with Jameson scheme $k_4 = 0.032$
	2	5	0	
	0	6	2	
$\kappa(A)$ APFT	1.0	2.72	1.0	
$\kappa(A)$ OPT	1.0	2.43	1.0	

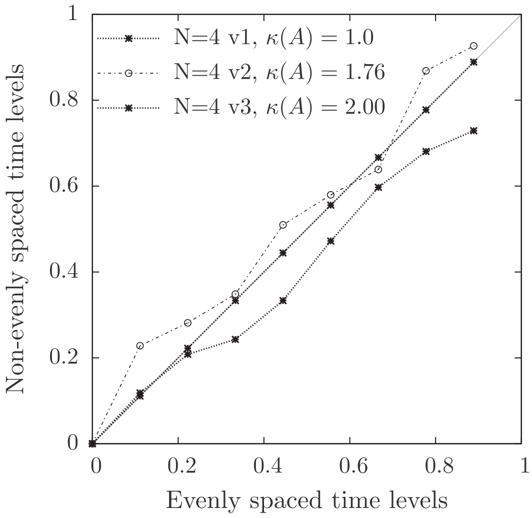

Fig. 13. Distribution of the time levels in the rotor for four frequencies over the base frequency $\text{BPF}_{IGV} - \text{BPF}_{RD1}$.

artificial dissipation coefficients $k_2 = 1.0$ and $k_4 = 0.032$). To understand how the frequency set influences the convergence of the computations, several of them were chosen according to the spectral analysis of the time signal from Fig. 12. They range from three to six frequencies. The present implementation of the HB method in *elsA* imposes to set the same number of frequencies in each blade row. It would not be too difficult to overcome this constraint in order to reduce the number of frequencies in single frequency rows, such as the IGV and RD1 in the present case. This will be addressed in future versions of the software. The frequency combinations used are summarized in Table 3. This table shows the coefficients $n_{k,i}$ from Eq. (32) chosen for each blade row. They are given by the immediately adjacent rows. For example, for $N = 4$ v1, the frequency set is $[\text{BPF}_{RM1}, 2\text{BPF}_{RM1}, 3\text{BPF}_{RM1}, 4\text{BPF}_{RM1}]$ in the IGV (*i.e.* $j = 1$ in Eq. (32)) and in the RD1 (*i.e.* $j = 3$) (which means that for these rows the frequency content is mono-frequential) whereas, it is $[\text{BPF}_{IGV} - \text{BPF}_{RD1}, \text{BPF}_{IGV}, \text{BPF}_{RD1}, \text{BPF}_{IGV} + \text{BPF}_{RD1}]$ in the RM1 (*i.e.* $j = 2$ in Eq. (32)). It is clear that the different blade rows have different frequency sets. The upstream injection block and RD1 only solve for the BPF of the rotor and its harmonics, thus the classic Fourier analysis ensures that the best conditioning of the matrix A^{-1} is given by evenly distributed time levels over the period $T = 1/\text{BPF}_{RM1}$. At this point, it should be noted that 80 and 96 are multiples of 16 (*i.e.* blade number of RD1 minus blade number of IGV). Thus all the frequency combinations of Table 3 for the rotor are multiples of the base frequency $\text{BPF}_{IGV} - \text{BPF}_{RD1}$. However, contrary to what is required by a mono-frequential method, not all the intermediate harmonics need to be taken into account. For example, in a six-frequency set, the highest frequency is 2BPF_{RD1} which is also $12 \times (\text{BPF}_{IGV} - \text{BPF}_{RD1})$. To perform a mono-frequential harmonic computation taking into account 2BPF_{RD1}, one would thus need $\text{BPF}_{IGV} - \text{BPF}_{RD1}$ as the fundamental and the 11 following harmonics, which implies a computation with 25 time samples. Such an approach would be inefficient, as the intermediate harmonics are not relevant here (see Fig. 12). The present multi-frequential HB method allows to perform the computation only on a set of chosen frequencies.

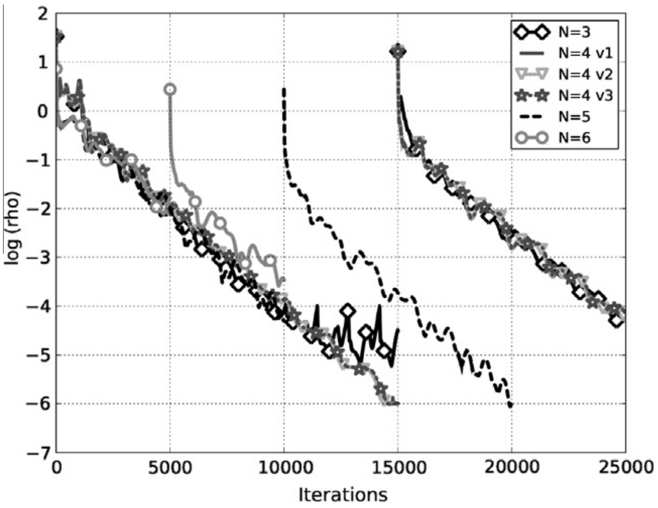

Fig. 14. Convergence history for the maximum of isentropic efficiency.

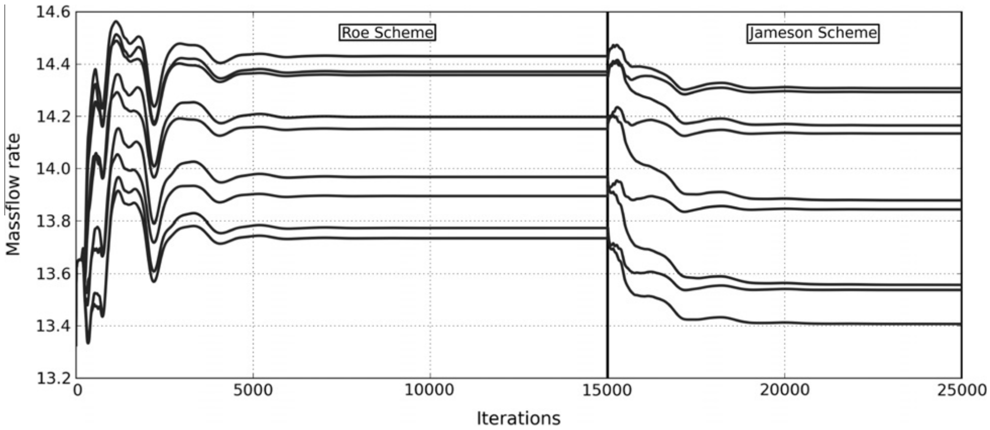

Fig. 15. Instantaneous mass flow rate history for HB $N = 4$ v1.

For such frequency ratios, the APFT algorithm provides good enough condition numbers of the matrix A^{-1} (as shown in Table 3) and the use of the OPT algorithm was not mandatory. As it would be too long and tedious to present the time levels distribution for all the frequency sets, Fig. 13 focuses on the three sets of four frequencies. It allows to observe, for the same number of frequencies, the impact of the frequency set on the APFT algorithm. The first remark that can be drawn from Fig. 13 is that the APFT algorithm is not always needed: for $N = 4$ v1, the best time levels distribution for the rotor is given by a uniform sampling whereas the APFT algorithm gives a condition number of 2.16. However, the gain is significant for the two other configurations: with evenly-spaced time levels, the condition numbers of the matrix A are respectively of 6.74×10^{15} for $N = 4$ v2 and 2.62×10^{15} for $N = 4$ v3, while with the time levels issued from the APFT algorithm they go down to 1.76 and 2.0, respectively.

The convergence of the HB computations depends on the choice of the frequency set as shown in Fig. 14, which depicts the convergence history at the peak-efficiency operating points. For all the computations, the residuals drop at least three orders of magnitude, which is considered to be enough to ensure convergence [45]. Fig. 15 plots the mass flow rate convergence for the first set of four frequencies. The instantaneous mass flow rates differ between the Roe and Jameson schemes. Grid convergence is actually not achieved for the Roe scheme but this not an issue as it is used only for initialization of the computation and the grid is fine enough for the target Jameson scheme. The latter is indeed considered as the reference scheme for the rest of the study since it is the scheme used for the DTS simulations.

5.2.2.2. Time-averaged compressor performance. Figs. 16 and 17 show the computed compressor map: the total pressure ratio Π and the isentropic efficiency η_{is} are plotted against the mass flow. They are non-dimensionalized by the values at the maximum-efficiency point. At blockage, the steady computations have a slightly higher mass flow rate and show a relative increase of the total pressure ratio by 1% near stall. Regardless of the number of frequencies, the overall agreement between the DTS and the HB technique for this variable is good. Indeed, the maximum relative difference is 0.4%. Up to the maximum

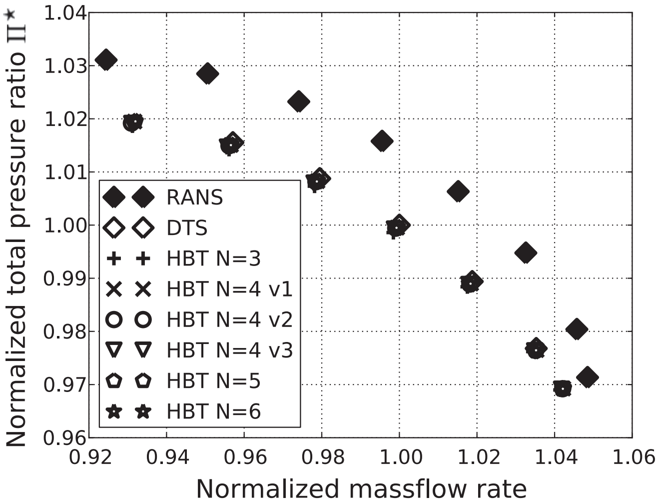

Fig. 16. Non-dimensional total pressure ratio map Π^*.

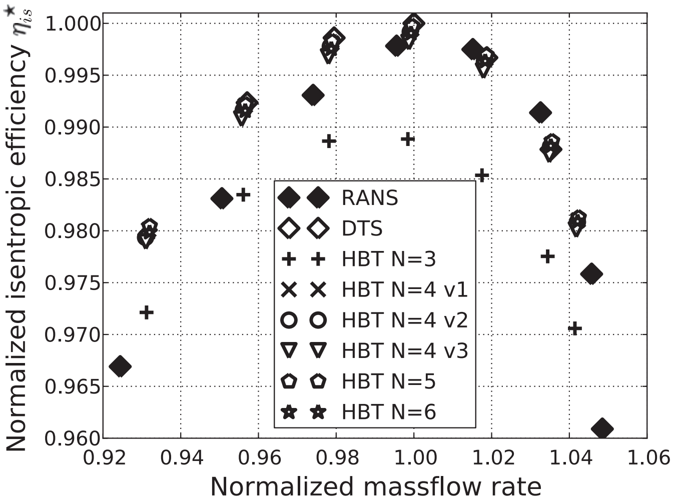

Fig. 17. Non-dimensional isentropic efficiency map η_{is}^{*}.

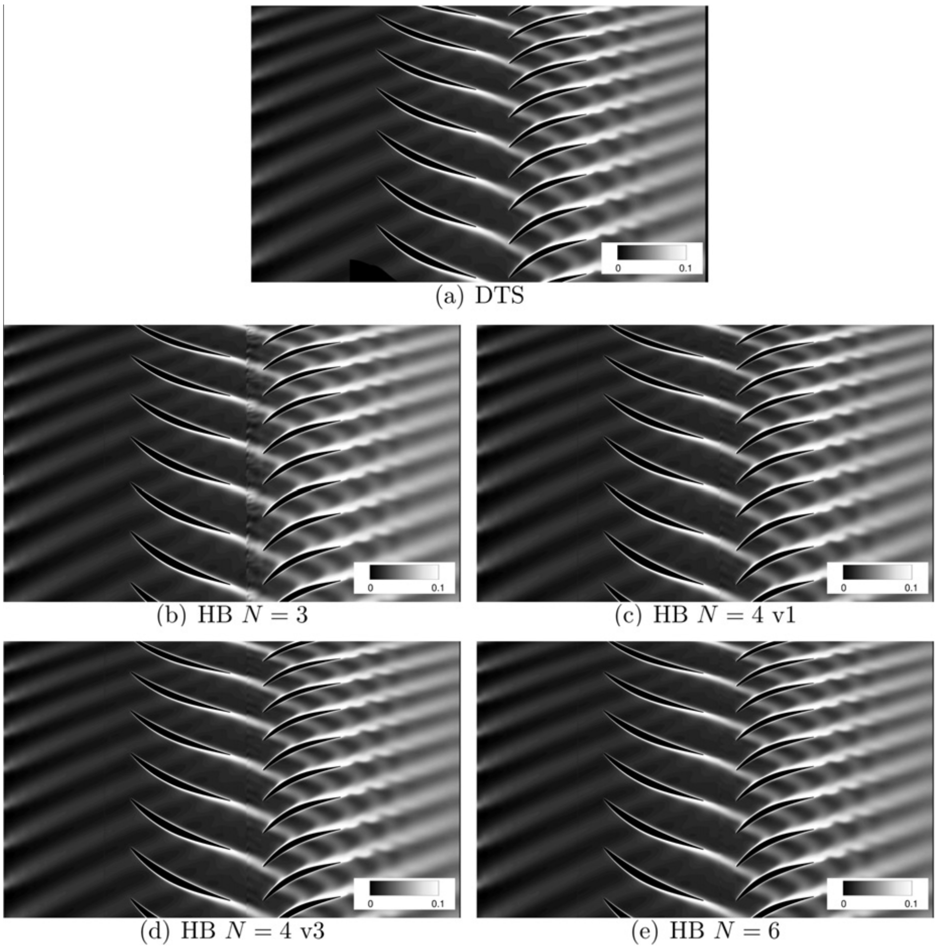

Fig. 18. Comparison of the entropy flow fields at $\eta_{is}^{*} = 1$ and $t = 0$.

isentropic efficiency, the steady curve matches well the one of the DTS, it then diverges to reach around 1% relative error near stall. The isentropic efficiency is more sensitive to the number of frequencies as there is a 1% difference for $N = 3$, which reduces below 0.1% for more frequencies. However, there are not many differences for more than four frequencies. Therefore, in term of global performance, the computations are converged with respect to the frequency content. Four frequencies are

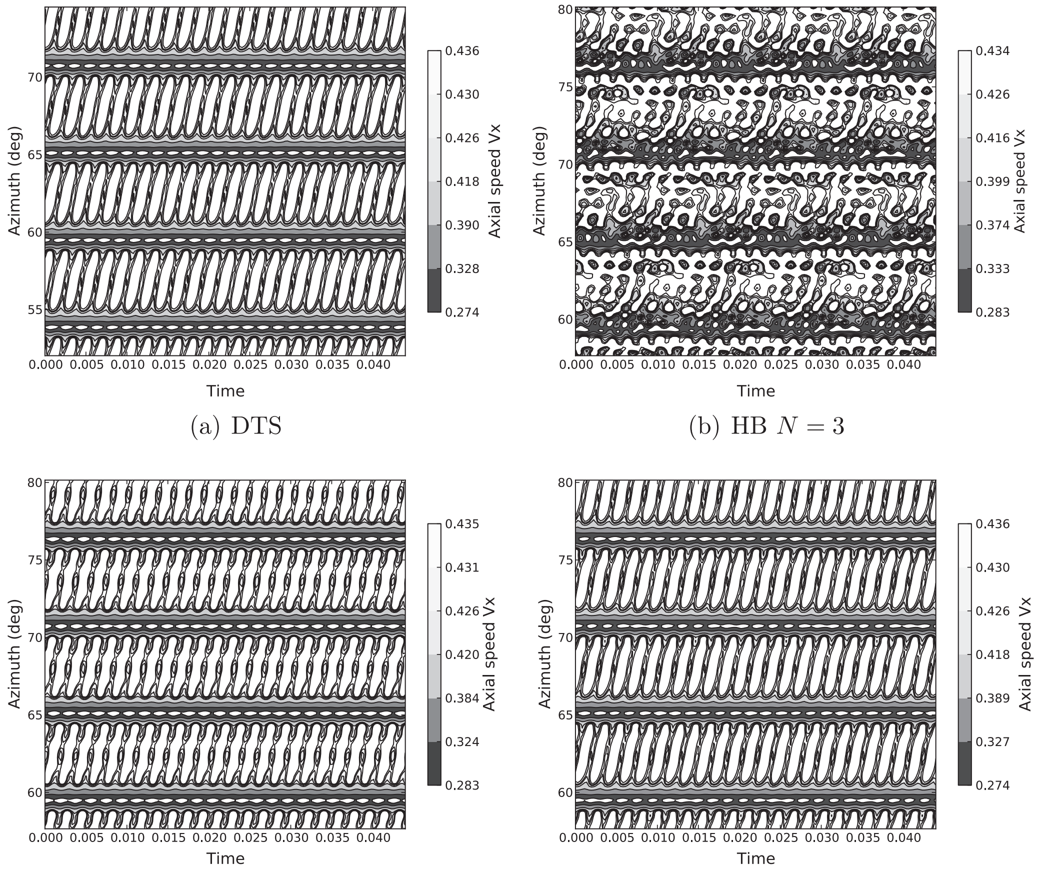

(a) DTS

(b) HB $N = 3$

(c) HB $N = 4$ v1

(d) HB $N = 6$

Fig. 19. Rotor outlet: Azimuth-time map of the non-dimensional axial speed at $\eta_{is}^{*} = 1$.

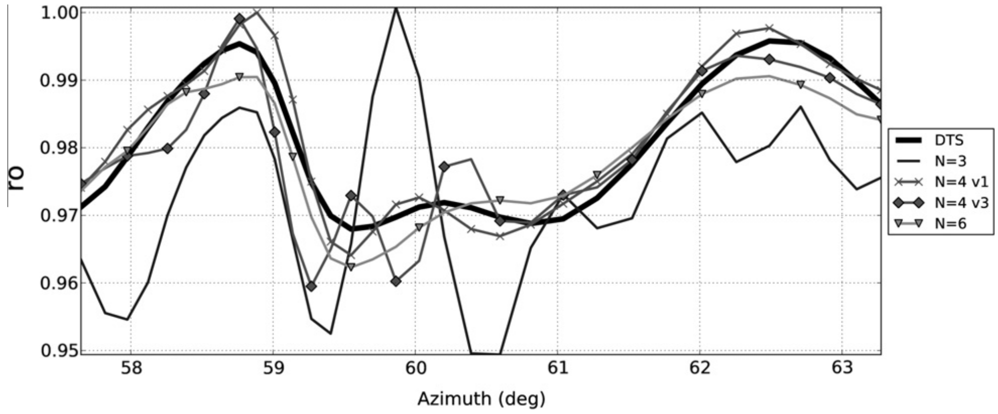

Fig. 20. Rotor exit: Comparison of the azimuthal evolution of non-dimensional ρ at $t = 0$.

consequently a minimum to compute correctly the aerodynamic performance. For clarity reasons and since the HB technique is an unsteady approach, the results from the mixing plane approach will not be plotted anymore.

5.2.2.3. Instantaneous results. Fig. 18 shows the instantaneous entropy flow field for the maximum-efficiency operating point $\eta_{is}^{*} = 1$. For the HB computations, the computed passage is duplicated using phase-lag to check that the azimuthal phase-lag boundary conditions ensure the continuity of the flow field between the original blade passage and the duplicated ones. All the wakes are correctly convected downstream and very few differences can be seen in the different flow fields. Some

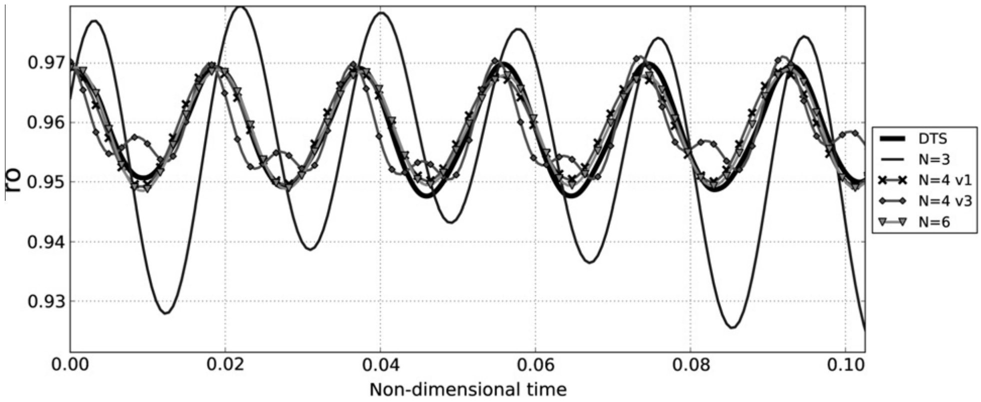

Fig. 21. Rotor outlet: Non-dimensional ρ time signal comparison between DTS and HB at mid pitch.

numerical wiggles can be observed downstream the RM1/RD1 interface, but the higher the number of frequencies, the better the solution, as already shown by Sicot et al. [28].

5.2.2.4. Unsteady results. To analyze the prediction of unsteady row interactions within the rotor, Fig. 19 shows the azimuthal evolution, in the relative frame, of the non-dimensional axial speed downstream of the rotor, as a function of time, for the DTS, HB $N = 3$, HB $N = 4$ v1 and HB $N = 6$ computations. In this diagram, the horizontal bands of low axial speed correspond to the wakes of the rotor itself, which remains steady in the relative rotating frame. The IGV wakes, cropped by the rotor and convected within the passage can also be observed as "oblique strips" of low velocity. Comparing Fig. 19(a) and (b) clearly shows that only three frequencies are not sufficient to reproduce correctly the time and space evolutions of the wakes. The

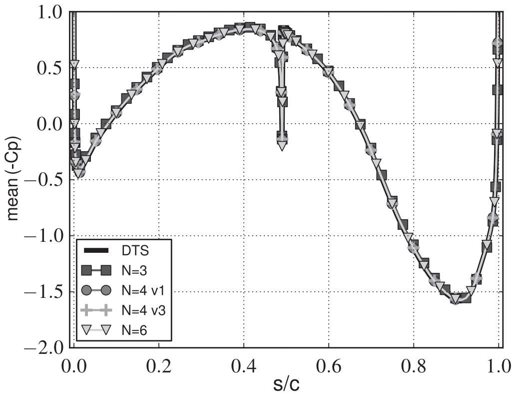

(a) Mean

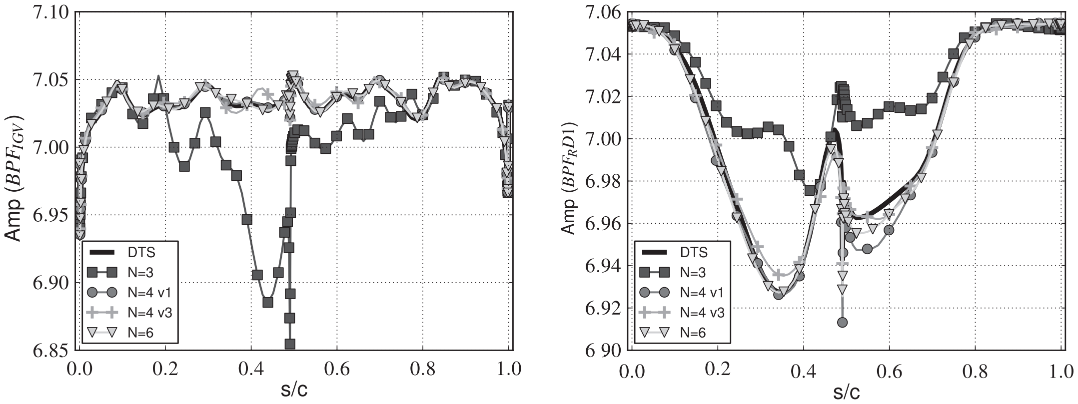

(b) Amplitude evolution of IGV BPF mode

(c) Amplitude evolution of RD1 BPF mode

Fig. 22. Rotor blade: Fourier analysis of C_p for $\eta^*_{is} = 1$.

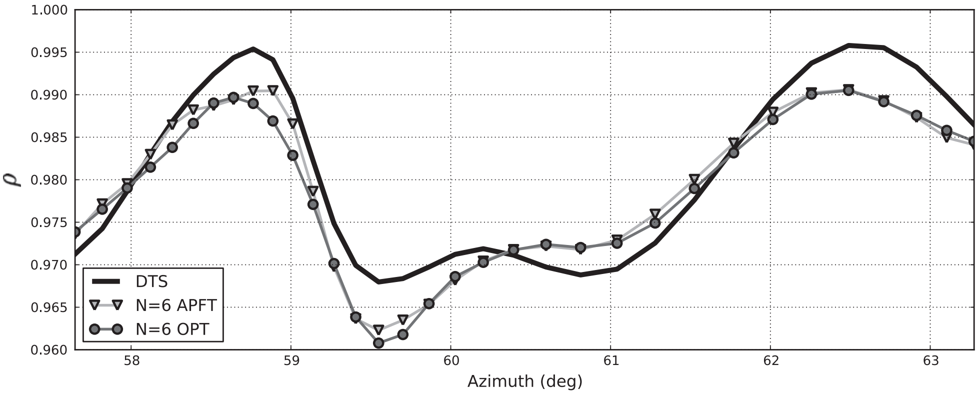

Fig. 23. Comparison of both algorithms for $N = 6$ HB computations at the rotor outlet.

Table 4

Frequency combination coefficients to compute only harmonics of the fundamental blade-passing frequencies.

	n IGV	*n* RM1	*n* RD1	Initialization
$N = 4$ v4	1 0 2 0	1 2 3 4	0 1 0 2	Restart from steady computation 15,000 it. in Roe second order scheme then 10,000 it. in Jameson scheme
$\kappa(A)$ APFT	1.0	2.73	1.0	
$N = 6$ v2	1 0 2 0 3 0	1 2 3 4 5 6	0 1 0 2 0 3	Restart from $N = 4$ v4 5000 it. in Jameson scheme $k_4 = 0.064$ then 5000 it. in Jameson scheme $k_4 = 0.032$
$\kappa(A)$ APFT	1.0	4.03	1.0	

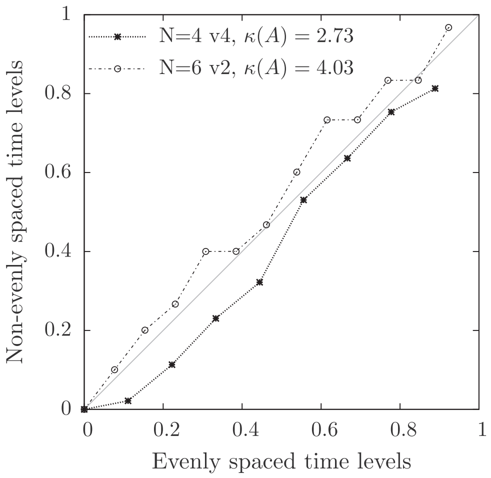

Fig. 24. Distribution of the time levels over the period of the IGV.

four-frequency set (Fig. 19(c)) gets the rotor and IGV wakes clearly visible, but a bit more twisted than in the reference solution. The minimum value is also under-predicted by 3.6%. The six-frequency solution (Fig. 19(d)) has the same features as the four-frequency one, except that the IGV wake is slightly better predicted and the minimum is now correct.

To facilitate comparisons between the different HB frequency sets and the DTS, the azimuthal evolution of the non-dimensional fluid density ρ along a line of constant radius is plotted in Fig. 20 for $t = 0$. This amounts to extracting a vertical line at $t = 0$ in Fig. 19, but this time density was chosen as it is a conservative variable and it is more subject to variations

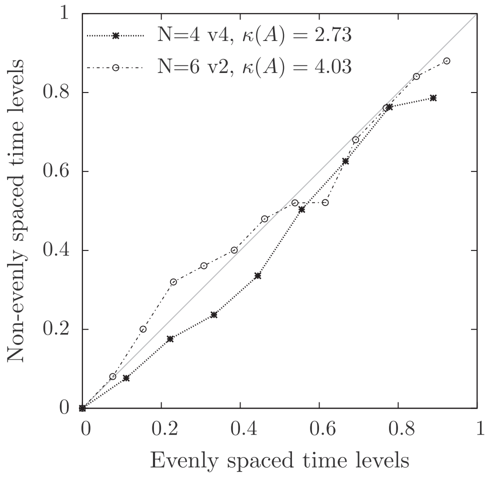

Fig. 25. Distribution of the time levels over the period of the RD1.

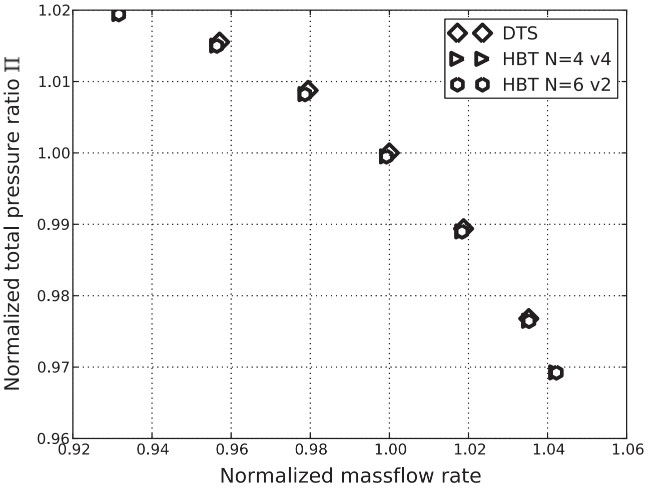

Fig. 26. Non-dimensional total pressure ratio map Π^*.

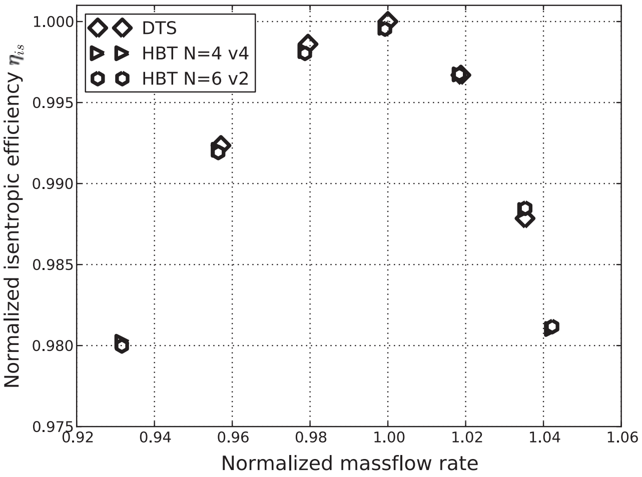

Fig. 27. Non-dimensional isentropic efficiency map η^*_{is}.

than the others. For the sake of clarity, the results for the second four-frequency ($N = 4$ v2) and five-frequency sets are not shown here. The results for three frequencies oscillate around the values of the DTS. Underlying the comments made on the convergence history, the two sets of four frequencies give quite different azimuthal results. Both results for four frequencies

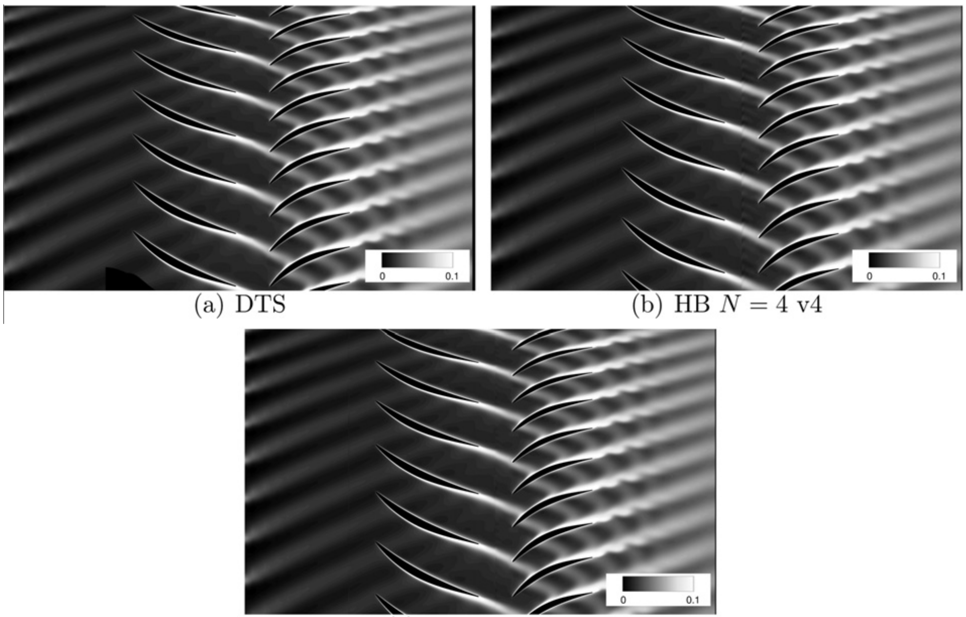

(a) DTS (b) HB $N = 4$ v4

(c) HB $N = 6$ v2

Fig. 28. Comparison of the entropy flow field at $\eta^*_{is} = 1.0$ and $t = 0$.

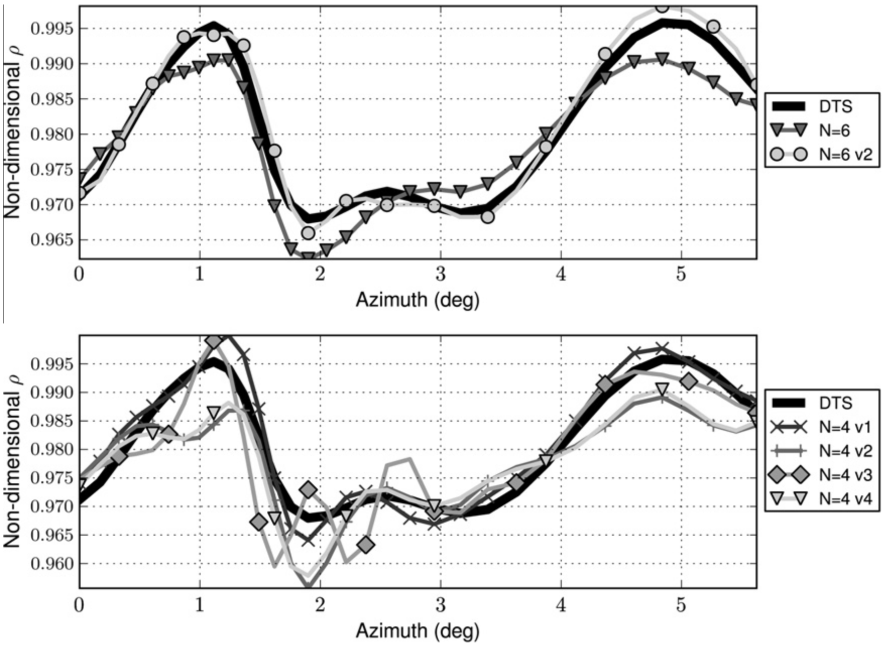

Fig. 29. Comparison of the azimuthal evolution of non-dimensional ρ at $\eta^*_{is} = 1$.

follow the variations of the DTS. The results for the first set of four frequencies are quite fair. Given the quality of the results given by HB $N = 4$ v1, it is surprising that HB $N = 6$ v1 does not perform better since its frequency content is merely an enrichment of HB $N = 4$ v2.

To further analyze unsteady interactions within the rotor, a probe was positioned downstream of the rotor in the middle of the passage. The unsteady density signal is plotted in Fig. 21. For four frequencies, the variations of non-dimensional ρ in time are almost the same and are matching the evolution of the DTS. To have an accurate approximation of the flow field, four frequencies seems to be the minimum required.

The unsteady pressure coefficient C_p at mid-span of the rotor blade is now studied, and the contribution of the upstream and downstream rows are isolated. Fig. 22(a) depicts the mean value on the rotor blade along the normalized curvilinear coordinates for DTS, HB $N = 3$, HB $N = 4$ v1 and HB $N = 6$, whereas (b) and (c) plot the amplitude evolution for, respectively,

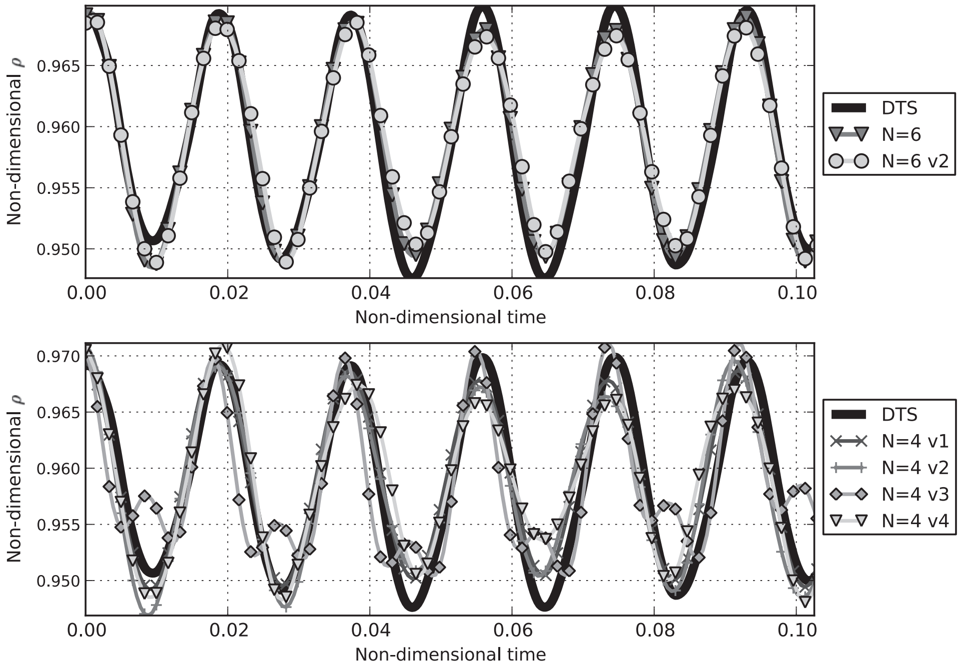

Fig. 30. Comparison of the temporal evolution of non-dimensional ρ at $\eta_{is}^{*} = 1$.

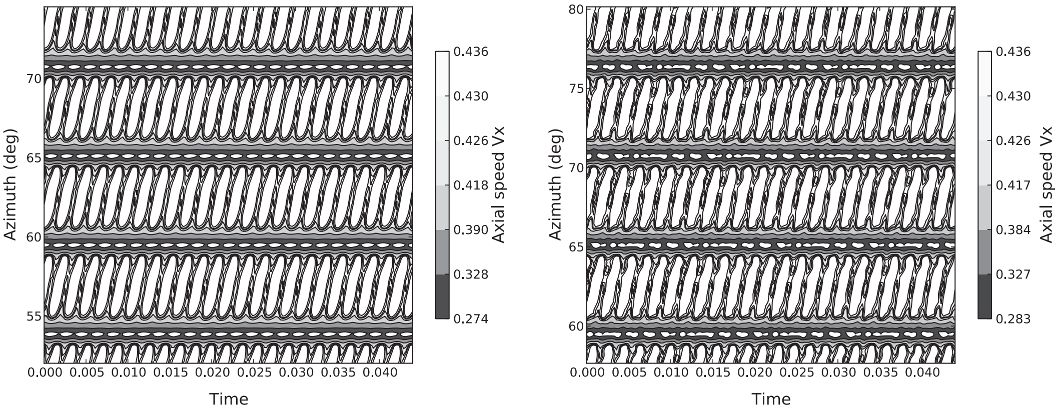

(a) DTS (b) HB $N = 4$ v4

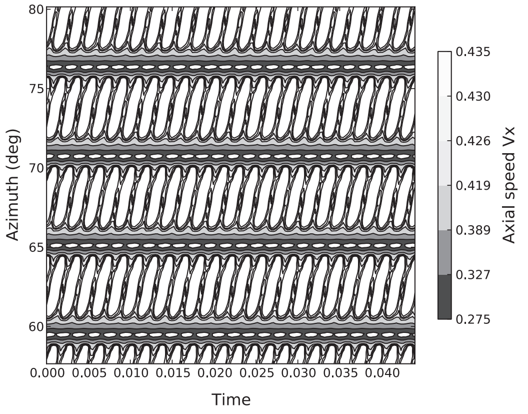

(c) HB $N = 6$ v2

Fig. 31. Azimuth-time map of the axial speed at $\eta_{is}^{*} = 1$.

the upstream and the downstream blade passing frequency. The leading edge corresponds to $s = 0$ or $s = 1$, whereas the trailing edge is located at $s = 0.5$. Between 0.0 and 0.5 is the suction side and between 0.5 and 1 is the pressure side. As shown in Fig. 22(a), three frequencies are enough to capture the mean C_p value around the blade. All four-frequency sets and the six-frequency set fit perfectly the DTS amplitudes for the passing frequency of the IGV blades, except for a wiggle at the end of the suction side. Concerning the amplitudes of the passing frequency of RD1, HB $N = 4$ v1 and HB $N = 6$ correctly predict the suction side and HB $N = 4$ v3 under-predicts the maximum of the amplitude. All frequency sets have trouble predicting the amplitude right after the trailing edge at the pressure side. Surprisingly, it is HB $N = 4$ v3 that is the best match, whereas one would have rather expected HB $N = 6$ to be so.

5.2.2.5. Comparison of the algorithms. Table 3 shows that the condition number $\kappa(A)$ for six frequencies with the APFT algorithm is the highest amongst the chosen frequency combinations. The OPT algorithm allows to reduce $\kappa(A)$ in the rotor from 2.72 to 2.43. Fig. 23 plots the azimuthal evolution of the density for the different algorithms and for six frequencies, along with the evolution of the DTS. The discrepancies are small and are mainly located around 58.6°. Given the closeness of the two harmonic solutions, the APFT algorithm gives, in this case, good enough condition numbers to perform HB computations.

5.2.3. A priori computations: HB computations with only the BPFs of the adjacent rows

The previous computations were made in the ideal case in which the flow spectrum is known *a posteriori*. This allows to choose the frequencies that are the most likely to give the best results. From this standpoint, HB $N = 4$ v1 is an especially good example. However, in practice, one does not have such an information. One solution would be to consider a significant number of harmonics of all rows BPF and their combinations. However the curse of dimension prevents of doing so as the total number of frequencies would quickly be too high. The usual first guess consists in using only the blade passing frequencies of the adjacent rows. This may appear as a great simplication but one has to keep in mind that HB methods are reduced-order models and provide much more information than steady computations, but not necessarily as much as

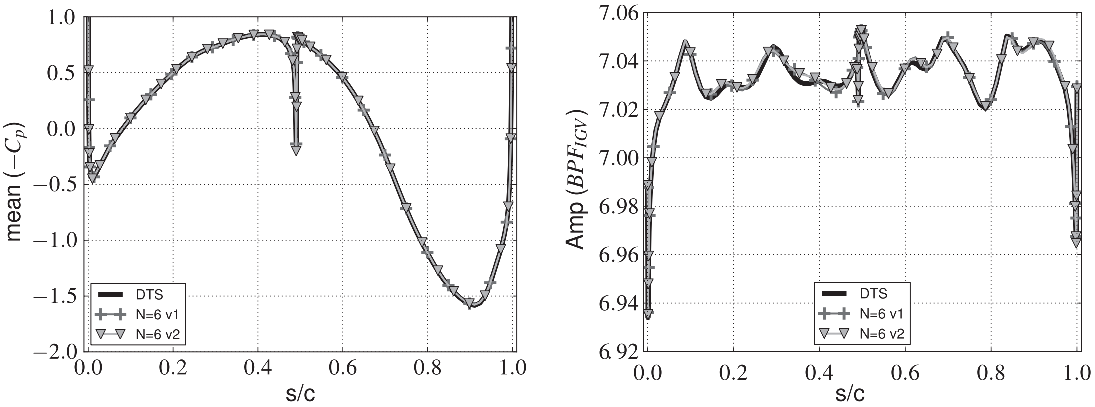

(a) Mean

(b) Amplitude evolution of IGV BPF mode

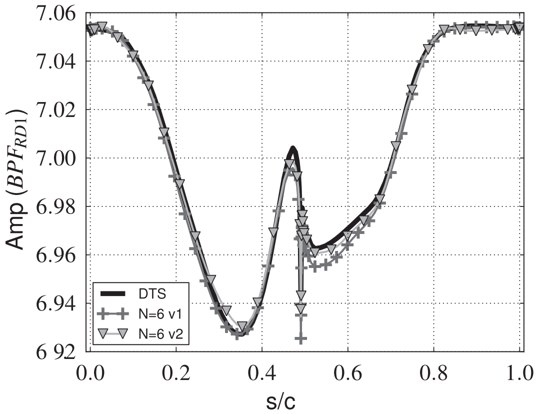

(c) Amplitude evolution of RD1 BPF mode

Fig. 32. Fourier analysis of C_p at $\eta^*_{is} = 1$.

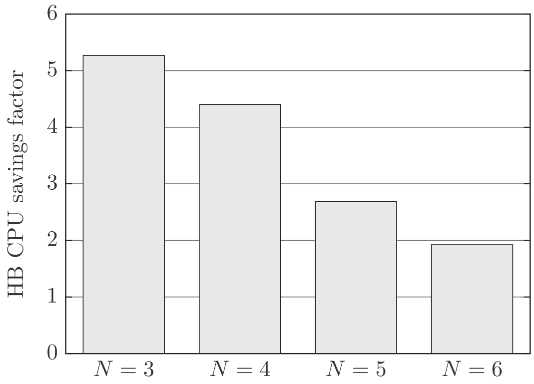

Fig. 33. CPU ratio DTS/HB.

a classical time-accurate computation. This leads to two new sets of frequencies (one of four and one of six frequencies), which are summarized in Table 4.

Figs. 24 and 25 show the associated time distributions found thanks to the APFT algorithm on both base frequencies (BPF_{IGV} and BPF_{RD1}) with the associated condition numbers.

As done previously, the first step consists in checking the aerodynamic values. Figs. 26 and 27 plot respectively the total pressure ratio and the isentropic efficiency for the new frequencies. Regarding both values, the relative error margins are almost the same as in the previous HB computations.

The resulting entropy flow fields for these new frequency sets are shown in Fig. 28. The reference DTS field is also plotted as a reminder in 28(a). They do not show any significant discrepancy with the previous figures. In compliance with the comments made on Fig. 18, some wiggles manifest at the interface RM1/RD1 with HB $N = 4$ v4, but disappear as the number of frequencies is increased. Figs. 29 and 30 compare respectively the azimuthal and temporal evolution of the new frequency sets with the old ones of corresponding number of frequencies. It comes out from Fig. 29 that, in this case, the importance of the blade passing frequencies cannot be denied, since with enough harmonics of the passing frequencies (top) the DTS curve is very well-matched by HB $N = 6$ v2. With fewer harmonics (bottom), HB $N = 4$ v4 behaves like HB $N = 4$ v2.

Fig. 30 shows no noticeable improvement (nor deterioration) of the local time evolution with the change of frequencies.

The time-azimuth maps are given in Fig. 31. The main difference lies the shape of the bubble in the wake of the rotor, which is better captured by the six-frequency set.

The previous figures point that the performances of HB $N = 6$ are not as good as HB $N = 6$ v2. Fig. 32 shows the C_p for both six-frequency sets. The mean value evolution in 32(a) exhibits no difference between the two frequency sets. The same remark can be made for the IGV BPF in 32(b) except for a minor difference at 80% of the suction side. Concerning RD1's BPF in 32(c), HB $N = 6$ v2 gives a better overall match with the DTS than HB $N = 6$ v1 and especially in the last third of the pressure side.

5.2.4. Computational gain

Fig. 33 shows that the HB computations allow a reduction of the CPU cost by a factor 4.5 for four frequencies, the gain being higher with fewer harmonics. However, it should be kept in mind that the reference DTS simulations are done on a $2\pi/16$ periodic sector, whereas practical turbomachinery configurations usually do not have such periodicity, thus requiring simulations on the whole 360° machine. In this case, an additional factor 16 in gain can thus be estimated, suggesting a gain of almost two orders of magnitude. Since the present mesh does not allow multigrid computation, it is also possible to expect a gain even higher as multigrid is a very efficient convergence-acceleration technique for steady computations. This leaves room for further improvements in CPU time reduction.

6. Conclusion

Classical time integration schemes for the Navier–Stokes equations are based on the hyperbolic nature of the problem: the state at a given time step is deduced from the previous one. For periodic flows, this approach is not well suited, as past and future do not have the same meaning. The harmonic balance approach relies on direct and inverse Fourier transforms to turn the time-marching problem into the coupled resolution of several mathematically steady problems representing snapshots of the unsteady solution. When unsteadiness is related to a single (main) frequency and its harmonics, Fourier analysis leads to a natural choice for time instants: they are evenly spaced over the period. In this case, the mathematical problem is numerically well-posed, which means that the conditioning of the operators ensures that the technique converges.

When several arbitrary frequencies are considered, as in multi-stage turbomachines, the HB approach can be theoretically extended, if (and only if) time instants are chosen such that the transformation matrix remains invertible. In the available literature, two approaches based on evenly spaced instants over the shortest period of interest are used: either $2N + 1$ or

$3N+1$ time samples are considered for N frequencies. Oversampling is left away for its higher computational cost and uniform sampling can lead to stability issues. As a consequence, the choice of the time sampling remains a key point.

In this paper, a non-uniform time-sampling approach has been proposed for the time-domain multiple-frequency harmonic balance method. Such an approach is particularly efficient for multiple-harmonics problems where the frequencies are widely separated, thus extending the application range of the method.

It is first demonstrated that the time sampling has a major effect on the stability of the method, due to the condition number of the Fourier transform matrix. To tackle this issue, two algorithms have been derived to find appropriate non-uniform sampling: the APFT algorithm improves the Fourier matrix orthogonality in order to reduce its condition number, while the OPT algorithm directly minimizes the condition number thanks to a gradient-based optimization method.

A channel flow test case with oscillating outlet pressure is then used to demonstrate the ability of the proposed algorithms to accurately capture a flow driven by two coprime frequencies, thus alleviating the stability issues that can arise even for such a simple problem.

Finally, the flow in a multi-stage axial compressor is computed to prove the maturity of the method. It is shown that nonlinear flows can be modeled to engineering accuracy with only four frequencies. This conclusion holds for subsonic flows: when shocks are present, previous studies with the proposed approach have shown that accurate and cost-effective solutions can still be obtained, but at the expense of an increased number of harmonic [4]. In the present case, the HB method is about 70 times faster than a classical time-marching computation over the whole annulus, thanks to the efficient spectral-integration scheme and to the generalized phase-lag boundary conditions. The conclusions obtained for the present quasi-2D case have been extended to 3D geometries without any new assumption [40].

It should be emphasized that the method is still a reduced-order model, as only selected frequencies are computed. In this respect, *a priori* computations using only adjacent rows BPFs are presented, showing good agreement with the reference time-marching solution, which suggests that the HB method can be used in an industrial context. However, full confidence in the HB solution can only be established by comparison with computations using more frequencies, quite similarly to grid independence demonstration.

Another point of interest is the shape optimization of industrial turbomachinery to improve their efficiency. Among other optimization approaches, gradient based optimization techniques using adjoint calculations have become popular for the design of complex systems parameterized by a large number of design variables since the pioneering work of Jameson [46]. However, both computational cost and technical difficulties can be prohibitive for unsteady flows: the adjoint system has to be solved in a reverse way and Navier–Stokes solutions have to be stored during the iterative process. These problems remain for periodic flows with classical time marching integration schemes. With the considered harmonic methods, computing sensitivities is much simpler since the residuals to be derived with respect to the state variables and the mesh nodes coordinates are similar to RANS equations of which adjoint state is classically computed. As a consequence, the computational cost for adjoint sensitivities of such flows is affordable and the overall complexity is finally moderate. Duta et al. [47] have used this technique in the context of aeroelastic turbomachinery design and a wide range of potential applications for the HB method is now opened.

Acknowledgments

The present harmonic balance formulation was developed thanks to the support of the *Direction des Programmes Aéronautiques Civils* (French Civil Aviation Agency) and of the *Aerospace Valley* (Midi-Pyrénées and Aquitaine world competitiveness cluster). The authors would also like to thank Snecma from the Safran group for their kind permission to publish this study.

References

[1] K. Hall, W.S. Clark, C.B. Lorence, A linearized Euler analysis of unsteady flows in turbomachinery, Journal of Turbomachinery 116 (1994) 477–488.
[2] W.S. Clark, K.C. Hall, A time-linearized Navier–Stokes analysis of stall flutter, Journal of Turbomachinery 122 (2000) 467–476.
[3] L. He, Harmonic solution of unsteady flow around blades with separation, AIAA Journal 46 (2008) 1299–1307.
[4] G. Dufour, F. Sicot, G. Puigt, C. Liauzun, A. Dugeai, Contrasting the harmonic balance and linearized methods for oscillating-flap simulations, AIAA Journal 48 (2010) 788–797.
[5] N. Gourdain, L. Gicquel, R. Fransen, E. Collado, T. Arts, Application of RANS and LES to the prediction of flows in high pressure turbine components, in: ASME Turbo Expo, GT2011-46518, Vancouver, Canada, 2011, pp. 1773–1785.
[6] P. Sagaut, S. Deck, Large-Eddy simulation for aerodynamics: status and perspectives, Philosophical Transactions of the Royal Society A 367 (2009) 2849–2860.
[7] L. He, Fourier methods for turbomachinery applications, Progress in Aerospace Sciences 46 (2010) 329–341.
[8] L. He (Ed.), Special Issue: Fourier-based method development and application, International Journal of Computational Fluid Dynamics, in press.
[9] L. He, W. Ning, Efficient approach for analysis of unsteady viscous flows in turbomachines, AIAA Journal 36 (1998) 2005–2012.
[10] W. Ning, L. He, Computation of unsteady flows around oscillating blades using linear and nonlinear harmonic Euler methods, Journal of Turbomachinery 120 (1998) 508–514.
[11] K.C. Hall, J.P. Thomas, W.S. Clark, Computation of unsteady nonlinear flows in cascades using a harmonic balance technique, AIAA Journal 40 (2002) 879–886.
[12] A. Gopinath, A. Jameson, Time spectral method for periodic unsteady computations over two- and three-dimensional bodies, in: 43rd Aerospace Sciences Meeting and Exhibit, AIAA Paper 2005-1220, Reno, USA, 2005.
[13] J. Tyler, T. Sofrin, Axial flow compressor noise studies, Society of Automotive Engineers Transactions 70 (1962) 309–332.
[14] A. Gopinath, E. Van Der Weide, J. Alonso, A. Jameson, K. Ekici, K. Hall, Three-dimensional unsteady multi-stage turbomachinery simulations using the harmonic balance technique, in: 45th AIAA Fluid Dynamics Conference and Exhibit, AIAA Paper 2007-0892, Reno, USA, 2007.
[15] K. Ekici, K.C. Hall, Nonlinear analysis of unsteady flows in multistage turbomachines using harmonic balance, AIAA Journal 45 (2007) 1047–1057.

[16] K. Ekici, K.C. Hall, Nonlinear frequency-domain analysis of unsteady flows in turbomachinery with multiple excitation frequencies, AIAA Journal 46 (2008) 1912–1920.

[17] C.E. Shannon, Communication in the presence of noise, Proceeding of the IRE 37 (1949) 10–21.

[18] E. van der Weide, A. Gopinath, A. Jameson, Turbomachinery applications with the time spectral method, in: 35th AIAA Fluid Dynamics Conference and Exhibit, AIAA Paper 2005-4905, Toronto, Canada, 2005.

[19] M. McMullen, A. Jameson, J. Alonso, Acceleration of convergence to a periodic steady state in turbomachinery flows, in: 39th Aerospace Sciences Meeting and Exhibit, AIAA Paper 2001-0152, Reno, USA, 2001.

[20] M. McMullen, A. Jameson, J. Alonso, Application of a non-linear frequency domain solver to the Euler and Navier–Stokes equations, in: 40th AIAA Aerospace Sciences Meeting and Exhibit, AIAA Paper 2002-0120, Reno, USA, 2002.

[21] M. McMullen, A. Jameson, The computational efficiency of non-linear frequency domain methods, Journal of Computational Physics 212 (2006) 637–661.

[22] F. Sicot, G. Puigt, M. Montagnac, Block-Jacobi implicit algorithms for the time spectral method, AIAA Journal 46 (2008) 3080–3089.

[23] X. Su, X. Yuan, Implicit solution of time spectral method for periodic unsteady flows, International Journal for Numerical Methods in Fluids 63 (2010) 860–876.

[24] M.A. Woodgate, K.J. Badcock, Implicit harmonic balance solver for transonic flow with forced motions, AIAA Journal 47 (2009) 893–901.

[25] S. Antheaume, C. Corre, Implicit time spectral method for periodic incompressible flows, AIAA Journal 49 (2011) 791–805.

[26] L. Cambier, S. Heib, S. Plot, The Onera Elsa CFD Software: input from research and feedback from industry, in: 28th International Congress of the Aeronautical Sciences, ICAS 2012-2.1.1, Brisbane, Australia, 2012.

[27] D. Hassan, F. Sicot, A time-domain harmonic balance for dynamic derivatives predictions, in: 49th AIAA Aerospace Sciences Meeting, Orlando, USA, 2011.

[28] F. Sicot, G. Dufour, N. Gourdain, A time-domain harmonic balance method for rotor/stator interactions, Journal of Turbomachinery 134 (2012) 011001.

[29] A.S. Besicovitch, Almost Periodic Functions, Cambridge University Press, 1932.

[30] K. Kundert, G. Sorkin, A. Sangiovanni-Vincentelli, Applying harmonic balance to almost-periodic circuits, IEEE Transactions on Microwaves, Theory and Techniques 36 (1988) 366–378.

[31] R.H. Byrd, P. Lu, J. Nocedal, C. Zhu, A limited memory algorithm for bound constrained optimization, SIAM Journal on Scientific Computing 16 (1994) 1190–1208.

[32] C. Zhu, R.H. Byrd, P. Lu, J. Nocedal, Algorithm 778: L-BFGS-B: Fortran subroutines for large-scale bound-constrained optimization, ACM Transactions on Mathematical Software 23 (1997) 550–560.

[33] A. Brambilla, Multitone signal harmonic balance method, Electronics Letters 35 (1999) 1809–1810.

[34] P.R. Spalart, S.R. Allmaras, A one-equation turbulence transport model for aerodynamic flows, in: 30th AIAA Aerospace Sciences Meeting and Exhibit, AIAA Paper 92-0439, Reno, USA, 1992.

[35] P.L. Roe, Approximate Riemann solvers, parameter vectors and difference schemes, Journal of Computational Physics 43 (1981) 357–372.

[36] A. Jameson, Time dependent calculations using multigrid, with applications to unsteady flows past airfoils and wings, in: 10th Computational Fluid Dynamics Conference, AIAA Paper 91-1596, Honolulu, USA, 1991.

[37] J.I. Erdos, E. Alznert, W. McNally, Numerical solution of periodic transonic flow through a fan stage, AIAA Journal 15 (1977) 1559–1568.

[38] A. Lerat, Z.N. Wu, Stable conservative multidomain treatments for implicit Euler solvers, Journal of Computational Physics 123 (1996) 45–64.

[39] N. Gourdain, X. Ottavy, A. Vouillarmet, Experimental and numerical investigation of unsteady flows in a high speed three stage compressor, in: Eighth European Turbomachinery Conference, B 107, Graz, Austria, 2009.

[40] F. Sicot, T. Guedeney, G. Dufour, Time-domain harmonic balance method for aerodynamics and aeroelastic simulations of turbomachinery flows, International Journal of Computational Fluid Dynamics (2012) http://dx.doi.org/10.1080/10618562.2012.740021.

[41] B. Lakshminarayana, R. Davino, Mean velocity and decay characteristics of the guide vane and stator blade wake of an axial flow compressor, in: Gaz Turbine Conference and Exhibit and Solar Energy Conference, ASME Paper 79-GT-9, San Diego, USA, 1979.

[42] E. Goncalves, R. Houdeville, Reassessment of the wall function approach for RANS computations, Aerospace Science and Technology 5 (2005) 1–14.

[43] A. Jameson, W. Schmidt, E. Turkel, Numerical solutions of the Euler equations by finite volume methods using Runge–Kutta time-stepping schemes, in: AIAA 14th Fluid and Plasma Dynamic Conference, AIAA-81-1259, Palo Alto, USA, 1981.

[44] B. Van Leer, Towards the ultimate conservative difference scheme. II: Monotonicity and conservation combined in a second order scheme, Journal of Computational Physics 14 (1974) 361–370.

[45] M. Casey, T. Wintergerste, ERCOFTAC Special Interest Group on Quality and Trust in Industrial CFD – Best Practice Guidelines, European Research Community on Flow, Turbulence and Combustion, 2000.

[46] A. Jameson, Aerodynamic design via control theory, Journal of Scientific Computing 3 (1988) 233–260.

[47] M.C. Duta, M.B. Giles, M.S. Campobasso, The harmonic adjoint approach to unsteady turbomachinery design, International Journal for Numerical Methods in Fluids 40 (2002) 323–332.

Journal of Computational Physics 229 (2010) 1425–1447

Contents lists available at ScienceDirect

Journal of Computational Physics

journal homepage: www.elsevier.com/locate/jcp

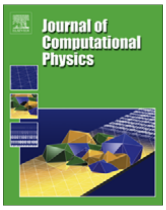

Discretisation of diffusive fluxes on hybrid grids

G. Puigt [a,*], V. Auffray [b], J.-D. Müller [c]

[a] CERFACS, European Center For Research and Advanced Training in Scientific Computations, 42 Avenue Coriolis, 31057 Toulouse Cedex 01, France
[b] ITK, 5 rue de la Cavalerie, 34000 Montpellier, France
[c] Queen Mary, University of London, Mile End Road, London E1 4NS, England, United Kingdom

ARTICLE INFO

Article history:
Received 3 October 2008
Received in revised form 21 October 2009
Accepted 21 October 2009
Available online 10 November 2009

Keywords:
Finite volume
Hybrid mesh
Gradient reconstruction
Consistence
Stability

ABSTRACT

The main approaches of discretising the viscous operator of fluid flow on hybrid meshes are analysed for accuracy, consistence, monotonicity and sensitivity to mesh quality. As none of these approaches is fully satisfactory, a novel method using an approximated finite-element approach is presented and analysed. The methods are compared for the linear heat equation and the Navier–Stokes equations. While the novel approximated finite-element method performs significantly better for the linear heat equation, a stabilised edge-based method performs equally well for the considered test-cases for the Navier–Stokes equations.

1. Introduction

Unstructured tetrahedral meshes have become widespread in use for low and medium Reynolds number flow computations as complex geometries can be meshed with little effort. Many applications in CFD however involve the simulation of high Reynolds number flows with strong shear layers which are best captured on regular and aligned meshes. Typical are the use of hexahedral or prismatic elements in the boundary layer, which significantly increases the accuracy in the presence of very strong gradients normal to the wall. In addition, a hexahedral mesh has fewer elements and edges compared to a tetrahedral one with the same number of nodes. Hence a versatile CFD discretisation needs to be able to perform well on meshes composed of triangles and quadrilaterals in two dimensions, and tetrahedra, pyramids, prisms and hexahedra in three dimensions.

The typical mesh generation algorithms that are currently used add a few further requirements. While irregular meshes can be avoided by switching away from tetrahedra, a discretisation should be able to cope with skewed but regular meshes as often encountered, e.g. along curved boundaries or in turbo-machinery simulations. Hence accuracy should be maintained on parallelograms. High Reynolds number flows involve thin boundary layers which may require element aspect ratios in excess of 1000 for an efficient resolution and a discretisation has to be able to cope with that. The emerging unstructured quadrilateral and hexahedral mesh generation algorithms often produce meshes with irregular cells when coping with complex geometry. Hence a desirable aspect of the discretisation is to maintain accuracy on irregular quadrilaterals and hexahedra.

One can argue that the discretisation of the convective operator in the Navier–Stokes equations on hybrid grids is relatively straightforward, see e.g. Barth [1]. There is a degradation of the accuracy due to poor mesh quality on the one hand and

---

[*] Corresponding author. Tel.: +33 5 61 19 30 94; fax: +33 5 61 19 30 00.
E-mail address: guillaume.puigt@cerfacs.fr (G. Puigt).

0021-9991/$ - see front matter © 2009 Elsevier Inc. All rights reserved.
doi:10.1016/j.jcp.2009.10.037

due to loss of regularity at the hybrid interface on the other [2]. These effects are also present on purely triangular and in particular tetrahedral grids and typically can be dealt with through small amounts of mesh refinement.

On the other hand, the discretisation of the diffusive fluxes on hybrid grids is more difficult and no fully satisfactory approach has been presented to date. This paper seeks to analyse the possible variants for accuracy, consistence, monotonicity and sensitivity to mesh quality using Taylor analysis and positivity. The theoretical results are then tested by applying the best approaches to the linear heat equation and the Navier–Stokes equations.

In Section 2, the test problem is introduced, the discretisation of the convective fluxes is presented and the existing discretisation approaches for the diffusive fluxes are reviewed. Section 3 defines the geometry and recalls the commonly used extension of the convective discretisation to hybrid grids. Section 4 reviews the popular approaches for the discretisation of the viscous operator, while in Section 5 the formulation of four alternative discretisations for the diffusive operators are presented in detail and applied to the heat equation. Their consistence, accuracy, monotonicity and sensitivity to mesh quality is compared and verified in numerical tests. This study is performed using Taylor expansions and only local behaviour is of interest. This choice is motivated by the necessity to recover the desired accuracy on meshes composed of quadrilateral elements. Comparative results for the two useful discretisations for the Navier–Stokes equations are presented in Section 6, followed by concluding remarks in Section 7.

2. Problem description

To analyse the properties of the investigated discretisations, two model problems will be considered: the heat equation and the Reynolds Averaged Navier–Stokes (RANS) equations.

2.1. Heat equation

As a model problem for gradient reconstruction, let us consider the linear heat equation:

$$\frac{\partial T}{\partial t} = \alpha \Delta T, \tag{1}$$

where T is the temperature, α is the constant diffusive coefficient and Δ is the Laplacian. As we consider steady-state applications the derivative with respect to time t is not relevant. In a general framework, defining a control volume C with volume V, a finite-volume semi-discrete scheme can be expressed as:

$$V\left(\frac{\partial T}{\partial t}\right) = \alpha \int_{\partial C} \nabla T \cdot n \, ds, \tag{2}$$

where ∂C represents the boundary of volume C and n is the outward local unit vector, normal to ∂C.

2.2. Navier–Stokes equations

The compressible Navier–Stokes equations for air, which is assumed as a perfect gas, are written in the following compact conservative form (Eq. (3)):

$$\frac{\partial W}{\partial t} + \nabla \cdot F(W) = \nabla \cdot D(W, \nabla W), \tag{3}$$

where W represents the vector of conservative variables $(\rho, \rho U, \rho E)^T$ with the density ρ, the total energy E and the velocity vector U. $F(W)$ represents the convective operator and $D(W, \nabla W)$ represents the diffusive operator which depends on gradients of the variables. Introducing the pressure p and the total energy $E = e + 1/2\|U\|^2$ which is the sum of internal and kinetic energies, the Euler fluxes F and the viscous fluxes D are defined by:

$$F = [\rho U, \rho U \otimes U + pI, U(\rho E + p)]^T, \quad D = [0, \mathbf{S}, \mathbf{S} \cdot U - q]^T. \tag{4}$$

$\mathbf{S}$ is the stress tensor which becomes for a Newtonian fluid

$$\mathbf{S} = \mu\left(\nabla U + \nabla U^T - \frac{2}{3} \nabla \cdot U \mathbf{I}\right). \tag{5}$$

The molecular viscosity μ is a function of the temperature T through the Sutherland's law:

$$\mu = \mu_0 \left(\frac{T}{T_0}\right)^{\frac{3}{2}} \frac{T_0 + C_s}{T + C_s} \quad \text{with } C_s = 110.4\ \text{K}, \tag{6}$$

where μ_0 is the molecular viscosity at the reference temperature T_0. The heat flux q is modeled by the Fourier's law:

$$q = -\lambda \nabla T \quad \text{with } \lambda = \frac{C_p \mu}{Pr}, \tag{7}$$

where T is the temperature and λ is the thermal conductivity. The Prandtl number is $Pr = 0.72$ and C_p is the heat capacity at constant pressure. Finally, the equations are closed by the perfect gas law $p = \rho RT$ with $R = 287$ J/kg K.

Applying the standard finite-volume integration to Eq. (3) on a control element C with volume V, one finds

$$\frac{d}{dt}\int_C W\,dv + \int_{\partial C} F(W)\cdot n\,ds = \int_{\partial C} D(W,\nabla W)\cdot n\,ds, \tag{8}$$

with n being the unit outward normal to the dual volume boundary ∂C. The volume flux integrals have been converted to surface integrals using the Green–Gauss theorem.

3. Discretisation

Let $\{\tau_i,\ i = 1, N_\tau\}$ denote the N_τ elements of the mesh. These elements are triangles and quadrilaterals in two dimensions or tetrahedra, prisms, pyramids and hexahedra in three dimensions. From now on, this mesh will be called the 'primal' mesh and its elements will be denoted as the 'primitive' elements. In the vertex-centred finite-volume approach considered here, the flux balance is evaluated on a dual mesh composed of cells C_i around mesh nodes i.

3.1. Definition of dual cells for a hybrid mesh

The well-known extension of the definition of the median dual volume from simplex to primitive elements introduced by Dervieux [3] for the Euler equations and by Rostand and Stoufflet [4] for the Navier–Stokes equations is adopted here (Fig. 1). Hence, in two dimensions, the volume around a mesh node is limited by 'facets' linking the midpoints of the edges in the primal mesh to the barycentres of the elements obtained by arithmetic averaging of the nodal coordinates. In three dimensions, the dual volume is delimited by triangular facets between the edge midpoints, the face barycentres and the element barycentres.

3.2. Computation of convective fluxes

The extension of the convective flux computation to hybrid meshes is well-known, e.g. following [1], and reported here for completeness. For the Navier–Stokes equations, the convective fluxes F in Eq. (8) are computed with upwind schemes based on approximated Riemann solvers [5] at the dual interface. For the first-order convection scheme, the extension to hybrid meshes is straightforward since the only required quantities are the flow states W_i and W_j at the left and right hand sides of the interface, respectively, the edge-normal and the surface area. The edge-normal for a mesh edge ij is the sum of both facets attached to that edge as shown in Fig. 2.

Second-order accuracy is obtained by using a MUSCL-like extension [6–8] which involves a combination of upwind and centred gradients. More precisely, let ∇W_i be an approximation of the gradient of W at node i. For edge ij between nodes i and j, a second-order accurate convection scheme is obtained by replacing the states W_i and W_j by the states W_{ij} and W_{ji}, respectively. They are defined by:

$$\begin{cases} W_{ij} = W_i + 0.5\Phi(\beta\nabla W_i\cdot ij, (1-\beta)(W_i - W_j)), \\ W_{ji} = W_j + 0.5\Phi(\beta\nabla W_j\cdot ij, (1-\beta)(W_j - W_i)). \end{cases} \tag{9}$$

In Eq. (9), Φ is a slope limiter and computations were performed using a Van Albada-type limiter [9]. The positive constant β represents the amount of up-winding and is chosen here as $\beta = 2/3$. The gradient ∇W_i at node i is evaluated using Green–Gauss integration over the dual volume. Therefore, the same approach as in the simplex case in adopted and the numerical extension to hybrid grids does not present any particular difficulties. However, the weakness of the approach remains for non-simplex elements and for distorted cells, second-order of accuracy may be lost.

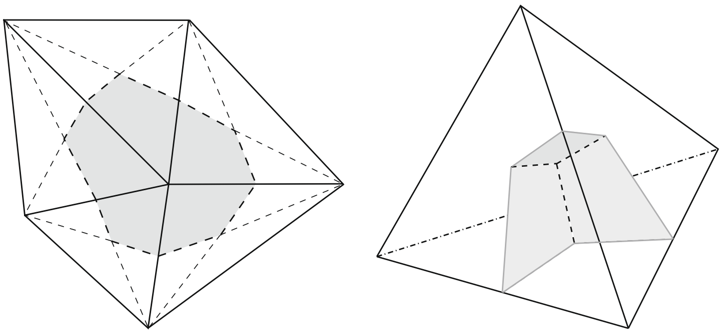

Fig. 1. Definition of the dual volume on a triangular mesh (left) and boundary of the dual volume inside a tetrahedron (right).

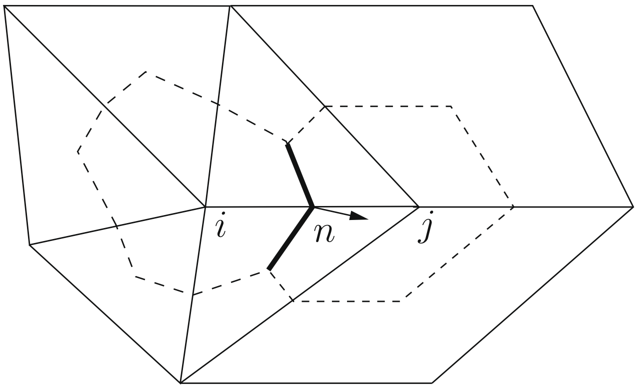

Fig. 2. Convection flux computation: definition of the surface and of the unit normal vector *n* for edge *ij*.

3.3. Computation of diffusive fluxes on simplices

On triangular and tetrahedral meshes, the standard P^1 finite-element discretisation induces a constant gradient over the element and a conservative scheme is built with the a "good" choice for diffusion coefficients. Moreover, following the definitions summarised in [10], a local analysis based on Taylor expansion shows that the P^1 finite-element discretisation is weakly consistent on any mesh composed of equilateral triangles. On the set of primitive mesh elements $E(i)$ containing node i, the diffusive term of Eq. (8) can be written as

$$\int_{\partial C_i} D(W,\nabla W)\cdot n\,ds = \sum_{T\in E(i)} \int_{\partial C_i\cap T} D(W,\nabla W)\cdot n\,ds. \tag{10}$$

The P^1 finite-element approach leads to a constant gradient on any simplex mesh element and for a diffusion term D which depends linearly of ∇W, the gradient can be factored out of the integral over $\partial C_i \cap T$. Billey et al. [11] demonstrated the equivalence of piecewise-constant finite-volume and P^1-Galerkin finite-element discretisation on a simplex mesh composed of triangles and Barth [1] gave a simple edge-based expression for the right hand side of Eq. (10).

However, the equivalence of these finite-volume and finite-element discretisations does not extend to non-simplex primitive elements. There is a range of possible discretisations for the viscous operator on hybrid grids with very distinct properties. An overview of existing methods is presented in the next section.

4. Computation of diffusive fluxes on non-simplex elements

A number of possible discretisations of the viscous terms on hybrid unstructured meshes have been presented in the literature.

4.1. "Edge-based" methods

Mavriplis and Venkatakrishnan [12] proposed an approach that consists of using the "thin shear layer" assumption in order to neglect cross-derivative terms, replacing the viscous term in the Navier–Stokes equations by the Laplacian. For a node i, this reduces the stencil to all the nodes j connected by an edge to node i and the diffusive flux balance on the dual cell can be split into edge contributions. This constitutes an advantage for the implementation in the popular edge-based framework [1,13] as contributions for convective and viscous fluxes can be computed in loops over edges only.

Haselbacher et al. [14] applied the edge-based discretisation of Mavriplis and Venkatakrishnan [12] to reconstruct the normal gradient component and a Green–Gauss formula to reconstruct the tangential gradient component. Numerical tests lead to the conclusion that the tangential component can be neglected without losing accuracy. This method is then equivalent to the "thin shear layer" assumption.

Instead of using the "thin shear layer" assumption, Galle [15] proposed to reconstruct the gradient at vertex i by a Green–Gauss formula applied on the dual cell C_i. The flux is then computed at mid-edge. He could show good agreement between computed and experimental results. Crumpton et al. [16] added a corrective term to the flux expression to improve stability on high aspect-ratio meshes. However, Eymard et al. [17] showed that this approach is second-order accurate only on a mesh composed of regular parallelograms. In conclusion, this approach is very simple and converges well but is only first-order accurate on irregular meshes.

4.2. “Cell-vertex” methods

In cell-vertex methods, a flux residual is computed over the primitive elements and is then distributed to each vertex using appropriate weights [18]. The stencil is compact and the scheme is linear preserving, i.e. second-order accurate. However, the scheme is not monotone on primitive elements and the use of an artificial viscosity model is required, which in turn reduces accuracy and may violate conservation.

Crumpton et al. [18] proposed three different gradient reconstructions defined in Fig. 3. The first one computes the NS and WE gradient components at node *i* (Fig. 3(a)). The reconstruction is simple but second-order accurate only on regular meshes. The second technique computes gradients on the primitive elements and interpolates the primitive element gradients to the mesh nodes (Fig. 3(b)). This approach is second-order accurate on meshes composed of parallelograms. Colin [19] showed that the scheme is not monotonic. Rudgyard [20] introduced a corrective term in the gradient expression to damp oscillatory chequer-board modes. The scheme is then monotonic but not conservative. Another variant of gradient reconstruction [21,22] consists of defining a control volume around each edge (diamond cell) and in applying a Green–Gauss formula (Fig. 3(c)). This method is shown to be inconsistent on stretched meshes [23].

Coirier [23] conducted an expansive and thorough study of the properties of discretisations of the viscous operator for regular, stretched and adaptive Cartesian meshes. In a cell-centred approach, he analysed the numerical behaviour of methods based on a Green–Gauss gradient reconstruction and methods based on a polynomial gradient reconstruction. The study revealed that the natural Green–Gauss reconstructions all lead to decoupled stencils which results in convergence problems.

Coirier also considered linear and quadratic reconstructions combined with a linear numerical scheme and found that the choice of the support volume is not straightforward. Only the quadratic approach reaches second-order accuracy but positivity is not guaranteed and the large required stencil leads to an ill-conditioned system for the polynomial coefficients. Studying in particular positivity and consistence, he concluded that it is impossible to define a general scheme for irregular meshes that is at the same time positive and consistent. He compared an accurate but not positive scheme to a positive but less accurate one. The study showed that both properties are important as they have a strong influence on convergence and stability.

Recently, Lipnikov et al. [24] proposed a new numerical scheme for general diffusion in two-dimension. Compared with Coirier’s approach, the new scheme does not need any interpolation at mesh nodes and the numerical flux is more complicated. Actually, for each surface S between two cells C_i and C_j, the flux for a quantity U is a linear combination of contributions from cells C_i and C_j and the weights depend both on the cells geometry and on U, leading to a non-linear numerical scheme. Second-order of accuracy is guaranteed since the scheme is exact for linear and piecewise-linear solutions.

Despite the problems raised by Coirier about Green–Gauss gradient reconstruction, Khawaja [25] applied the Green–Gauss method to model turbulent flows on meshes composed of tetrahedra and prisms (subsonic flat plate, transonic flow over ONERA M6 wing, supersonic flow over HSTC aircraft, etc.). He obtained numerical results in close agreement with the experimental data.

Peroomian et al. [26] used a polynomial gradient reconstruction coupled with slope limiters to avoid oscillatory phenomena. The method does not seem to be completely satisfactory since slope limiters must be applied either to the conservative or to the primitive variables, depending the case.

4.3. Tessellation-like methods

A novel method for hybrid meshes was presented recently by Papin [27].

Papin uses the nodes of the primal mesh and the barycentres of faces and elements to define for each facet of the dual volume one specific triangle or tetrahedron, a “third mesh element”, which contains that facet. As each third mesh element is a simplex, a constant gradient is defined using Green/Gauss integration or the equivalent standard P^1 finite-element approach. The proposed method is not a classical tessellation method since the facets of the dual volume are unchanged: the

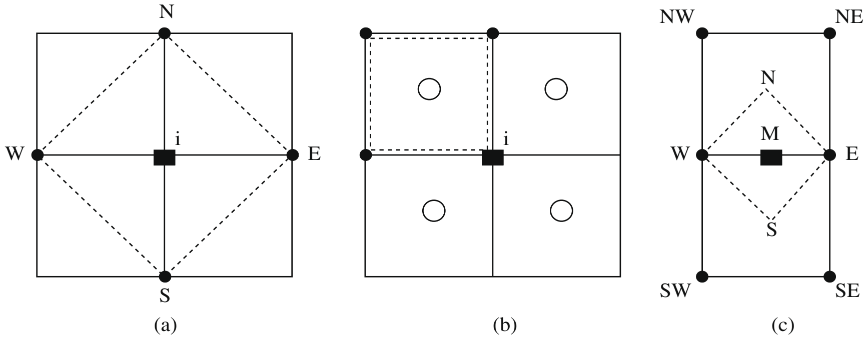

(a) (b) (c)

Fig. 3. Gradient reconstruction techniques (a) directly at node *i*, (b) from the element centroids and an interpolation, (c) edge-based approximation.

third mesh is only used to construct the gradient for the viscous flux computation. An example of a third mesh element used by Papin is given on Fig. 4.

The main interest of this technique is that the diffusive flux can be computed straightforwardly on this third mesh using the standard finite-element approach for simplex elements. Papin has shown that the third mesh elements can be obtained on any convex initial mesh. Second-order accuracy, conservation and consistence are obtained on regular parallelograms. Monotonicity is only obtained on rectangles. However, the scheme is computationally expensive since additional gradient evaluations are needed, such as in the barycentre of each element. Moreover, for meshes composed of elements with high aspect-ratio such as in a boundary layer, the third mesh elements can be of very poor quality.

4.4. "Discontinuous Galerkin" approach

Another kind of method is based on the Discontinuous Galerkin (DG) technique. The DG technique was first introduced by Reed and Hill in 1973 [28] for neutron transport and by Nitsche [29] in 1971 for the approximation of elliptic equations. Following the work of Cockburn and Shu [30] in 1989, several authors have worked on this technique for the last decades.

The DG method uses a piecewise polynomial data representation over the element that allows discontinuities at the cell interfaces. A DG method if limited to only piecewise-linear data and a second-order MUSCL finite-volume method [31] have the same data representation. However, while the MUSCL method reconstructs the gradients from the conservative flow field, the DG method solves a transport equation for the unknown cellwise gradient. Hence, as opposed to a piecewise-linear finite-element approach with a continuous reconstruction [1], a full DG diffusion scheme cannot be simply implemented within the context of a MUSCL-based finite-volume method, however, a finite-volume viscous flux approximation could take inspiration from the DG formulation of the viscous flux limited to P^1 elements only. The aim to achieve would be to exploit the discontinuous representation to arrive at an accurate and consistent flux formulation for steep gradients over very few mesh points, similarly to the resolution of shock waves with shock-capturing finite-volume schemes.

The DG discretisation of the diffusive flux is presented here for completeness and to stimulate further development, we do not aim to present an exhaustive discussion here. The reader is referred to the broad summary of Arnold et al. [32].

Zhang and Shu [33] use Fourier analysis to show that simple Taylor analysis as performed by the present authors can produce misleading results for DG discretisations of the diffusion equation.

As our aim is to develop a viscous approximation that can be used transparently with the existing popular MUSCL-based finite-volume discretisations, we focus on two approaches closest to the finite-volume method.

The approach presented by van Leer and Nomura [34] in 1D performs a smooth reconstruction at the cell interfaces. A particular choice of approximation to the interface terms based on physical reasoning leads to a conservative stabilisation term which is of $O(1/\Delta x)$ and which had not been presented in the unified formulation of Arnold et al. [32].

Gassner et al. [35] derive a solution for a diffusive generalised Riemann problem leading to a space–time formulation for the convection–diffusion equation. To achieve second-order accuracy within a finite-volume method a polynomial reconstruction of order 3 would be required, which does not easily fit within the framework of existing finite-volume MUSCL methods. Second-order accuracy can only be achieved within a DG framework that formulates an adjoint-consistent update equation for the gradient [35].

4.5. Summary

This overview demonstrated the difficulties in defining a numerical scheme for hybrid meshes that is consistent, conservative, sufficiently accurate, positive with a good convergence property and with a reasonable computational cost. In the next section, we shall analyse four of the most promising approaches and evaluate their performance for the heat equation.

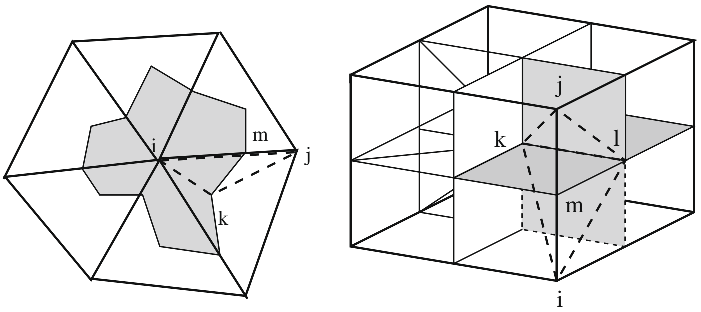

Fig. 4. Left hand side: triangle *ijk* is used for the computation of the flux on dual cell facet *mk*. Right hand side: tetrahedron *ijkl* is needed for the computation of the gradient for flux balance on facet *klm*.

5. Comparison of four discretisations for the diffusive operator and application to the heat equation

5.1. Notations

All explanations are based on the notations introduced in Fig. 5 in a two-dimensional context. In the following, let $N(i)$ be the set of nodes j that are linked to node i through the mesh edge ij and let $\tau(i)$ be the set of mesh elements τ formed with node i. The dual cells C_i and C_j around nodes i and j, respectively, share the interface $\partial C_{ij} = \partial C_i \cap \partial C_j$. The facets of the dual volume C_i around node i that lie within the primal mesh element τ are $\partial C_i \cap \tau$ and have the outward normal n_i^τ.

5.2. Necessary properties

An efficient numerical method should satisfy the following properties [1]:

(i) consistence,
(ii) conservation,
(iii) monotonicity,
(iv) second-order accuracy,
(v) insensitivity of precision and convergence to deterioration in mesh quality,
(vi) compact support.

Property (ii) is necessary to ensure a global mass conservation. Even if this point is not so clear for a perfect gas solver, conservation of the solver guarantees that mass fractions are bounded during the computation of multi-species flows with chemical reactions. A monotone discretisation (iii) ensures that the solution observes a maximum principle, which is required on the one hand for bounded fields in turbulence modelling and multi-species flows, and on the other hand for good stability and good convergence rates. Compact support (vi) is important for effective parallelisation and for resolution of the highest frequency modes.

Local analysis of consistence is conducted using Taylor analysis and monotonicity is analysed by a positivity argument [1]. These properties are analysed in the following for an edge-based discretisation, a cell-vertex discretisation the standard finite-element method and a novel approximated finite-element method based on nodal gradients.

5.3. The edge-based approach

As an example for an edge-based discretisation, we shall start from Galle's formulation [15]. The principle is to define a gradient at node i by integration over the dual cell boundary associated with node i, assuming linear variation of T along each edge:

$$\nabla T_i = \frac{1}{V_i} \iint_{\partial C_i} T n \, ds = \frac{1}{V_i} \sum_{j \in N(i)} \frac{T_i + T_j}{2} \iint_{\partial C_{ij}} n \, ds. \tag{11}$$

The gradient at ∂C_{ij} is then taken as the mean value of the gradient at nodes i and j:

$$\nabla T_{ij} = \frac{\nabla T_i + \nabla T_j}{2}. \tag{12}$$

Finally, the stability is improved with Crumpton's correction [16] for the interface gradient:

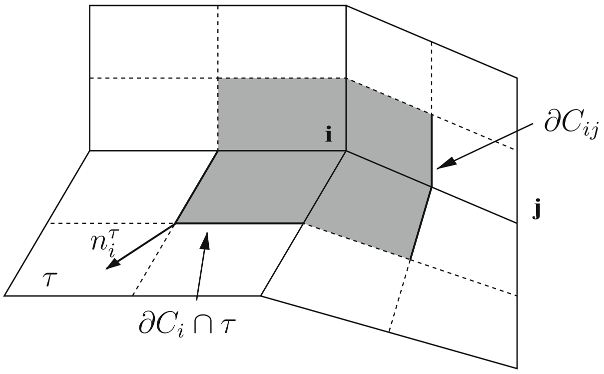

Fig. 5. Definition of sub-surfaces of the dual cell C_i around node i.

$$\nabla T_{ij}^{corr} = \nabla T_{ij} - \left(\nabla T_{ij} \cdot \delta_{ij} - \frac{T_j - T_i}{\|x_j - x_i\|}\right)\delta_{ij}, \tag{13}$$

with

$$\delta_{ij} = \frac{x_j - x_i}{\|x_j - x_i\|} \tag{14}$$

and $x_i,\ x_j$ representing the coordinates of vertex $i,\ j$, respectively.

Using Eqs. (12), (13) and the definition of δ_{ij} (Eq. (14)), the scheme is shown to be conservative. The discretisation is consistent, monotonic and second-order accurate on rectangular meshes only [36]. On regular parallelograms, the discretisation is consistent and second-order accurate.

A truncation error analysis on arbitrary quadrilaterals demonstrates a first-order error. Moreover, in this case, the method is neither consistent nor monotone. In the following, the method will be denoted “EB”.

5.4. The cell-vertex approach

As an example of the cell-vertex approach, let us consider the approach proposed by Crumpton et al. [18], Fig. 3(b). Applying the Green–Gauss theorem, one obtains a constant gradient for each primal mesh element:

$$\nabla T^{\tau} = \frac{1}{V_i}\iint_{\partial\tau} T n\, ds, \tag{15}$$

where τ is an element of the primal mesh. The diffusive flux at node i is then computed from:

$$\alpha \iint_{C_i} \nabla T \cdot n\, ds = \alpha \sum_{\tau\in\tau(i)} \nabla T^{\tau} \cdot n_i^{\tau}. \tag{16}$$

This formulation is easy to implement and is interesting because the cell gradient is also required for the computation of convective terms in cell-vertex methods [37], resulting in computational savings. Truncation error analysis shows that the numerical scheme is second-order accurate and consistent on meshes composed of parallelograms [36]. On meshes composed of other types of elements, consistence has not been demonstrated. However, the stability analysis reveals that the discretisation is not monotone and oscillatory solutions can develop. To avoid these spurious chequer-board modes, a correction similar to the one for the edge-based method (Eq. (13)) is added to the gradient expression [20]. The stabilised flux expression becomes:

$$\alpha \iint_{C_i} \nabla T \cdot n\, ds = \alpha \sum_{\tau\in\tau(i)} \nabla T_i^{\tau} \cdot n_i^{\tau}, \tag{17}$$

with the following gradient expression:

$$\nabla T_i^{\tau} = \nabla T^{\tau} - \delta_c \left(\nabla T^{\tau} \cdot \delta s_i - \frac{(T^{\tau} - T_i)}{\|x^{\tau} - x_i\|}\right) \cdot \delta s_i. \tag{18}$$

∇T^{τ} is defined by Eq. (15), δ_c is a modelling parameter, T^{τ} is the mean value of T on $\tau,\ x^{\tau}$ the centroid coordinates and δs_i is defined by:

$$\delta s_i = \frac{x^{\tau} - x_i}{\|x^{\tau} - x_i\|}. \tag{19}$$

This correction introduces a modification of the gradient in the direction of the “diagonal” of the element and this correction makes the formulation non-conservative.

A theoretical analysis that takes into account this correction (Eq. (18)) shows that the scheme is consistent on regular rectangular meshes only and that the discretisation is monotonic if the value for δ_c is chosen in an interval which depends on the mesh geometry [36]. In two dimensions and for a quadrilateral element denoted $ABCD$ with diagonals of length AC and BD and with area $\mathcal{A},\ \delta_c$ must satisfy:

$$\frac{|AB^2 - AC^2|AC^2}{2\mathcal{A}} < \delta_c < \frac{BD^2 AC^2}{2\mathcal{A}}. \tag{20}$$

In the following, the method will be denoted “CV”.

5.5. Finite-element reconstruction approach

As an alternative to both previous formulations, the P^1 finite-element method can be extended to primitive elements: the idea is to reconstruct the gradient using the finite-element basis functions of the specific element class. One of the advantages of this approach is that the method reverts to the P^1 formulation on simplex elements, which is popularly used.

The gradient at any point (x, y) of an element τ can be evaluated with the finite-element approach:

$$\nabla T(x,y) = \sum_{k \in S^\tau} T_k \nabla N_k^\tau(x,y), \tag{21}$$

where (x, y) are the coordinates of a point which belongs to element τ of the primal mesh. N_k^τ denotes the shape function of element τ associated with node k and S^τ is the set of nodes of τ. The gradient computation is therefore transferred to the evaluation of the shape function gradients. The computation of the shape function gradient is based on the transformation to iso-parametric coordinates.

As an example, one may consider in two dimensions the integration of the flux on $\partial C_A \cap \tau$ where C_A is the dual cell around node A and τ is the quadrilateral $ABCD$, as described on Fig. 6.

Using the Jacobian transformation J^τ from original (x, y) to iso-parametric (ξ, η) space, the numerical flux I becomes

$$I = \int_{\partial C_A \cap \tau} \alpha \nabla T \cdot n\,dl = \int_{\partial C_A \cap \tau} \alpha \left(\sum_{i=1}^{4} T_i \nabla_{xy} N_i^\tau \right) \cdot n\,dl = \int_{\partial C_A \cap \tau} \alpha \left(\sum_{i=1}^{4} T_i [J^\tau]^{-T} \nabla_{\xi\eta} N_i^\tau \right) \cdot n\,dl, \tag{22}$$

where J is the Jacobian matrix associated with the transformation from (x, y) space to (ξ, η) one. Using the transformation (Fig. 6), $n\,dl$ becomes:

$$n\,dl = \begin{pmatrix} -dy \\ dx \end{pmatrix} = \begin{pmatrix} -\frac{\partial y}{\partial \xi}(\xi,\eta)d\xi - \frac{\partial y}{\partial \eta}(\xi,\eta)d\eta \\ +\frac{\partial x}{\partial \xi}(\xi,\eta)d\xi + \frac{\partial x}{\partial \eta}(\xi,\eta)d\eta \end{pmatrix}. \tag{23}$$

Defining functions a and b by:

$$\sum_{i=1}^{4} T_i [J^\tau]^{-T} \nabla_{\xi\eta} N_i^\tau = \begin{pmatrix} a(\xi,\eta) \\ b(\xi,\eta) \end{pmatrix}, \tag{24}$$

the flux I (Eq. (22)) can be written as:

$$\begin{aligned} I &= \int_{\partial C_A \cap \tau} \alpha \left[a(\xi,\eta)\left(-\frac{\partial y}{\partial \xi} d\xi - \frac{\partial y}{\partial \eta} d\eta \right) + b(\xi,\eta)\left(\frac{\partial x}{\partial \xi} d\xi + \frac{\partial x}{\partial \eta} d\eta \right) \right] \\ &= \int_{mOm'} \alpha \left[\left(b(\xi,\eta)\frac{\partial x}{\partial \xi} - a(\xi,\eta)\frac{\partial y}{\partial \xi} \right) d\xi + \left(b(\xi,\eta)\frac{\partial x}{\partial \eta} - a(\xi,\eta)\frac{\partial y}{\partial \eta} \right) d\eta \right] \\ &= \int_{-1}^{0} \alpha \left(b(\xi,0)\frac{\partial x}{\partial \xi}(\xi,\eta) - a(\xi,0)\frac{\partial y}{\partial \xi}(\xi,\eta) \right) d\xi + \int_{0}^{-1} \alpha \left(b(0,\eta)\frac{\partial x}{\partial \eta}(\xi,\eta) - a(0,\eta)\frac{\partial y}{\partial \eta}(\xi,\eta) \right) d\eta \\ &= \int_{-1}^{0} f(\xi,0)\,d\xi + \int_{0}^{-1} g(0,\eta)\,d\eta. \end{aligned} \tag{25}$$

Once $a(\xi, \eta)$ and $b(\xi, \eta)$ are expressed analytically, the integral I can be computed using a Gauss integration with two points for the integrals for f and g. One finds [36] that the integral I is finally equivalent to:

$$I = \int_{\partial C_A \cap \tau} \alpha \nabla T \cdot n\,dl = \alpha \left[\frac{1}{2}(\nabla T_M + \nabla T_G) \cdot n_{MG} + \frac{1}{2}(\nabla T_G + \nabla T_{M'}) \cdot n_{GM'} \right]. \tag{26}$$

This discretisation is consistent on meshes composed of regular parallelograms [36]. The truncation error remains of order $O(h^2)$ on all other kinds of elements. On regular parallelograms, the scheme is monotonic if the elements are not too sheared and have a low aspect-ratio: the ratio between the element length and width must be lower than $\sqrt{3}$ and the minimum angle in the parallelogram ζ must satisfy $0 \leqslant \cos(\zeta) \leqslant 0.5$. This point is clearly a drawback for using this finite-element

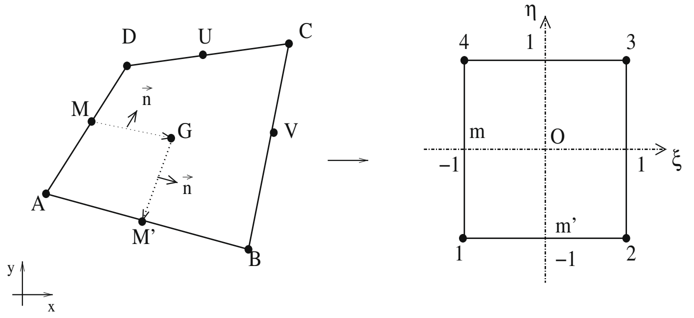

Fig. 6. Definition of the quadrilateral in classical coordinates and in iso-parametric ones. The arrow on the dual cell boundary of the left figure shows the integration direction and its normal unit vector *n*.

discretisation for high Reynolds number boundary layers where the element aspect-ratio can exceed 10^4. Moreover, for a hexahedron the computation of the diffusive flux on $\partial C_A \cap \tau$ requires the inversion of seven 3×3 Jacobian matrices. The numerical cost is therefore too large for practical applications.

In the following, this method will be denoted "EXact Finite-Element" approach (EXFE) as opposed to the "APproximated Finite-Element" method (APFE) presented in the following section.

5.6. Approximated finite-element reconstruction approach

It is the local and accurate evaluation of the gradient at the interface which bestows the good numerical properties to the EXFE method. Hence we seek a new method that uses locally varying gradients in the element, but gradients that are much less expensive and more robust to evaluate.

An obvious approach to nodal gradient computation is to use Green–Gauss integration over the primal mesh which has already been analysed by Coirier and Jorgenson [38]. Using the "centroidal path", an integration path over the forming nodes of both elements containing the interface leads to a rotated Laplacian with decoupled face neighbours, which gives rise to a checker-board instability and is inconsistent for meshes with strongly varying mesh size (stretching). This approach has been adopted by Khawaja et al. [25] and can lead to acceptable results, but Coirier demonstrates its robustness problems. As an alternative, one could reconstruct face gradients from a linear variation of the nodal gradients computed for the MUSCL scheme, equivalent to Coirier's "existing faces co-volume" approach. This approach leads to a non-compact stencil with decoupling of all immediate neighbours, resulting in a large number of spurious undamped modes. Using the "diamond" path where auxiliary state averages are computed at the barycentres leads to an inconsistent method on stretched meshes.

As an alternative approach to Green–Gauss integration, Papin's tessellation method calculates local facet gradients on "third elements" formed within the primal elements. However, the computation of a gradient for each facet does not offer any savings over the EXFE method and the tessellation can produce poor quality third elements on high aspect-ratio grids or can fail on non-convex elements.

As a novel approach, let us propose to evaluate nodal gradients in each element on a "third element" formed from the edges joined at that node. In the case of simplex elements this recovers the P^1 gradients of the EXFE formulation. In the case of primitive elements except one case this results in the third element being a simplex of all edges joining at that node. The exception case is the apex node of a pyramid where four edges join: in this case Green–Gauss integration over the pyramid seems appropriate. Note that the quality of these third elements centred at the nodes maintains the quality of the primal element and does not degrade under aspect-ratio as Papin's tessellation does. As a further approximation let us consider to base-facet gradients the average of the two nodal gradients at either end of the edge that the facet is attached to.

As an example, the gradient computation for node A for the two-dimensional quadrilateral in Fig. 6 would be based on the triangle ABD and equivalently for the other nodes.

The diffusion flux I (Eq. (22)) is then computed from:

$$I = \alpha \frac{\nabla T_D + \nabla T_A}{2} \cdot n_{MG} + \alpha \frac{\nabla T_A + \nabla T_B}{2} \cdot n_{GM'}. \tag{27}$$

A Taylor analysis shows that this scheme is conservative, and consistent on meshes composed of regular parallelograms. The truncation error remains of order $O(h^2)$ on all other kinds of elements, as for the EXFE method. On the other hand, the discretisation is monotonic on rectangles whatever their aspect-ratio.

5.7. Numerical experiments

The steady numerical solution is compared with the analytic solution for a pure heat diffusion problem on the square $[0,L] \times [0,L]$:

$$\int_{C_i} \frac{\partial T}{\partial t}\, dS = \int_{\partial C_i} \alpha \nabla T \cdot n\, dl, \tag{28}$$

with the constant diffusion coefficient α. In the following, $\alpha = 0.75$ has been used. Explicit time marching is used and local time steps are chosen according to stability restrictions for the heat equation. Dirichlet conditions are considered on the boundaries:

$$T_B(x,y) = \begin{cases} 0 & \forall x \in [0,L] \text{ and } y = 0, \\ \sin\left(\pi \frac{x}{L}\right) & \forall x \in [0,L] \text{ and } y = L, \\ 0 & \forall y \in [0,L] \text{ and } x = 0, \\ \sin\left(\pi \frac{y}{L}\right) & \forall y \in [0,L] \text{ and } x = L. \end{cases} \tag{29}$$

The exact stationary solution of the problem is:

$$u^{ex}(x,y) = \frac{1}{\sinh \pi}\left[\sinh\left(\pi \frac{x}{L}\right) \sin\left(\pi \frac{y}{L}\right) + \sinh\left(\pi \frac{y}{L}\right) \sin\left(\pi \frac{x}{L}\right)\right], \tag{30}$$

and is shown on Fig. 7.

The numerical error between exact and approximated solutions is measured in the L_2 norm using the following discrete expression:

$$\varepsilon = \left[\sum_{i=1}^{N_C} V_i \left(u_i^{ex} - u_i^{st}\right)^2\right]^{1/2}, \tag{31}$$

where u_i^{ex} is the exact solution value at node i, u_i^{st} the numerical solution value at node i, V_i the dual cell volume. Assuming a general error distribution ε such that $\varepsilon = O(h^p)$, where h is the element diameter, p is the order of accuracy of a chosen method on a sequence of refined meshes composed of the same kinds of elements. In practice, p is deduced from mesh convergence analysis of numerical results by:

$$\log(\varepsilon) = p\log(h) + C, \tag{32}$$

with C a constant.

The four proposed methods will be denoted with the acronyms defined in Table 1. On triangles, methods EXFE, APFE and CV reduce to the classical P^1 finite-element method and hence are denoted P^1 in these cases.

Four kinds of meshes are considered and are associated with acronyms defined in Table 2.

A view of the different kinds of meshes considered is shown on Fig. 8. The irregular perturbed meshes are obtained from the square-based one through the random process:

$$\begin{cases} x_{pert} = x_{sq} + \frac{h}{c} d_1, \\ y_{pert} = y_{sq} + \frac{h}{c} d_2, \end{cases} \tag{33}$$

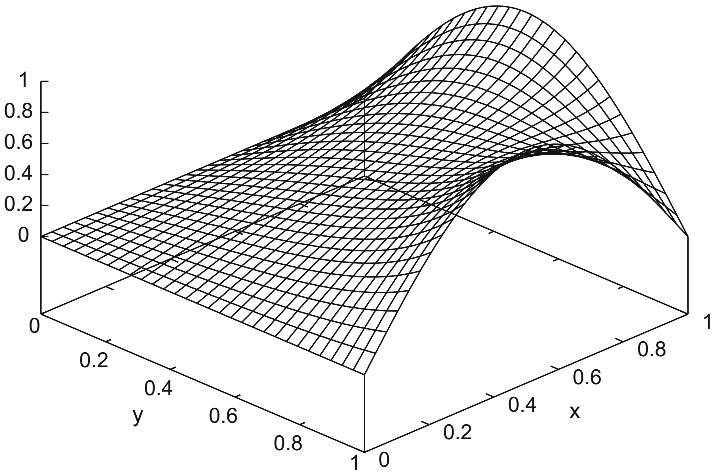

Fig. 7. Representation of the exact solution of the pure diffusion problem defined by Eqs. (28) and (29).

Table 1
Acronyms for the considered methods.

Acronym	Method for the gradient computation
EB	Edge-based method defined in Section 5.3
CV	Cell-vertex method defined in Section 5.4
EXFE	Exact finite-element method defined in Section 5.5
APFE	Approximated finite-element method defined in Section 5.6
P1	Classical P^1 finite-element method on triangles

Table 2
Acronyms for the considered meshes.

Acronym	Mesh
SQ	Mesh composed of regular squares
RE	Mesh composed of rectangles (two aspects ratio)
IQ	Mesh composed of irregular quadrilaterals
TR	Mesh composed of Delaunay-like triangles

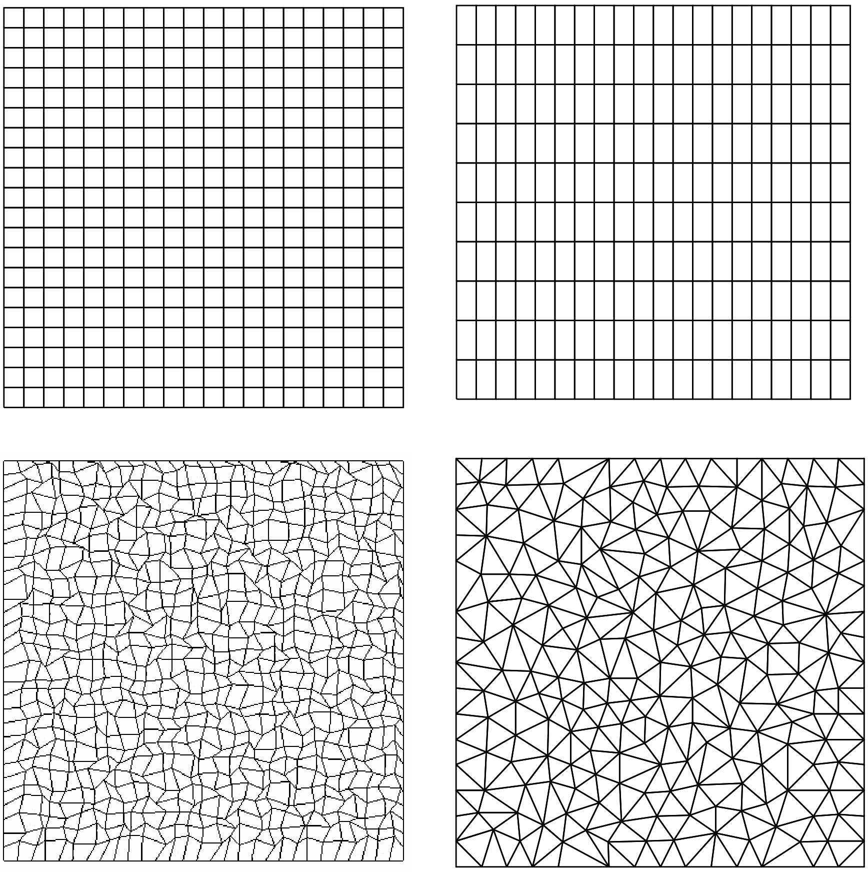

Fig. 8. Examples of meshes SQ, RE, TR and IQ, clockwise from top left.

where x_{sq} and y_{sq} are coordinates of the square-based mesh. d_1 and d_2 are random numbers defined in $[0,1]$, h is the element diameter and C is a coefficient chosen in order to have no reversed cells.

For each kind of mesh, three meshes are generated with three different element diameters. The pure diffusion test-case of Eq. (28) is solved with each of the four methods CV, EB, EXFE and APFE on all the meshes.

Fig. 9 presents the evolution of the logarithm of the error versus the logarithm of the element diameter for the different meshes, except for squares on which all discretisations are second-order accurate. The orders of accuracy obtained with the different discretisations are summarised in Table 3. In order to show the impact of the parameter δ_c for the CV method, two values are chosen. For method CVf, $\delta_c = 0.1$ is fixed while for method CVv, δ_c is the mean between maximum and minimum values of the stability interval (Eq. (20)).

The CV and APFE methods lose accuracy on perturbed quadrilateral meshes, but remain second-order accurate on triangular meshes. It can be observed that the accuracy of the EB method is particularly affected on the irregular quadrilaterals and triangular meshes. The EXFE method remains second-order accurate for meshes composed of triangles, of irregular quadrilaterals and of squares.

On rectangular meshes, high aspect ratios of 2 and 10 are tested. As for squares, the order of accuracy is about 2 for the CV methods, whatever the choice of the parameter δ_c (Eq. (18)). This is quite surprising for $\delta_c = 0.1$ which may not be in the stability interval of the CV method. The EB, APFE and EXFE methods are second-order accurate whatever the value of the aspect-ratio.

5.8. Linear preservation

Three methods arise as of most interest for the discretisation of viscous fluxes, namely the EXFE, APFE and EB methods. The CV methods will not be considered due to the lack of conservation. Here we test whether they are able to preserve an exact linear solution on a test-case suggested by Breil and Maire [39].

On the unit square $[0,1] \times [0,1]$, the heat equation with a constant diffusion coefficient equation (28) is solved with the following set of boundary conditions:

$$\begin{cases} T(x,y) = \begin{cases} 0 & \forall x \in [0,1] \text{ and } y = 0, \\ 0 & \forall x \in [0,1] \text{ and } y = 1, \end{cases} \\ \frac{\partial T}{\partial y} = \begin{cases} 0 & \forall y \in [0,1] \text{ and } x = 0, \\ 0 & \forall y \in [0,1] \text{ and } x = 1. \end{cases} \end{cases} \tag{34}$$

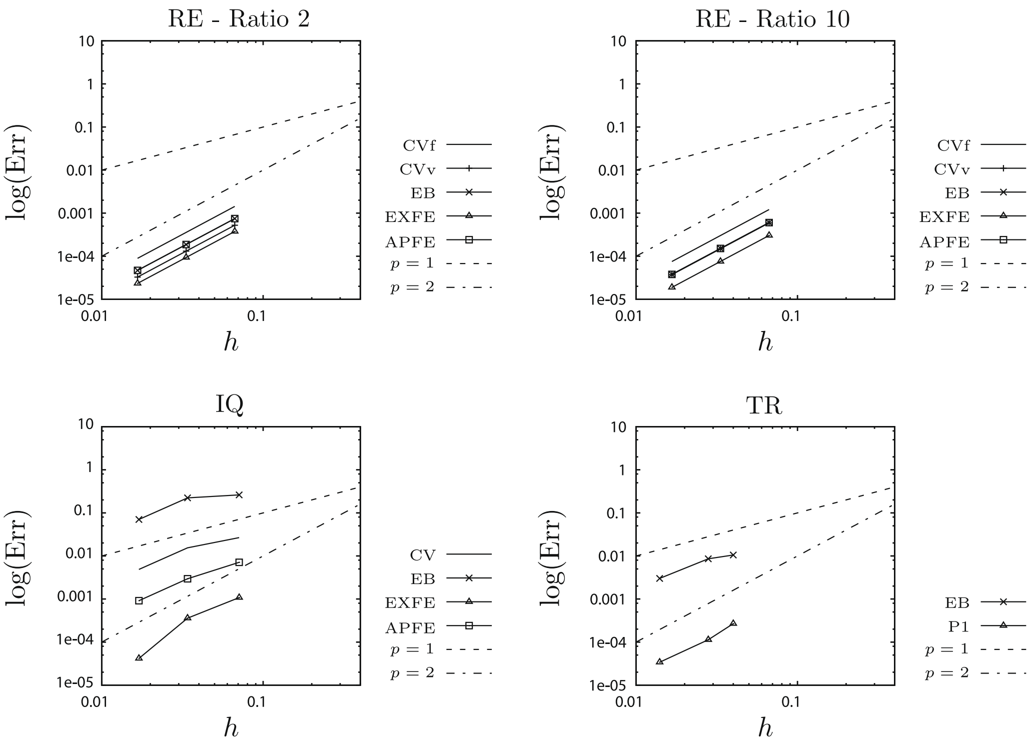

Fig. 9. Order p of convergence of the considered methods. On triangles, methods CV, APFE and EXFE are exactly the classical P^1 finite-element formulation.

Table 3
Order of accuracy according to mesh element types.

Element	CV		EB	EXFE	APFE
Square	2.01		2.01	2.00	1.98
Quadrilateral	1.18		0.92	2.27	1.44
Triangle	1.96		1.19	1.96	1.96
	$\delta_c = 0.1$	$\delta_c = f(h)$			
Rect., $r = 2$	2.00	1.998	1.999	2.001	1.998
Rect., $r = 10$	2.00	1.998	1.998	2.001	1.998

With the diffusion coefficient $\alpha = 1$, an exact analytical solution of Eq. (28), Eq. (34) is $T_{ex}(x, y) = x$.

Three meshes with square elements are considered based on a uniform discretisation in the x and y directions with 11, 21 and 41 nodes in each direction, resulting in diameters h of 0.1, 0.5 and 0.025.

Defining x_{sq} and y_{sq} as the coordinates of the nodes of a square-based mesh, a perturbed mesh is obtained with a smooth distortion using the following transformation:

$$\begin{cases} x_{pert} = x_{sq} + a_0 \sin(2\pi x_{sq}) \sin(2\pi y_{sq}), \\ y_{pert} = y_{sq} + a_0 \sin(2\pi x_{sq}) \sin(2\pi y_{sq}), \end{cases} \tag{35}$$

with the distortion parameter a_0. In the computations $a_0 = 0.1$ was used.

A perturbed mesh with an irregular distortion obtained through a random process is also considered. The transformation is the same as in Section 5.7, Eq. (33). Examples of square-based and perturbed meshes are shown in Fig. 10.

On the square-based meshes, the EXFE, APFE and EB methods reproduce the exact linear solution $T_{ex}(x, y) = x$. On the distorted meshes, the EXFE and APFE methods also reproduce the exact linear solution as shown in Fig. 11.

However, this is not the case for the EB method. As an example, an iso-line of the exact solution is compared with the same iso-line of the EB computation on Fig. 12.

Based on the L_2 norm of the error between the exact solution and the numerical one (Eq. (31)), the order of accuracy is about 1.9 on smoothly distorted meshes and reduces to about 1 on irregularly distorted meshes (Fig. 13). The correction added to the EB method for stability in the edge direction works well when the mesh and the diffusion direction are aligned. For the perturbed mesh, however, the correction induces a perturbation in the solution and a reduction in accuracy which depends on mesh quality.

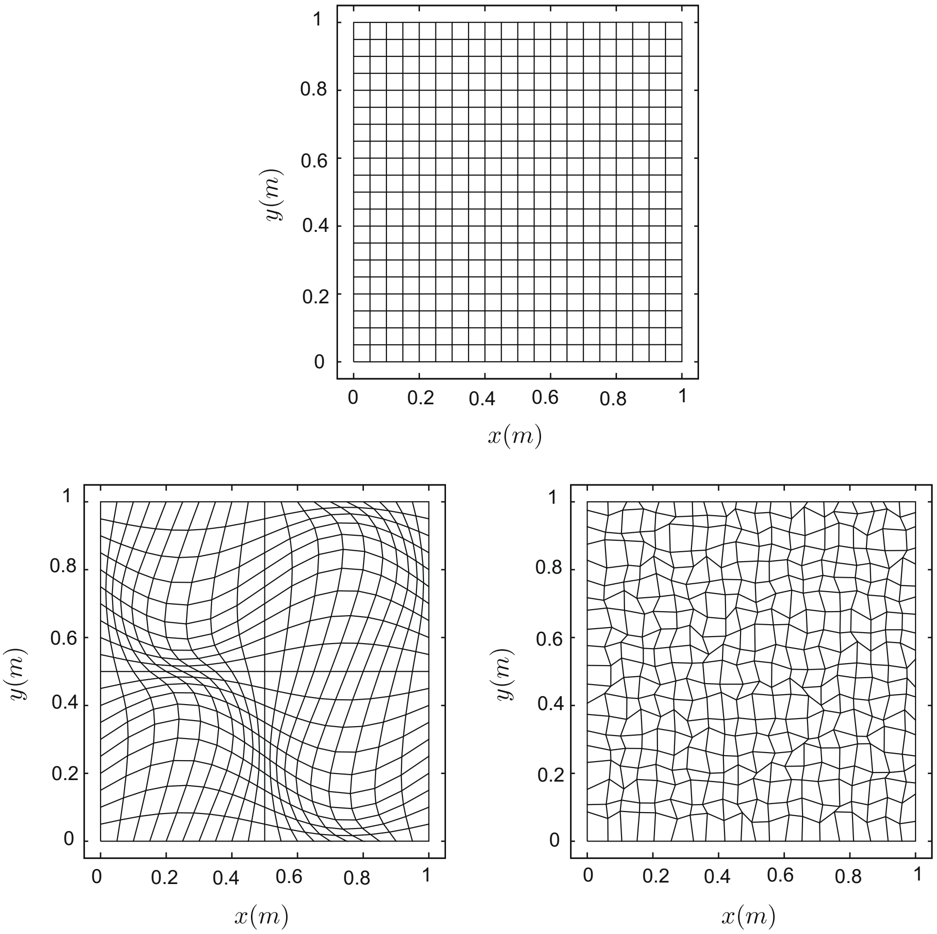

Fig. 10. Initial mesh composed of squares (up) and distorted ones obtained with Eq. (35) (bottom left) and Eq. (33) (bottom right). All meshes have 21 points in directions *x* and *y*.

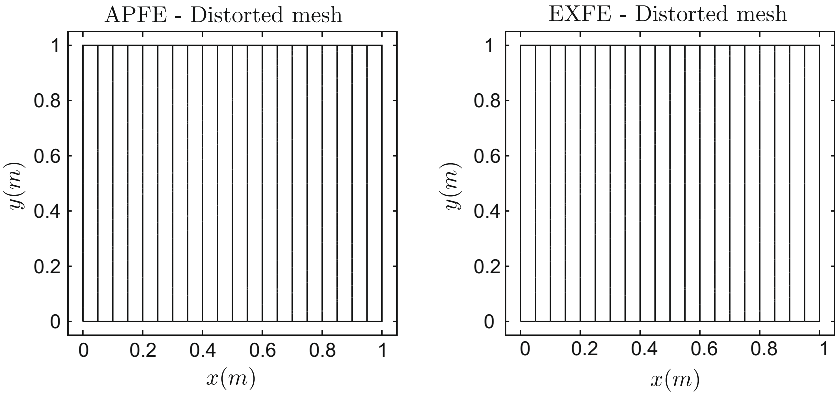

Fig. 11. Numerical solutions with APFE method on mesh composed of 20 × 20 distorted quadrilaterals (Eq. (35)) and with EXFE method on mesh composed of 20 × 20 distorted quadrilaterals (Eq. (33)).

Moreover, the numerical simulations show that the EB method allows the highest values of the CFL-like number, close to the maximum theoretical value for the linear heat equation of 0.5. Simulations with the EXFE approach require lowering the CFL-like number to 0.1 for the finest deformed mesh and 0.3 for the medium deformed mesh. The large values of CFL for the EB method may be explained by the high numerical diffusion of the scheme. For EXFE, the low CFL numbers are associated with the lack of monotonocity. Simulations with APFE method needs CFL-like numbers between those for EB and EXFE approaches.

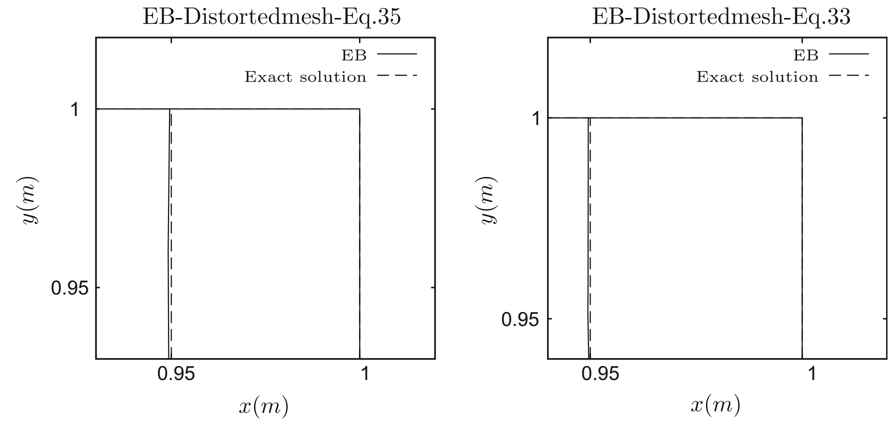

Fig. 12. Comparison of an iso-line of the temperature obtained with EB method and the same iso-line obtained with the exact solution on two meshes composed of 20 × 20 distorted quadrilaterals.

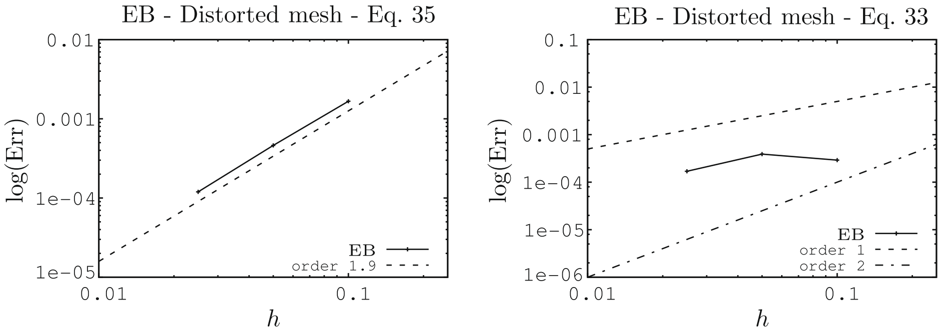

Fig. 13. Order *p* of convergence for the EB method on the distorted meshes.

5.9. Summary of the results for the heat equation

The results for the heat equation do not advise clearly against using a CV discretisation of the viscous fluxes: second-order of accuracy is obtained on smooth meshes composed of quadrilaterals. The lack of conservation is the main drawback of the method and it is the reason why the CV approach will not be considered in the following.

The EB method is very sensitive to grid irregularity. This may be a disadvantage on meshes from unstructured quadrilateral/hexahedral mesh generators with irregular elements and meshes produced with prismatic layers at the boundary extruded from surface triangulations. The method will perform well on regular structured grids which are aligned with the shear layers.

The best methods for the heat equation are the finite-element-based EXFE and APFE methods. The APFE method appears most suitable as it is only moderately less accurate on distorted quadrilaterals than EXFE method, but maintains full accuracy on high aspect-ratio elements. Both the EXFE and APFE methods are linear preserving on perturbed meshes where the EB method incurs a loss of accuracy.

6. Numerical results for the Navier–Stokes equations

After a short introduction to the base solver NSC2KE, the linearisation of the diffusion in the Navier–Stokes equations is discussed. Numerical results are presented for the flow over a laminar adiabatic flat plate and for the transonic turbulent flow over the RAE2822 airfoil.

6.1. NSC2KE solver

NSC2KE [9] is an unstructured vertex-based solver developed at INRIA (French National Agency for Research in Computer Science and Automation) and is freely available on the web [40]. NSC2KE uses a coupled finite-volume/finite-element technique to discretise convection and diffusion.

6.2. Non-linear diffusion

The diffusion coefficient in the RANS equations is not constant and a linearisation needs to be defined. Let us consider the two-dimensional configuration presented in Fig. 14 with the rectangle ABCD with barycentre *G*. *M*′, *V*, *U* and *M* refer to the midpoints of segments [*AB*], [*BC*], [*CD*] and [*DA*], respectively. To simplify the explanations, expressions will be given for the temperature gradient ∇T.

For a laminar computation with the EXFE scheme one has to compute the integral *I*:

$$I = \int_{[MG]} \lambda \nabla T n\, ds + \int_{[GM']} \lambda \nabla T n\, ds, \tag{36}$$

where $[MG]$ and $[GM']$ represent the facets of the dual cell C_A on the rectangle *ABCD*. The computation of Eq. (36) is based on a trapezoidal rule which guarantees second-order accuracy in the computation of the integral. This means that *I* is computed from:

$$I = \frac{\lambda_M + \lambda_G}{2} \frac{\nabla T_M + \nabla T_G}{2} n_{[MG]} + \frac{\lambda_G + \lambda_{M'}}{2} \frac{\nabla T_G + \nabla T_{M'}}{2} n_{[GM']}, \tag{37}$$

where *n* is the area-scaled facet normal. This linearisation is applied similarly to the other discretisations.

Alternative linearisations which interpolate the diffusion flux directly are possible and should be preferred in cases with strong gradients in the diffusion coefficients, in particular the formulation of Lörcher et al. [41] is based on the exact solution of a generalised diffusive Riemann problem. However, in order to demonstrate that the presented methods can be used in general existing finite-volume codes, we have conducted our numerical experiments with the formulation (Eq. (37)).

6.3. Laminar flat plate simulations

All computations with NSC2KE use the same parameters:

- a four-step Runge–Kutta explicit time stepping [9],
- local time steps account for convection and diffusion limits for stability,
- Roe's approximated Riemann solver [5],
- CFL number fixed at 0.5,
- inflow and outflow boundary conditions based on Steger–Warming flux splitting, as presented in [9].

6.3.1. Numerical and physical parameters

Laminar flow above an adiabatic wall is computed with NSC2KE. The flat plate is 1 m long, the inflow Mach number is $M_\infty = 0.8$ and the Reynolds number is $Re_\infty = 3 \times 10^4$. Four meshes are considered and are defined in Table 4. The mesh nodes are uniformly spaced in the tangential direction and a geometric law is applied in the direction normal to the plate. Table 4 lists the following properties of the meshes in the experiment:

- the distance between the first node above the wall and the wall, denoted *h*,
- the stretching *R* of successive cell heights,
- the number of nodes in the direction normal to the plate which fixes the domain height.

Each mesh has a triangular variant obtained by tessellation of the corresponding quadrilateral mesh. Meshes 3 based on rectangles and triangles are shown on Fig. 15.

6.3.2. Effect of diffusion schemes for rectangle-based meshes

In Fig. 16, the pressure and the friction coefficients distributions at the wall are shown for mesh 1 and mesh 4. Mesh 1 is not sufficiently refined to capture the compression near the leading edge, resulting in low values of C_p and an under-estimation of the friction coefficient C_f. All methods lead to very similar results. Good agreement is found between the theoretical law of Blasius for the friction coefficient and the numerical values for C_f. Similar results are obtained for meshes 2, 3 and 4 (results for meshes 2 and 3 are not presented).

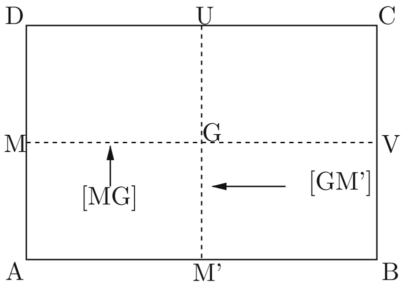

Fig. 14. Notations introduced for the non-linear diffusion explanations.

Table 4
Meshes definition for the laminar flat plate test-case.

Mesh name	Number of nodes on the plate	*h* (m)	*R*	Number of nodes normal to the plate
Mesh 1	51	1×10^{-3}	1.2	29
Mesh 2	51	2.5×10^{-4}	1.2	36
Mesh 3	51	5×10^{-5}	1.1	78
Mesh 4	51	2×10^{-5}	1.09	95

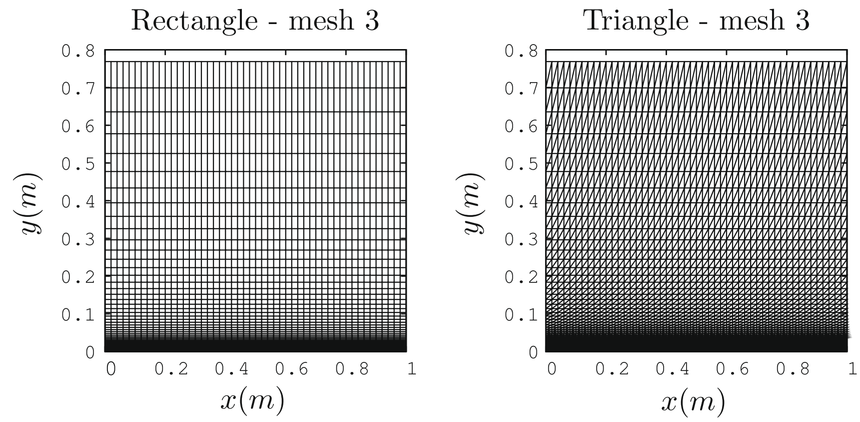

Fig. 15. Rectangle- and triangle-based meshes at refinement level 3 (Table 4).

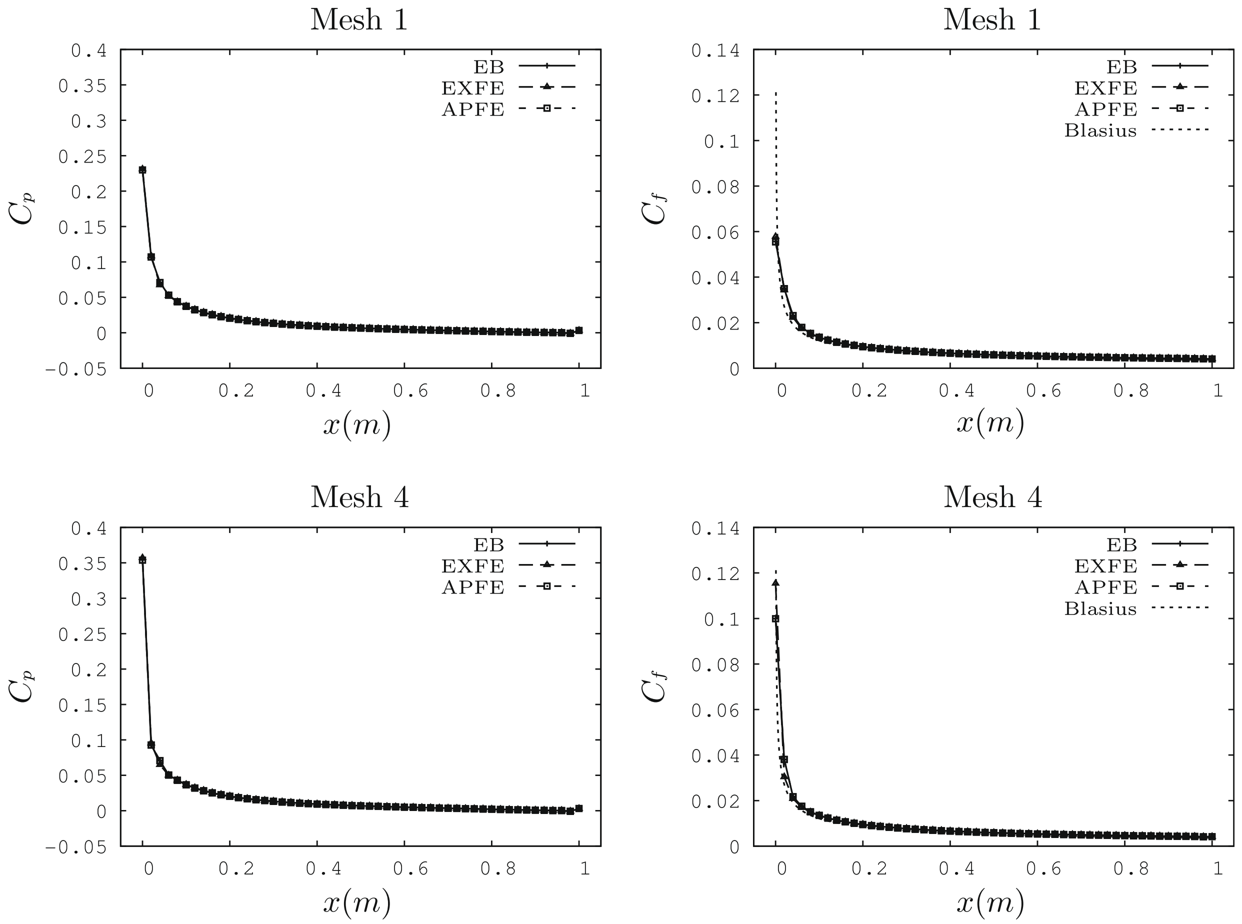

Fig. 16. Wall pressure and skin friction coefficients distribution obtained on meshes 1 and 4 composed of rectangles (second-order accuracy for the convection scheme).

6.3.3. Mesh refinement effect for method APFE

The results of a mesh convergence study for the APFE method are shown in Fig. 17. At sufficient distance from the leading edge the results are very close. Differences can be observed near the leading edge on the mesh 1 which is too coarse (Fig. 18).

6.3.4. Comparison of APFE solution on rectangles with P^1 finite-element on triangles

In this section, results obtained with the APFE method on the quadrilateral mesh 4 are compared with results obtained on its triangulated variant using the P^1 finite-element formulation (Table 4). Let us be reminded that on triangular meshes the APFE method reverts to the classical P^1 finite-element method. As shown on Fig. 19, differences occur near the leading edge. In this case, a rectangle-based mesh leads to the strongest compression, with a higher value of C_p and to a shorter expansion region. The EB scheme on triangular elements is strongly affected by the deformation of the control volume in the standard definition of the median dual volume which is used here. This effect may be reduced when using the 'containment circle' dual volume suggested by Barth [1], which connects the mid-edges to the containment circle rather than the barycentre, resulting in rectangular control volumes for this triangulated mesh.

Using a regular rectangle-based mesh improves the convergence rate (Fig. 20). The residual is normalised by the residual at iteration 1 and the simulation is terminated when the root mean square of the residual is smaller than 5×10^{-11}. The triangle-based mesh requires 3 times number of iterations to reach convergence compared to the rectangle-based mesh. On the rectangular-based mesh, the convergence for the EB and APFE methods is virtually identical. On a triangle-based mesh, the EB method converges slightly faster than the P^1 finite-element method, which is consistent with the slightly more diffusive nature of the EB solution. Moreover, as a quadrilateral mesh has fewer edges for the same number of nodes, the triangle-based mesh requires 3.4 times the CPU time obtained using the APFE method on mesh 4.

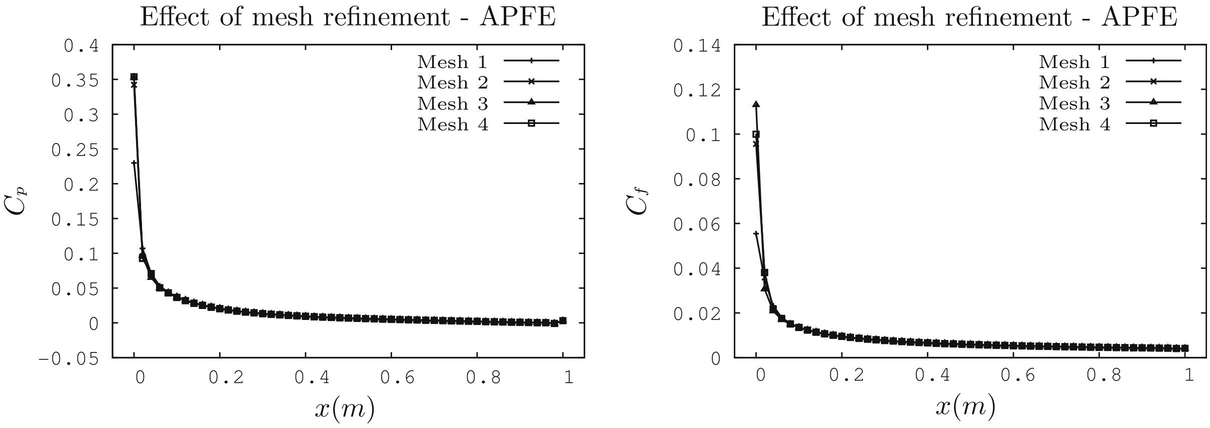

Fig. 17. Mesh convergence for the APFE method with second-order accuracy. Pressure coefficient (left hand side) and wall friction coefficient (right hand side).

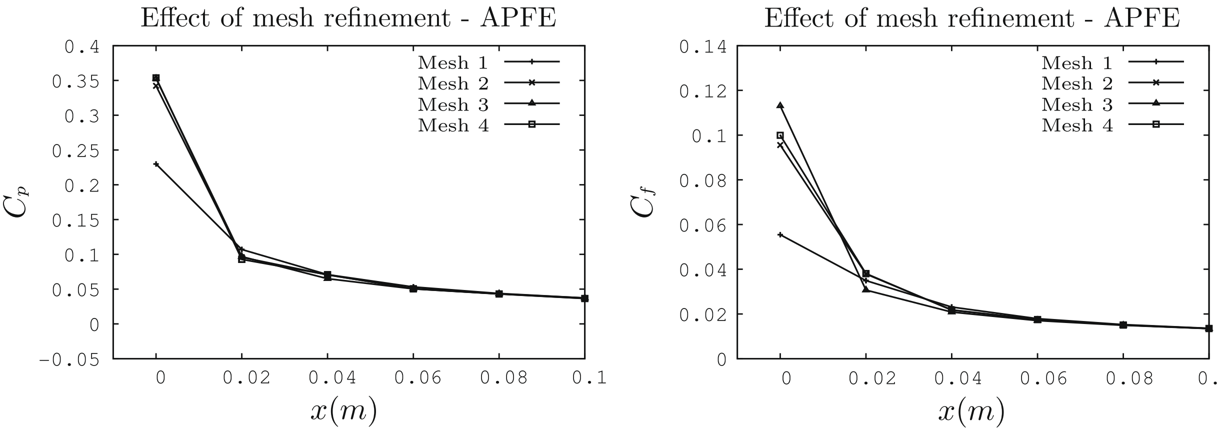

Fig. 18. Mesh convergence for the APFE method with second-order accuracy near the flat plate leading edge. Pressure coefficient (left hand side) and wall friction coefficient (right hand side).

6.3.5. Conclusions on the flat plate results

For the laminar flat plate only small differences can be observed in friction or wall-pressure coefficients between the classical P^1 finite-element method applied on triangles and the studied methods for rectangles. The EB, APFE and EXFE schemes exhibit good numerical properties for the laminar flat plate case. Rectangle-based meshes result in a gain in accuracy and an appreciable reduction in CPU time and number of iterations.

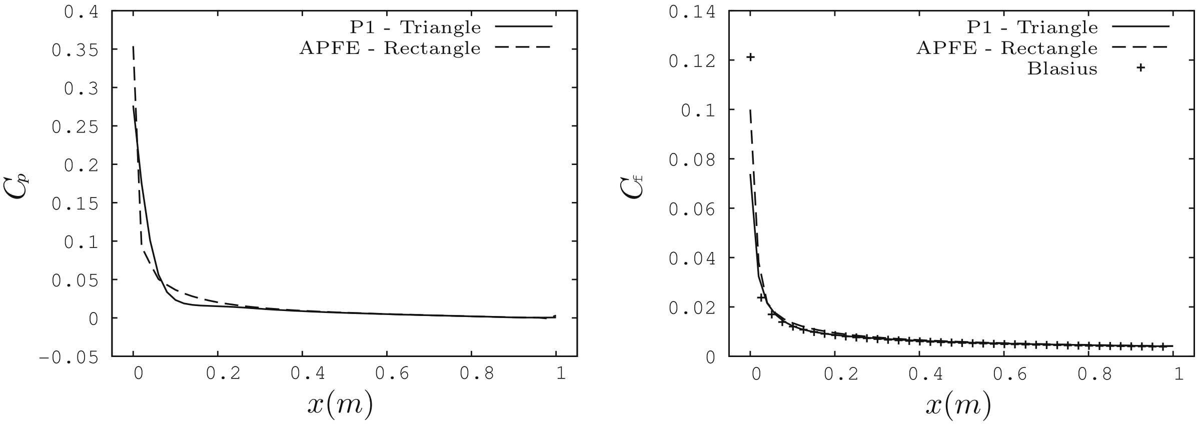

Fig. 19. Comparison of pressure coefficient obtained on triangle and rectangle mesh. Second-order accuracy for the convection scheme, mesh 4.

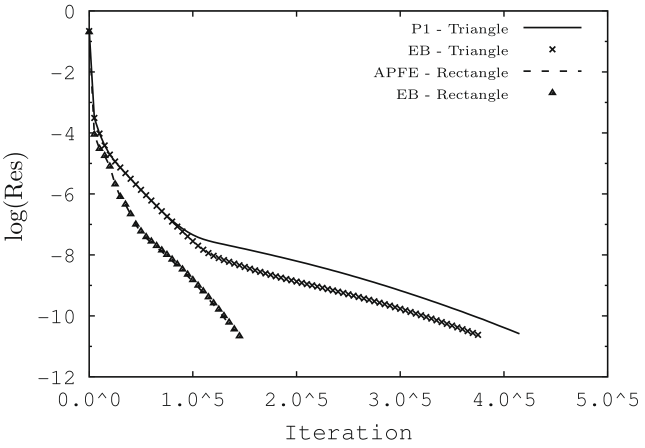

Fig. 20. Comparison of convergence obtained on the triangle and rectangle meshes with second-order accuracy.

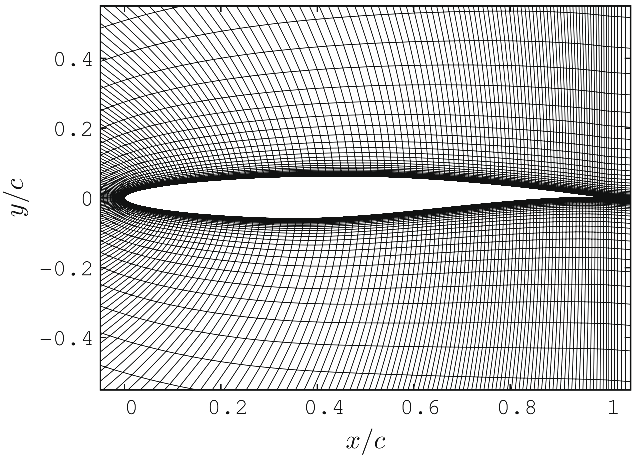

Fig. 21. RAE2822: partial view of the mesh.

6.4. Turbulent flow around the RAE2822 airfoil

The turbulent transonic flow over a RAE2822 profile is a well-documented test-case for which there are experimental data for the wall-pressure and skin-friction coefficients. The considered test-case is referenced as test-case 9 in [42]. The flow is fully attached to the adiabatic wall boundary and inflow variables are $M_\infty = 0.734$, $Re_\infty = 6.5 \times 10^6$ for a normalised chord

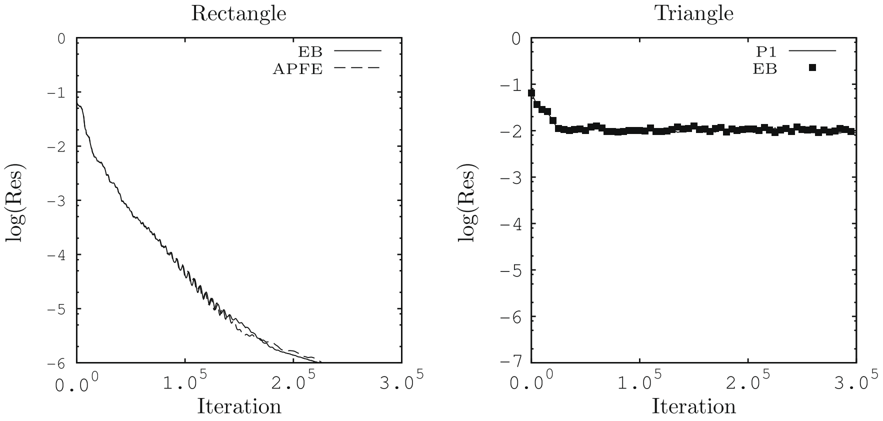

Fig. 22. RAE2822: convergence residuals on rectangle and triangle meshes.

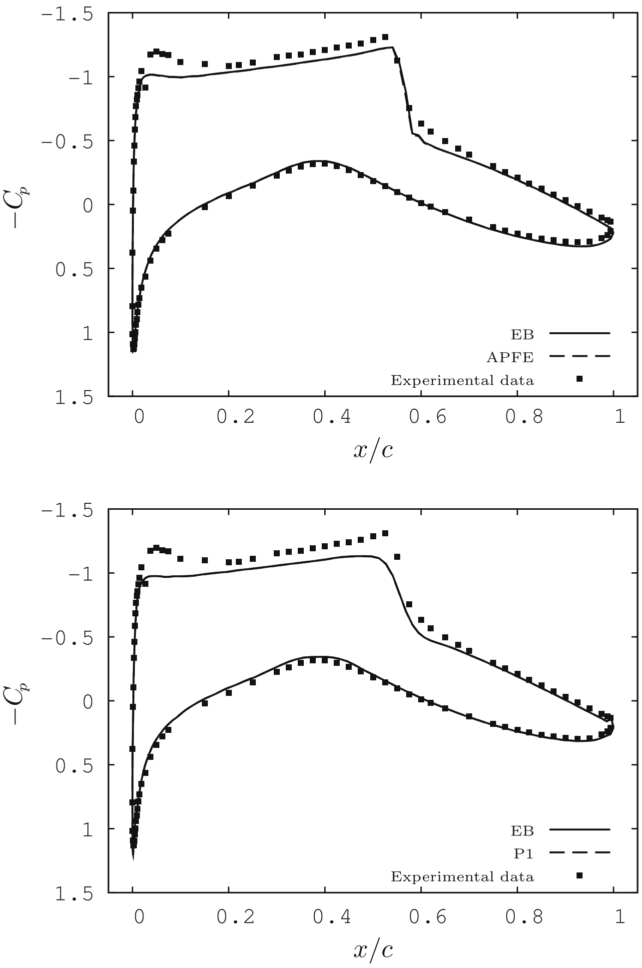

Fig. 23. RAE2822: pressure coefficient distribution on the wing for rectangle-based mesh (up) and triangle-based mesh (down).

of 1 m. The angle of attack is 2.54°. Compared with experimental values, inflow data are modified as prescribed by the EUROVAL validation project [43]. The turbulence modelling is based on a two-layer k—ε turbulence model [44]. As was done for the laminar flat plate, only the APFE, EB and EXFE methods are considered.

A partial view of the mesh is presented in Fig. 21. The triangle-based mesh is obtained by tessellation of the rectangle-based one. The numerical parameters chosen for the computations are:

- second-order Roe scheme with van Albada slope limiters,
- CFL = 0.1,
- four stage explicit Runge–Kutta time-integration scheme with local time stepping.

Convergence results are shown in Fig. 22 for rectangles and triangles for the EB and APFE methods. On triangular meshes the EB and P^1 finite-element methods converge only by an order of magnitude due to the deformed control volumes.

On quadrilateral meshes the EXFE computation does not converge when started from an initial solution based on the inflow state, even if the CFL number is strongly reduced: the computation leads to negative pressure and density. This can be linked to a lack of monotonicity as the mesh violates the monotonicity constraint on the element aspect-ratio, which is 9.9 near the leading edge, 148 near the trailing edge and exceeds 1000 in the mid-section. However, the EB and APFE method converge well and at similar rates.

The solution on the quadrilateral mesh is also very similar as shown in with the C_p profiles in Figs. 23 and 24 for the APFE and EB methods. This good performance is due to the strong alignment of shear layer and grid. However, the EB method cannot be expected to work similarly well for detached shear layers which are oblique to the grid. Figs. 23 and 24 also demonstrate that the shock is captured more sharply on the aligned quadrilateral mesh, a result well-known from Euler simulations.

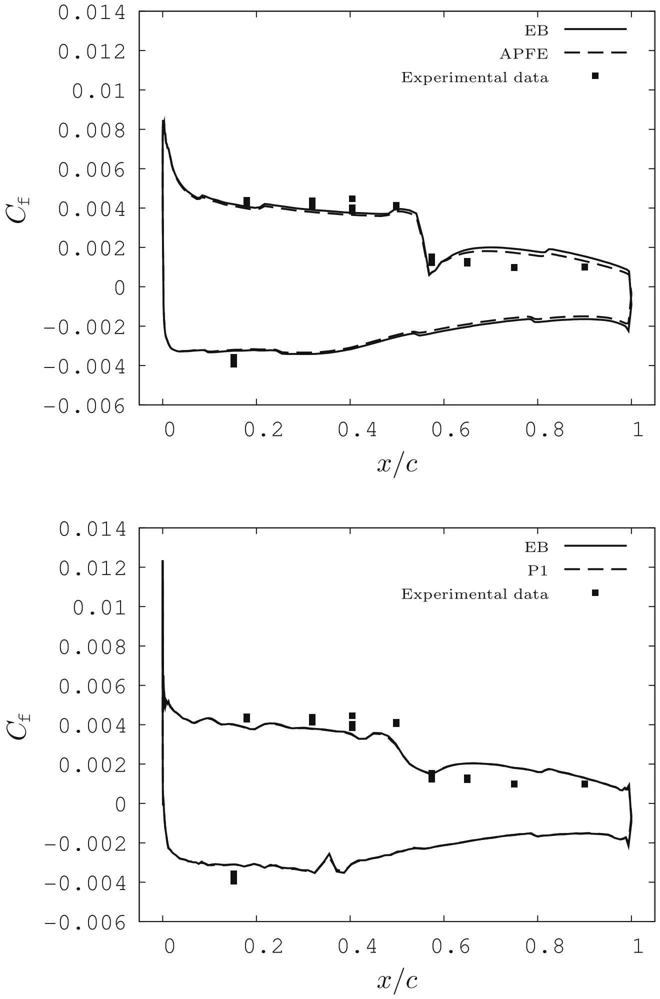

Fig. 24. RAE2822: skin friction coefficient distribution on the wing for rectangle-based mesh (up) and triangle-based mesh (down).

7. Conclusion

Four different approaches to model the diffusive fluxes on hybrid meshes have been studied and compared. The first one is based on a cell-vertex approximation (CV), the second one on an edge-based approach (EB) and the two last ones on finite-element reconstruction of the gradient (APFE and EXFE methods). The theoretical analysis of local consistence and monotonicity reveals that the methods based on a finite-element-like gradient reconstruction exhibit the best properties, which is confirmed by the numerical experiments with the linear heat equation. The cell-vertex method needs a corrective term to be monotonic which makes the formulation non-conservative. The edge-based method is second-order accurate on regular isotropic parallelograms, but only of order one on irregular and on high aspect-ratio meshes.

The methods based on finite-element reconstruction are consistent on meshes composed of regular parallelograms and their truncation error is of order $O(h^2)$. These methods reduce to the classical P^1 finite-element formulation on triangles and tetrahedra, which is desirable for the extension of simplex solvers as their behaviour on simplex meshes remains unaltered.

The exact (EXFE) and approximated finite-element (APFE) methods however perform differently on high aspect-ratio meshes. The EXFE method is monotonic on parallelograms with a ratio between the length and width below $\sqrt{3}$ and the angle of the parallelogram ζ bounded as $0 \leqslant \cos(\zeta) \leqslant 0.5$. The APFE method is monotonic on any regular mesh and maintains second-order accuracy on high aspect-ratio rectangles.

The exact and approximated finite-element approaches (APFE, EXFE) are the only methods which can recover exactly the linear solution on a smoothly distorted isotropic mesh, while the order of accuracy for the edge-based (EB) method drops below second-order.

The conservative methods EB, APFE and EXFE have been implemented in the Navier–Stokes solver NSC2KE and results have been obtained for the RANS equations coupled with a two-layer $k-\varepsilon$ turbulence model using an aligned regular grid. The use of a mesh composed of rectangles leads to an increase of the precision of gradient-based quantities such as wall friction. On the high aspect-ratio quadrilateral mesh, the exact finite-element (EXFE) approach fails to converge due to a lack of monotonicity. The boundary layer is computed with similar accuracy by both the approximated finite-element and edge-based methods and with similar convergence rates. This is certainly due to the strong alignment of the flow and the mesh. This result may not hold for shear layers that are oblique to the mesh as often arise in detached flows or for hybrid meshes with less regularity in the shear layers.

References

[1] T. Barth, Aspects of unstructured grids and finite-volume solvers for the Euler and Navier–Stokes equations, in: VKI Lecture Series 1994-05, Von Kármán Institute, Rhode-St.-Genèse, Belgium, 1995.
[2] P. Roe, The influence of mesh quality on solution accuracy, in: 19th VKI Lecture Series on Computational Fluid Dynamics 1989-04, Von Kármán Institute, Rhode-St.-Genèse, Belgium, 1989.
[3] A. Dervieux, Steady Euler simulations using unstructured meshes, in: 16th VKI Lecture Series on Computational Fluid Dynamics 1985-04, Von Kármán Institute, Rhode-St.-Genèse, Belgium, 1985.
[4] P. Rostand, B. Stoufflet, Finite volume Galerkin methods for viscous gas dynamics, Tech. Rep. RR-863, INRIA (1988).
[5] P.L. Roe, Approximate Riemann solvers, parameter vectors and difference schemes, Journal of Computational Physics 43 (2) (1981) 357–372.
[6] A. Dervieux, Steady Euler simulations using unstructured meshes, in: J. Geymonat (Ed.), Partial differential Equations of hyperbolic type and Applications, World Scientific, 1987, pp. 34–112 (Ch. 2).
[7] B. Stoufflet, J. Periaux, F. Fezoui, A. Dervieux, 3D hypersonic Euler numerical simulations around space vehicles usinf adapted finite elements, in: 25th Aerospace Sciences Meeting and Exhibit, AIAA Paper 86-0560, 1986.
[8] F. Fezoui, B. Stoufflet, A class of implicit upwind schemes for Euler simulations with unstructured meshes, Journal of Computational Physics 84 (1) (1989) 174–206.
[9] B. Mohammadi, Fluid dynamics computation with NSC2KE. An user-guide. Release 1.0., Tech. Rep. RT-0164, INRIA (1994).
[10] R. Eymard, T. Gallouët, R. Herbin, Finite volume methods, in: P. Ciarlet, J. Lions (Eds.), Handbook of Numerical Analysis, vol. VII, North Holland, 2000, pp. 713–1020.
[11] V. Billey, J. Periaux, B. Stoufflet, A. Dervieux, L. Fezoui, V. Selmin, Recent improvements in Galerkin and upwind Euler solvers and application to 3D transonic flow in aircraft design, Computer Methods in Applied Mechanics and Engineering 75 (1–3) (1989) 409–414.
[12] D.J. Mavriplis, V. Venkatakrishnan, A unified multigrid solver for the Navier–Stokes equations on mixed element meshes, International Journal of Computational Fluid Dynamics 8 (4) (1997) 247–263.
[13] P. Moinier, J. Müller, M. Giles, Edge-based multigrid schemes and preconditioning for hybrid grids, AIAA Journal 40 (10) (2002) 1954–1960.
[14] A. Haselbacher, J. McGuirk, G. Page, Finite volume discretization aspects for viscous flows on mixed unstructured grids, AIAA Journal 37 (2) (1999) 177–184.
[15] M. Galle, Unstructured viscous flow solution using adaptive hybrid grids, ICASE/LaRC workshop on adaptive grid methods, NASA Langley Research Center (1995).
[16] P. Crumpton, P. Moinier, M. Giles, An unstructured algorithm for high Reynolds number flows on highly stretched grids, in: C. Taylor, J.T. Cross (Eds.), Numerical Methods in Laminar and Turbulent Flow, Pineridge Press, 1997, pp. 561–572.
[17] R. Eymard, T. Gallouët, R. Herbin, Finite volume approximation of elliptic problems and convergence of an approximate gradient, Applied Numerical Mathematics 37 (2001) 31–53.
[18] P. Crumpton, J. Mackenzie, K. Morton, Cell vertex algorithms for the compressible Navier–Stokes equations, Journal of Computational Physics 109 (1) (1993) 1–15.
[19] O. Colin, A finite element operator for diffusion terms in AVBP, Tech. Rep., Institut Français du Pétrole (2003).
[20] CERFACS CFD Team, The AVBP handbook, Tech. Rep., CERFACS (2007).
[21] D. Pan, J. Cheng, Upwind finite-volume Navier–Stokes computation on unstructured triangular meshes, AIAA Journal 31 (9) (1993) 1618–1625.
[22] L. Flandrin, P. Charrier, B. Dubroca, A robust finite-volume method for computations of two-dimensional unstructured hybrid meshes, in: S. Wagner, E.H. Hirschel, J. Priaux, R. Riva (Eds.), Computational Fluid Dynamics'94, Wiley, New York, 1994, pp. 301–308.
[23] J. Coirier, An adaptatively-refined, cartesian, cell-based scheme for the Euler and Navier–Stokes equations, Tech. Rep. TM-106754, NASA (1994).
[24] K. Lipnikov, D. Svyatskiy, Y. Vassilevski, Interpolation-free monotone finite volume method for diffusion equations on polygonal meshes, Journal of Computational Physics 228 (3) (2009) 703–716.

[25] A. Khawaja, Y. Kallinderis, V. Parthasarathy, Implementation of adaptive hybrid grids for 3D turbulent flows, in: AIAA, 34th Aerospace Sciences Meeting and Exhibit, AIAA Paper 96-0026, Reno, January 1996.
[26] O. Peroomian, S. Chakravarthy, U. Goldberg, A 'grid-transparent' methodology for CFD, in: AIAA, 35th Aerospace Sciences Meeting and Exhibit, AIAA Paper 97-0724, Reno, January 1997.
[27] M. Papin, Contribution à la modélisation d'écoulements hypersoniques particulaires. Etude et validation d'un modèle diphasique discret., Ph.D. Thesis, Université de Sciences et Technologies de Bordeaux 1 (2005).
[28] W. Reed, T. Hill, Triangular mesh methods for the neutron transport equation, Tech. Rep. LA-UR-73-479, Los Alamos Scientific Laboratory (1973).
[29] J. Nitsche, Über ein Variationsprinzip zur Lösung von Dirichlet-Problemem bei Verwendung von Teilräumen, die keinen Ransbedingungen unterworfen sind, in: Abhandlungen aus dem mathematischen Seminar der Unisertität Hamburg, No. 36, 1971, pp. 200–212.
[30] B. Cockburn, C. Shu, Tvb Runge–Kutta local projection discontinuous Galerkin finite element method for conservation laws. II: General framework, Mathematics of Computation 52 (186) (1989) 411–435.
[31] B. van Leer, Towards the ultimate conservative difference scheme. V. A second-order sequel to Godunov's method, Journal of Computational Physics 32 (1) (1979) 101–136.
[32] D. Arnold, F. Brezzi, B. Cockburn, L. Marini, Unified analysis of discontinuous Galerkin methods for elliptic problems, SIAM Journal of Numerical Analysis 39 (5) (2002) 1749–1779.
[33] M. Zhang, C. Shu, An analysis of three different formulations of the discontinuous Galerkin method for diffusion equations, Mathematical Models and Methods in Applied Sciences 13 (3) (2003) 395–413.
[34] B. van Leer, S. Nomura, Discontinuous Galerkin for diffusion, in: 17th AIAA Computational Fluid Dynamics Conference, AIAA Paper 2005-5108, 2005.
[35] G. Gassner, F. Lörcher, C. Munz, A contribution to the construction of diffusion fluxes for finite volume and discontinuous Galerkin schemes, Journal of Computational Physics 224 (2) (2007) 1049–1063.
[36] V. Auffray, Étude comparative de schémas numériques pour la modélisation de phénomènes diffusifs sur maillages hybrides, Ph.D. Thesis, Institut National Polytechnique de Toulouse (2007).
[37] T. Schönfeld, M. Rudgyard, Steady and unsteady flows simulations using the hybrid flow solver AVBP, AIAA Journal 37 (11) (1999) 1378–1385.
[38] J. Coirier, C.P. Jorgenson, A mixed volume grid approach for the Euler and Navier–Stokes equations, in: AIAA, 34th Aerospace Sciences Meeting and Exhibit, Reno, AIAA Paper 96-0762, January 1996.
[39] J. Breil, P.-H. Maire, A cell-centered diffusion scheme on two-dimensional unstructured meshes, Journal of Computational Physics 224 (2) (2007) 785–823.
[40] Source files of NSC2KE. <http://pauillac.inria.fr/cdrom/www/nsc2ke/eng.htm>.
[41] F. Lörcher, G. Gassner, C. Munz, An explicit discontinuous Galerkin scheme with local time-stepping for general unsteady diffusion equations, Journal of Computational Physics 227 (11) (2008) 5649–5670.
[42] T. Hellström, L. Davidson, A. Rizzi, Reynolds stress transport modelling of transonic flow around the RAE2822 airfoil, in: AIAA, 32nd Aerospace Sciences Meeting, Reno, AIAA Paper 94-0309, January 1994.
[43] An European initiative on validation of CFD-codes, in: W. Haase, F. Brandsma, E. Elsholtz, M. Leschziner, D. Schwamborn (Eds.), Notes on Numerical Fluid Mechanics, Vieweg Verlag, 1993.
[44] B. Mohammadi, Complex turbulent flows computation with a two-layer approach, International Journal for Numerical Methods in Fluids 15 (7) (1992) 747–771.